Abundances of Lithium, Beryllium and Boron in Phenocrysts from Santorini Volcano (Greece): Implications on Magma Genesis and Eruption Mechanisms

INAUGURAL-DISSERTATION
zur Erlangung der Doktorwürde
der Naturwissenschaftlich-Mathematischen Gesamtfakultät
der Ruprecht-Karls-Universität
Heidelberg

vorgelegt von
Master of Science in Geology
Ma. Edweena Joan Alincastre Cabato
aus Iloilo, Philippinen

Heidelberg, im Dezember 2006

Gutachter:
Prof. Dr. Rainer Altherr
Prof. Dr. Alan Woodland

Tag der mündlichen Prüfung: 07.02.2007

Gedruckt mit Unterstützung
des Deutschen Akademischen Austauschdienstes

"But if of ships I now should sing, what ship would come to me,
What ship would bear me ever back across so wide a sea?"

(Galadriel singing to the winds; JRR Tolkien)

Contents

ACKNOWLEDGEMENT

My warmest gratitude to those who have made, and still make, my "deutsches Abenteuer" a pleasant and worthwhile one. Being away from the tropical home for the first time, for a long time, could prove difficult. That is, until one meets friends, colleagues and Professors who let you ease into "normal life" while earning the degree.

I sincerely thank Prof. Rainer Altherr for the privilege of pursuing my doctorate studies here in Heidelberg, for his guidance and patience throughout the duration of this work.

...Thomas Ludwig and Peter Meyer for always being helpful with the machines and other "technical" problems. Also Alexander Varychev, who tutored SEM sessions.

...Iris, Emily, Zackie, Sonja, George and Paula for making days more sunny than they sometimes really are …Jens Hopp, who often says something sensible about work. Also those who have moved on to other places: Melanie, Uschie, Stephan Klemme, Stephan Prowatke, Horst and Angela …Maren and Katrin, for Mathematica and coffee.

...Oliver and Ilona for not losing their cool when asked for the nth time to polish thin sections, sometimes in a hurry, so I could do SIMS analysis again …and again.

I am grateful to the other professors for being an encouragement and an inspiration, including the members of my thesis committee who remained despite the delays.

I used the LA-ICPMS facility at the Institut für Mineralogie in Frankfurt and thank Yann Lahaye for that opportunity. I did not include the data in this work, though.

I thank Nadja and Klaus, who are like foster parents to me; Jutta and Joe for being great friends, not to mention Jutta being a super-teacher! Mylin, Angelyn and Rilag for being my sisters here, and good old friends in Frankfurt who always have a dash of Pinoy.

Thanks Connie, for the steadfast, although quiet, support... Martina and Annette too, and Alicia and Helena. And all the great people in church! Jerry, Pierrot… Thanks Sonja and Merle, former and current housies, for maintaining nice living conditions.

Thanks so much Pa, Ma, Peep, Bam, Ba, Boo, Tab, Bette – you always pray and want the best for me. Thanks little ones for forgiving Tita when she forgets your birthdays because she's just disorganised, beneath the pretence of intense thesis work. I love you, Lord, for taking good care of all of us no matter where we are on earth and in life.

Thank you, Ian, for standing by me. For making me see beyond human frailty and prejudice. Thanks Mariton, Hazel, Kin, Joel for keeping me sane ...somehow.

Thanks Doc Tolits, Ando and Kelvin, for the continued support across the miles.

I am here through a scholarship grant from DAAD, which I truly appreciate.

This effort is for the Filipino people, survivors of volcanoes, amongst many things!

ABSTRACT

Volcanic eruptions remain a crucial part of human existence, yet many aspects of volcanic systems continue to elude comprehension. The frontier of geochemistry therefore, is also occupied with new tools and schemes to explain more of the magmatic enigma. Among these new approaches is the use of the light elements lithium, beryllium and boron and their isotopes: incompatible in common mineral phases in the magma and sensitive as tracers of source components and material recycling in subduction zones.

Analyses through Secondary Ion Mass Spectrometry (SIMS) yield Li, Be and B concentration and δ^7Li profiles that have extraordinary implications on our present knowledge of crystal formation and volcanic eruptions. Populations of plagioclase, pyroxene and olivine phenocrysts in the Nea Kameni dacites and Thera andesites reveal complex and disparate crystallisation histories suggestive of magma injection, mixing and/or mingling. These processes are of particular importance in understanding volcanic systems because mafic intrusions may trigger explosive silicic eruptions, as already observed in several volcanoes.

An even more significant, and no less surprising, offshoot of light element analyses in this study are the estimates for magma residence time using certain plagioclase phenocrysts. If our present knowledge of Li diffusion and partition coefficients were correct, data on these phenocrysts suggest very short residence times that could preserve primary Li abundances in entire crystals or their overgrowths. Such indicate extremely rapid crystallisation, occurring within hours, possibly due to decompression and degassing, immediately before or even during eruption.

Being one of the first attempts at investigating the behaviour of the three lithophile light elements in situ and in detail, this work further attests to the affluence of information to be derived from phenocrysts. These may start to form early in the magma and continue to grow through varying physico-chemical conditions, forming an archive of crystallisation histories and magma geneses. Hence, these phenocrysts contribute not only to our understanding of the volcanic centre being considered, but would have implications on similar magma systems as well. It is therefore also the aim of this study to forge further investigations on crystals or inclusions, which could yield information that would otherwise be lost in bulk analyses. Through such meticulous work we shall definitely learn more about the driving mechanisms within volcanoes. For some people, this could mean avoiding life-threatening outbursts.

Kurzfassung

Vulkaneruptionen stellen nach wie vor eine für den Menschen natürliche Bedrohung dar. Nicht zuletzt deshalb stehen vulkanische Systeme noch immer im Blickpunkt geowissenschaftlicher Forschung. Dies gilt auch für den Bereich der Geochemie, die fortwährend neue „Werkzeuge“ entdeckt, mit denen die Prozesse der Magmenentstehung und –veränderung erhellt werden können. Hierzu gehören die leichten Elemente Lithium, Beryllium und Bor und ihre Isotope. Diese Elemente verhalten sich bezüglich der meisten magmatischen Minerale inkompatibel und stellen empfindliche Tracer für Magma-Eduktkomponenten und den Stofftransfer in Subduktionszonen dar.

Mit Hilfe von Sekundärionenmassenspektrometrie können die Konzentrationen von Li, Be und B sowie die δ^7Li-Werte in Phänokristen von Vulkaniten und teilweise auch in deren Matrix ortsaufgelöst bestimmt werden. Entsprechende Profile durch Querschnitte von Phänokristen stellen wichtige Informationsquellen für die magmatische Kristallisation und anschließende Eruption in vulkanischen Systemen dar. Populationen von Plagioklas-, Pyroxen- und Olivin-Einsprenglingen in Daziten von Nea Kameni und Andesiten von Thera (Santorin-Vulkankomplex, Ägäis) enthüllen komplexe und verschiedene Kristallisationsgeschichten, die auf Magma-Nachschub und Magma-Mischung hinweisen. Diese Prozesse sind für das Verständnis vulkanischer Systeme besonders wichtig, da nach allgemeiner Ansicht der Nachschub basischen Magmas in eine bereits differenzierte Magmakammer zur Eruption führen kann.

Ein weiterer Aspekt der in dieser Studie durchgeführten ortsaufgelösten Analyse der leichten Elemente ist die Möglichkeit, aus den Konzentrations- und Isotopen-Profilen Rückschlüsse auf die Magma-Verweilzeiten einzelner komplexer Phänokristalle zu ziehen. Sofern unsere derzeitige Kenntnis des Verteilungsverhaltens von Li zwischen Plagioklas und Schmelzen sowie der Diffusivität von Lithium in Plagioklas richtig ist, lassen die hier gewonnenen Daten keinen anderen Schluß zu als dass die Magma-Verweilzeiten sehr kurz (in der Größenordnung von wenigen Stunden) sind. Dies wiederum impliziert schnelle Kristallisation, höchstwahrscheinlich getriggert durch Dekompression und Entgasung des Magmas.

Diese Studie ist einer der ersten Versuche, das Verhalten der leichten Elemente in vulkanischen Systemen im Detail aufzuklären. Die Kerne der Phänokristen können früh gebildet sein, weiteres Wachstum kann dann bei sich ändernden physiko-chemischen Bedingungen erfolgen, vielleicht sogar syn-eruptiv. Somit tragen diese komplex zusammengesetzten Phänokristalle nicht nur zum Verständnis einzelner Vulkane bei, sondern lassen sich verallgemeinern. Diese Studie sollte dazu anregen, weitere detaillierte Untersuchungen an Phänokristallen und Glaseinschlüssen durchzuführen, da hierdurch Erkenntnisse zu erwarten sind, die mit chemischer Analyse von Gesamtgesteinsproben nicht zu erlangen sind. Hierdurch werden wir mehr über die Prozesse im Inneren von Vulkanen lernen und somit zur Minderung des Risikos durch Vulkaneruptionen beitragen.

1. INTRODUCTION

Volcanoes have always been objects of fascination and awe, the best manifestations of our dynamic, if sometimes unpredictable, planet. As far back as the beginnings of human existence, curiosity about these fiery mountains and the utter need to escape their dangers, have fuelled thought and theory, exploration and experiment. To the most part volcanoes have been identified and classified, their eruptions characterised, their products scrutinised, and even solutions to their aftermaths drawn out. But many questions remain of the magma yet beneath the surface and the inner workings that lead to outbursts. Conditions in the magma chamber, processes through plumbing systems, even the very nature of materials before they are extruded as lavas or fragments to the more familiar visible realm – much of these remain speculative. Where such "hidden" aspects are concerned, we sometimes find ourselves in a state akin to man's earliest curiosity.

This is not to say that our understanding of the internal intricacies of volcanoes has not progressed at all. Indeed, seismic data, tomography, telluric studies and petrology have been used to probe deeper into volcanoes. But the search continues to find the best clues. A good candidate for such investigation are phenocrysts in volcanic rocks, which may form early in the magma chambers and/or conduits. These crystals record magmatic history as they grow, and although portions may be dissolved and overprinted by physico-chemical fluctuations, the overall evolution of the magma may be followed all the way through ascent and eruption. Compositional variations within each crystal reflect certain regimes: e.g., sluggish elements reveal early crystallisation events, while rapidly diffusing ones reflect the last stages of crystal formation. The latter are useful tools for geospeedometry and provide insights for our concerned efforts to predict magma residence times, specifically addressed in this study, and the ensuing volcanic activity. Moreover, studying several phenocrysts of different phases and differing compositional trends is like having pieces of a puzzle; putting them together may yield a coherent, although possibly complex, picture that elucidates at least certain aspects of the magmatic enigma.

Santorini being an active volcano along the Hellenic Arc, an investigation of the phenocrysts of its eruption products would reflect the complexities of magmatism in convergent margins, including implications on source components and material recycling. In this study, porphyritic to glomeroporphyritic volcanic rock samples were taken from the pre-caldera units on the main island of Thera and the lava flows on the post-caldera island of Nea Kameni, thus allowing examination of both andesitic and dacitic systems, respectively.

Phenocrysts of different mineral phases and matrix material were analysed for major and trace elements, with particular attention to the light elements lithium, beryllium and boron.

Li, Be and B evince excellent potential as geochemical tracers of source components and metasomatic agents, especially along convergent plate boundaries. The utility of these light elements as sensitive indicators of the slab-to-mantle transfer of matter, whether as fluid or melt, stems from their relative enrichment in the oceanic crust and intrinsically low concentrations in the upper mantle (e.g. Tera et al., 1986; Ryan & Langmuir, 1987; Leeman & Sisson, 1996). Hydrothermally altered igneous rocks and pelagic sediments comprising the oceanic crust contain significant amounts of these three lithophile elements; on the other hand, abundances of these elements in mantle reservoirs are low, as compared to bulk earth values. A component derived from the subducted oceanic crust, therefore, is manifested by elevated concentrations in island arc volcanic rocks compared to mid-ocean ridge basalts (MORBs) or ocean-island basalts (OIBs) (e.g. Ryan & Langmuir, 1987, 1988, 1993; Morris et al., 1990; Ryan et al., 1996; Brenan et al., 1998; Regelous et al., 1999; Danyushevsky et al., 2000; Kamenetsky et al., 2000; Ryan & Kyle, 2004).

Li and B are mobile in high-temperature hydrothermal processes (Seyfried et al., 1984) and metamorphic devolatilisation (Moran et al., 1992; Bebout et al., 1993). Li elucidates partial melting, crystal fractionation, metasomatism and low-temperature alteration histories (e.g Woodland et al., 2002; Zack et al., 2003; Bouman et al., 2004). The cosmogenic isotope ^{10}Be, owing to its short half-life of 1.5 my, may further indicate the recent incorporation of young marine sedimentary components into subduction-related magmas. Enhanced ^{10}Be abundances as a result of weathering may be identified and eliminated by examining covariations with ^{9}Be and B (Tera et al., 1986; Monaghan et al., 1988).

Experiments have been undertaken to characterise the behaviour of Li, Be and B during partial melting and magmatic crystallisation. Results have consistently shown the highly incompatible nature of Be and B and the moderately incompatible behaviour of Li in the mafic igneous composition range (Seitz, 1973; Ryan, 1989; Chaussidon & Libourel, 1993; Hart & Dunn, 1993; Dunn & Sen, 1994; LaTourette et al., 1995; Brenan et al., 1998b; Bindeman et al., 1998; Van Westrenen et al., 1999, 2000; Schmidt et al., 1999; Bindeman & Davis, 2000; Hill et al., 2000; Blundy & Dalton, 2000; Herd et al., 2004; Gaetani et al., 2003; McDade et al., 2003; Tiepolo et al., 2004; Zanetti et al., 2004; Adam & Green, 2006).

The great interest in studying the lithium stable isotopes lies in their large relative pass difference: around 16% with 7.5 for ^{6}Li and 92.5 for ^{7}Li (Tomascak, 2004). The consequent fractionation of these isotopes in different parts of the solid earth makes it a suitable

geochemical tracer for crust-mantle recycling processes, providing a characteristic fingerprint for certain sources. Like other stable isotope pairs, however, Li isotope fractionation is very limited in the elevated temperatures of magmatic processes such as melting or crystallisation of mantle magma (Tomascak et al., 1999; Chan & Frey, 2003; Zack et. al, 2003). Hence, discrepancies in the isotopic signature of volcanic arc magmas inevitably suggest the contribution of surface materials, such as the subducted slab (Bouman, 2004). Studies have thus far shown that Li fractionation is apparently not related to major element composition, although it correlates with radiogenic isotope variations in the mantle (Tomascak, 2004).

Reported isotopic values for MORB range between +1.5 to +5.6 δ^7Li, but it remains to be seen whether this range is intrinsic to the upper mantle, or due to other factors like contamination and the extent by which bulk samples can represent a rather heterogeneous reservoir. Altered MORB have higher δ^7Li, commonly >12 μg/g, and thus subduction zone fluids should be isotopically heavier than MORB, having altered oceanic crust as its primary source of Li (Tatsumi et al., 1986). Indeed, Li isotope and fluid mobile element concentration trends correlate in the Izu arc (Moriguti & Nakamura, 1998) and Mt. Shasta of the Cascade Range (Magna et al., 2003). But the majority of other arc studies do not show such strong correlation. Tomascak et al. (2000, 2002) explain this anomaly as possibly resulting from the decoupling of Li from fluid mobile elements, where Li from the slab is extracted from fluids or melts during mineral-fluid equilibration in the lower subarc mantle. Furthermore, analyses of eclogites and metasomatized mantle xenoliths demonstrate that strong Li fractionation in crustal sources translate into the Li isotopic composition of the mantle (Heinrich, 1986; Brooker et al., 2000; Zack et al., 2003; Rudnick et al., 2003; Nishio et al., 2004), and subduction zone processes seem to control the Li isotopic signature of different portions of the mantle (Tomascak, 2004).

2. Geologic Setting

Santorini is the most active Quaternary volcanic centre along the Hellenic Arc of the Aegean Region (Fig. 2-1). Located ~120 km north of Crete, the arc is about 500 km long and extends from mainland Greece through the islands Aegina, Methana, Poros, Milos, Kimolos, Santorini, Kos, Yali, Nisyros, and the Bodrum Peninsula in Turkey. The Aegean evolved from a long geologic history of significant orogenic, extensional, and subduction-related tectonics in a continental setting (Jackson, 1994). The small Aegean microplate includes part of mainland Greece, the Cyclades, Crete, Rhodes, and western Turkey. South of Crete, the Eastern Mediterranean portion of the African Plate subducts beneath the Aegean at rates of 4-6 cm/yr (Kalogeropoulos & Paritsis, 1990; Jackson, 1994; LePichon et al., 1984) in a N50°E direction (Druitt et al., 1999). The resulting Hellenic Trench system has two main branches: the thrust-dominated Ionian Trench that strikes nearly perpendicular to the subduction direction, and the strike-slip-dominated Pliny and Strabo Trenches that are almost parallel to subduction. Relative to Asia, the Aegean microplate moves southwestward at about 3.5 cm/yr, probably in response to the westward motion of Turkey along the North Anatolian Fault System (Jackson, 1994).

The 20-32 km-thick continental crust of the Aegean consists of a Variscan basement overlain by Permian to Tertiary metamorphic and sedimentary rocks. The pre-volcanic basement is characterised by nappes piled by collisional events, which may be grouped into two tectonic units (e.g. Dürr et al., 1978; Robertson and Dixon, 1984; Dürr, 1986; Altherr & Siebel, 2002, and references therein). The lower units underwent significant deformation and metamorphism during the Alpine Orogeny: a Paleocene to Eocene high-pressure regime and a Miocene low- to medium-pressure episode (e.g. Altherr et al., 1979, 1982; Wijbrans and McDougall, 1988; Bröcker et al., 1993; Okay and Kelley, 1994; Bröcker and Enders, 1999). The upper units, generally unaffected by Tertiary metamorphism, are found along normal faults and detachments of the back-arc. These are comprised of Upper Jurassic ophiolite fragments, Paleogene molasses deposits and late Cretaceous high-temperature/low-pressure metamorphic rocks with related I- and S-type granitoids (e.g. Altherr et al., 1994; Bröcker & Franz, 1998).

Back-arc extension started around 25 Ma, with an average extension of 1.0-1.5 cm/yr, resulting to thrust faulting and block rotation in the late Oligocene to Recent (e.g. Jolivet, 2001; Altherr and Siebel, 2002). Such transformation of an overthickened crust from compression-dominated tectonics to extension, crustal thinning, and subsidence was

Figure 2-1. Map of the Aegean region with the major tectonic structures (after Jackson, 1994; Jolivet et al., 1994, 1996). NAT: North Aegean Trough, also called Anatolian Trough, CAP: Central Aseismic Plateau, CT: Cretan Trough. Numbered triangles are the volcanoes of the Hellenic Arc: (1) Crommyonia, (2) Aegina, (3) Methana, (4) Poros, (5) Milos, (6) Kimolos, (7) Santorini, (8) Kos (9) Yali and (10) Nisyros. Arrow on lower left is the subduction vector.

accompanied by the intrusion of extensive granitic plutons and transport of high-pressure metamorphic rocks to mid-crustal levels. Subduction is believed to have been initiated at 13 Ma (Angelier et al., 1982) or 16 Ma (Mercier et al., 1989), and the modern arc system developed in the late Pliocene to Recent. Considering the 40-60 km thickness of the crust beneath mainland Greece and Turkey, the Aegean may have been stretched to half its original thickness in the last 5 Ma (McKenzie, 1978). This stretching is concentrated along the deep grabens of the Cretan and Anatolian Troughs, which define the boundaries of a relatively stable block called the Central Aseismic Plateau (Druitt et al., 1999).

The modern volcanic arc lies on the faulted southern margin of the Central Aseismic Plateau, and volcanism began about 4 Ma ago. Five major NE-SW rupture zones, believed to extend deep into the lithosphere, have been identified to pass through the volcanic centres of Crommyonia, Methana, Milos, Santorini, and Nisyros (Papazachos & Pangiotopoulos, 1993). Santorini developed on the northern extension of the Santorini-Amorgos Ridge, a horst produced by a series of normal faults in this extensional setting (Heiken & McCoy, 1984; Jackson, 1994; Mountrakis et al., 1998). Many vents and dykes are located along this 70 km-long NE-SW trend. Tectonic controls are further defined by the volcanic centres of Columbos and Christiana, 7 km northeast and 20 km southwest of Santorini, respectively (Fig. 2-2). Much of the volcanism has occurred along the Kameni Line, which extends between a northwestern graben and a southeastern horst where basement rocks and submarine volcanic deposits outcrop (Druitt et al., 1999). Along this line are the volcanic centres of Christiana islands, the Akrotiri Peninsula, and Palea and Nea Kameni. To the northeast, a parallel structure runs through Megalo Vouno and Columbo volcanoes (Heiken & McCoy, 1984).

Santorini, also called Thira, is a complex of 5 islands: (1) the main island of Thera, 75.8 km^2, which defines more than half of the caldera's eastern outline; (2) Therasia, 9.3 km^2, to the northwest; (3) the small island of Aspronisi, only 0.1 km^2, to the southwest; and (4) Palea and (4) Nea Kameni, 0.5 km^2 and 3.4 km^2, respectively, at the centre of the caldera. The only basement units of Santorini that remain exposed are Mount Profitis Ilias and Gavrillos Ridge in southeastern Thera (Fig. 2-3). Volcanism began around 650 ka and the explosive regime commenced about 360 ka (Druitt et al., 1999). The earliest Quaternary volcanic activity occurred on Akrotiri Peninsula in southern Thera, where only small remnants of the oldest volcanoes are preserved. Products of twelve main eruptions and at least a hundred smaller ones have been recognized over large areas of the islands (see summary in the table within this chapter). However, explosive eruptions may have numbered in thousands, the

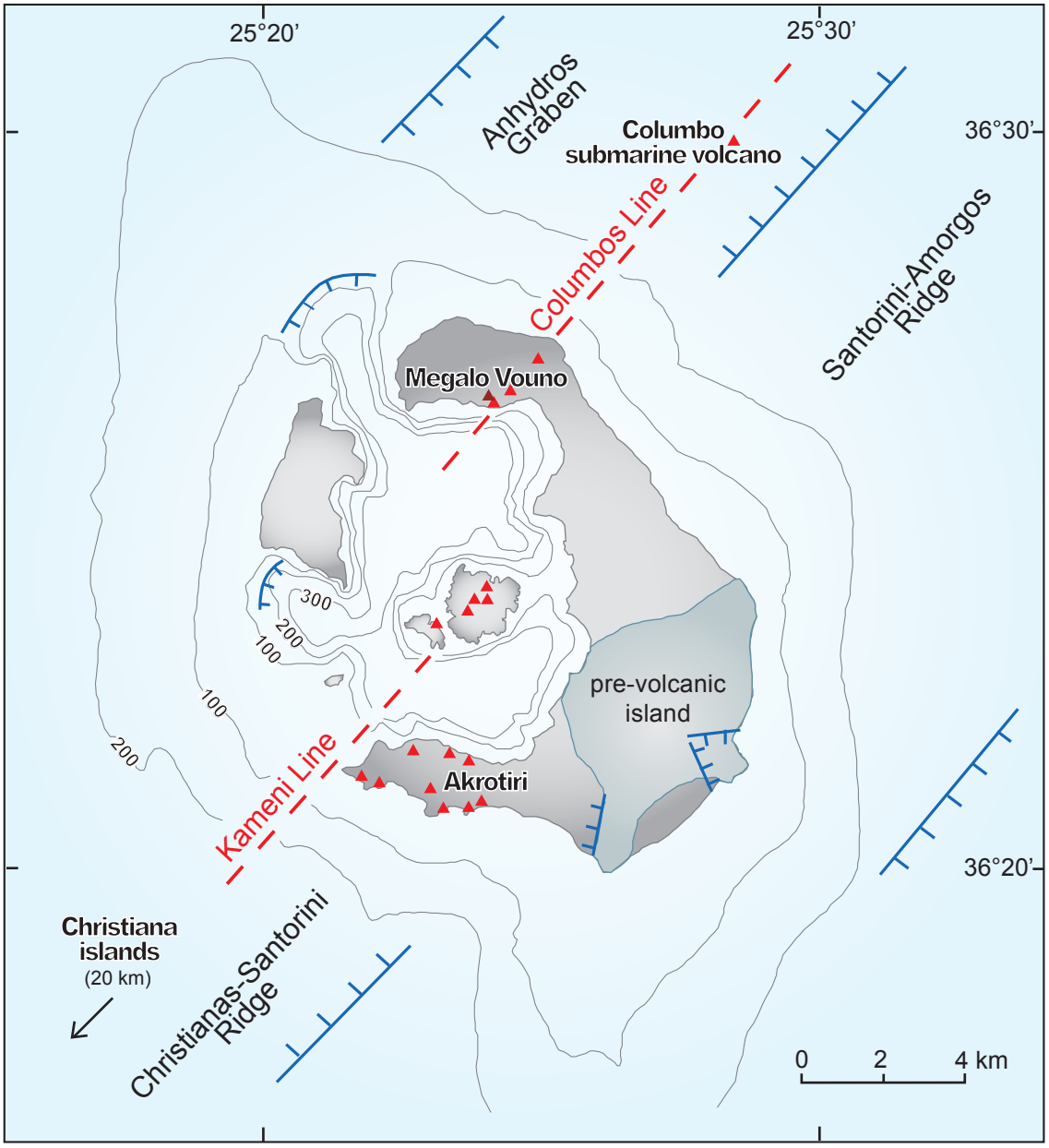

Figure 2-2. Tectonic map showing Santorini with some of its volcanic centres, in the context of structural controls and related volcanism (from Heiken & McCoy, 1984).

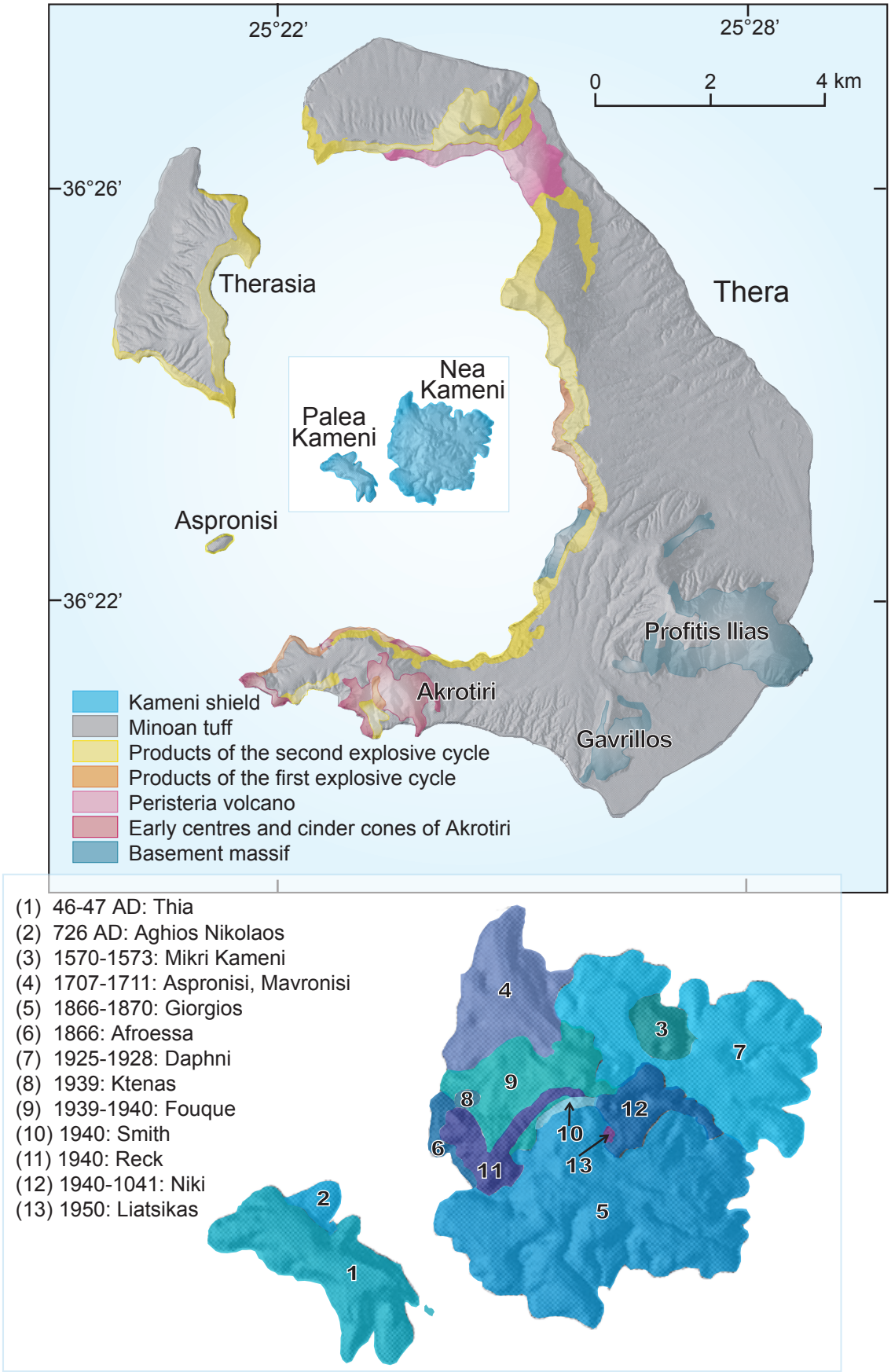

Figure 2-3. Geologic map of the Santorini Volcanic field (top) and the intracaldera islands of Palea and Nea Kameni (bottom) [modified from Druitt et al., 1999].

minor ones not surviving incorporation into the geologic record. Recent mapping (Druitt et al., 1999) reduce these events into six main units: early centres of the Akrotiri Peninsula, cinder cones of the Akrotiri Peninsula, Peristeria Volcano, products of the first eruptive cycle, products of the second eruptive cycle, and the Kameni shield. The best known of these are the Minoan pyroclastic deposits from the 3.6 ka explosion, towards the end of the second eruptive cycle (Bond & Sparks, 1976; Heiken & Mc Coy, 1984; Sparks & Wilson, 1990). The Minoan eruption was the most recent of probably four explosive events that formed the present-day composite caldera structure (Druitt & Francaviglia, 1992). Thereafter, renewed volcanism formed the islands of Palea Kameni in ~197 B.C. and Nea Kameni, where the last eruption occurred in 1950.

Thera, Therasia, and Aspronisi are capped by an almost continuous layer of tuff from the Minoan eruption, with the gently-sloping coasts of the first two islands consisting mostly of Minoan ignimbrite. The intracaldera islands of Palea and Nea Kameni, subaerial expressions of a dominantly submarine volcano, have blocky flows and domes. These are all dacitic in composition, although produced from several volcanic centres that were active at different times within a period of more than 2,000 years (also in Table 1). Historic records yield nine subaerial eruptive episodes for the Kamenis (Fytikas et al., 1990), starting with the 197 BC explosive activity that built up Iera, a pyroclastic cone, no longer exposed above sea level. In AD 46 – 47, Thia island, or the present-day Palea Kameni, emerged. After almost 700 years, a nearby volcanic centre extruded the Aghios Nikolaos lavas. In 1570, activity switched to the northeast, forming Mikri Kameni. Subsequent volcanism concentrated within this area, where five more episodes occurred: the alternating extrusive and explosive eruptions of Aspronisi and Mavronisi in 1707-1711; the continuous eruptions of Georgios, the slow then rapid extrusions of Aphroessa, and the emergence of May's Islands in 1866-1870; the explosions and terminating extrusion of Daphni in 1925-1928; lava and dome formation of Triton, Ktenas, Fouque, Smith, Reck and Niki in 1939-1941; and the extrusion of the Liatsikas lava in 1950. These latter activities created Nea Kameni, within timespans that consistently decreased until the last eruption. Solfataric and fumarolic activity still occur around the Kameni islands.

Event	Magma composition	Age (Historic Records)
Kameni lava shield formation:	Dacite	197 BC to1950
Iera		197 BC
Palea Kameni: Thia		46-47 AD
Aghios Nikolaos lavas		726 AD
Nea Kameni: Mikri Kameni		1570-1573
Aspronisi, Mavronisi		1707-1711
Georgios, Aphroessa, Islets of May		1866-1870
Daphni, Nautilus		1925-1928
Triton, Ktenas, Fouque, Smith, Reck, Niki		1939-1941
Liatsikas		1950
Caldera collapse 4		
		Dating (ka)
Minoan eruption	Rhyodacite, andesite	3, 6 [1]
Caldera collapse 3		
Cape Riva eruption	Rhyodacite, andesite	21 [2]
Formation of Therasia lava shield	Rhyodacite, andesite	
Eruption of the andesites of Oia	Andesite	
Upper Scoriae 2 eruption	Andesite	40 [3]; 54 ± 3, 67 ± 9 [4]
Construction of Skaros lava shield	Basalt, andesite	
Caldera collapse 2		
Upper Scoriae 1 eruption	Andesite	60-40 [3]
Vourvoulos eruption	Andesite, dacite	
Megalo Vouno & Kokkino Vouno cinder cones	Andesite	76 ± 28, 54 ± 23 [4]
Aspronisi tuff ring (also Kolumbus tuff ring?)		
Middle Pumice eruption	Dacite, andesite	60 [3]; 100 [4]
Cape Thera eruption	Andesite	
Construction of Simandiri lava shield	Andesite	172 ± 33 [4]
Caldera collapse 1		
Lower Pumice 2 eruption	Rhyodacite, andesite	180 [5]
Lower Pumice 1 eruption	Rhyodacite, andesite	203 ± 24 [4]
Cape Therma 3 eruption	Andesite	
Extrusion at Cape Alonaki & NE Thera	Rhyodacite	257 ± 36, 224 ± 5 [4]
Cape Therma 2 eruption	Rhyodacite	
Cape Therma 1 eruption	Andesite	
Extrusion of the andesites of Cape Alai	Andesite	568 ± 18, 364 ± 85, 229 ± 85 [4]
Balos, Kokkinopetra & Mavrorachidi cinder cones	Basalt, andesite	344 ± 25 (Balos), 522 ± 104, 451 ± 27 (Mav) [4]
Eruption of lavas of Peristeria 3	Basalt, andesite	480 ± 5, 464 ± 5, 433 ± 8 [4]
Extrusion of domes & flows of Peristeria 2	Andesite	496 ± 16 [4]
Construction of Peristeria 1 core complex	Andesite	528 ± 8 [4]
Eruption of early submarine centres of Akrotiri	Rhyodacite	ca. 2,000-600 [3,4]

[1] Mean of radiocarbon ages on plant remains in tuffs (Friedrich and others, 1990)
[2] Mean of radiocarbon ages on plant remains in tuffs (Pichler and Friedrich, 1976) corrected using the data of Bard and others (1990)
[3] Friedrich (2000)
[4] Ar 39-40 data (Druitt and Sparks, 1996)
[5] Constrained by age of Lower Pumice 1 and Simandiri Shield

3. Petrogenetic Models

3.1 Santorini

Palea and Nea Kameni lavas are uniformly dacitic with andesitic inclusions (Francalanci et al., 1998) whilst those of the main island Therasia range from basaltic to rhyodacitic. Amongst lavas of the same suit, however, the Kameni dacites have lower K_2O and incompatible element concentrations compared to the pre-caldera dacites and rhyodacites (Barton and Huijmans, 1986).

Varying geochemical and petrological characteristics of the Santorini volcanic products may be largely attributed to fractional crystallisation of mantle-derived basaltic arc magma, alongside other processes (Nicholls, 1971; Mann, 1983; Huijmans, 1985; Huijmans et al., 1988, Druitt et al., 1999). Differences in the magmatic evolution of the products reflect different physico-chemical conditions in the magma chambers, such as silica enrichment or Fe concentration related to oxidation states or the extent of crustal contamination (Grove and Kinzler, 1986). Moreover, compositional zoning and temporal chemical trends may be explained by sidewall crystallisation (Druitt et al., 1999) and zoned chambers (Huijmans, 1985). Isotopic data demonstrate heterogeneity that cannot be ascribed solely to fractional crystallisation, but rather to a combination of fractionation and crustal assimilation (Druitt et al., 1999). Magma mixing in open-system magma chambers is invoked from the occurrence of magmatic mafic inclusions with textures that imply rapid incorporation into silicic magma resulting to quenching and solidification (Sparks et al., 1977; Sparks and Marshall 1986, Bacon, 1986; Cottrell et al., 1999). A study of plagioclase phenocrysts from Thera (Stamatelopoulou-Seymour et al., 1990) points to influx and most probably, mixing of magmas of contrasting compositions, evidenced by phenocryst sub-populations in chemical and textural disequilibrium with their host lavas. These phenocrysts show major and trace element decoupling and differing incompatible trace element concentrations, although it should be noted that the felsic lavas do not necessarily exhibit features indicative of thorough mixing.

On the other hand, using trace elements that signify considerable geochemical differences among lavas of the Santorini volcanic centres, Tarney et al. (1996) suggest that Santorini did not evolve as a fractionating magma chamber, but instead, as a number of chemically distinct magma batches. They argue that source mantle composition and mixing,

along with spatial rather than temporal variations, primarily controlled magma generation. Their data further show that elements such as V, U, Pb and Mn have large consistent variations in Santorini lavas that imply injection of oxidised fluids into the magmas. Magmas rising into Thera underwent decompression and, apart from the early Akrotiri eruptions, are relatively hot and dry, only subsequently deriving water through the penetration of overlying crater lake water. But as Druitt et al. (1999) point out, models implying source mantle diversity would prove highly speculative, especially when the lavas have major, trace, and isotopic element signatures that may simply be explained by a combination of fractional crystallization, crustal assimilation, and magma mixing. For instance, Fe, Ti, and P enrichment are attributed to fractional crystallization. Mingled and homogeneous magmas with anomalously low concentrations of the aforementioned major elements and more calc-alkaline affinities, on the other hand, may have resulted from mixing of compositionally contrasting magmas in large, prevalently silicic chambers.

Druitt et al. (1999) explain the evolution of Santorini by means of the large volume of mantle-derived magma that has passed through and been emplaced within the crust. Batches of magma rose through the crystalline basement of the Aegean microplate, and hence, assimilation and/or partial melting of the continental crustal rocks may have inevitably contributed to magma genesis. For at least 650 ka, basaltic magmas repeatedly passed through continental crust of rather limited extent, ~60 km^2. These magmas partially melted the crust and were contaminated by incompatible trace-element-rich silicic partial melts as they fractionated into andesites and rhyodacites. Through time, the crustal rocks would have lost incompatible elements and radiogenic components to the intruding magmas, contributing progressively less of these components to ensuing batches. Thus, a systematic temporal trend in incompatible elements among rocks of similar SiO_2 content has been observed: from 539 ka to the present, LILE (K, Rb, Th) and HFSE (Zr, Nb) between different eruptions have generally decreased. Concurrently, plutonic intrusions would have replaced the crust, decreasing the chance for assimilation of crustal components into the later rising magmas, thereby also decreasing the incompatible element concentrations. Crustal contamination by the upper Aegean continental suite accounts for the trends of Sr, Nd, and Th, isotopes, which correlate as expected from variable amounts of assimilated crust. This is especially true for predominantly silicic units presumably from high-level magma chambers, as evidenced by the isotopic disequilibrium between coexisting plagioclase phenocrysts and melt. Oxygen isotope data are also consistent with fractional crystallisation alongside minimal crustal assimilation, while Pb isotopic signatures fall outside the fields of the main mantle reservoirs and suggest

crust-derived radiogenic Pb. $^{87}Sr/^{86}Sr$ and $^{143}Nd/^{144}Nd$ plotted against SiO_2, 1/Sr, and Rb/Sr all show that crustal contamination accompanied fractional crystallisation. The temporal decrease in incompatible elements, associated with a decrease in $^{87}Sr/^{86}Sr$ and an increase in $^{143}Nd/^{144}Nd$ may be due to decreasing crustal contamination or changes in assimilant composition (Druitt et al., 1999). In general, good agreement is found for trace element and isotope trends using AFC models of typical Santorini basalts and assimilants with the composition of Aegean basement rocks.

3.2 Palea and Nea Kameni

The post-caldera lavas of Santorini, i.e., those found on the Kameni islands, are believed to have evolved from andesitic to basaltic parental magmas that are compositionally different from those of the pre-caldera dacites. Coming from a chamber 2.2-4.2 km deep, pre-eruptive temperatures are estimated at 960-1012°C with calculated oxygen fugacities of $10^{-9.6}$-$10^{-9.9}$ bars. Water content is 3-4 wt% and is lost through the slow upwelling of magma along cylindrical channels that later developed into fissures of a dike system (Barton & Huijsmans, 1986). The magma chamber is modelled as being zoned, with more mafic components underlying silicic layers, and crystal-liquid differentiation causing compositional variations.

The relatively restricted range of composition of erupted products for the past 2,200 years may be explained by limited crystal settling, a close approach to equilibrium crystallisation, and a minimal decrease in temperature of probably <50°. Such thermal buffering may be due to the exeistence of a large magma chamber surrounded by country rocks still warm from previous volcanism and underlain by choked feeders (Nicholls, 1971; Huijsmans & Barton, 1983). The other possibility, more favoured by Barton and Huijsmans (1986), is heating provided by periodic influx of more mafic magma. The lack of evidence for magma mixing, however, implies that the influx does not penetrate upwards within the chamber.

In contrast to this rather static model characterized by thermal buffering and minimal crystal settling, Higgins (1996) prefers a more dynamic scenario based on crystal size distributions (CSD) of the plagioclase in the porphyritic lava samples. His model suggests that the magma chamber beneath the Kamenis may have undergone refill and incomplete extraction over at least 2000 years. He describes the eruptive cycle as consisting of three phases: refilling of dacitic magma into a shallow chamber within a depth of only a few kilometres and subsequent mixing with the partly crystallised dacite from previous eruptions,

eruption of the mixture of old and new magma, and a repose phase where the remaining magma continued to crystallise in the chamber until the next refilling event.

More recent and detailed petrographic, chemical and isotopic investigation of the Kameni rocks reveal systematic variations that may be due to xenocryst accumulation and/or crustal assimilation (Francalanci et al., 1996; Conticelli et al., 1996). Different mafic enclaves have also been found in these rocks, with textures suggesting incorporation in a molten state, implying interaction between injected mafic and host silicic magmas. Such mingling - mixing processes probably also explain the trend towards a less evolved composition among the Kameni dacites.

Later studies further emphasize the significance of mafic inclusions in reconstructing the magmatic evolution at Santorini, implying the presence of a persistent and complex conduit and chamber system feeding the active Nea Kameni volcano. Cumulate and quenched enclaves representing three varieties of replenishing magma were identified, the distinct inclusion population of each lava flow believed to reflect the changing state of the emptying magma chamber (Martin et al., 2006). Contrary to Higgin's observation, however, the characteristic occurrence of a dominant enclave type in each flow is believed to indicate nearly complete extraction of the new magma during the consequent eruption.

Absence of chilled margins and correlation between enclave and groundmass sizes may have resulted from the emplacement of the magmatic influx as a dense layer at the base of the dacite chamber, which underwent a decrease in density through crystallisation-induced vesiculation. The latter condition, contolled by the H_2O contents of the host and recharge magmas, results to layer overturn and mixing (Holness et al., 2005). Scrutiny of groundmass textures also showed that the relative volumes of erupted and replenishing magmas are directly proportional (Martin et al., 2006). This suggests that the addition, crystallisation and vesiculation of the new magma produce an overpressure that ruptures chamber walls and initiate eruption. Extraction of magma then ensues through decompression, until the overpressure is relaxed and the pressure and volume of the magma chamber are restored (Blake et al., 1981; Tait et al., 1989; Bower & Woods, 1997).

In this work, the various types of phenocrysts amongst the major mineral phases also attest to the complexity of the processes that produced the Santorini lavas. In particular, the light elements lithium, beryllium and boron are used to further interpret magmatic conditions and eruption mechanisms, with possible implications on the rates of crystallisation, not only in Santorini Volcano but possibly in other volcanic systems as well.

4. ROCK TEXTURES

4.1 Dacites from Nea Kameni

Nea Kameni lava flows are all dacitic, and samples taken from the 1939 – 1941 lava flows are very similar. The collected specimens, *San 1, San 2, San 3, San 35 San 36* and *San 37*, cannot be distinguished one from the other in terms of texture, mineral assemblage, nor crystal populations. Although variations occur in terms of flow structure and crystal distribution, these are observed within particular portions of each sample or flow, and not exclusively in any one sample or set of samples. Hence, the descriptions in this chapter apply to all six samples collected.

The 1939-1941 lavas are blocky and produced from several volcanic centres approximately central to the island of Nea Kameni. These units include domes but are otherwise only as thick as a meter or a few meters. Aerially, they extend almost a kilometre towards opposite shores of the island: the Fouque, Smith and Reck lavas towards the west; the Niki lavas towards the east. Due to the overlapping distribution of these lavas and the limited extent of each flow, it is difficult to pinpoint the exact volcanic source edifice of each of the gathered samples; hence these are discussed here according to sample numbers.

Hand specimens are dark-coloured with white specks of plagioclase commonly 2 mm in length. The groundmass is grey to black and usually shiny (Fig. 4-1), suggesting a glassy constitution, although microscopic investigation yields much less glass than expected. Pore space takes up a significant volume in particular portions of the blocks (Fig. 4-2). Besides the porous parts, however, the samples are rather competent and fresh breaks expose unaltered portions ideal for detailed analyses (Fig. 4-3).

Microscopic observation further shows the samples to be porphyritic to glomero-porphyritic (Figs. 4-4 and 4-5). These consist of ~ 15 vol.% phenocrysts and ~ 65 vol.% matrix, the rest being pore space, which comprise up to 30 % of the total rock volume. The phenocryst grains are plagioclase, pyroxene and magnetite, in this order of abundance. These minerals occur either individually or as intergrowths, complex intergrowths being especially exhibited by plagioclase. Microlites of the same minerals are found in the intersertal matrix, almost in the same degree of abundance as in the phenocrysts. Glass is clear to light brown in thin sections and occupies only small pockets left after the crystallisation of the microlites. Certain portions of the rocks show flow structure, especially evident through the subparallel orientation of elongated phenocrysts, microlites and/or pore spaces.

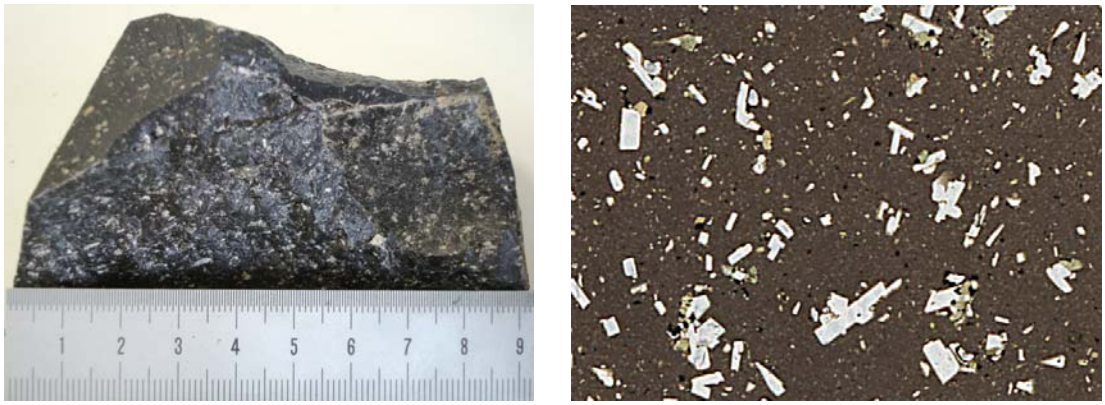

Figure 4-1. (On the left is a photograph of the collected hand specimen, the numbers on the ruler scale are in centimetres (cm). On the right is a scanned image of the thin section, the width of this picture is 1 cm. These also hold true for the succeeding pairs of macroscopic pictures.): *San 37* displays the dark groundmass with glassy appearance typical of the 1939-1941 Nea Kameni dacites.

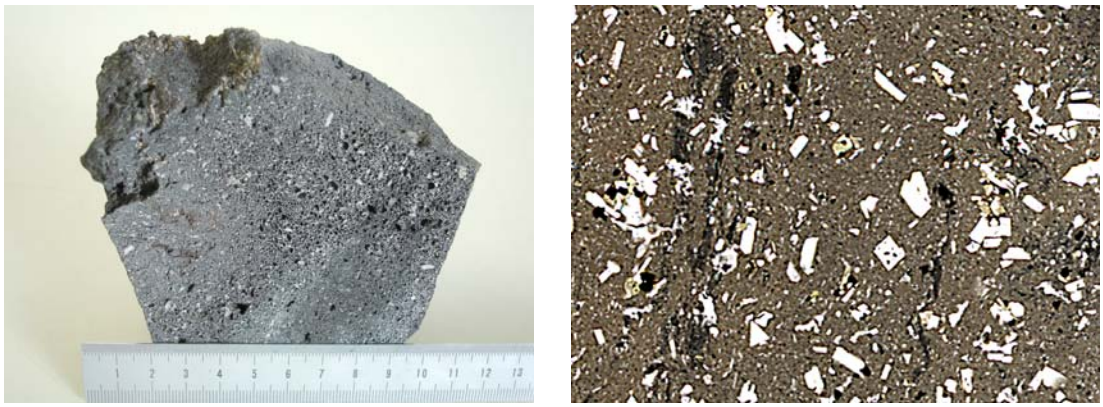

Figure 4-2. A porous block is exemplified by this sample, *San 35*. In some portions, the pore spaces are aligned parallel to the crystals, conveying flow direction.

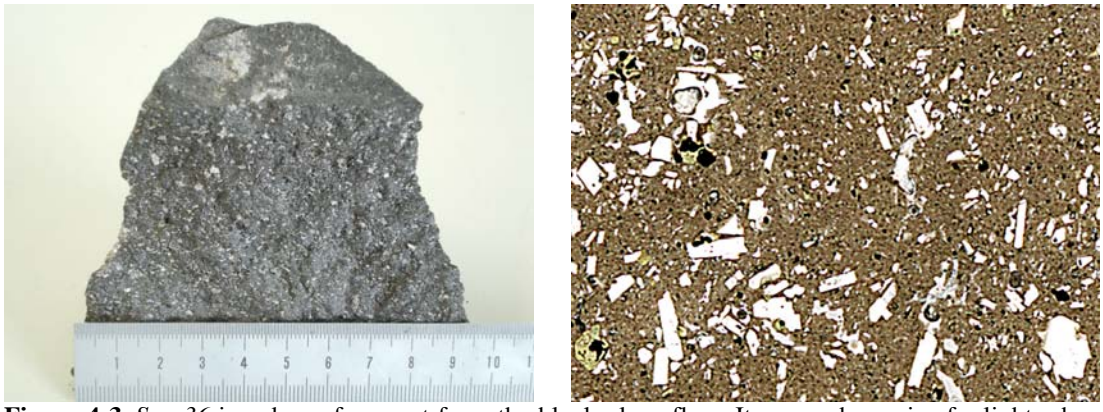

Figure 4-3. *San 36* is a dense fragment from the blocky lava flow. Its groundmass is of a lighter hue but still imparts the glassy appearance.

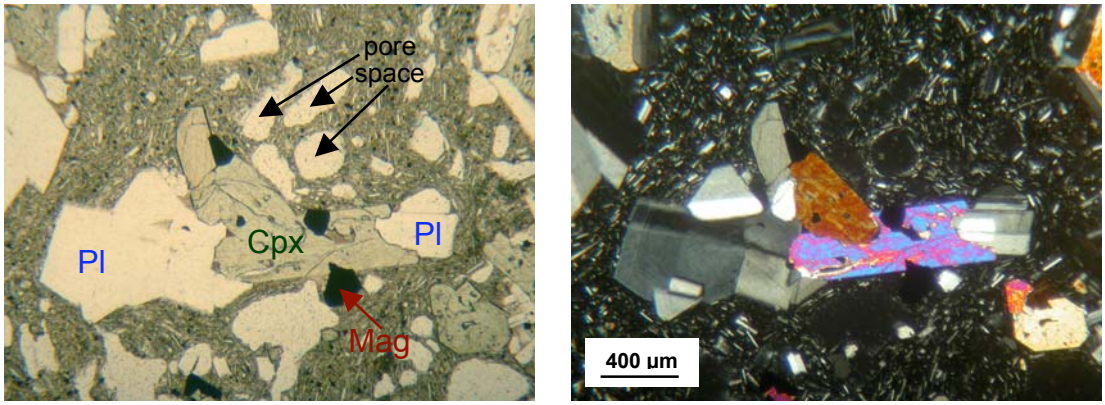

Figure 4-4. (Photomicrograph of a thin section; on the left uncrossed polars, on the right crossed polars, here and in succeeding pairs of colour photographs.): Intergrown crystals of plagioclase, pyroxene and magnetite in sample *San 2*. Plagioclase crystals display oscillatory and concentric zoning, while pyroxene grains show euhedral to subhedral forms and fluid inclusions.

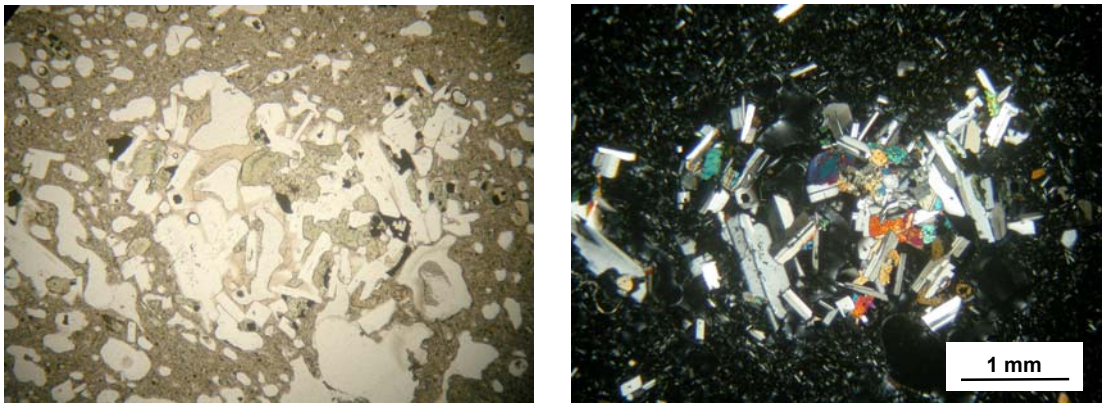

Figure 4-5. A complex intergrowth of plagioclase, pyroxene and magnetite crystals amidst glass and pore space, found in *San 36* but common in other samples as well.

Plagioclase is the most prevalent phase among both phenocrysts and microlites. Plagioclase grains are euhedral and mostly elongated, with lengths reaching ~ 2 mm among the phenocrysts. Lath-shaped crystals are common, and nearly equant grains also occur, although to a much lesser degree. In addition, plagioclase microlites are acicular, and rarely, with swallow-tail shapes. Most crystals are primarily twinned, with either Albite or Carlsbad twinning (Fig. 4-6). Zoning is typical, ranging from subtle oscillations to conspicuous compositional changes, the trends and thicknesses differing significantly from crystal to crystal (Figs. 4-7 and 4-8). Skeletal texture is observed, although only in a few crystals. Certain grains show evidence for resorption through disruption of and overgrowth on earlier concentric zones (Fig. 4-8). Solution, on the other hand, is shown by sieve texture (Fig. 4-9). Glass inclusions are also observed in some crystals (e.g. Fig. 4-6).

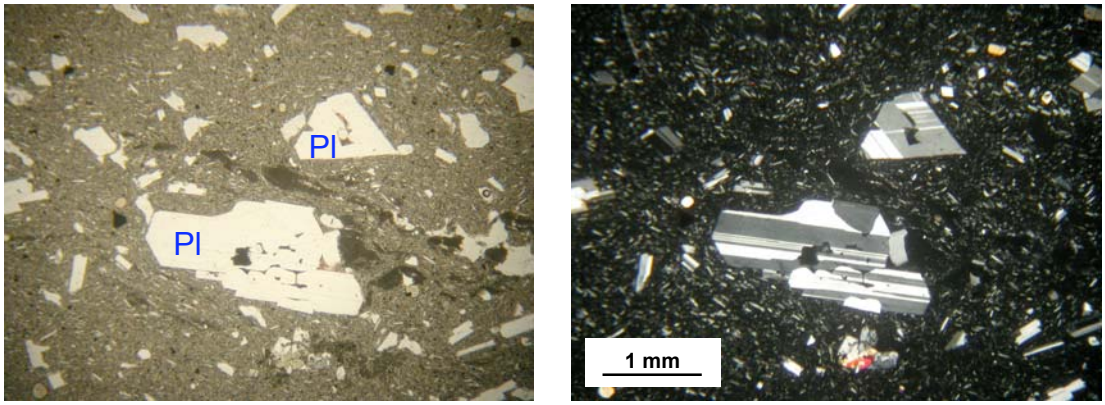

Figure 4-6. This section from *San 35* shows twinning in plagioclase, a very prevalent feature occurring in varying types and degrees. Magnetite and glass inclusions are also observed.

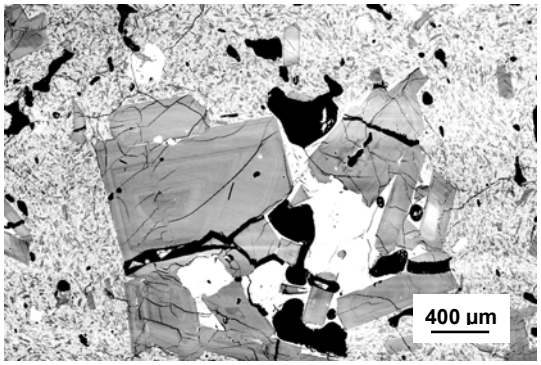

Figure 4-7. (BSE image of a thin section, here and in succeeding greyscale photographs): A clump of phenocrysts in *San 37*. Note the zoning in plagioclase.

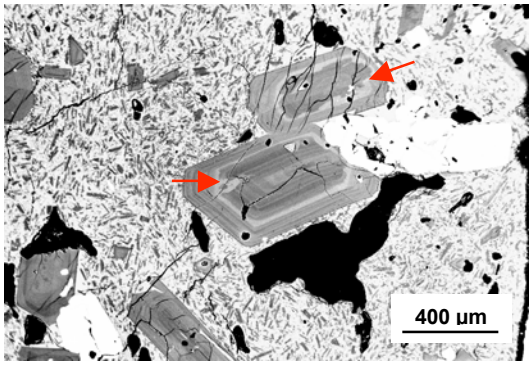

Figure 4-8. Plagioclase crystals in *San 37*, showing different concentric growth zones and resorbed texture (red arrows).

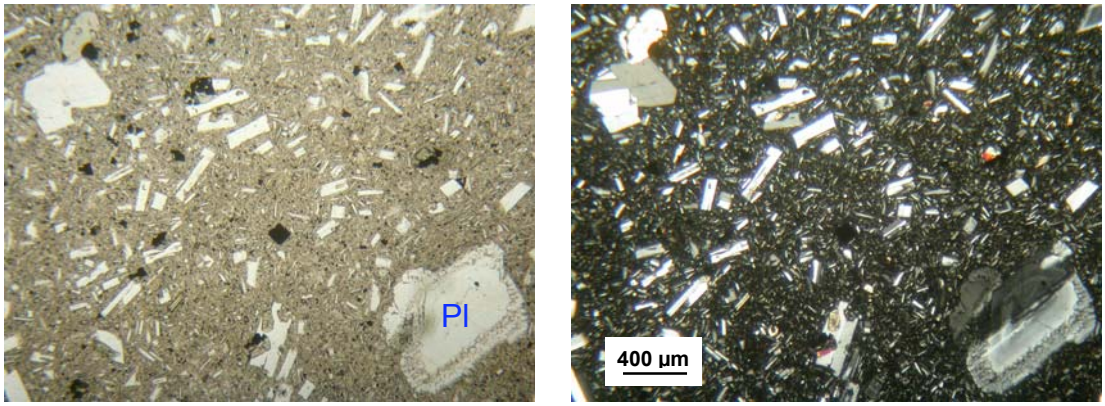

Fig. 4-9. Notice the varying sizes and shapes of plagioclase in *San 3*. The subhedral crystal on the lower right exhibits a solution rim.

Four types of plagioclase phenocrysts occur among the dacite samples investigated, here designated as types N, O, C and A. Type N is normally-zoned in terms of An content, with values ranging from 62 in the core to 40 at the rim, although accompanied by slight oscillatory variations. This is the type expected among plagioclase formed during normal crystallisation, but is actually rare and very few such crystals have been documented in this study. The most common plagioclase are type O, which also exhibit oscillatory variations in

An content, but wherein the pattern does not show a consistent trend from core to rim (e.g. the largest crystal in Fig. 4-7). Instead, the An profile remains generally flat within the range of 57 – 40. Type-C phenocrysts have cores with higher An content than the mantling rim (Fig. 4-10). An content is between 63 and 54 mole % within the core, and along a rather abrupt boundary, lowers to values of 54 – 40 mole % towards the rim. Type-A plagioclase grains are anomalous: entire crystals, or portions of these, have An contents too high for a dacitic system. In one example, An is at 93 – 87 throughout the whole grain. In other crystals, the core has An_{59-49}, increasing to An_{88-81} towards the rim, and declining again to An_{51-48} at the rim, thus defining 3 different zones.

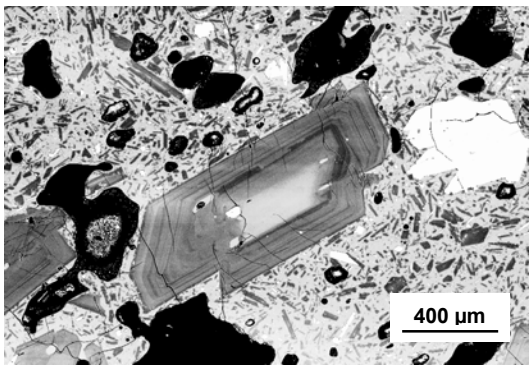

Figure 4-10. One type-C plagioclase in *San 36*, showing the light-coloured high-An core.

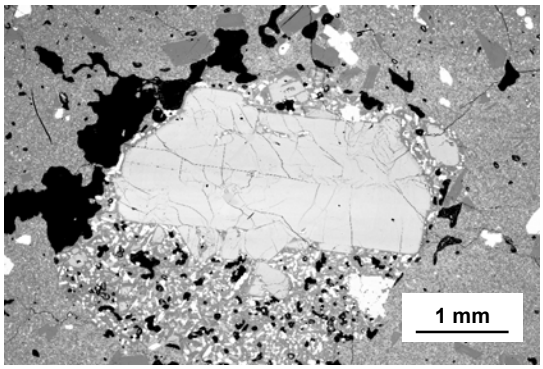

Figure 4-11. High-An plagioclase in *San 37*, surrounded by minute crystals of pyroxene and magnetite.

Pyroxene is the second major phenocryst phase: clinopyroxene is ubiquitous, while orthopyroxene is less common. Both pyroxenes occur as euhedral to anhedral grains generally smaller than plagioclase. These have growth zoning patterns that sometimes indicate compositional reversals, although certainly not as intricately as those in plagioclase. Well-oriented crystals may reveal sector zoning along with the concentric growth zones. Glass inclusions are common. Skeletal texture is rarely observed. Pyroxenes form intergrowths with plagioclase in glomeroporphyritic portions of the rocks (Figs. 4-1 to 4-3), and are also included in isolated plagioclase crystals. Minute pyroxene grains comprise a significant part of the matrix.

Clinopyroxene phenocrysts are augite and fall into two types. Type L has relatively low Mg# of 72 – 64. One crystal exhibits both concentric and sector-zoning and is here designated as type H, due to its higher Mg# of 81 – 79. Orthopyroxene grains are enstatite and have Mg# between 68 and 59, except that the general trend from core to rim may vary.

Type-I crystals exhibit a general core-to-rim increase in Mg#, while a core-to-rim decrease is observed in type D.

Magnetite is common among both phenocrysts and matrix. The crystals are euhedral squares to anhedral or irregularly-shaped. The primary crystals are also intergrown with or included in plagioclase and pyroxene. Olivine occurs as a minor phenocryst phase, the grains being small and anhedral. One grain large enough for analysis has Mg# of 77 – 75 almost throughout the crystal, except for the thin rims where values abruptly drop to a minimum of 67. Apatite occurs as accessory mineral included in plagioclase phenocrysts and in the groundmass.

The rock samples contain fragments that appear to have been entrapped from older igneous rocks. One such fragment contains a plagioclase crystal ~ 3.5 mm-long with $An_{\sim 90}$, surrounded by fine grains of clinopyroxene and magnetite (Fig. 4-11). Another such fragment contains a rather large grain of olivine, apparently unstable, with a mosaic of small orthopyroxene crystals and lamellar magnetite around it (Fig. 4-12).

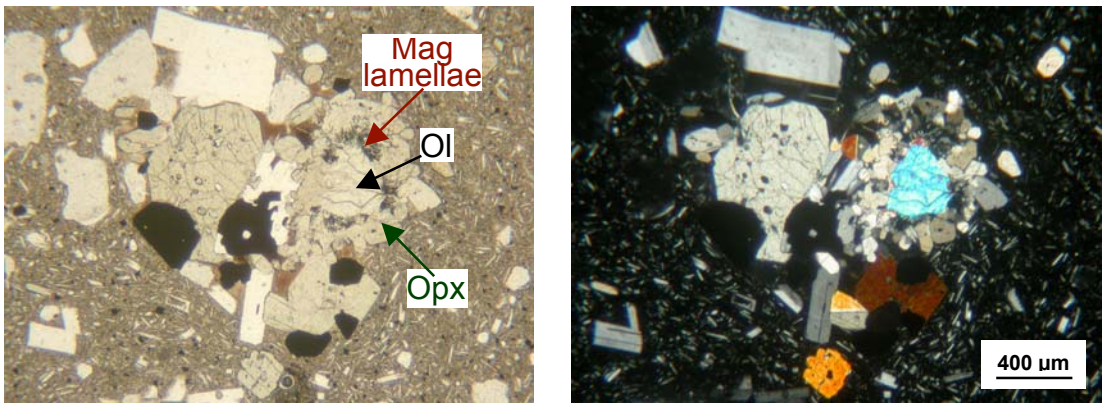

Figure 4-12. An uncharacteristic olivine in *San I* (in the right half of the photograph), surrounded by orthopyroxene crystals and magnetite lamellae.

4.2 Andesites from Thera

San 22

San 22 is a porphyritic andesite sample taken from the coast of Cape Mavrorachidi in Akrotiri. This unit is defined as part of the "Andesites and Basalts of Akrotiri", consisting of cinder cones with subordinate agglutinate and lava (Druitt et al., 1999; also see Geologic Map). The sample is grey with a grainy, vitreous appearance, apparently afforded by the large plagioclase crystals that reach 4 mm in length (Fig. 4-13). Green crystals of pyroxene are also evident, although these are commonly smaller. Pore spaces are elongated in a consistent direction, the cavities up to several millimetres in diameter and several centimetres in length. Most of the rock, however, is dense, as the pore spaces are discretely distributed within it.

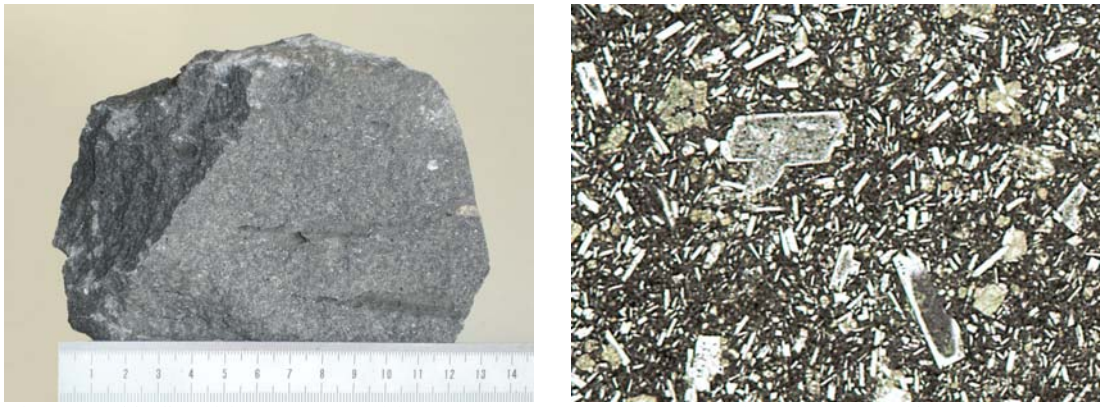

Figure 4-13. *San 22* is a porphyritic andesite sample with rather large crystals of plagioclase and pyroxene. Note the elongated, subparallel pore cavities on the left photo.

Thin sections show about ~ 15 vol.% phenocrysts, the rest being groundmass and pore space, the latter making up a very minimal percentage of the whole rock. Plagioclase phenocrysts are in euhedral laths that commonly show concentric and oscillatory zoning (Fig. 4-14). Pyroxene grains are euhedral to subhedral and also exhibit concentric and sector zoning (Fig. 4-15). Twinning and intergrowth are also observed among these phenocrysts (Figs. 4-16 and 4-17). Numerous grains of both minerals exhibit sieve texture that imparts a generally rough and dirty appearance, except for the rims, which appear unaltered (e.g. plagioclase in Fig. 4-17). Few olivine crystals are observed, showing very irregular shapes. Plagioclase and pyroxene microlites occur in the groundmass, along with magnetite and brown glass.

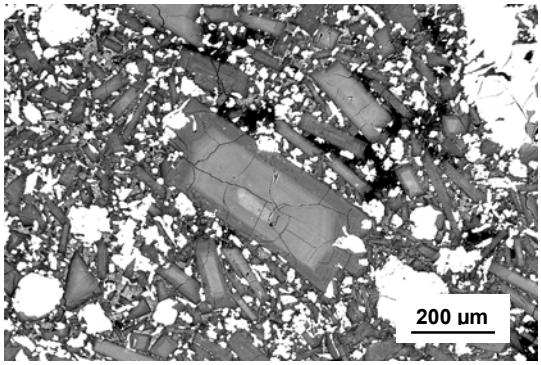

Figure 4-14. Plagioclase laths with concentric growth zones in San 22.

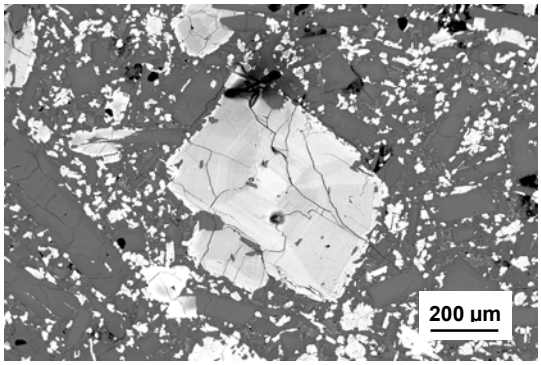

Figure 4-15. Clinopyroxene showing both concentric and sector zoning.

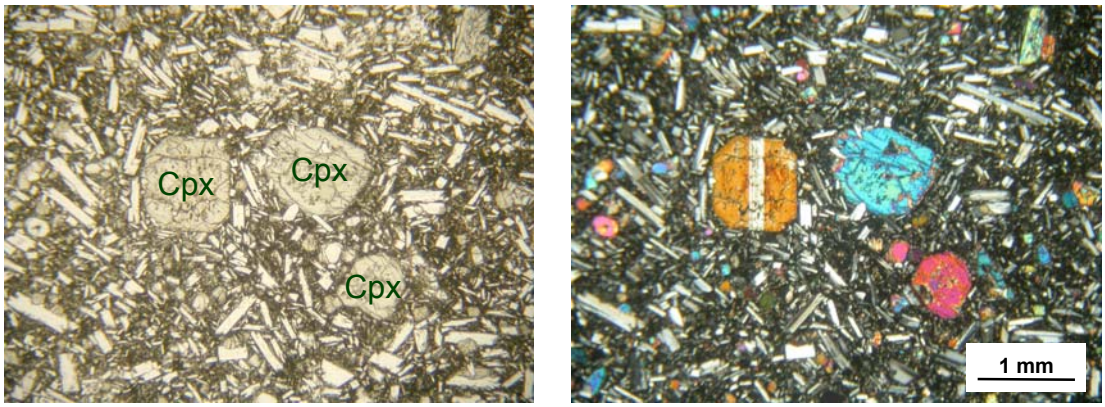

Figure 4-16. Clinopyroxene occurs as euhedral to subhedral, and mostly equant, grains. Some of these show twinning, as in the crystal on the upper right corner.

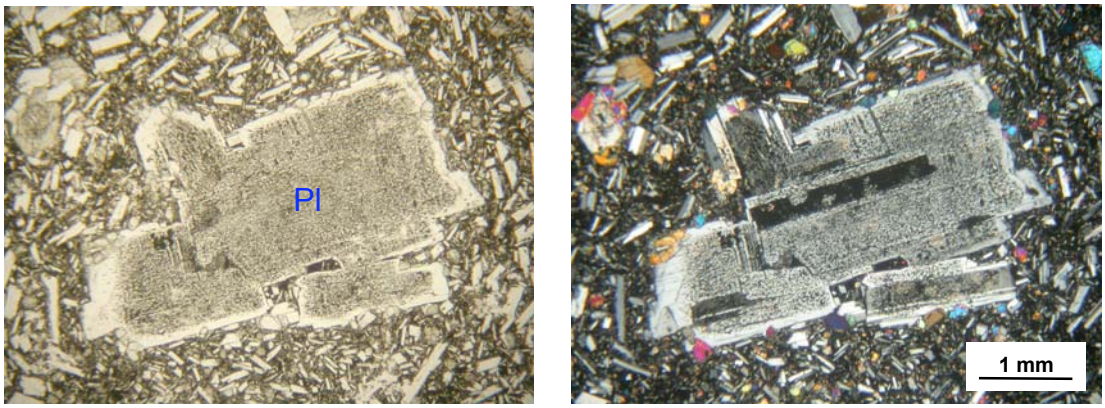

Figure 4-17. Intergrown plagioclase crystals with sieve texture except for the outermost rims.

Most unaltered plagioclase phenocryts are of type C, having An_{85-80} in the core and An_{78-55} at the rim (e.g. Fig. 4-14). Clinopyroxene crystals are augite and are of type H, with Mg# of 88 – 73. Olivine crystals have Mg# of ~ 82 for the most part, except along the rim where this drops to 74.

San 26

Collected from an agglutinate on the road to Oia, *San 26* is a bomb (fiame) within a unit erupted from Peristeria Volcano, in previous work designated as part of the "Andesites, Basalts and Dacites of Peristeria 3" (Druitt et al., 1999; also see Geologic Map). This sample has porphyritic to glomeroporphyritic texture and rather high porosity (Fig. 4-18). The sample is dark gray with white specks of plagioclase and vitreous green grains of pyroxene. It is slightly oxidised, but closer examination reveals that the phenocrysts are largely unaltered. Flow structure is evident through the subparallel orientation of elongated crystals and pore spaces (Fig. 4-19).

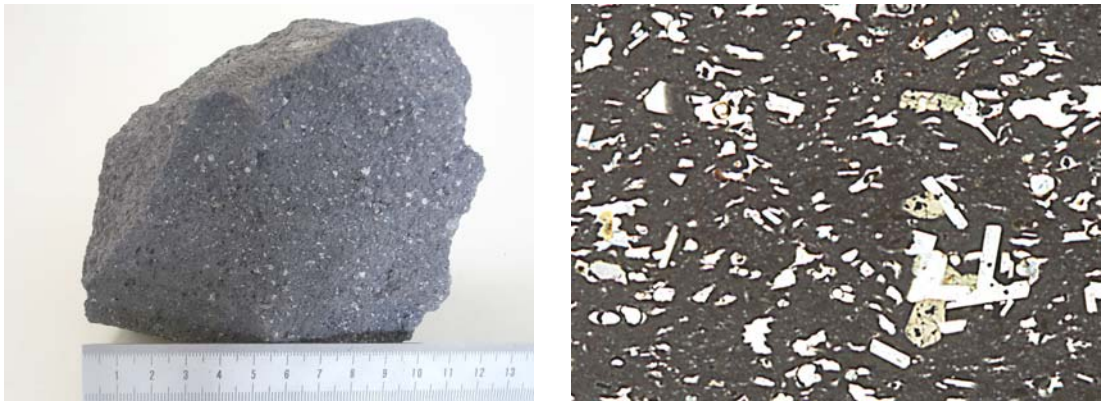

Figure 4-18. Although porous and slightly oxidised, *San 26* contains phenocrysts of plagioclase and pyroxene ideal for detailed analyses.

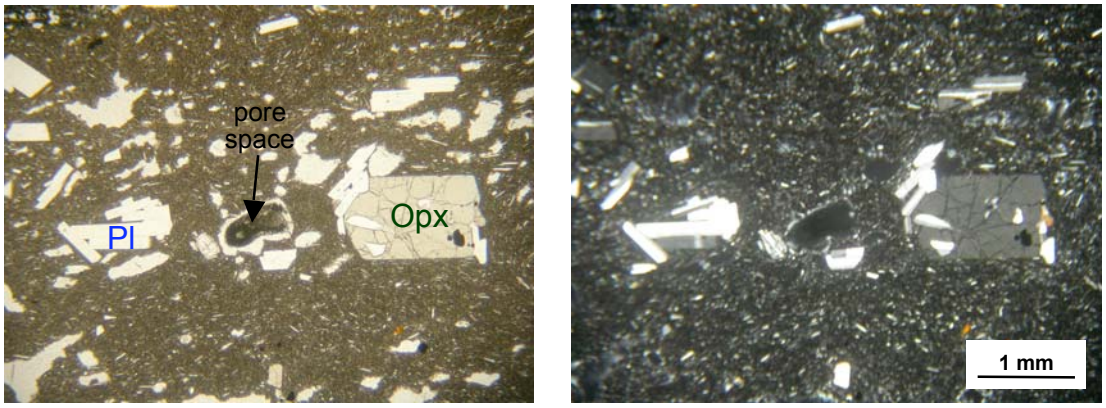

Figure 4-19. Flow structure is evident through subparallel crystals and pore spaces.

Phenocrysts comprise ~ 10 vol.% of the rock and the matrix ~ 80 vol.%, pore space taking up the rest of the rock volume. Although plagioclase occurs profusely as a phenocryst phase, pyroxene crystals are larger, the euhedral to subhedral grains reaching lengths of 2 mm (Figs. 4-19 and 4-20). Plagioclase phenocrysts are euhedral and mostly elongated instead of lath-shaped. These are twinned and show concentric and oscillatory zoning (Figs. 4-20 and 4–21). Magnetite occurs as inclusions in the other phenocrysts or is intergrown with them.

The groundmass is made up of very fine crystals of plagioclase, pyroxene and magnetite, with minimal brown glass.

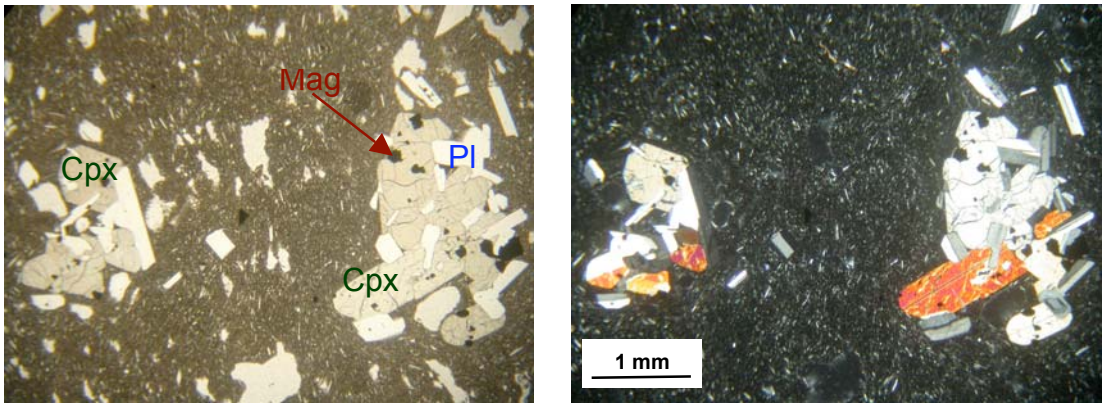

Figure 4-20. This sample (*San 26*) has rather large pyroxene phenocrysts, here intergrowm with plagioclase and magnetite.

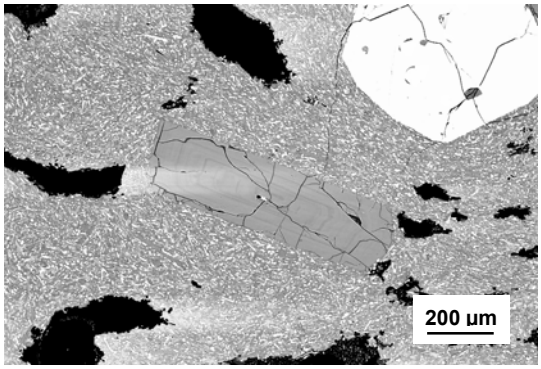

Figure 4-21. Zoned plagioclase in *San 26*. The white crystal on the upper right corner is ortho-pyroxene.

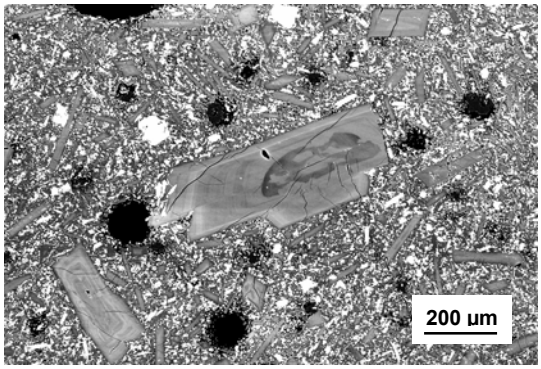

Figure 4-22. Plagioclase crystals in *San 27* showing concentric growth zones and, in the larger crystal at the centre, traces of resorption.

Plagioclase phenocrysts belong to type O, having only oscillatory variations in An within the range 58 to 54. Orthopyroxene occurs as enstatite and these phenocrysts have almost flat Mg# profiles of around 62.

San 27

San 27 was collected near to San 26, but from an andesitic flow of light grey colour and finer texture, also belonging to the Peristeria 3 unit of Druitt et al. (1999). Pore space is minimal and occurs in isolated portions without apparent consistent orientation (Fig. 4-23). Under the microscope, the sample is porphyritic to glomeroporphyritic, with a flow foliation defined by elongated phenocrysts and microlites (Fig. 4-24). Phenocryts make up ~ 10 vol.% of the rock, the rest being dense groundmass.

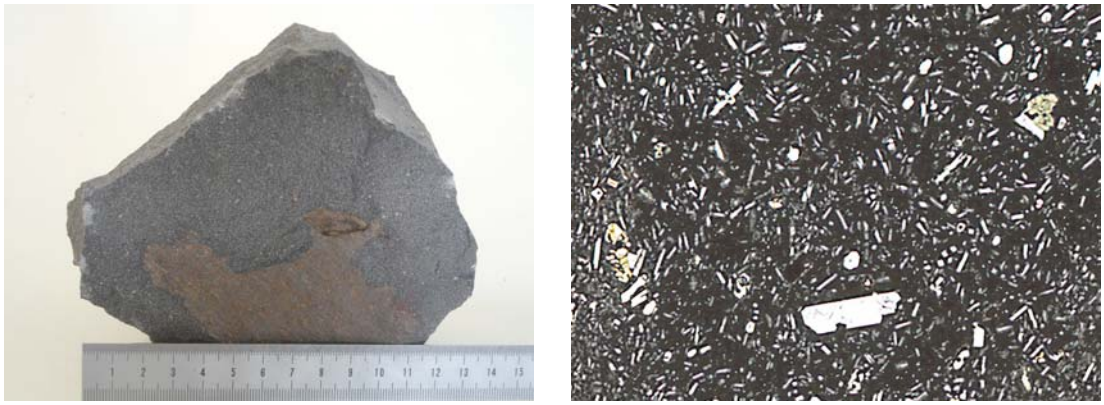

Figure 4-23. *San 27* is porphyritic like most other samples, but shows a finer texture and minimal porosity. The enlarged photo shows isolated cavities with oxidised walls.

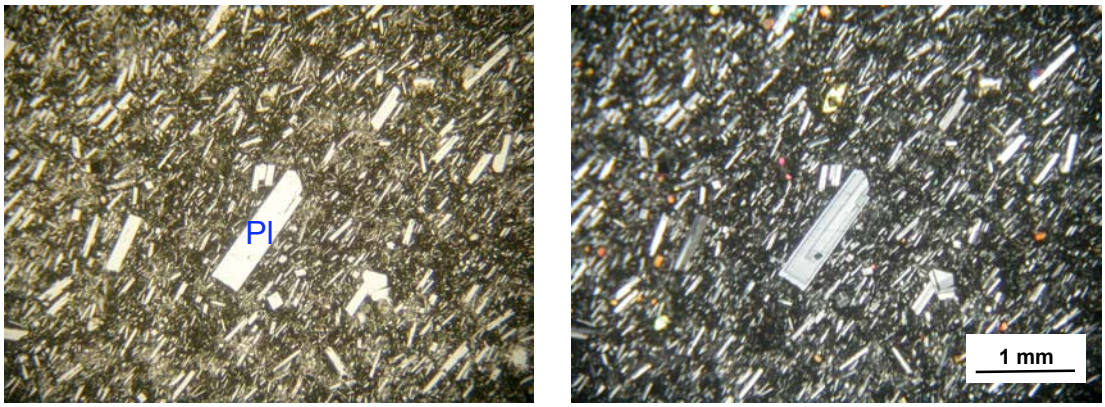

Figure 4-24. Phenocrysts and microlites show orientations parallel to the flow direction.

Plagioclase phenocrysts are euhedral and elongated (up to 2 mm). The laths are twinned, zoned, and in certain grains, resorbed (Fig. 4-22). These are of the type-O population with An contents of 67 to 45 mole %. Swallow-tail forms are common among the microlites. Pyroxene crystals are euhedral to anhedral, with magnetite and glass inclusions (Fig. 4-25). These phenocrysts may be intergrown. The same minerals comprise the very fine microlites in the matrix, together with brown glass.

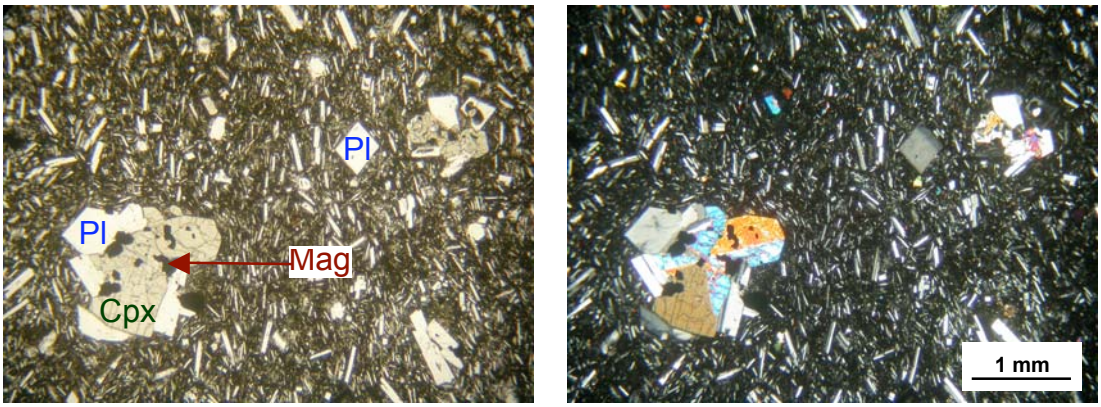

Figure 4-25. Intergrowths of plagioclase and pyroxene minerals also occur in *San 27*. It is common for clinopyroxene to include magnetite.

San 28

Also along the road to Oia and among the Peristeria 3 deposits, *San 28* was taken from what appears to be a coarse-grained lava flow. Upon closer inspection, however, the rock looks fragmental, the grains probably annealed together during emplacement and through compaction from overlying weight (Fig. 4-26). Nevertheless, it displays almost no porosity and therefore affords the unit a lava flow, instead of a pyroclastic (agglutinate) character. Moderately altered, the rock is porphyritic to glomeroporphyritic with plagioclase as the most conspicuous component. The matrix is generally greenish brown, although hues may vary depending on the degree of oxidation (evident in pictures under uncrossed polars; Figs. 4–27 to 4–29).

Figure 4-26. *San 28* is coarse grained, with large phenocrysts of plagioclae and pyroxene in a groundmass rendered greenish-brown by oxidation.

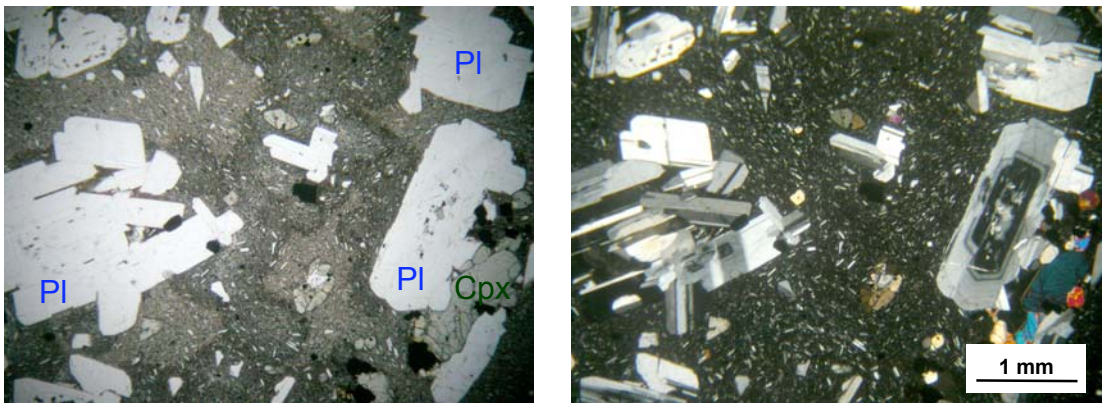

Figure 4-27. A large percentage of *San 28* is comprised by intergrown plagioclase phenocrysts of various sizes, shapes and textures.

Phenocrysts comprise nearly 40 vol.% of the rock, the rest being fine-grained matrix. Plagioclase crystals are commonly in fractured laths or elongated crystals that may be more than 2 mm in one dimension. These exhibit twinning and intergrowths (Figs. 4-27 and 4-28). Zoning occurs both as oscillatory and delineated concentric patterns, the latter defining high-

An cores and low-An rims that place these phenocrysts into the type-C group. An content in the core is within the range 90 – 78 and at the rim 64 – 48. Glass inclusions are also common, and in some crystals these render a brain-like, convoluted texture (Fig. 4-29).

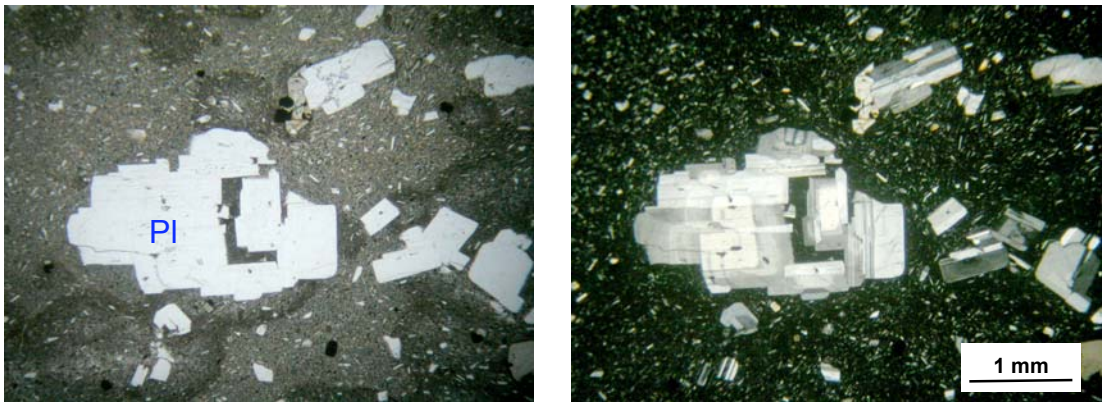

Figure 4-28. Plagioclase crystals are relatively large and show twinning, zoning patterns and complex intergrowths.

Orthopyroxene crystals are anhedral and largely altered by oxidation. These also display intergrowths and fractures. Mg# is within the range 68 – 64, in a trend that decreases towards the rim and therefore falls into type D.

Euhedral to subhedral magnetite is commonly included in the pyroxene, and also occurs as a component of the groundmass, with microlites of plagioclase and pyroxene, and some glass.

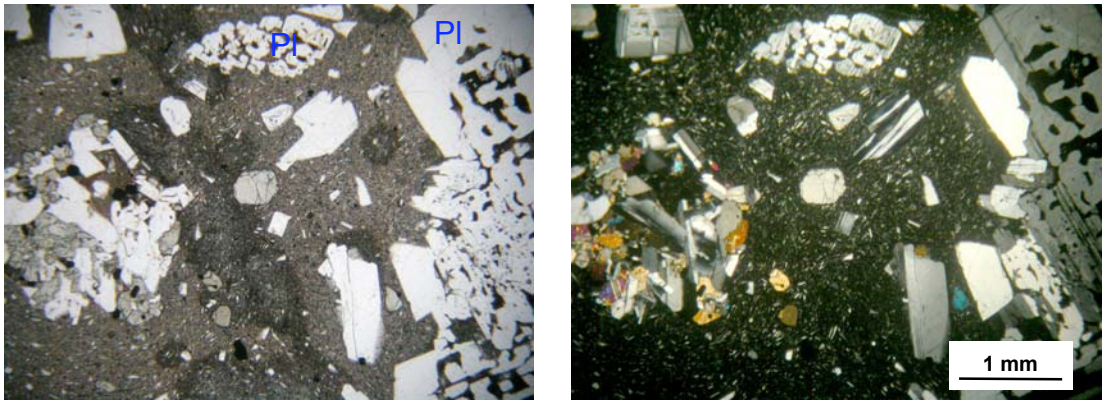

Figure 4-29. Some large plagioclase crystals include much glass and have a strange convoluted appearance. Smaller phenocrysts in the photo are intergrown with pyroxene.

San 30

San 30 is from a lava flow on the road near Oia, and part of the Megalo Vouno and Kokkino Vouno "Middle Tuff" of the Second Explosive Eruptive Cycle (Druitt et al., 1999, also see

Geologic Map). It is dense, light-grey in colour and appears aphanitic, except for isolated phenocrysts of plagioclase and orthopyroxene which add up to about 5 % of the total rock volume (Fig. 4-30). Flow structure and pore cavities are hardly observed. Plagioclase crystals have differing characteristics. The largest grain in one thin section, about 5 mm in length, consists of unaltered, twinned, and complexly intergrown crystals. The smaller ones are sparsely distributed, and may exist as euhedral laths or subhedral, equant crystals. Orthopyroxene phenocrysts are anhedral and also intergrown. Glass inclusions and sieve texture are exhibited by some grains (Figs. 4-31 and 4-32). Few magnetite crystals are large enough to be considered phenocrysts. The matrix consists of acicular plagioclase, fine grains of pyroxene, magnetite and brown glass.

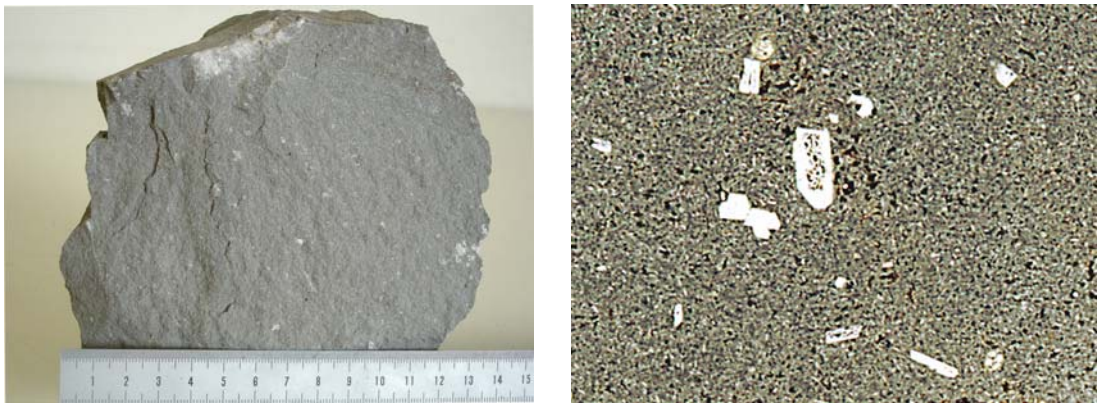

Figure 4-30. San 30 is almost aphanitic; plagioclase and pyoxene phenocrysts make up a limited percentage of the total rock volume.

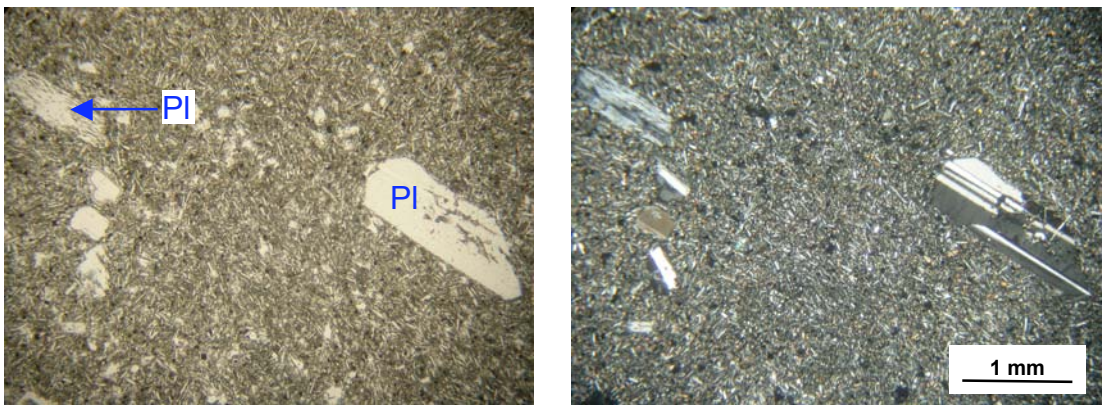

Figure 4-31. Plagioclase laths show twinning, oscilatory zoning, and may have glass inclusions.

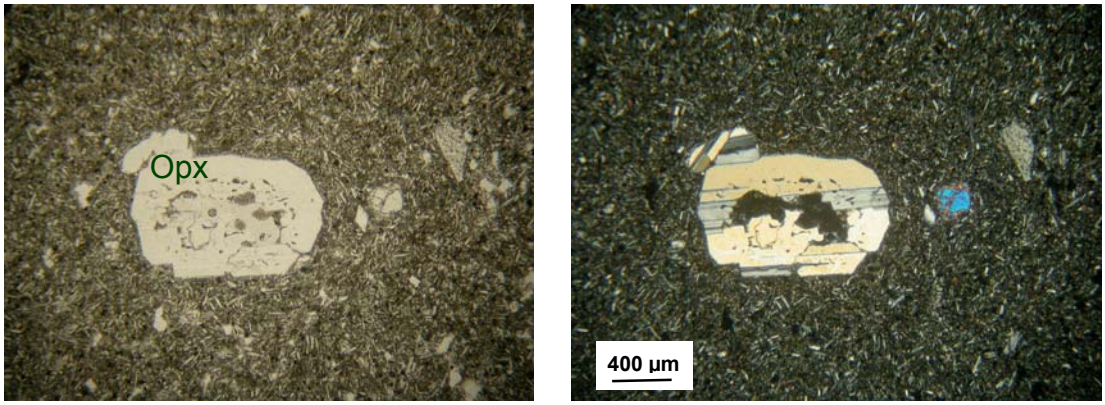

Figure 4-32. This relatively large orthopyroxene phenocryst exhibits twinning and has inclusions of glass.

Plagioclase phenocrysts are of type A with An_{90-83}, except at the outermost rim where the value abruptly decreases to An_{68}. Orthopyroxenes, with Mg# between 64 and 70, belong to type D.

San 31

San 31 was collected in Oia, from what is known as the "Andesites and Basalts of Cape Skaros", also a product of the Second Explosive Eruptive Cycle Phase (Druitt et al., 1999). It shows a slight flow texture and is dark gray, with about 12 vol.% phenocryst and 5 vol.% pore space (Fig. 4-33). Plagioclase phenocrysts are mostly in euhedral laths normally ~ 1 mm in length, although a few anhedral grains also occur. These exhibit twinning, oscillatory zoning, and intergrowths (Fig. 4-34). Sieve texture is common, the degree of solution varying among grains and the particular zones within them (Fig. 4-35). Few large grains of clinopyroxene are observed, also euhedral to anhedral, with zoning and, sometimes, sieve texture. Olivine has map-like or nearly skeletal forms. The groundmass consists of acicular plagioclase, acicular and equant pyroxene and subhedral magnetite.

The plagioclase phenocrysts fall under type A, with An_{92-88}, although this could drop to as low as An_{74} at the outermost margin. Clinopyroxenes are of type H, having Mg# 85-90. Olivine grains have cores with Mg# of up to 88, decreasing to 72 towards the rim.

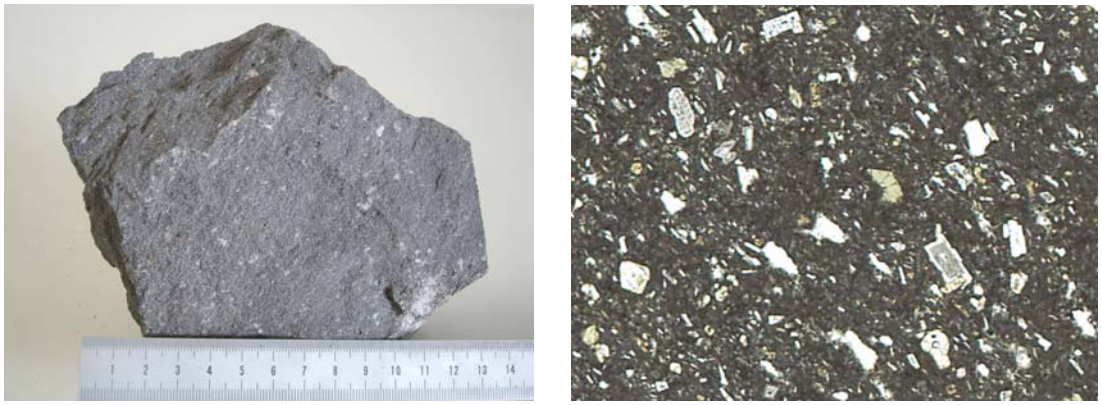

Figure 4-33. *San 31* has a slight flow structure, its orientation on both photographs is from the lower left to the upper right corner.

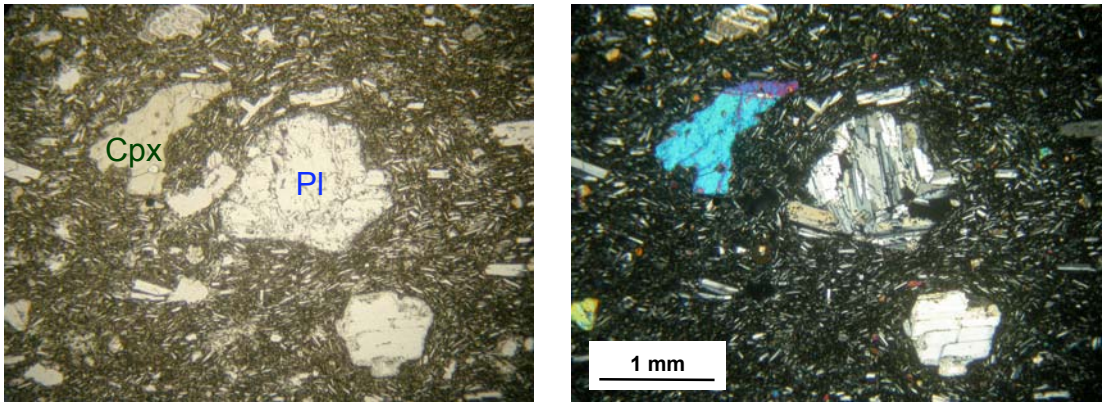

Figure 4-34. Anhedral clinopyroxene and twinned and intergrown plagioclase are the phenocrysts in *San 31*. Many of these crystals have glass inclusions.

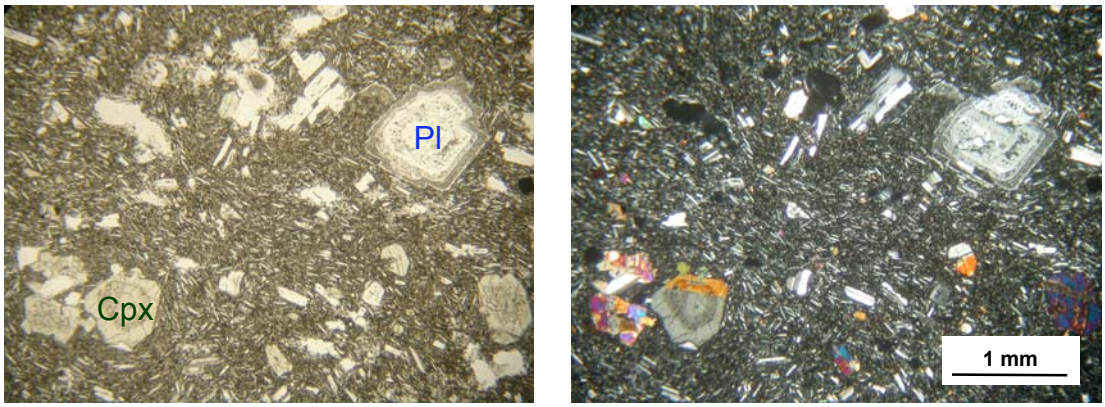

Figure 4-35. Some plagioclase and clinopyroxene phenocrysts exhibit sieve texture restricted to particular growth zones; the degree of solution among different zones vary.

San 32

San 32 is from the Oia andesites of the Second Explosive Eruptive Cycle (Druitt et al., 1999) and has porphyritic texture consisting of ~ 5 vol.% phenocryst and ~ 2 vol.% pore space. It shows a subtle flow structure. Plagioclase phenocrysts occur as euhedral laths usually 0.5 mm long. These are twinned, show oscillatory zoning, commonly have sieve texture, and

sometimes intergrown with other plagioclase crystals or with pyroxene (Figs. 4-37 and 4-38). Certain large crystals convey resorption (Fig. 4-39). Clinopyroxene grains are smaller, with euhedral to anhedral shapes (Fig. 4-40), and in some cases, have glass inclusions.

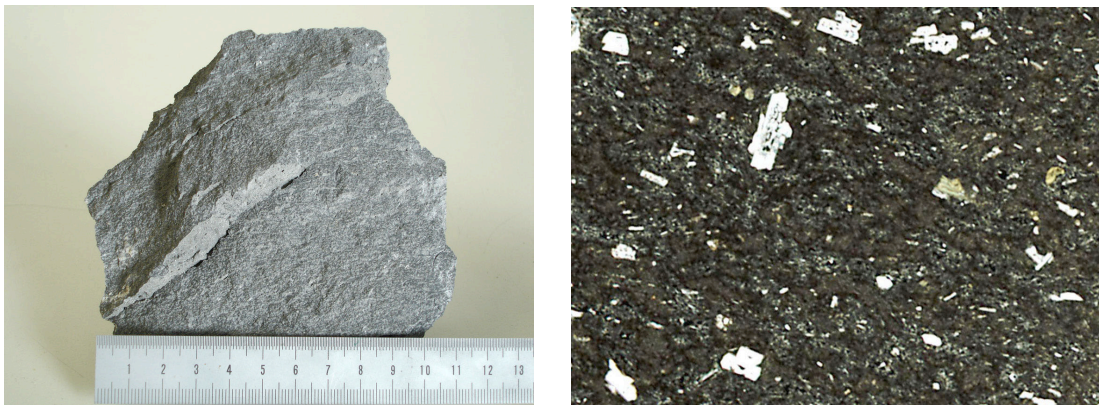

Fig. 4-36. San 32 is porphyritic but the phanocrysts, mostly plagioclase, are rather small. Hence, the the entire flow appears nearly aphanitic.

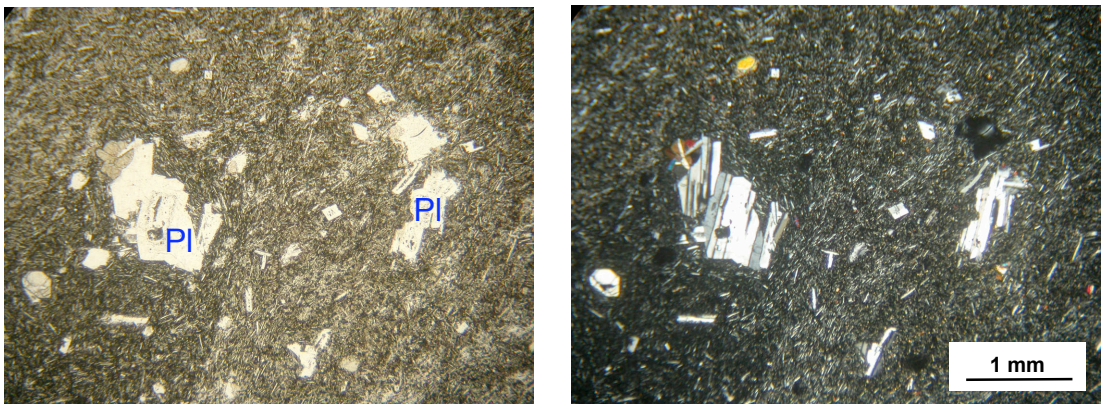

Fig. 4-37. San 32 has twinned and intergrown plagioclase, sometimes with glass inclusions.

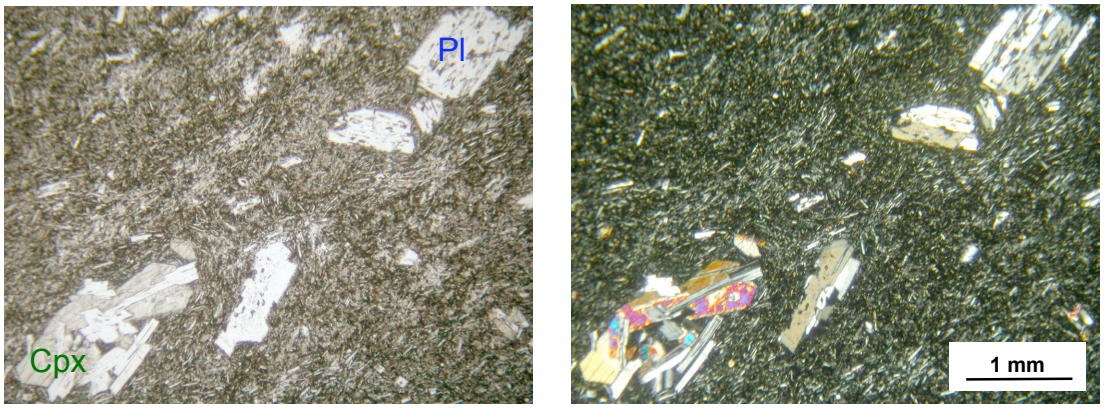

Fig. 4-38. Glass inclusions are common in plagioclase phenocrysts. Here, smaller crystals of a different texture are intergrown with clinopyroxene.

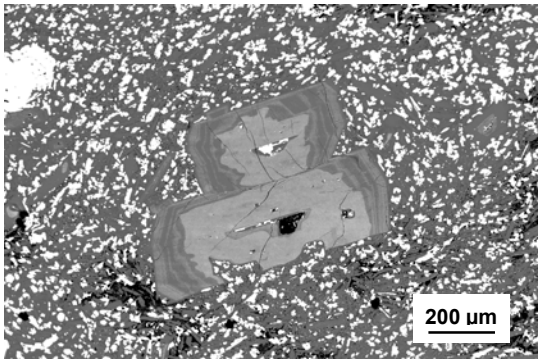

Figure 4-39. Certain plagioclase crystals in San 32 show distinct resorbed boundaries.

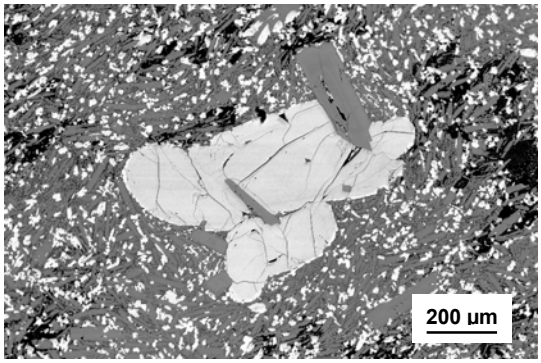

Figure 4-40. Most clinopyroxene crystals in sample San 32 are anhedral.

The matrix contains acicular plagioclase, pyroxene of varying shapes, and equant grains of magnetite, the latter nearly uniform in size (~100 μm). Subtle flow structure is also observed for this sample.

Plagioclase phenocrysts are of types A and C. An content for A is 72-83, which in rare cases is surrounded by a thin rim of An 55. For type C, An in the core is 82-87 and at the rim, 67-78. Clinopyroxenes are of Type H, with Mg# 76-78.

5. PHENOCRYST COMPOSITIONS

5.1 Nea Kameni Dacites

5.1.1 Plagioclase

Thirty plagioclase phenocrysts from the Nea Kameni dacites were investigated in terms of major and light element composition. These were classified into different types according to their major element trends, and subsequently designated into subtypes according to further significant variations in the gross composition and/or light element concentrations. As mentioned in the previous chapter, four main types of plagioclase have been identified. The following discussion describes each of these types and their respective subtypes in detail.

Type N

Type-N phenocrysts have anorthite (An) contents that decrease from core to rim, suggesting 'normal' crystallisation. Only three such crystals were found, in samples *San 3* and *San 36*. In the core of these phenocrysts, the mole fraction of anorthite may reach a maximum of 63 % (An_{63}), decreasing to as low as An_{32} at the rim. This decrease is generally gradual, although small (< 5 mole %) discontinuities along the boundary of concentric growth zones may be observed. A rim-ward drop of about 10 mole % is common within the outermost zones (< 100 μm) of the grains. Concentrations of ferric iron in the *San 3* crystals roughly mimic the An profiles (e.g. Fig. 5-1), with cpfu values ranging from 0.009 to 0.022. The Fe^{3+} profile in the *San 36* phenocryst (Fig. 5-2) is different, as it exhibits a slight peak halfway from the core to the rim, a pattern that is not shown by any of the other elements analysed. Nevertheless, this plagioclase grain has a more restricted range of Fe^{3+} contents (0.018 – 0.024 cpfu). Magnesium concentrations, measured only for *San3b Pl2* (Fig. 5-1), are ~ 0.003 cpfu in the core to ~ 0.001 cpfu at the rim, generally correlating with the An and Fe^{3+} profiles. Potassium concentrations show an inverse relationship to An, Fe^{3+} and Mg, with a low of 0.004 cpfu in the core and reaching 0.024 cpfu at the rim.

Note: In the figures within this chapter and the next, the top-left picture is a backscattered-electron (BSE) image of the phenocryst, the yellow line showing the electron-probe micro-analysis (EPMA). The top-right picture is a photomicrograph with white spots resulting from the secondary-ion mass spectrometry (SIMS) measurement. Major element profiles show the complete EPMA analysis points, but the table includes only selected points that coincide with the SIMS analysis. Where δ^7Li data are shown, the table may neither include the exact number of analysis points nor the accurate distance for the location of SIMS spots; these have been adjusted to the number and location of the SIMS analysis for light-element concentrations. Analysis results for Li are given in three decimal places only to be consistent with other values and render an orderly presentation of the data. Error bars in the light element profiles depict $\pm 2\sigma$.

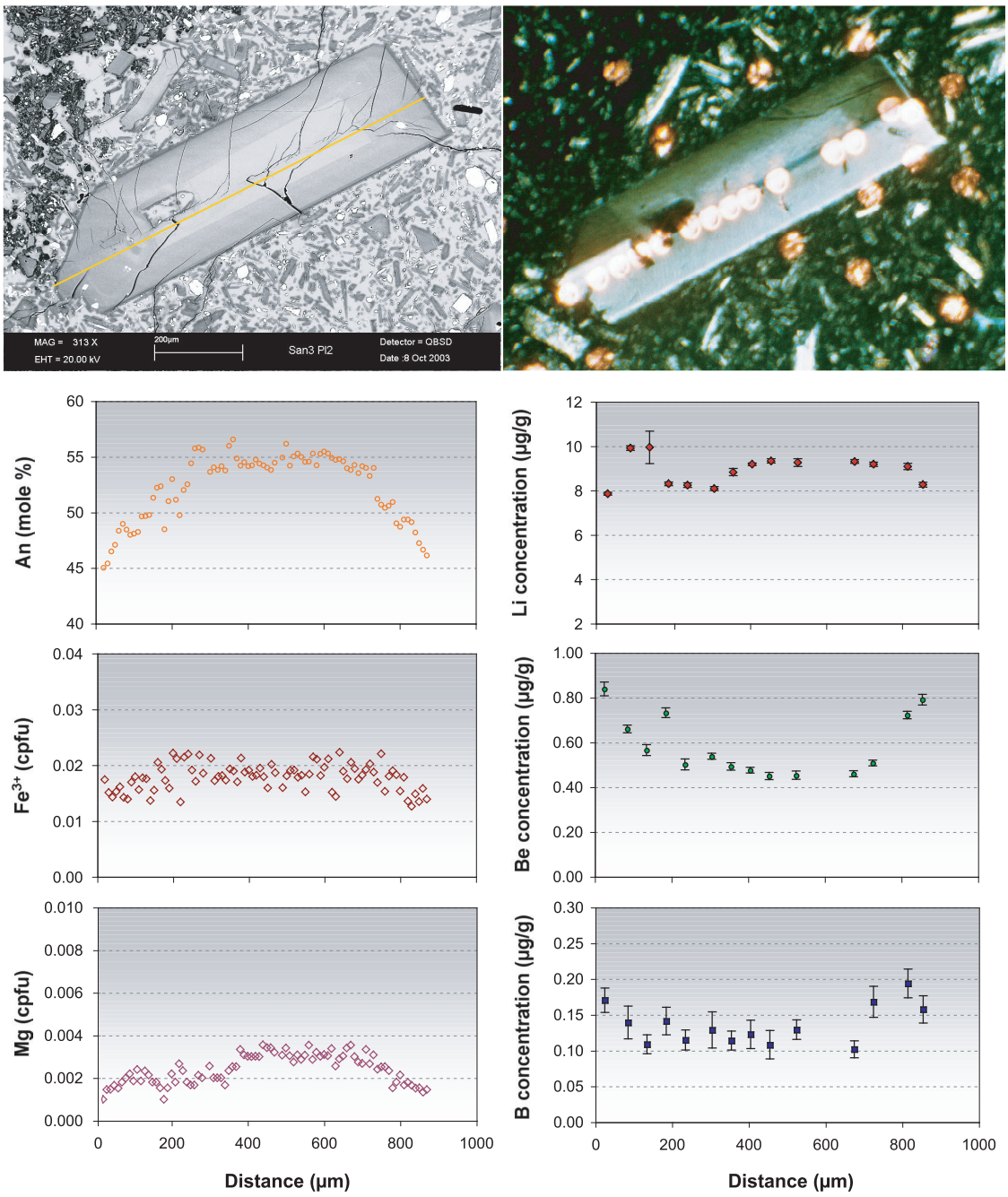

(µm)	Distance	30	90	140	190	240	310	360	410	460	530	680	730	820	860
(cpfu)	Si	2.532	2.511	2.493	2.479	2.448	2.451	2.437	2.449	2.462	2.434	2.440	2.466	2.495	2.526
	Al	1.459	1.482	1.501	1.510	1.537	1.535	1.549	1.537	1.523	1.550	1.541	1.521	1.495	1.467
	Fe^{3+}	0.015	0.017	0.014	0.016	0.022	0.017	0.019	0.018	0.020	0.018	0.019	0.019	0.014	0.016
	Mg	0.001	0.002	0.002	0.002	0.002	0.002	0.003	0.003	0.003	0.003	0.003	0.003	0.002	0.001
	Ca	0.449	0.470	0.489	0.504	0.523	0.537	0.557	0.537	0.529	0.551	0.544	0.528	0.490	0.457
	Na	0.538	0.508	0.493	0.484	0.472	0.456	0.427	0.453	0.453	0.445	0.458	0.449	0.502	0.522
	K	0.011	0.007	0.008	0.011	0.007	0.008	0.005	0.007	0.005	0.007	0.006	0.006	0.009	0.008
	Total	5.006	4.998	5.000	5.006	5.012	5.005	4.995	5.003	4.996	5.008	5.012	4.992	5.007	4.997
(mole %)	An	45.4	48.0	49.8	51.0	52.6	54.1	56.6	54.3	53.9	55.3	54.3	54.0	49.4	46.7
(µg/g)	Li	7.843	9.905	9.939	8.294	8.237	8.084	8.823	9.178	9.325	9.255	9.302	9.176	9.079	8.260
	Be	0.838	0.660	0.565	0.732	0.501	0.538	0.493	0.475	0.449	0.453	0.460	0.508	0.722	0.791
	B	0.170	0.139	0.109	0.141	0.115	0.129	0.114	0.123	0.108	0.129	0.102	0.168	0.194	0.157

Figure 5-1. *San3b Pl2* is a type-N plagioclase phenocryst, showing normal zoning in the major elements. Beryllium and Boron tend to show the expected core-to-rim increase for incompatible elements, but Lithium varies unsystematically.

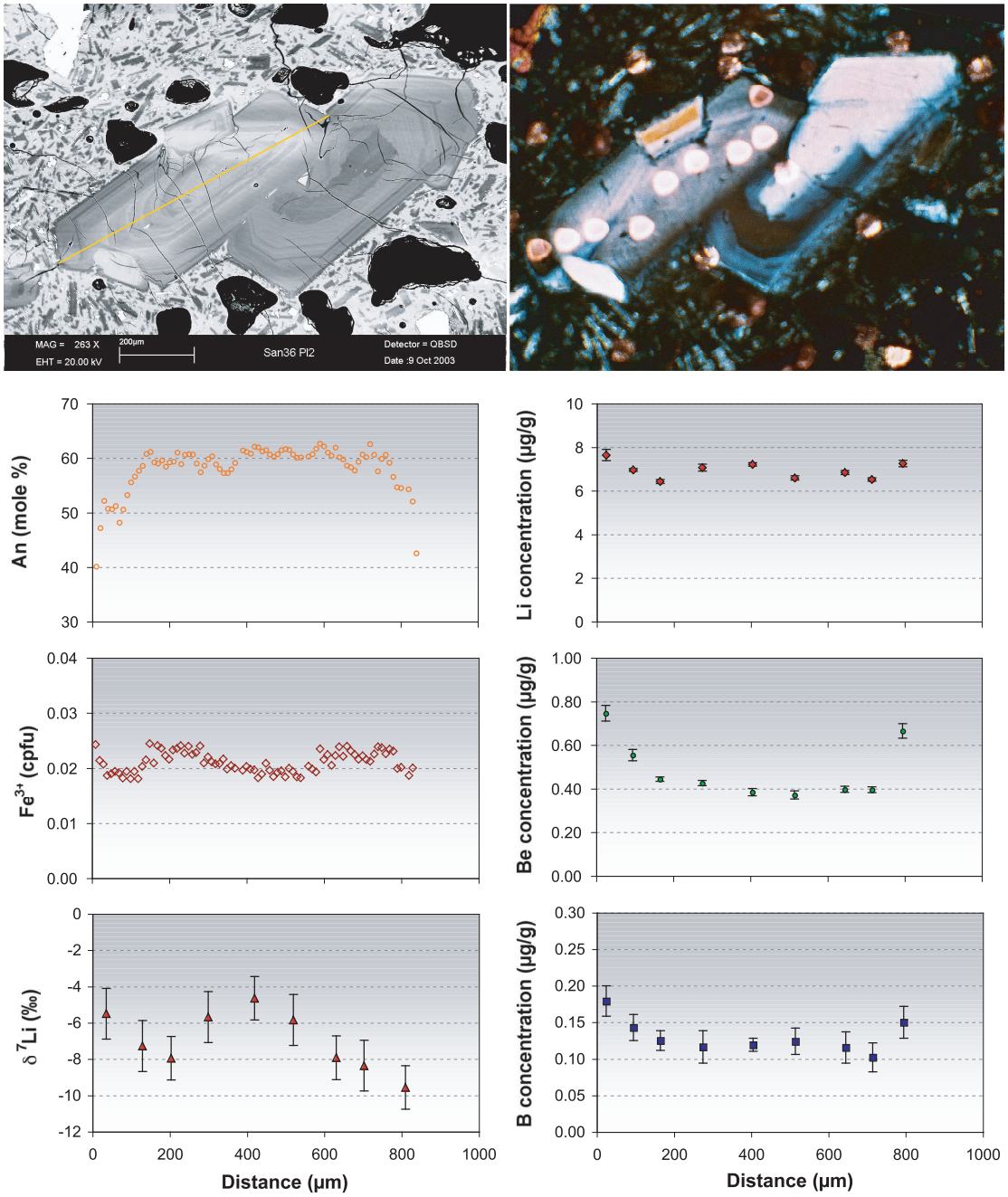

(µm)	Distance	30	100	170	280	410	520	650	720	800
(cpfu)	Si	2.489	2.444	2.396	2.426	2.386	2.400	2.405	2.384	2.459
	Al	1.496	1.542	1.583	1.558	1.605	1.589	1.581	1.603	1.532
	Fe^{3+}	0.021	0.018	0.024	0.024	0.020	0.019	0.022	0.021	0.020
	Ca	0.508	0.549	0.591	0.564	0.596	0.593	0.586	0.610	0.528
	Na	0.465	0.438	0.410	0.418	0.384	0.384	0.394	0.364	0.440
	K	0.012	0.006	0.006	0.005	0.006	0.005	0.007	0.007	0.009
	Total	4.991	4.998	5.009	4.995	4.997	4.990	4.994	4.989	4.989
(mole %)	An	52.2	55.6	59.1	57.5	60.9	60.7	59.8	60.6	54.5
(µg/g)	Li	7.627	6.945	6.417	7.052	7.197	6.579	6.827	6.504	7.236
	Be	0.745	0.553	0.443	0.425	0.383	0.371	0.396	0.394	0.664
	B	0.179	0.142	0.125	0.116	0.119	0.124	0.115	0.102	0.150
(‰)	$\delta^{7}Li$	-5.511	-7.290	-7.961	-5.696	-4.661	-5.860	-7.938	-8.371	-9.578

Figure 5-2. *San36b Pl2* is a type-N plagioclase with a large An range and a curious Fe^{3+} profile. The light elements show the expected increase towards the rim, except that core values for Li are rather inconsistent. $\delta^{7}Li$ seems to show the opposite trend, but values towards the left of the profile are not consistent.

Lithium concentrations amongst type-N crystals cannot be correlated to major element compositions (Figs. 5-1 and 5-2). Values for the *San 3* plagioclase range from 7.84 to 10.8 μg/g. Those for *San36b Pl2* are lower, at 6.42 – 7.63 μg/g. Beryllium and Boron concentrations generally increase from core to rim, inversely related to An. Such a pattern is consistent with the assumption that incompatible elements become progressively enriched in the melt during the course of normal crystallisation, and are therefore, increasingly forced into the developing rims of growing crystals. Be concentrations are 0.45 – 1.00 μg/g in *San 3* and 0.37 – 0.74 μg/g in *San 36*. Boron in *San 3* is 0.102 – 0.194 μg/g, although one crystal yields a high value of 0.639 μg at the rim, along with a significantly large standard deviation ($2\sigma = 0.06$, instead of the usual 0.02). Boron in the *San 36* plagioclase is within the same range, but with a lower maximum value of 0.179 μg/g at the rim.

Type O

The majority of the plagioclase phenocrysts are of type O, characterized by compositions between An_{58} and An_{40}. Zoning is commonly oscillatory, the variation within each crystal being restricted to a range of about 10 mole % of the An component. Some of the concentric growth zones, however, are disrupted by embayed surfaces brought about by resorption. Sieve textures, probably due to solution of existing zones, are also observed. Zoning, resorption and solution features vary from crystal to crystal, thus their development cannot be established alongside specific ranges of An content. K is commonly 0.005 – 0.015 cpfu and roughly inversely related to An. Fe^{3+} contents correspond to 0.013 – 0.023 cpfu, the values usually defining a flat profile. Mg concentrations were measured in only four phenocrysts, as the values consistently fall between 0.002 and 0.003 cpfu, almost at the detection limit.

An inverse relation to An content is generally shown by the concentrations of Be, and to a lesser degree of B, with values of 0.538 – 0.970 μg/g and 0.128 – 0.239 μg/g, respectively. In terms of Li, type-O phenocrysts are subdivided into two populations. Amongst the analysed crystals, exactly half – eight out of sixteen – belong to either subtype. Type-O1 crystals have Li profiles that are rather flat or display unsystematic variations, with values in the range of 6.60 – 10.8 μg/g (e.g. Fig. 5-3). In some cases, the variation may exhibit a subtle inverse relation to An content, and therefore mimic the patterns of Be and B. On the other hand, type-O2 phenocrysts have Li concentrations that markedly decrease from core to rim, with a maximum of 23.4 μg/g in the core and a minimum of 6.45 μg/g at the rim (Figs. 5-4, 5-5, 5-6). Such pronounced decline in Li concentrations is commonly consistent

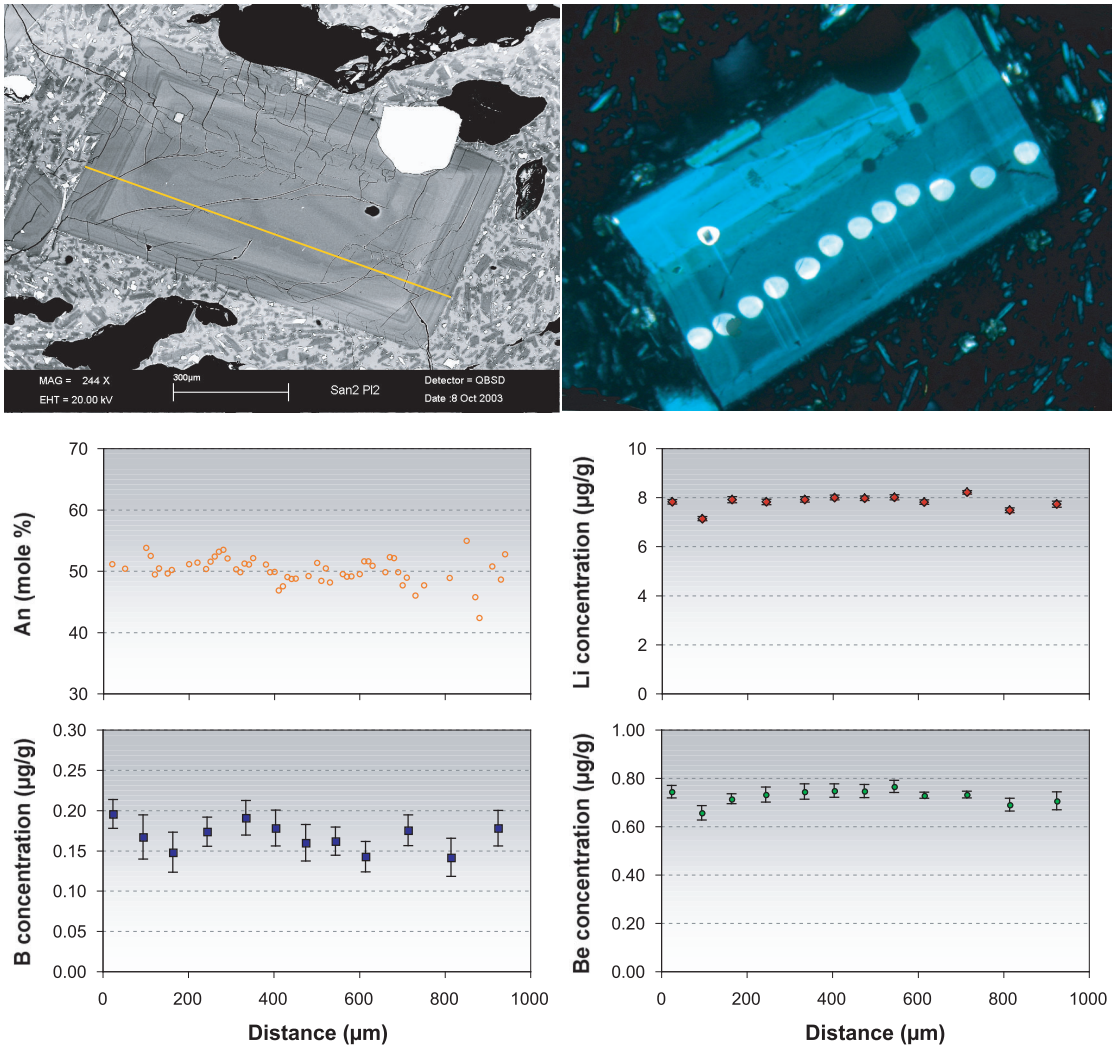

(µm)	Distance	20	100	160	250	340	410	480	560	620	700	810	930
(cpfu)	Si	2.504	2.455	2.480	2.458	2.489	2.508	2.500	2.517	2.482	2.518	2.500	2.524
	Al	1.464	1.539	1.505	1.505	1.494	1.466	1.468	1.451	1.507	1.457	1.455	1.480
	Ca	0.509	0.524	0.501	0.540	0.506	0.482	0.508	0.501	0.509	0.484	0.515	0.464
	Na	0.485	0.451	0.497	0.507	0.484	0.546	0.525	0.511	0.477	0.531	0.538	0.490
	K	0.012	0.010	0.009	0.012	0.010	0.011	0.008	0.007	0.013	0.012	0.010	0.010
	Total	5.000	4.997	5.011	5.040	5.002	5.030	5.024	5.006	5.002	5.018	5.036	4.980
(mole %)	An	51.2	53.8	50.18	51.6	51.1	49.9	49.2	49.5	51.6	47.7	48.9	48.6
(µg/g)	Li	7.808	7.121	7.895	7.803	7.903	7.979	7.953	7.989	7.798	8.196	7.463	7.715
	Be	0.742	0.655	0.713	0.731	0.743	0.747	0.745	0.764	0.728	0.730	0.688	0.704
	B	0.195	0.166	0.147	0.173	0.190	0.178	0.159	0.161	0.142	0.175	0.141	0.177

Figure 5-3. Type-O1 phenocrysts, like *San2b Pl2*, have intermediate An compositions and oscillatory zoning. Light element profiles are commonly inversely related to An; Li concentrations may vary unsystematically.

with the growth symmetry of the phenocrysts, the peak value coinciding with the core and decreasing towards the rim. δ^7Li patterns may appear like smoothened reversals of the Li concentration profile, with δ^7Li values increasing from core to rim. Added to the fact that Li abundances in these crystals exhibit absolutely no dependence on An content, the profiles suggest loss of Li in the magma during crystallisation, as shall be discussed further in the next chapter.

San37b Pl1 (Fig. 5-4) is the best example for type-O2 plagioclase phenocrysts. An content is within a restricted range of An_{52-45}, and the Mg profile is flat. Be concentrations show a reversed resemblance to An, and B slightly follows this pattern. Lithium concentration, however, is at a peak of 23.4 μg/g in the core and declines on both sides to a value of ~ 7 μg/g at the rim. The asymmetry of the crystal and the Li concentration profile coincide. The reverse is shown by the isotope pattern, except for the 'smoothened' δ^7Li values near the core.

San37b Pl2 (Fig. 5-5) shows the same general trends. It has a larger range of anorthite content, An_{57-39}, the changes in the composition of the system being also visible from several embayment surfaces on the phenocryst itself. For instance, the 'erratic' An measurements occur across defined embayment surfaces on either end of the profile; but surprisingly, near one end, this registers a peak and on the other a trough. Nevertheless, the pattern appears to be inversely reflected by Be and B. Li concentration is at a maximum of 23.1 μg/g nearly halfway through the profile, which is at the core of the crystal, and decreases to a minimum of 6.84 μg/g at the rim. The specific values for Li within particular zones are difficult to establish along the profile, as the zones and embayment surfaces cannot be followed throughout the crystal, except for the most pronounced one that corresponds to the An peak and trough. But even the extent of this surface is debatable, in view of the discrepancy in An content. The δ^7Li profile, however, seems to suggest two zones bounded by this embayment surface. Within the core, δ^7Li increases from –6.63 ‰ in the centre to +2.82 ‰ at the rim. External to this surface, i.e., three points on the left and two on the right end of the profile, the values are more restricted between –0.27 ‰ and –1.22 ‰.

San36a Pl2 (Fig. 5-6) is also a type-O2 phenocryst with An_{55-46}. Be and B concentrations are roughly inversely related to An (Fig. 5.6). However, the correspondence between An and Be may be further defined by considering the crystal zoning. Although the core has an intermediate An content of around 50, Be concentrations in this portion are the lowest at 0.562 – 0.613 μg/g, while other portions with the same An content have ~0.7

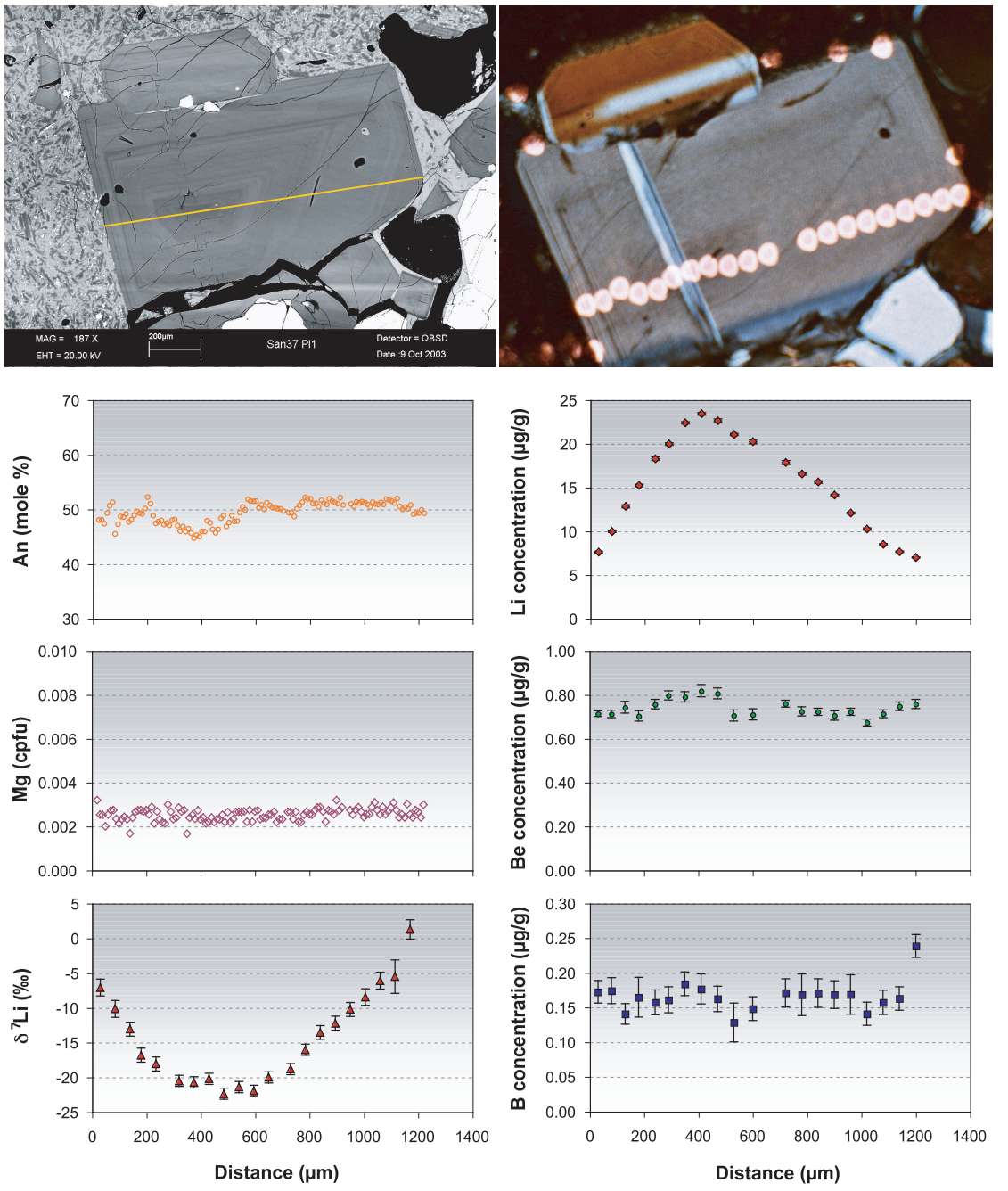

Figure 5-4. *San37b Pl1* is an excellent example of a type-O2 phenocryst. Major element compositions are much like those of type-O1, showing only oscillatory variations, which are inversely reflected by Be and B. Concentrations of Li, however, are rather high in the core and decrease dramatically towards the rim. For this particular crystal, Li concentration is highest in the core, revealed on the BSE image and microphotograph through the concentric growth zones. The core registers a trough on the δ^7Li profile, which displays a smoothened trend in contrast to the sharp peak in concentration. The δ^7Li profile has one point more than the concentration analysis, and the values on the table are for those points that are near the locations of the concentration analysis.

(µm)	Distance	30	80	130	180	240	290	350	410	470	530	600	720	780	840	900	960	1020	1080	1140	1200
(cpfu)	Si	2.522	2.532	2.523	2.499	2.515	2.514	2.539	2.536	2.513	2.522	2.476	2.499	2.473	2.476	2.480	2.487	2.482	2.460	2.496	2.502
	Al	1.467	1.459	1.467	1.488	1.474	1.481	1.456	1.452	1.474	1.469	1.516	1.493	1.513	1.514	1.508	1.498	1.499	1.522	1.487	1.480
	Mg	0.003	0.003	0.002	0.003	0.003	0.003	0.002	0.002	0.002	0.003	0.003	0.003	0.003	0.003	0.003	0.003	0.003	0.003	0.003	0.003
	Ca	0.468	0.449	0.464	0.489	0.469	0.466	0.449	0.453	0.480	0.466	0.503	0.484	0.519	0.509	0.505	0.499	0.503	0.522	0.500	0.489
	Na	0.503	0.535	0.507	0.503	0.511	0.502	0.515	0.531	0.509	0.506	0.472	0.494	0.474	0.474	0.482	0.487	0.493	0.483	0.498	0.501
	K	0.010	0.011	0.010	0.010	0.010	0.011	0.013	0.011	0.010	0.010	0.008	0.007	0.009	0.009	0.009	0.008	0.011	0.008	0.008	0.010
	Total	4.992	5.004	4.993	5.006	5.000	4.993	4.989	5.001	5.002	4.993	4.997	4.996	5.004	5.001	5.003	5.001	5.011	5.016	5.006	5.004
(mole %)	An	48.2	45.6	47.8	49.3	47.8	48.1	46.6	46.0	48.5	48.0	51.6	49.5	52.3	51.8	51.2	50.6	50.5	52.0	50.1	49.4
(µg/g)	Li	7.592	9.958	12.839	15.227	18.286	19.961	22.381	23.417	22.630	21.045	20.240	17.862	16.534	15.623	14.124	12.080	10.253	8.501	7.652	6.997
	Be	0.714	0.713	0.743	0.704	0.757	0.797	0.791	0.818	0.806	0.706	0.711	0.760	0.725	0.722	0.706	0.722	0.674	0.714	0.748	0.758
	B	0.173	0.174	0.141	0.165	0.157	0.161	0.184	0.177	0.162	0.128	0.148	0.171	0.168	0.171	0.168	0.169	0.141	0.157	0.163	0.239
(‰)	δ^7Li	-7.088	-10.156	-13.070	-16.823	-18.081	-20.509	-20.718	-20.207	-22.371	-21.391	-21.943	-18.811	-16.034	-13.554	-12.227	-10.235	-8.453	-6.104	-5.508	1.277

	(µm) Distance	30	70	120	170	220	270	320	390	490	540	610	660	710	760	820
(cpfu)	Si	2.513	2.529	2.488	2.514	2.527	2.519	2.498	2.559	2.559	2.517	2.524	2.512	2.495	2.639	2.509
	Al	1.476	1.459	1.502	1.473	1.461	1.474	1.488	1.430	1.439	1.470	1.474	1.475	1.491	1.341	1.473
	Ca	0.477	0.462	0.499	0.468	0.466	0.465	0.488	0.441	0.443	0.474	0.468	0.470	0.495	0.378	0.489
	Na	0.489	0.514	0.479	0.522	0.518	0.516	0.504	0.537	0.513	0.521	0.498	0.517	0.489	0.584	0.497
	K	0.011	0.013	0.007	0.010	0.010	0.011	0.009	0.012	0.010	0.010	0.010	0.010	0.010	0.019	0.010
	Total	4.988	4.995	4.995	5.006	4.998	5.000	5.005	4.994	4.977	5.006	4.986	5.004	4.999	4.982	4.998
(mole %)	An	49.4	47.3	51.0	47.3	47.3	47.4	49.2	45.1	46.3	47.6	48.4	47.6	50.3	39.3	49.6
(µg/g)	Li	6.843	7.765	7.357	8.082	10.487	11.222	15.271	23.133	21.147	18.751	17.876	14.978	11.429	10.098	7.792
	Be	0.776	0.773	0.719	0.730	0.846	0.761	0.786	0.846	0.845	0.800	0.802	0.732	0.798	0.888	0.738
	B	0.738	0.166	0.157	0.172	0.191	0.184	0.170	0.176	0.169	0.170	0.183	0.168	0.169	0.204	0.175
(‰)	δ^7Li	-0.653	-1.085	-1.174	0.294	-3.396	-2.333	-6.142	-6.628	-5.135	-2.866		-1.370	2.821	-0.268	-1.219

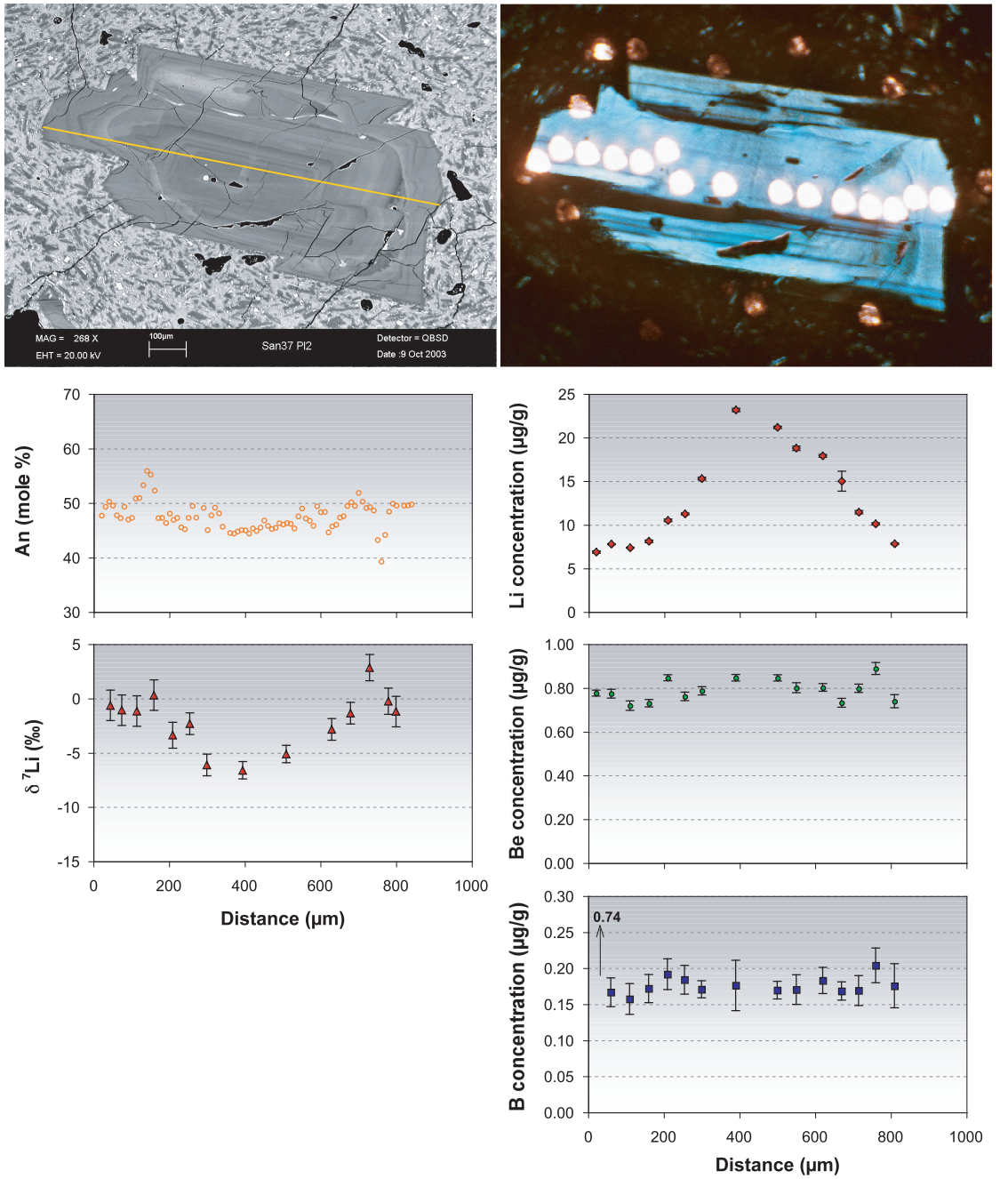

Figure 5-5. Another type-O2 plagioclase, *San37b Pl2* exhibits at least one pronounced resorption surface. Such is reflected in the An profile, but with opposite trends on either end of the crystal. Li concentration decreases from the core towards this surface, although asymmetrically. Between the surface and the rim, Li concentrations are more constant. The opposite pattern is displayed by the δ^7Li profile, where values increase from the core to the surface, then remain almost constant towards the rim. The δ^7Li analysis is one point less than that for the light element concentrations; on the table these are given according to the nearest-located concentration analysis point.

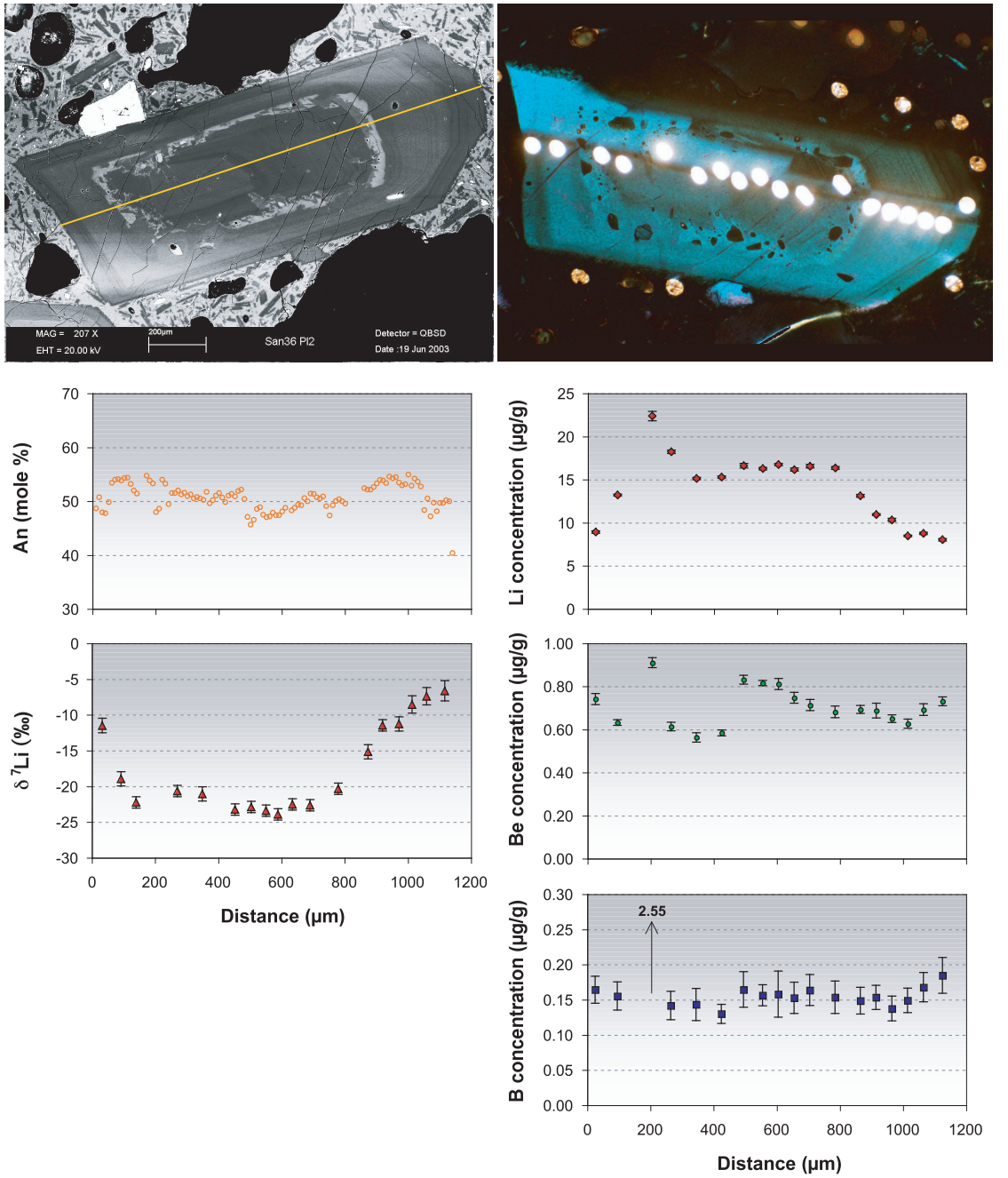

Figure 5-6. A type-O2 plagioclase, *San36a Pl2* has a sieve-textured zone between the core and the rim. The core (lighter-grey in the BSE image, near the left end of the crystal), despite its intermediate An content, contains the lowest concentrations of Be and B. This is surrounded by a zone (thicker towards the right) where Be is more abundant. Li and B show this trend to a lesser degree, with values remaining almost constant throughout the zone. Where An declines from the sieve-textured portion towards the rim, Be and B increase, while Li drops. The peak value in the Li concentration profile, marked by a higher error, is evidently due to the inclusion of the sieve-textured portion in the analysis. The δ^7Li presents a striking horizontal mirror image of the Li concentration, except for the third point, which has been moved away from the sieve texture.

(µm)	Distance	30	90	200	260	340	420	490	550	600	650	700	780	860	910	960	1010	1060	1120
(cpfu)	Si	2.522	2.444	2.519	2.475	2.473	2.482	2.522	2.517	2.516	2.493	2.490	2.500	2.472	2.457	2.453	2.464	2.497	2.505
	Al	1.461	1.534	1.463	1.510	1.501	1.495	1.468	1.473	1.471	1.491	1.499	1.483	1.503	1.526	1.528	1.515	1.488	1.478
	Ca	0.474	0.545	0.477	0.516	0.519	0.505	0.467	0.466	0.476	0.493	0.502	0.500	0.528	0.537	0.544	0.532	0.498	0.497
	Na	0.514	0.466	0.516	0.484	0.507	0.508	0.524	0.524	0.513	0.505	0.475	0.492	0.478	0.457	0.454	0.473	0.487	0.491
	K	0.011	0.009	0.012	0.009	0.008	0.009	0.011	0.012	0.013	0.011	0.010	0.010	0.009	0.008	0.007	0.008	0.009	0.010
	Total	5.001	5.016	5.005	5.009	5.026	5.019	5.005	5.007	5.004	5.010	4.994	5.001	5.010	5.003	5.004	5.010	4.997	4.998
(mole %)	An	48.0	53.9	48.0	51.6	50.6	49.9	47.1	47.1	48.1	49.4	51.4	50.4	52.5	54.0	54.6	53.0	50.6	50.3
(µg/g)	Li	8.899	13.178	22.347	18.207	15.111	15.264	16.594	16.253	16.724	16.130	16.536	16.317	13.101	10.922	10.304	8.448	8.754	8.002
	Be	0.741	0.632	0.909	0.613	0.562	0.584	0.830	0.815	0.811	0.746	0.712	0.681	0.693	0.687	0.650	0.626	0.691	0.730
	B	0.164	0.155	2.550	0.141	0.143	0.130	0.164	0.156	0.158	0.152	0.163	0.153	0.148	0.153	0.137	0.149	0.168	0.184
(‰)	δ^7Li	-11.521	-18.967	-22.295	-20.694	-21.084	-23.282	-22.909	-23.434	-23.957	-22.551	-22.682	-20.359	-15.202	-11.497	-11.312	-8.576	-7.422	-6.665

μg/g Be. This may imply an overall increase in the abundance of Be in the magma after crystallisation of the core. The sieve-textured zone is marked by questionably high values of the light elements (third point from left on the Li, Be and B profiles), along with a rather large range of error. Some groundmass must have been included in this analysis; this data point may therefore be omitted. The δ^7Li profile (for which the third point was moved away from the sieve-textured zone) shows a striking horizontal mirror image to that of the Li concentration. As in the previous two examples, this suggests a loss of Li in the system, preferentially of the lighter isotope ^{6}Li, which may be explained through degassing of the water-rich magma (see Chapter 6).

Type C

Certain plagioclase phenocrysts have cores with higher An compared to the rims, and are classified as type-C phenocrysts. The boundary between core and rim may be abrupt and step-like, or marked by a steep but continuous slope of decreasing An content. The range of An, especially within the core, actually varies among different grains. Certain crystals, called C1, have cores with $An_{58–64}$; those of others, called C2, have $An_{73–85}$. The rims of both subtypes, however, have similar An values, commonly $An_{\sim 50}$, or within the range of $An_{55\text{-}38}$. K concentrations are within the range 0.003 – 0.005 cpfu in the core and 0.005 – 0.007 cpfu at the rim of the grains. Fe^{3+} roughly coincides with An and is around 0.025 cpfu in the core and 0.018 – 0.020 cpfu at the rim. Mg is in some crystals inversely related to An, whereby core values are 0.001 – 0.002 cpfu and rim values 0.002 – 0.004 cpfu.

Be concentration is generally inversely related with An and may show a distinct discrepancy between core and rim; for type-C1 cores it is between 0.309 and 0.604 μg/g, and for type-C2 between 0.132 and 0.235 μg/g. Be in the rims of both subtypes is between 0.458 and 0.969 μg/g. B concentration is also inversely related with An but the transitions between core and rim are less conspicuous; a lowest value of 0.050 μg/g was measured in the core and a highest value of 0.242 μg/g at the rim. Li behaviour in these crystals is rather varied and therefore difficult to define. In type-C2 crystals, except for *San36b Pl1*, Li concentrations are markedly lower in the core than at the rim, with values of 2.87 – 3.99 μg/g and 6.09 – 7.40 μg/g, respectively. In type-C1 crystals, however, Li concentrations are simply at a minimum of ~ 5.33 μg/g in the core and generally increase, although variably, to values of 6.09 – 13.99 μg/g in the surrounding rim.

San36a Pl1 (Fig. 5-7) is a type-C1 phenocryst characterised by a core with An_{64-60} and a rim of An_{38-55}. The broad range of values for the rim is due to a low-An zone on one side of the crystal section, which is reflected as a trough in the profile. Mg concentration is at 0.002 – 0.004 cpfu, and peaks slightly in the core, although the overall trend is flat. Li, Be and B concentration profiles are similar, and show only a moderate dependence on An. Within the core, despite the flat An pattern, the light element concentrations increase from the central portion outwards. The concentrations of Be and B are especially high at the low-An portion, while that of Li shows less dependence on An. Outside the core of the crystal, the concentrations of all three elements decrease towards the rim, in much the same manner as in type-O2 plagioclase. δ^7Li values do not show a clear systematic variation, except for a crude decrease from the central to the outer portions of the core, and a roughly increasing trend from the core boundary to the rim.

San2a Pl4 and *San36b Pl1* are type-C2 phenocrysts with cores of An_{85-79}. *San2a Pl4* (Fig. 5-8) is a small grain that shows an abrupt, step-like compositional transition between the core and rim. An and Mg exhibit reverse patterns, the latter having values of approximately 0.001 cpfu in the core and 0.002 – 0.003 at the rim. All three light elements show the same reverse trend to An, one of the rare cases where Li concentration appears dependent on major element composition. Such may also be considered a strong evidence for the preservation of the primary Li concentration profile, and therefore, the unexpectedly fast crystallisation of this phenocryst. The established rapid diffusion of Li within plagioclase would have unavoidably homogenised the concentrations into a smoother, more flat profile, unless suddenly arrested by the cooling and solidification of the magma. This shall also be further discussed in the next chapter.

In *San36b Pl1* (Fig. 5-9), An values within the core appear to gradually decline near the boundary with the rim, although such boundary is still characterised by a drop of ~10 mole %. The rim exhibits oscillatory zoning, but the values are at least 15 mole % lower than those of the core. Mg also inversely correlates with An, although the variations in the outer zone cannot be distinguished, perhaps owing to the very low concentrations. Nevertheless, values are slightly higher than those in *San2a Pl4*, being 0.002 cpfu or less in the core and 0.003 – 0.004 cpfu in the immediate surrounding of the core, and lowering slightly to 0.002 cpfu at the rim. Li concentrations do not show any clear systematic variation with An or Mg content. Li is relatively low in the core, increasing outwards, but halfway through the outer zone declines towards the outermost rim. Be and B are similar: these are also of low

(µm)	Distance	30	40	50	80	150	170	250	330	430
(cpfu)	Si	2.528	2.532	2.507	2.497	2.513	2.517	2.519	2.523	2.435
	Al	1.453	1.435	1.480	1.488	1.464	1.467	1.466	1.458	1.545
	Mg	0.003	0.003	0.003	0.003	0.002	0.002	0.002	0.003	0.003
	Ca	0.495	0.527	0.475	0.497	0.496	0.482	0.481	0.483	0.561
	Na	0.468	0.432	0.508	0.486	0.494	0.504	0.503	0.500	0.426
	K	0.011	0.008	0.010	0.008	0.009	0.009	0.011	0.010	0.006
	Total	4.977	4.959	5.002	4.997	4.997	4.998	4.997	4.995	4.998
mole %)	An	51.4	55.0	48.3	50.6	50.1	48.9	48.9	49.1	56.9
(µg/g)	Li	6.838	7.204	7.719	8.114	10.571	11.348	13.991	13.845	9.540
	Be	0.612	0.628	0.708	0.757	0.756	0.798	0.785	0.773	0.604
	B	0.160	0.141	0.160	0.164	0.165	0.167	0.180	0.166	0.161
(‰)	δ^7Li	-4.997			-3.261		-4.884	-5.192	-6.421	-6.994

(µm)	Distance	440	450	500	580	700	780	840	860	900	920	990	1050	1120
(cpfu)	Si	2.384	2.382	2.384	2.397	2.395	2.421	2.367	2.410	2.490	2.586	2.590	2.543	2.525
	Al	1.591	1.588	1.585	1.566	1.578	1.547	1.619	1.556	1.492	1.395	1.394	1.442	1.458
	Mg	0.004	0.003	0.003	0.004	0.003	0.004	0.003	0.003	0.003	0.003	0.003	0.002	0.003
	Ca	0.607	0.628	0.625	0.635	0.614	0.611	0.601	0.623	0.513	0.415	0.411	0.460	0.471
	Na	0.388	0.367	0.376	0.362	0.367	0.366	0.389	0.367	0.478	0.577	0.568	0.517	0.516
	K	0.007	0.006	0.006	0.006	0.007	0.005	0.006	0.006	0.010	0.013	0.013	0.010	0.012
	Total	5.005	4.998	5.003	4.993	4.990	4.979	5.009	4.987	5.000	5.004	4.995	4.991	5.002
mole %)	An	61.0	63.1	62.4	63.7	62.6	62.5	60.7	62.9	51.8	41.9	42.0	47.1	47.7
(µg/g)	Li	7.721	8.331	6.554	7.799	6.924	8.098	7.518	9.560	10.643	9.596	8.662	7.922	7.820
	Be	0.347	0.532	0.309	0.510	0.345	0.530	0.412	0.575	0.969	0.887	0.787	0.746	0.661
	B	0.097	0.151	0.112	0.146	0.117	0.140	0.129	0.161	0.242	0.213	0.180	0.177	0.155
(‰)	δ^7Li	-7.804		-8.924	-6.756	-4.868	-5.08		-4.95	-7.359	-5.854	-5.927	-6.17	-4.586

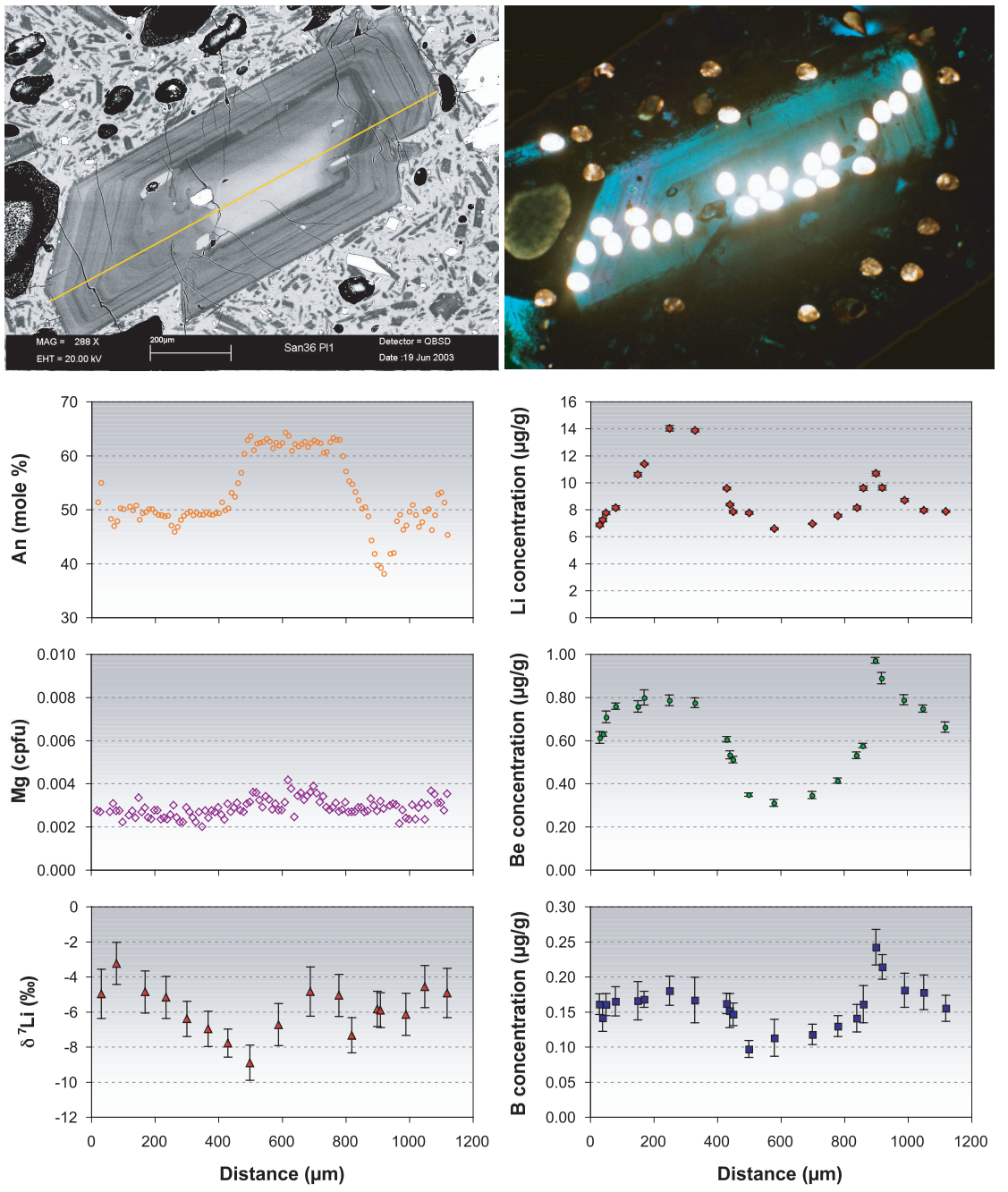

Figure 5-7. *San36a Pl1* is a type-C1 plagioclase where the core has a flat An profile that steeply declines to intermediate values towards the rim. Light elements increase in concentration from the centre to the outer portion of the core; these are elevated in the zone surrounding the core, then decline towards the rim. The δ^7Li pattern is a rough reversal of Li concentration. Resorption is evident on the crystal, especially for the low-An zone (dark-grey in the BSE image) that has disappeared towards the right portion. For this particular crystal, Mg does not show any correlation with major element composition. Numerous analysis points were done for light element concentrations; on profile the points have been projected to the EPMA line according to the zones where they were measured. The δ^7Li analysis involves less data points, which on the table are arranged according to their proximity to the concentration analysis.

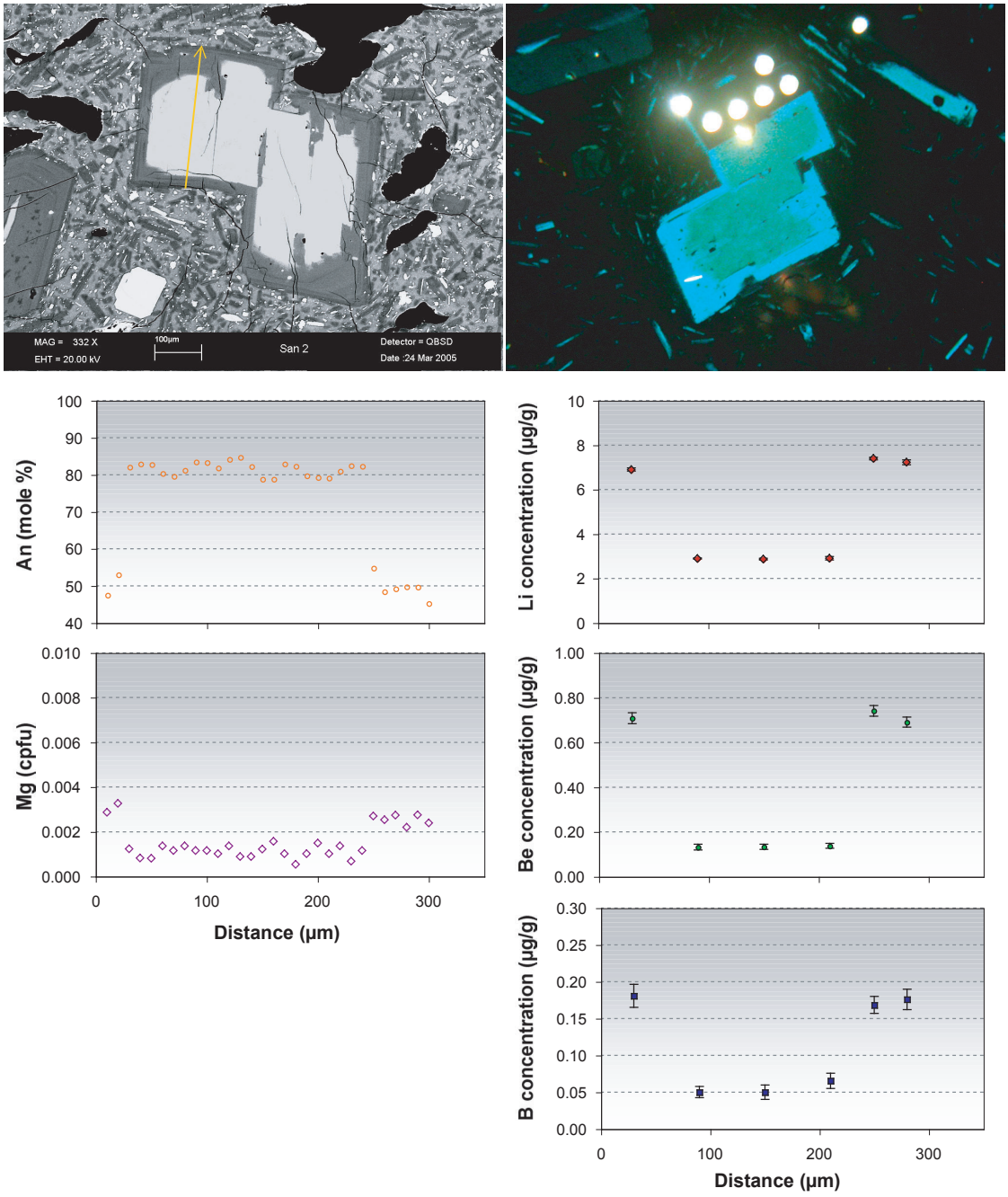

(µm)	Distance	10	60	130	200	270	280
(cpfu)	Si	2.501	2.150	2.114	2.179	2.488	2.490
	Al	1.486	1.829	1.862	1.808	1.490	1.498
	Mg	0.003	0.001	0.001	0.001	0.003	0.002
	Ca	0.471	0.817	0.863	0.791	0.497	0.492
	Na	0.520	0.200	0.156	0.207	0.512	0.496
	K	0.013	0.001	0.002	0.002	0.009	0.009
	Total	5.013	5.023	5.022	5.011	5.018	5.005
(mole %)	An	47.522	80.336	82.222	79.257	49.233	49.812
(µg/g)	Li	6.901	2.898	2.874	2.911	7.395	7.227
	Be	0.708	0.132	0.133	0.138	0.741	0.691
	B	0.181	0.050	0.050	0.065	0.169	0.176

Figure 5-8. *San2a Pl4*, a type-C2 phenocryst, shows a more abrupt change in An content between the core and rim, from $An_{\sim 80}$ to $An_{\sim 50}$. Mg and the light elements exhibit the reverse trend. Interestingly, in contrast to the previous figure, both major and trace elements in this crystal have nearly constant concentrations within the core, and the same holds true for the rim.

(µm)	Distance	60	120	180	240	330	410	480	550	640	710	780	850	920	990	1050	1110
(cpfu)	Si	2.477	2.458	2.499	2.463	2.421	2.398	2.342	2.174	2.164	2.201	2.346	2.350	2.328	2.403	2.433	2.489
	Al	1.506	1.528	1.494	1.525	1.564	1.587	1.639	1.815	1.814	1.791	1.631	1.639	1.658	1.586	1.554	1.491
	Mg	0.003	0.003	0.003	0.003	0.003	0.003	0.004	0.002	0.002	0.002	0.003	0.003	0.003	0.003	0.003	0.003
	Ca	0.507	0.531	0.484	0.515	0.559	0.583	0.635	0.795	0.814	0.770	0.637	0.620	0.646	0.580	0.553	0.510
	Na	0.488	0.451	0.487	0.475	0.420	0.406	0.359	0.193	0.192	0.202	0.360	0.365	0.344	0.392	0.424	0.474
	K	0.010	0.009	0.010	0.010	0.007	0.007	0.005	0.003	0.003	0.003	0.005	0.006	0.005	0.008	0.008	0.008
	Total	5.009	4.999	4.994	5.008	4.998	5.005	5.008	5.004	5.014	4.994	5.008	5.005	5.007	4.994	4.996	4.996
(mole %)	An	51.0	54.1	49.8	52.1	57.1	59.0	63.9	80.5	80.9	79.2	63.9	62.9	65.2	59.7	56.6	51.8
(µg/g)	Li	7.961	9.377	11.842	11.733	11.245	10.799	10.010	8.880	9.775	11.580	12.164	12.466	9.960	10.567	10.027	9.055
	Be	0.713	0.652	0.717	0.596	0.512	0.384	0.271	0.235	0.229	0.279	0.296	0.306	0.302	0.360	0.528	0.728
	B	0.162	0.121	0.167	0.131	0.129	0.102	0.088	0.076	0.076	0.087	0.100	0.098	0.103	0.101	0.134	0.164
(‰)	δ^7Li	-5.699	-6.241	-7.635	-9.220	-9.843	-11.162	-12.259	-16.642	-14.815	-17.771	-16.657	-14.346	-12.934	-12.104	-10.220	-10.704

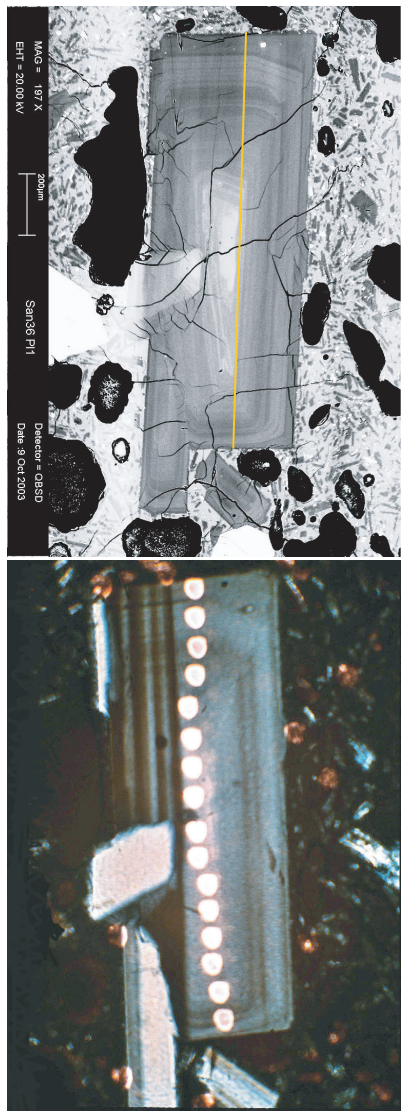

Figure 5-9. *San36b PI1* is a type-C2 crystal that exhibits more variations in An content within the relatively thick rim. Mg also shows a distinct difference between core and rim values, but the rim variations are lost in the detection of this trace element. Be and B adhere to their inverse relationship with An, while Li behaves rather unsystematically. Li concentration appears to increase from the core then decrease halfway through the rim. The δ^7Li profile is more consistent, and in fact similar to that of *San36a PI1* (Fig. 5-7), decreasing from the centre of the core towards the boundary with the rim, and increasing from this boundary towards the outermost rim.

abundance in the core and increase towards the rim. Closer inspection of the profiles reveals an inverse relationship between the concentrations of Be and B with An, but the usual marked discrepancy between Be values in the high-An core and the low-An rim is not evident for this crystal. δ^7Li values are more hinged with the major element composition, with a general trend towards heavier values from core to rim. This may have resulted from the inherent lighter isotopic composition of the magma that formed the high-An core, which after the intrusion of the less mafic magma suffered loss of the lighter isotope through degassing. As in type-O2 crystals, degassing may be inferred from the decreasing Li concentrations towards the rim.

Type A

A few crystals in the Nea Kameni samples are considered 'anomalous', and designated as Type A, because they have anorthite contents too high for a dacitic system. These are most likely xenocrysts from earlier, less differentiated magmas. The crystals either have $An_{\sim 90}$ throughout, or have cores and rims with moderate An contents separated by intermediate zones with high An. The latter case may be due to how the sections have been cut through the crystal, i.e., what appears to be a low-An core is actually part of the rim that has an undulating surface boundary with the real high-An core. Hence, the description here shall be limited to an example that has consistently high An.

San37a Pl4 (Fig. 5-10) is within a small xenolith. It is nearly 3 mm long and besides the high-An composition, it is surrounded by microlites of pyroxene and magnetite in stark contrast with the dacitic groundmass. Li concentration has a peak value of 10.92 μg/g within the crystal, although this portion does not appear to be the core. Li then decreases to almost nothing towards the rim on one side, and to values of 5.73-6.99 μg/g across the crystal's central portion on the other side, where the decline also continues to a value of nearly zero towards the rim. Be and B concentrations are lower than in other plagioclase phenocrysts, with 0.054-0.086 μg/g Be and 0.017-0.080 μg/g B. The δ^7Li plot is very interesting in that it is similar to those of the type-O2 crystals. The lightest Li isotope composition of –30 ‰ occurs where Li concentration is highest, and becomes heavier towards the rim. The minor rim-ward decrease in δ^7Li on the left end of the profile may be disregarded in consideration of the analytical uncertainties, and the progressively large errors toward both ends of the profile is simply due to the very low Li concentrations at the rim. As in several previously described examples, degassing may explain the Li concentration and isotope pattern of this phenocryst.

(µm)	Distance	30	130	240	350	460	710	840
(cpfu)	Si	2.151	2.077	2.068	2.081	2.081	2.082	2.081
	Al	1.828	1.906	1.914	1.906	1.897	1.900	1.897
	Ca	0.831	0.901	0.919	0.895	0.905	0.899	0.907
	Na	0.182	0.108	0.092	0.099	0.106	0.101	0.094
	K	0.003	0.002	0.000	0.001	0.001	0.001	0.002
	Total	5.016	5.015	5.012	5.004	5.013	5.007	5.006
(mole %)	An	82.1	89.3	90.9	90.1	89.5	89.9	90.6
(µg/g)	Li	0.349	0.843	1.245	2.742	3.730	4.929	6.981
	Be	0.060	0.054	0.058	0.069	0.085	0.086	0.079
	B	0.030	0.042	0.034	0.030	0.027	0.080	0.055
(‰)	δ^7Li	-0.317	1.595	3.328	-7.745	-17.391	-19.435	-23.576

(µm)	Distance	1030	1240	1440	1610	1720	1850	2000	2200	2400	2530	2710
(cpfu)	Si	2.066	2.074	2.072	2.088	2.073	2.083	2.070	2.074	2.101	2.090	2.051
	Al	1.910	1.908	1.908	1.885	1.905	1.894	1.907	1.911	1.883	1.889	1.929
	Ca	0.920	0.906	0.912	0.907	0.914	0.903	0.920	0.908	0.877	0.902	0.936
	Na	0.094	0.097	0.097	0.108	0.094	0.108	0.094	0.097	0.126	0.108	0.071
	K	0.000	0.001	0.001	0.001	0.001	0.002	0.000	0.000	0.000	0.000	0.002
	Total	5.014	5.009	5.012	5.012	5.010	5.013	5.013	5.009	5.010	5.009	5.010
(mole %)	An	90.7	90.3	90.4	89.4	90.6	89.3	90.7	90.3	87.4	89.3	93.0
(µg/g)	Li	10.915	7.884	6.508	5.728	6.475	6.495	6.990	6.523	6.666	2.589	0.188
	Be	0.066	0.071	0.059	0.054	0.074	0.066	0.058	0.055	0.060	0.052	0.054
	B	0.017	0.035	0.030	0.022	0.036	0.024	0.040	0.037	0.034	0.037	0.032
(‰)	δ^7Li	-30.200	-29.306	-29.363	-26.359	-23.209	-21.514	-17.364	-14.740	-10.944	-6.780	9.037

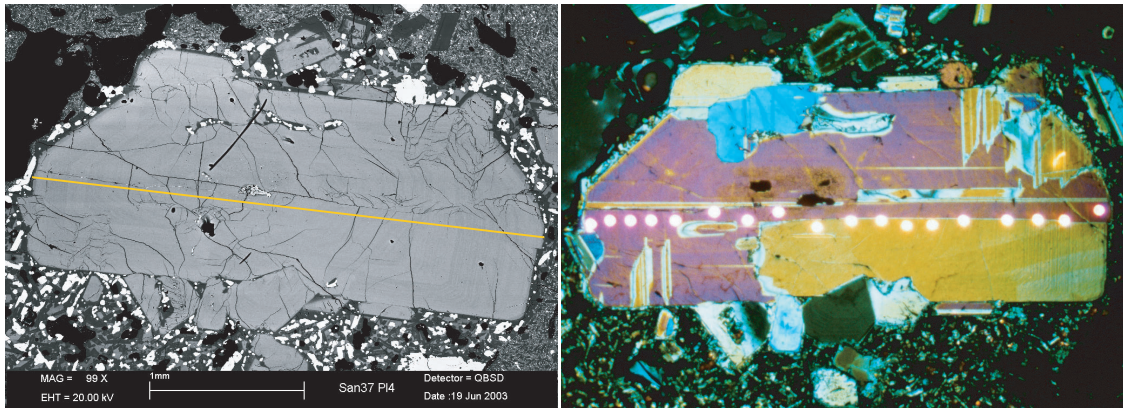

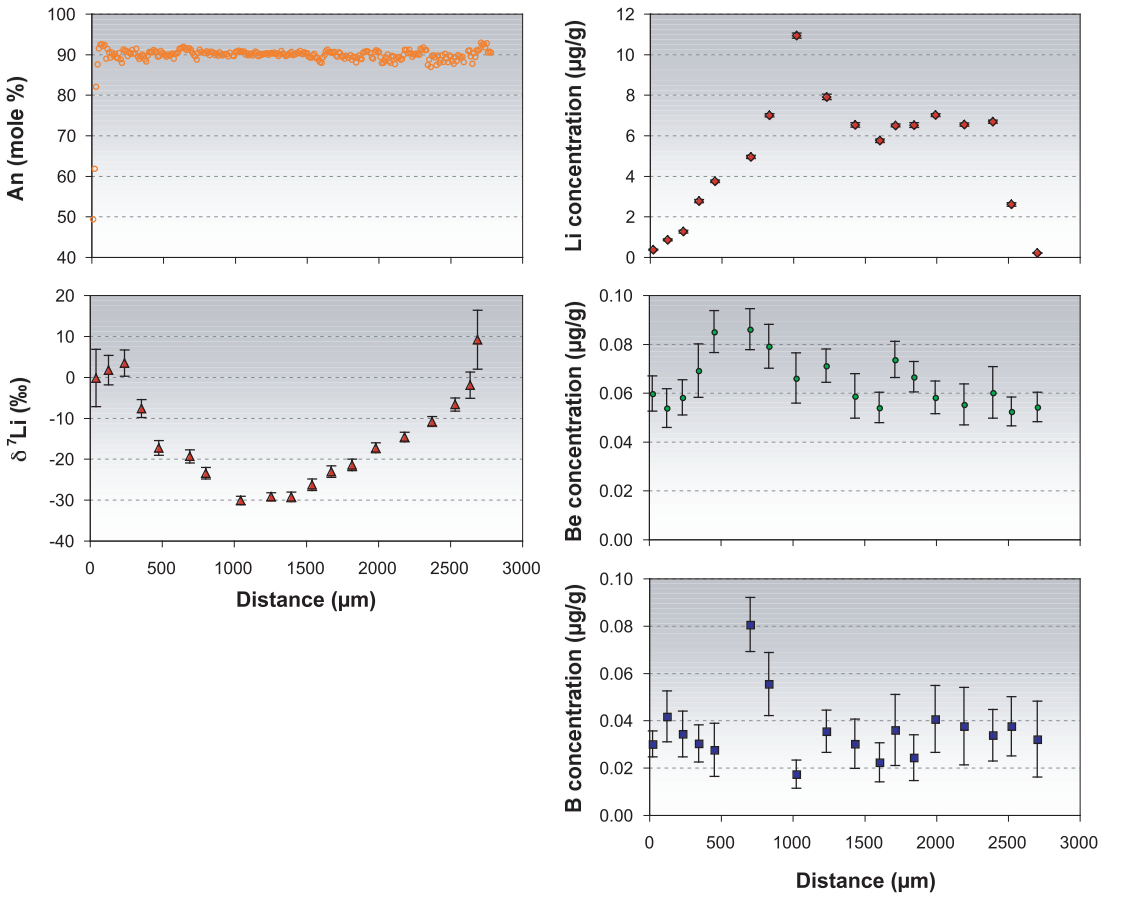

Figure 5-10. This fragment within *San 37* is apparently a xenolith from a more mafic fraction, consisting of a relatively large plagioclase crystal, *San37a Pl4*, surrounded by a matrix of smaller pyroxene crystals. Phenocryst major element composition is very homogeneous, but light elements vary unsystematically. The Li concentration peak may have to do with the cracks within the crystal, but otherwise concentration in the central portion is rather consistent. Despite the smoothened δ^7Li profile, the peak Li concentration coincides with the δ^7Li trough, and the general decrease in concentration towards the rim is accompanied by an increase in δ^7Li. The large error values for δ^7Li at the rim is because of the near-absence of Li.

5.1.2 Clinopyroxene

Type H

Clinopyroxene phenocrysts in the dacites are not as varied as those of plagioclase. In terms of the range of Mg numbers [Mg# = 100 × Mg/(Mg+Fe_{tot})], there are but two populations. Type H has relatively high Mg#, but only one such crystal suitable for analysis was found. The Mg# of *San2b Px1* (Fig. 5-11) is 83 in the core and decreases to 74 at the rim. The crystal exhibits well defined concentric and sector zoning in the back-scattered electron (BSE) image. Mg# values and Fe_{tot} profiles, inversely correlated, do not reveal anything about the zoning patterns, but individual elements show a distinct change across the boundaries between different sectors. Concentrations of Al, Ca and Ti are elevated in the core of the crystal at values of ~ 0.30, 0.87 and 0.04 cpfu, respectively, while those towards the rim are more erratic and straddle along values of 0.07, 0.75 and 0.01 cpfu, respectively. Si and Mg concentrations are low in the core, approximately 1.77 and 0.74 cpfu, respectively. At the rim, these increase to about 1.95 and 0.93 cpfu, respectively.

Li concentration does not appear to vary with the zoning, but seems to be dependent on Mg#, or the general growth pattern of the crystal, as it simply increases from core to rim. The concentration profile is smooth, with a minimum of 1.50 μg/g in the core. The rim values are not consistent, because the two measured points were not of the same distance from the crystal's margin. Perhaps the more reliable value is 4.18 μg/g, for which the analysis was done clearly within the crystal. The other spot probably included some matrix material, as Li is unusually high at 11.04 μg/g, accompanied by a slightly larger error. The profiles for Be and B are rather erratic, probably due to the exceptionally low concentrations. Neither does the δ^7Li data show any systematic pattern.

Type L

The rest of the clinopyroxene phenocrysts belong to type L, characterised by lower Mg# of 66-77. No phenocryst of this kind was found to show sector zoning, but subtle concentric zoning is common. Concentrations of Si, Al, Mg and Fe are typically within the ranges of 1.95 – 2.00, 0.05 – 0.10, 0.75 – 0.85 and 0.31 – 0.41 cpfu, respectively. Ca is consistently at ~ 0.8 cpfu. Li concentrations usually show a core-to-rim increase, although this is very slight except for the outermost rims. The lowest value measured in a core is 2.44 μg/g Li and the maximum concentration at the rim is 13.7 μg/g. Concentrations of Be (0.10 – 0.25 μg/g) and

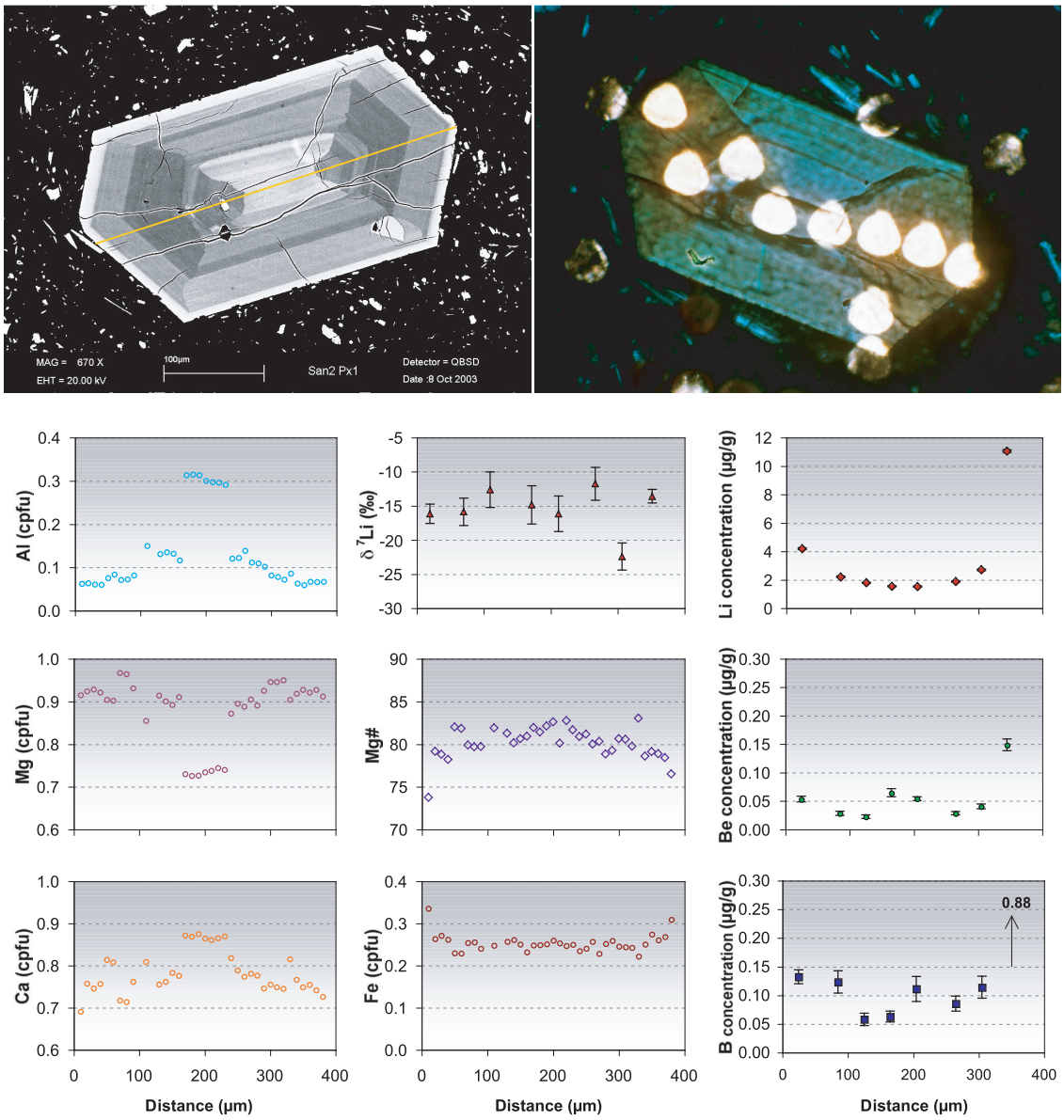

(µm)	Distance	30	90	130	170	210	270	310	350
(cpfu)	Si	1.957	1.954	1.904	1.766	1.788	1.934	1.947	1.954
	Al	0.061	0.082	0.132	0.314	0.298	0.112	0.078	0.060
	Mg	0.271	0.241	0.257	0.249	0.253	0.228	0.244	0.274
	Ca	0.928	0.931	0.915	0.730	0.738	0.906	0.946	0.928
	Fe	0.747	0.762	0.756	0.872	0.862	0.782	0.750	0.749
	Ti	0.009	0.008	0.013	0.041	0.034	0.014	0.010	0.009
	Total	4.000	4.000	4.000	4.000	4.000	4.000	4.000	4.000
	Mg#	78.8	79.7	81.2	81.9	80.1	80.3	80.5	79.1
(µg/g)	Li	4.176	2.185	1.767	1.533	1.504	1.863	2.687	11.036
	Be	0.053	0.028	0.022	0.064	0.054	0.028	0.040	0.148
	B	0.132	0.123	0.058	0.063	0.111	0.085	0.114	0.882
(‰)	δ 7Li	-16.209	-15.902	-12.659	-14.890	-16.197	-11.801	-22.466	-13.620

Figure 5-11. *San2b Px1* is a type-H clinopyroxene. The concentric and sector zones are clearly evident in the pictures and the profiles for Aluminium, Magnesium and Calcium. Fe, Mg#, and the light elements do not show the zoning patterns. The Li concentration profile is smooth and increases towards the rim, although the drastically high value at the rim probably involves some matrix component. δ^7Li and concentrations of Be and B vary unsystematically.

B (0.11 – 0.22 μg/g) are more variable, although in some cases the profiles may be flat or slightly upturned at the rims.

San35 Px2 (Fig. 5-12) is a good example of a type–L phenocryst. It is weakly zoned, with a reversal in the subtly decreasing Mg# at the rim. Li and B concentrations increase towards the rim, while those of Be show an inverse relationship with Mg#. *San37a Px1* (Fig. 5-13) is an unusual clinopyroxene in that the major element compositions exhibit a wider range of values. The crystal has two distinct zones: a core pockmarked with glass inclusions, and a rim with much less inclusions. The concentrations of Al and Mg, and the Mg# generally decrease from the central portion of the core until the core-rim boundary, then increase and decrease again towards the outermost rim. Ca and Fe show the reverse. Li also reflects the existence of these zones. Li concentrations seem to increase from the central portion of the core to its boundary, while rim values are within a more restricted range and form a flat profile. Be appears to show the same pattern in the core, but rim concentration values are erratic, as are the B concentrations.

5.1.3 Orthopyroxene

Two main types of orthopyroxene occur in the dacites. Mg# within these crystals is generally between 58 and 68, but in type D, Mg# generally decreases from core to rim. The reverse is true for type I, which may shift near the rim to a rising trend. Despite these contrasting trends, all major elements are within the same range of values, except for Ca: 1.93 – 2.02 cpfu for Si, 0.02 – 0.07 cpfu for Al, 1.09 – 1.28 cpfu for Mg and 0.63 – 0.72 cpfu for Fe. Concentrations of Ca are 0.03 – 0.07 cpfu for type D and 0.06 – 0.07 cpfu for type I.

Type D

Lithium concentrations in type-D crystals increase from core to rim, with values of 1.7 – 4.7 μg/g. Be and B concentrations do not show consistent trends and may be within 0.028 – 0.053 μg/g and 0.069 – 1.175 μg/g, respectively. *San36b Px1* (Fig. 5-14) is an example of type-D orthopyroxene for which the Li isotopic composition was also measured. δ^7Li decreases from –0.93 ‰ in the core to –22.34 ‰ at the rim, the difference in values being pronounced at the rim.

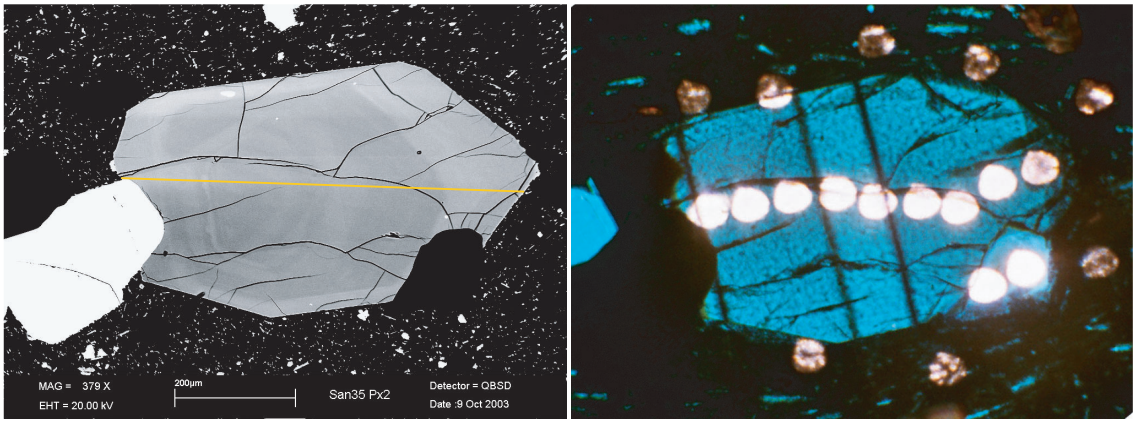

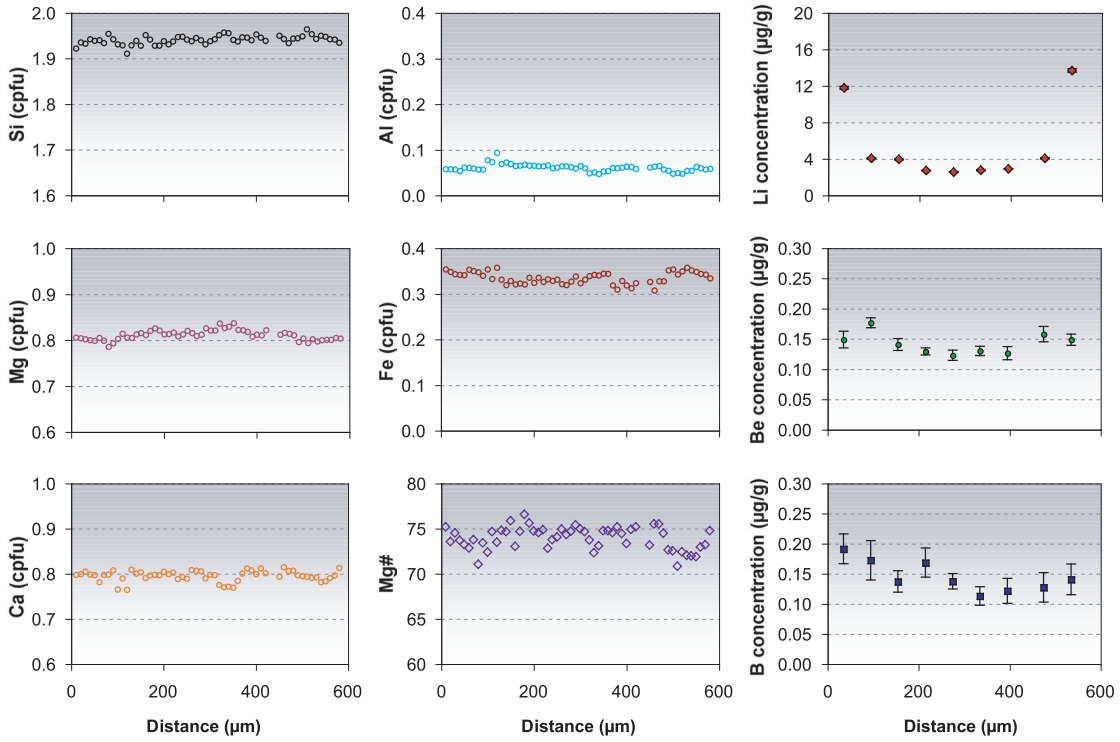

(µm)	Distance	40	100	160	220	280	340	400	490	550
(cpfu)	Si	1.943	1.932	1.953	1.938	1.941	1.956	1.954	1.945	1.949
	Al	0.054	0.078	0.065	0.064	0.063	0.048	0.064	0.054	0.063
	Mg	0.801	0.803	0.812	0.817	0.812	0.830	0.812	0.797	0.802
	Fe	0.343	0.354	0.321	0.327	0.328	0.341	0.320	0.352	0.349
	Ca	0.800	0.766	0.791	0.803	0.806	0.772	0.800	0.798	0.784
	Total	4.000	4.000	4.000	4.000	4.000	4.000	4.000	4.000	4.000
	Mg#	73.7	72.4	73.0	74.9	74.7	73.1	73.3	72.6	71.9
(µg/g)	Li	11.763	4.036	3.915	2.702	2.543	2.740	2.879	4.033	13.652
	Be	0.149	0.177	0.141	0.129	0.123	0.130	0.126	0.158	0.149
	B	0.191	0.172	0.137	0.168	0.137	0.113	0.121	0.127	0.140

Figure 5-12. *San35 Px2* is a type-L clinopyroxene with nearly homogenous major and trace element compositions. A general core-to-rim increase may be observed for the light elements, which in terms of Li concentration, is pronounced at the rim.

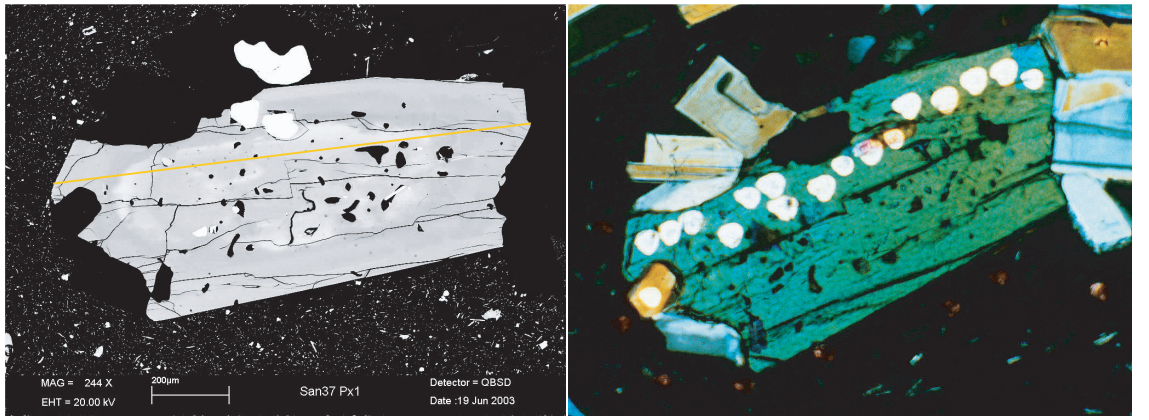

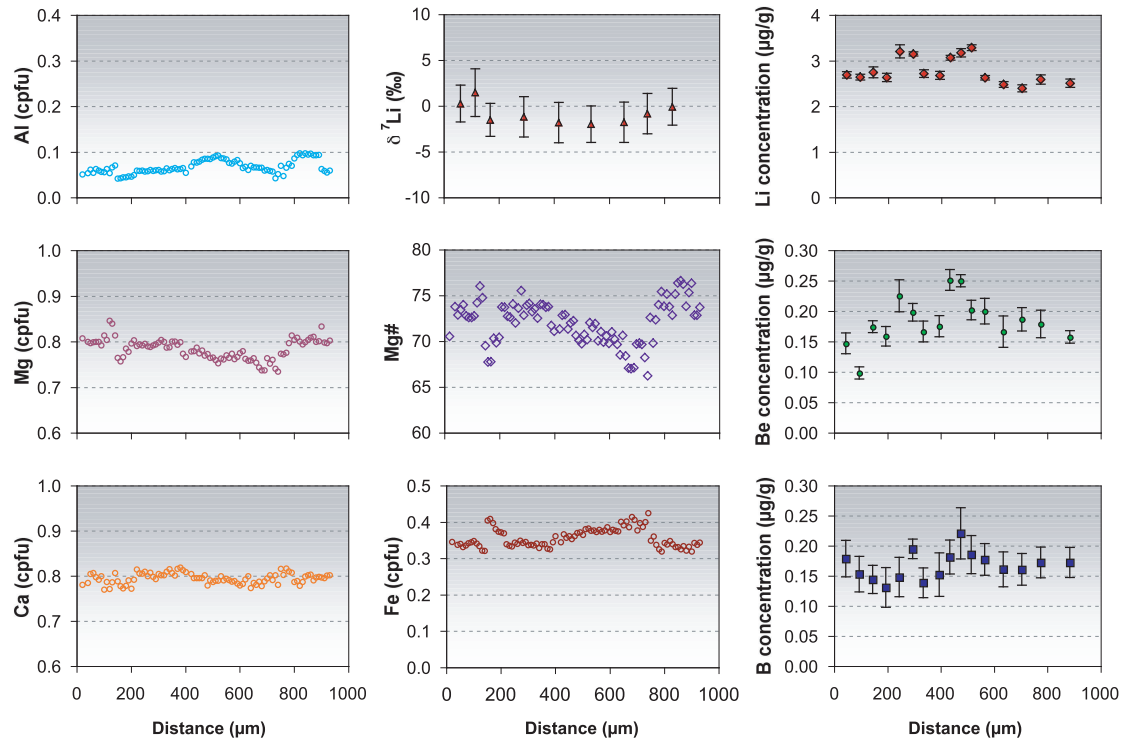

Figure 5-13. *San37a Px1* is also a type-L clinopyroxene. It is much larger than the usual pyroxene phenocrysts, and has two distinct zones in terms of major element composition. The Mg# decreases from the central to the outer portion of the inner zone. In the outer zone, Mg# increases from the boundary with the inner zone and decreases towards the rim. Light element concentrations do not show a preferred trend, while δ^7Li slightly increases from core to rim.

(µm)	Distance	50	100	150	200	250	300	340	400	440	480	520	570	640	710	780	890
(cpfu)	Al	0.062	0.056	0.042	0.046	0.058	0.061	0.060	0.055	0.077	0.086	0.093	0.075	0.070	0.059	0.075	0.094
	Mg	0.797	0.814	0.765	0.796	0.796	0.798	0.788	0.767	0.788	0.773	0.753	0.774	0.759	0.752	0.797	0.802
	Ca	0.805	0.770	0.789	0.772	0.810	0.805	0.815	0.809	0.796	0.779	0.790	0.788	0.774	0.802	0.811	0.798
	Fe	0.341	0.349	0.405	0.373	0.344	0.337	0.329	0.361	0.357	0.370	0.383	0.374	0.401	0.398	0.326	0.333
	Total	4.000	4.000	4.000	4.000	4.000	4.000	4.000	4.000	4.000	4.000	4.000	4.000	4.000	4.000	4.000	4.000
	Mg#	72.8	72.6	69.5	70.4	74.0	73.9	72.5	71.1	72.9	70.6	70.2	71.0	68.5	69.7	73.9	75.3
(µg/g)	Li	2.681	2.630	2.739	2.624	3.196	3.140	2.709	2.669	3.057	3.166	3.277	2.617	2.471	2.388	2.582	2.498
	Be	0.147	0.098	0.174	0.158	0.225	0.198	0.166	0.175	0.251	0.249	0.201	0.199	0.166	0.186	0.179	0.157
	B	0.178	0.152	0.143	0.130	0.147	0.194	0.138	0.152	0.181	0.220	0.185	0.177	0.161	0.160	0.172	0.172
(‰)	δ^7Li	0.223	1.423	-1.570			-1.213		-1.841			-2.030		-1.821	-0.885	-0.124	

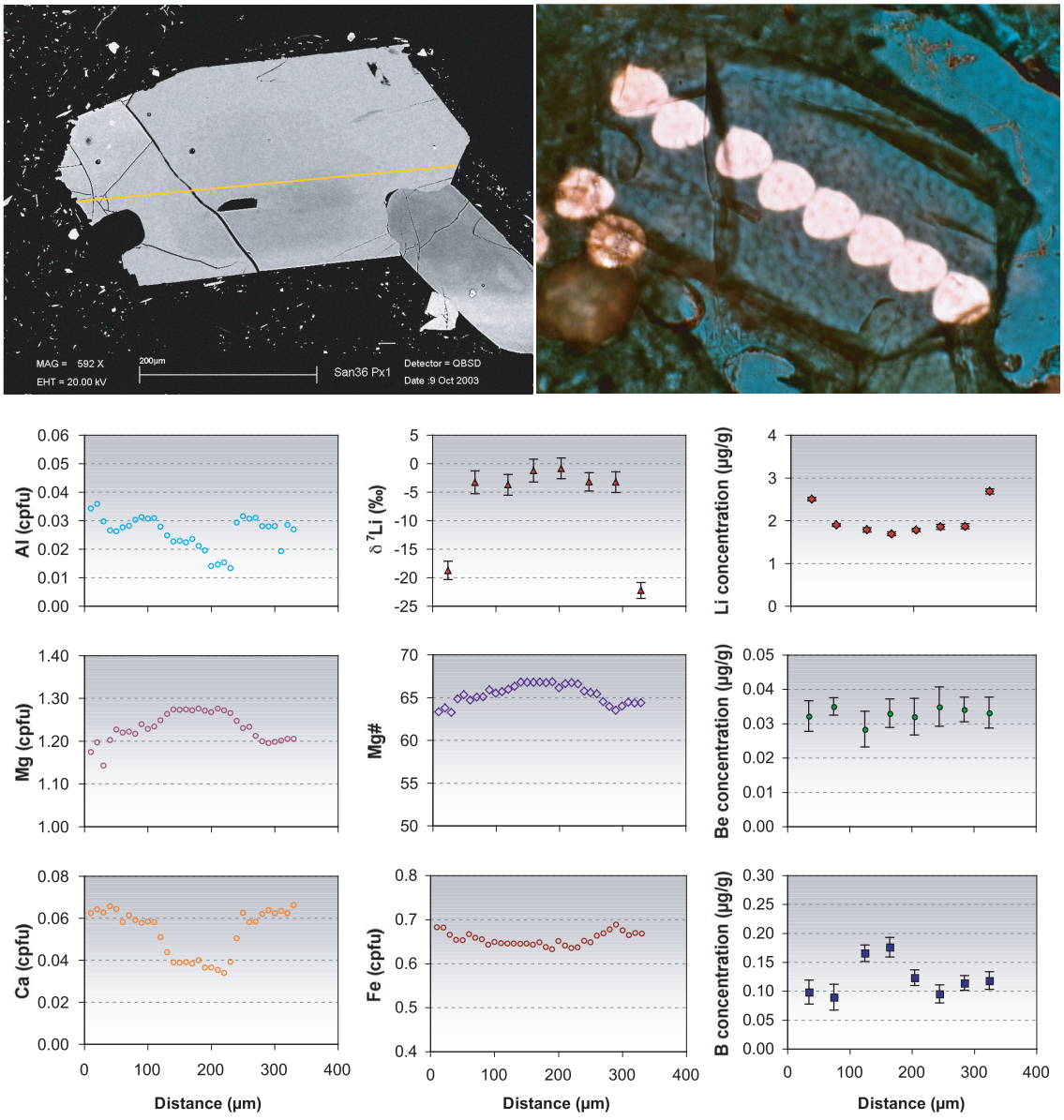

(µm)	Distance	40	80	130	170	210	250	290	330
(cpfu)	Al	0.027	0.030	0.025	0.024	0.015	0.032	0.028	0.027
	Mg	1.203	1.217	1.264	1.272	1.277	1.231	1.196	1.206
	Ca	0.066	0.059	0.044	0.038	0.035	0.063	0.064	0.066
	Fe	0.654	0.655	0.646	0.649	0.641	0.649	0.689	0.669
	Total	3.984	3.992	4.000	4.000	3.995	3.995	4.000	3.995
	Mg#	64.8	65.0	66.3	66.7	66.6	65.5	63.4	64.3
	Li	2.492	1.885	1.775	1.679	1.766	1.843	1.854	2.670
(µg/g)	Be	0.032	0.035	0.028	0.033	0.032	0.035	0.034	0.033
	B	0.098	0.089	0.165	0.175	0.123	0.095	0.113	0.118
(‰)	δ^{7}Li	-18.834	-3.395	-3.813	-1.310	-0.928	-3.288	-3.340	-22.341

Figure 5-14. In type-D orthopyroxene phenocrysts such as *San36b Px1*, Mg# decreases towards the rim. Li concentration increases from core to rim, as expected for incompatible elements, while δ^{7}Li shows the reverse. Be and B do not show systematic variation.

Type I

Type-I orthopyroxene phenocrysts fall under two subtypes: I1 has Li concentrations of 1.68-3.30 μg/g that increase from core to rim, while in I2 Li is more abundant at 5.68 – 15.58 μg/g and decrease from core to rim. Be and B occur in both subtypes within the same range of concentrations, 0.028 – 0.053 μg/g and 0.069 – 0.175 μg/g, respectively. δ^7Li was determined only for a Type I1 crystal (Fig. 5-15), the values are at a maximum of –3.64 ‰ in the core, approximately where Mg# and Li concentration are lowest. The isotopic composition generally becomes lighter towards the rim, although the minimum value of –14.01 ‰ occurs ~100 μm from the rim. *San35 Px1* (Fig. 5-16) is an I2 orthopyroxene with a strange Al profile that goes up to values of around 0.07 cpfu. Li concentrations decrease from core to rim, unlike trends in all other pyroxene types. Be and B do not show systematic variation.

5.1.4 Olivine

Only one olivine phenocryst (Fig. 5.17) suitable for analyses was found in the Nea Kameni thin sections. This has a fairly homogeneous composition throughout, except for a steep trend in the profiles near the rim. Mg is at ~1.5 cpfu and drops to 1.3 cpfu at the rim. Fe^{2+} shows the reverse with values of ~ 0.48 cpfu that increase to 0.65 cpfu at the rim. Mg# is 75 – 77 in most of the crystal and decreases to 67 at the rim. Li shows a general inverse relation to Mg#, with concentrations in the range of 1.32 – 5.70 μg/g. Be concentration seems to increase from core to rim, but the measured values are near to the detection limit, 0.001 – 0.006 μg/g, with large errors in the rim values. Boron behaves unsystematically within the range 0.038 – 0.108 μg/g.

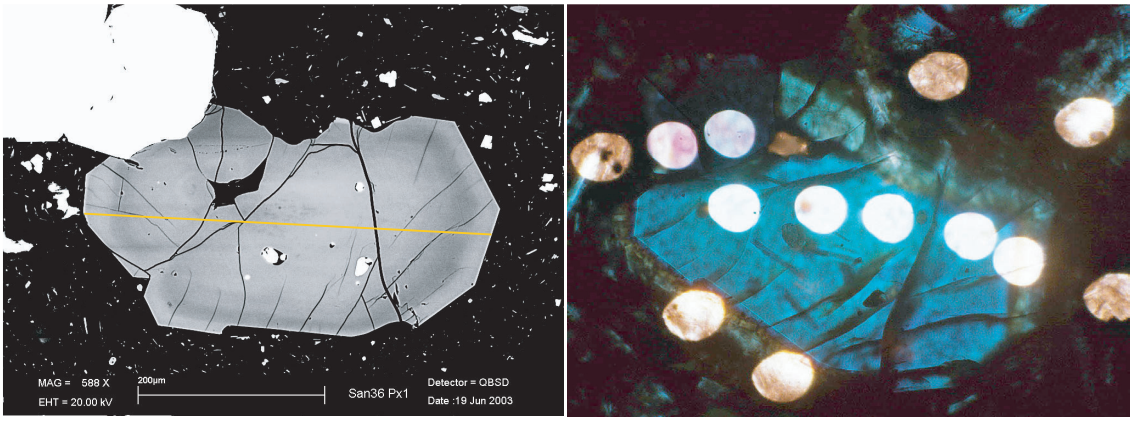

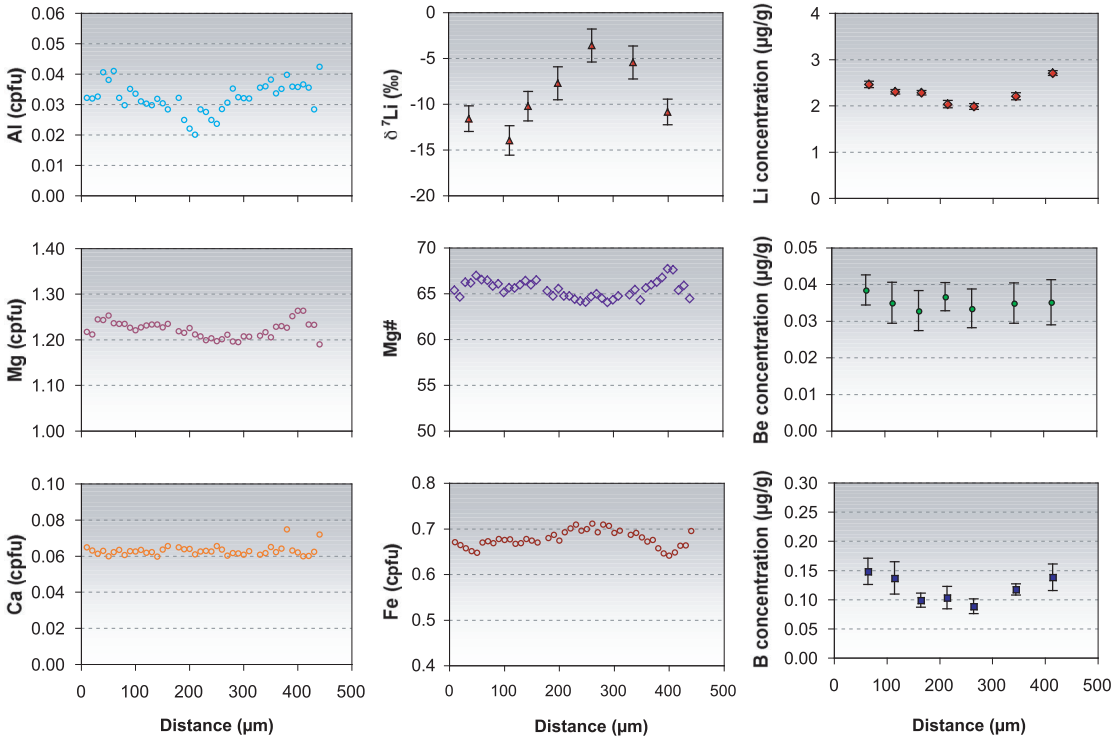

(µm)	Distance	60	110	160	210	260	340	410
(cpfu)	Al	0.041	0.031	0.028	0.020	0.029	0.036	0.037
	Mg	1.236	1.227	1.235	1.212	1.201	1.216	1.264
	Ca	0.062	0.063	0.066	0.061	0.064	0.062	0.060
	Fe	0.670	0.677	0.670	0.693	0.712	0.691	0.649
	Total	4.000	4.000	4.000	4.000	4.000	4.000	4.000
	Mg#	66.5	65.6	66.4	64.7	64.6	65.4	67.5
(µg/g)	Li	2.450	2.290	2.271	2.024	1.971	2.193	2.695
	Be	0.038	0.035	0.033	0.037	0.033	0.035	0.035
	B	0.147	0.136	0.098	0.103	0.088	0.117	0.138
(‰)	δ 7Li	-11.635	-14.012	-10.277	-7.777	-3.641	-5.504	-10.902

Figure 5-15. Mg# increases from core to rim in type-I1 orthopyroxene crystals, accompanied by Li concentrations that generally increase towards the rim. In *San36a Px1*, δ^7Li values seem to decrease from core to rim, with the minimum value coinciding with maximum concentration.

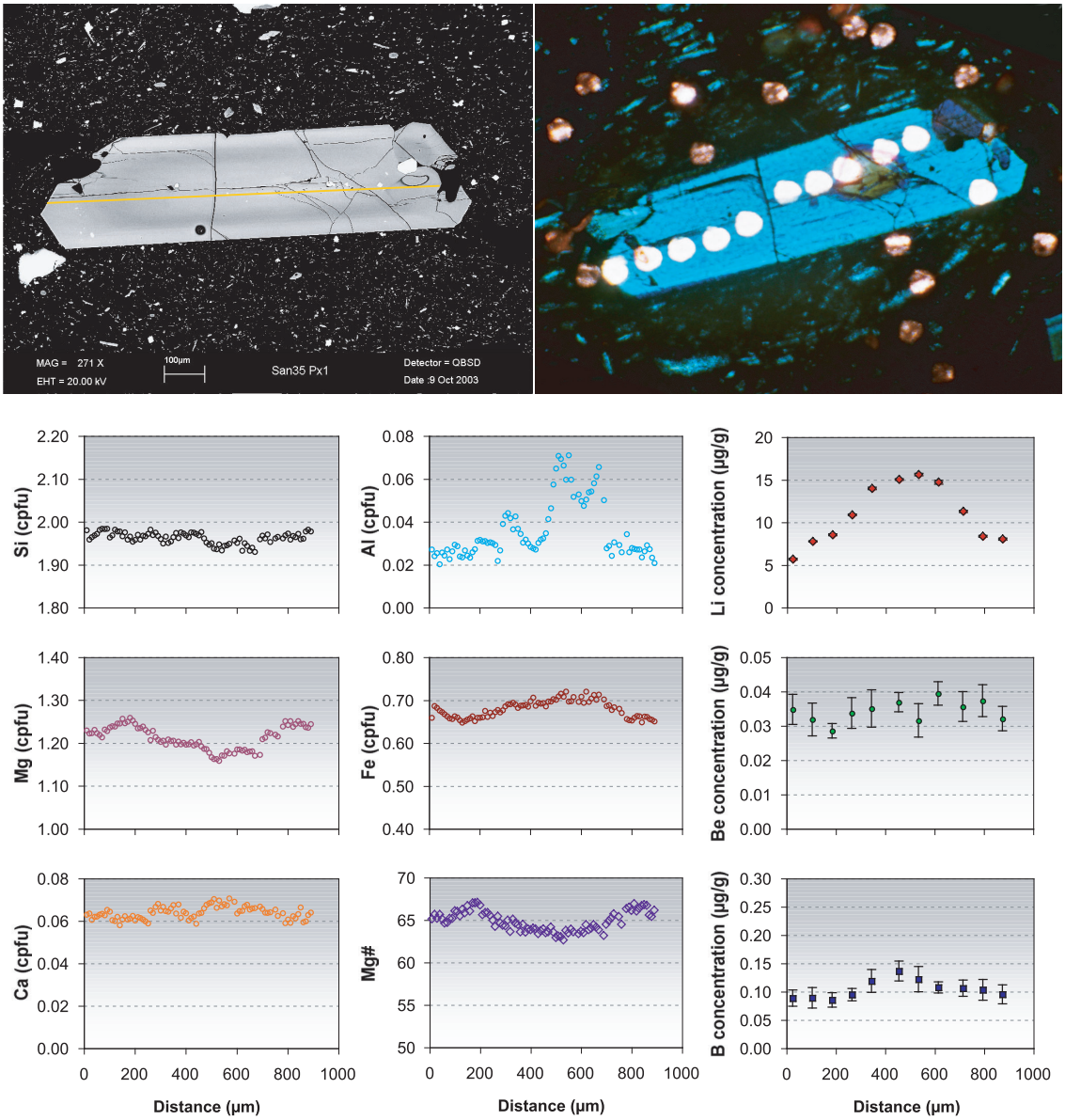

(µm)	Distance	30	110	190	270	350	460	540	620	720	800	880
(cpfu)	Si	1.965	1.969	1.954	1.970	1.965	1.977	1.934	1.934	1.971	1.973	1.982
	Al	0.026	0.029	0.031	0.022	0.037	0.035	0.060	0.051	0.024	0.028	0.023
	Mg	1.224	1.240	1.253	1.230	1.206	1.193	1.172	1.183	1.226	1.243	1.237
	Fe	0.683	0.661	0.660	0.678	0.683	0.686	0.721	0.720	0.678	0.654	0.655
	Ca	0.061	0.061	0.063	0.064	0.068	0.064	0.067	0.065	0.064	0.061	0.063
	Total	4.000	4.000	4.000	4.000	4.000	3.998	4.000	4.000	4.000	4.000	4.000
	Mg#	65.2	66.0	67.1	65.4	64.4	63.5	63.7	64.4	65.2	66.1	65.4
(µg/g)	Li	5.658	7.750	8.511	10.863	13.947	15.006	15.585	14.685	11.272	8.348	8.009
	Be	0.035	0.032	0.029	0.034	0.035	0.037	0.032	0.039	0.036	0.037	0.032
	B	0.088	0.089	0.085	0.094	0.119	0.136	0.122	0.107	0.106	0.103	0.095

Figure 5-16. In *San35 Px1*, a type-I2 orthopyroxene, Mg# generally increases from the core outwards, except for a reversal near the rim. Al varies much more than the other major elements, probably due to a slightly different phase in certain portions of the crystal, as seen in the photomicrograph. A particular characteristic of this subtype is the Li concentration that is relatively high in the core, and declines towards the rim. In this crystal B seems to mimic the Li pattern, although the slight variation and the degree of error for B do not warrant anything conclusive. Note that in contrast to all other pyroxene sections shown in the figures, this has been cut parallel to the crystal's C-axis.

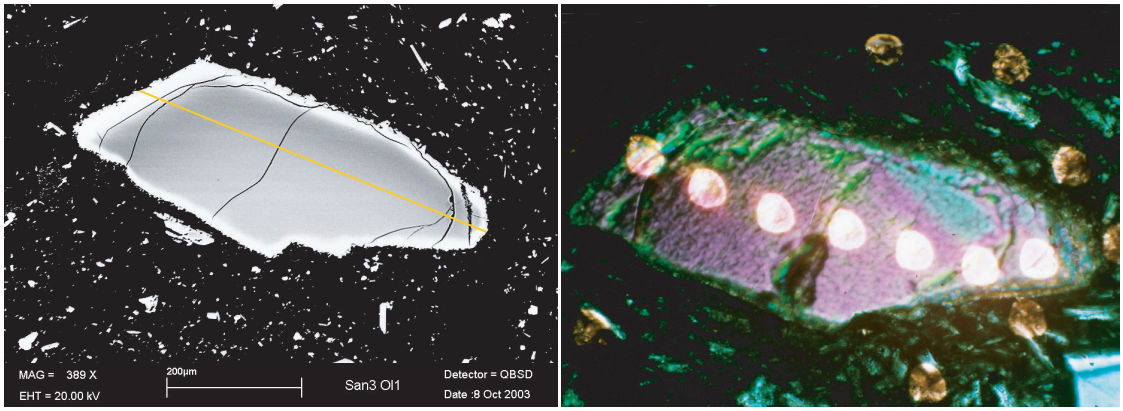

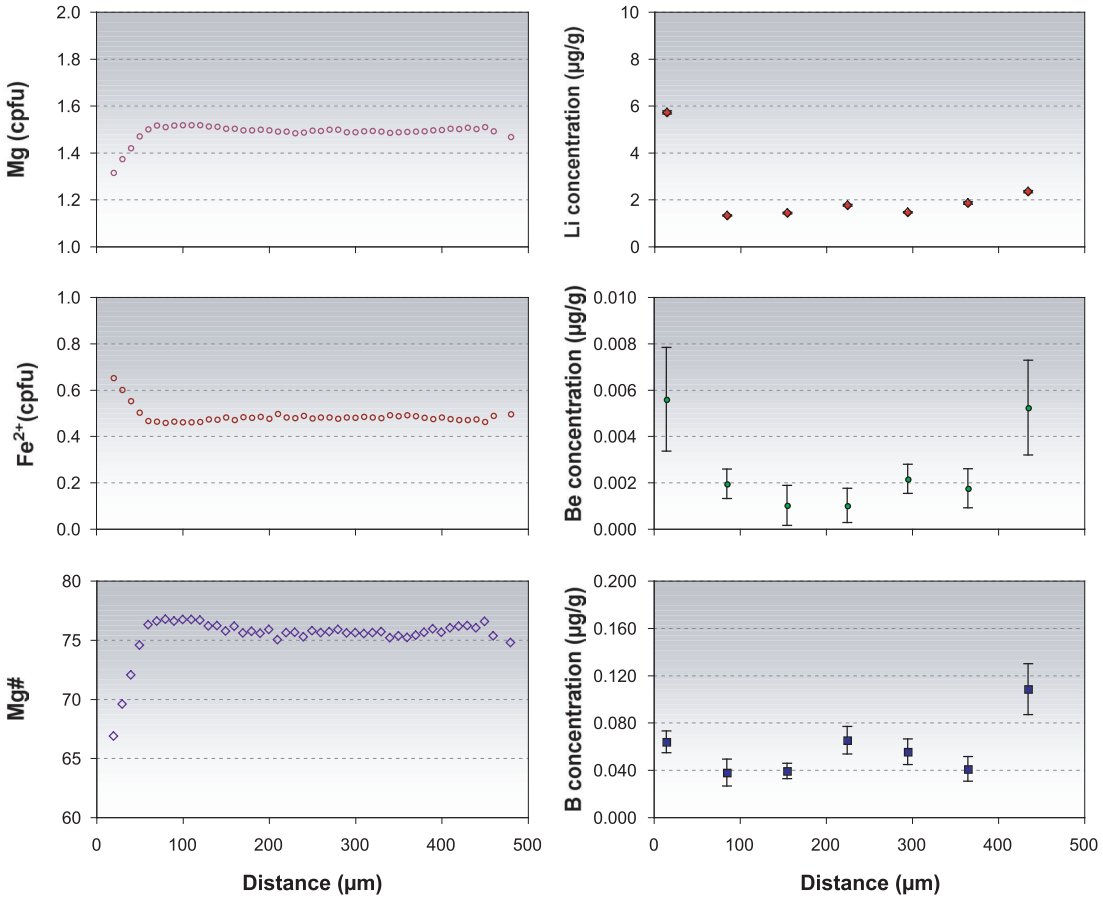

(µm)	Distance	30	100	170	240	310	380	450
(cpfu)	Mg	1.373	1.519	1.497	1.487	1.492	1.492	1.510
	Fe^{2+}	0.601	0.462	0.484	0.490	0.484	0.481	0.463
	Total	2.999	2.998	2.998	2.996	2.997	2.996	2.994
	Mg#	69.6	76.7	75.6	75.2	75.5	75.6	76.5
(µg/g)	Li	5.703	1.315	1.413	1.749	1.445	1.841	2.330
	Be	0.006	0.002	0.001	0.001	0.002	0.002	0.005
	B	0.064	0.038	0.039	0.065	0.055	0.041	0.108

Figure 5-17. Both major and trace element compositions of the only olivine phenocryst analysed, *San3b Ol1*, are rather homogeneous except for the rim. Here Mg# drops to much lower values and Li concentration suddenly increases. Be and B are within the detection limit. The large error for Be measurements must be due to the concentration being at the detection limit.

5.2 Thera Andesites

5.2.1 Plagioclase

Collected from different lava flows on Thera, the plagioclase populations of the andesites are more difficult to segregate into types. Twelve crystals were analysed in detail. In some of these, An content comprises a wide range, resulting to overlaps with those of other phenocrysts and a broad spectrum of An values. No type-N phenocryst was found in these samples, and type-A are no longer anomalous for the andesitic system, but make up the higher end of the An values in type O.

Type-O

An contents of type-O crystals are between 90 and 46 mole %, with the values in each crystal varying within a range of 5 to 33 mole %. The similarity lies in the almost flat or oscillatory nature of the An profiles for these phenocrysts. Mg also comprises a relatively broad range of 0.003 – 0.008 cpfu, with trends that are hardly related to An content. According to the shape of the Li profiles, in a scheme previously used for the dacites, type O is divided into two subgroups.

There are only two type-O1 crystals; both come from *San 26* and have a relatively narrow range of An_{58} to An_{54}. *San26 Pl2* (Fig. 5-18) was analysed for Mg, and yielded 0.003 – 0.004 cpfu. Li concentrations are either consistent or show no systematic variation, with values of 12.9 – 14.9 μg/g. The concentrations of Be and B tend to increase towards the rim and cracks, with values of 0.602 – 0.620 μg/g and 0.204 – 0.422 μg/g, respectively.

Type-O2 plagioclase is more common and occurs in *San 27*, *San 28*, *San 30* and *San 32*. An contents are in a broader range and Li concentrations generally decrease from core to rim, although with profiles more flat than those in the Nea Kameni dacites. The overall range of observed values is 33.2 to 2.74 μg/g Li. *San30 Pl1* (Fig. 5-19) is such a crystal. As opposed to the type-O2 phenocrysts of the Nea Kameni dacites, this does not exhibit a peak Li concentration value in the core, but an almost homogeneous, if not irregular, profile. Nevertheless, a decrease is observed at the rim, which reflects loss of Li from the system during rim formation or cooling of the magma. *San27 Pl2* (Fig. 5-20) shows a much higher and larger range of values for Li: 21.5 – 33.2 μg/g. The syn-crystallisation degassing hypothesis earlier proposed for type-O2 plagioclase in the dacites, cannot be invoked for this crystal, because it is actually cut off at one end. Thus, the lower concentration of Li at this

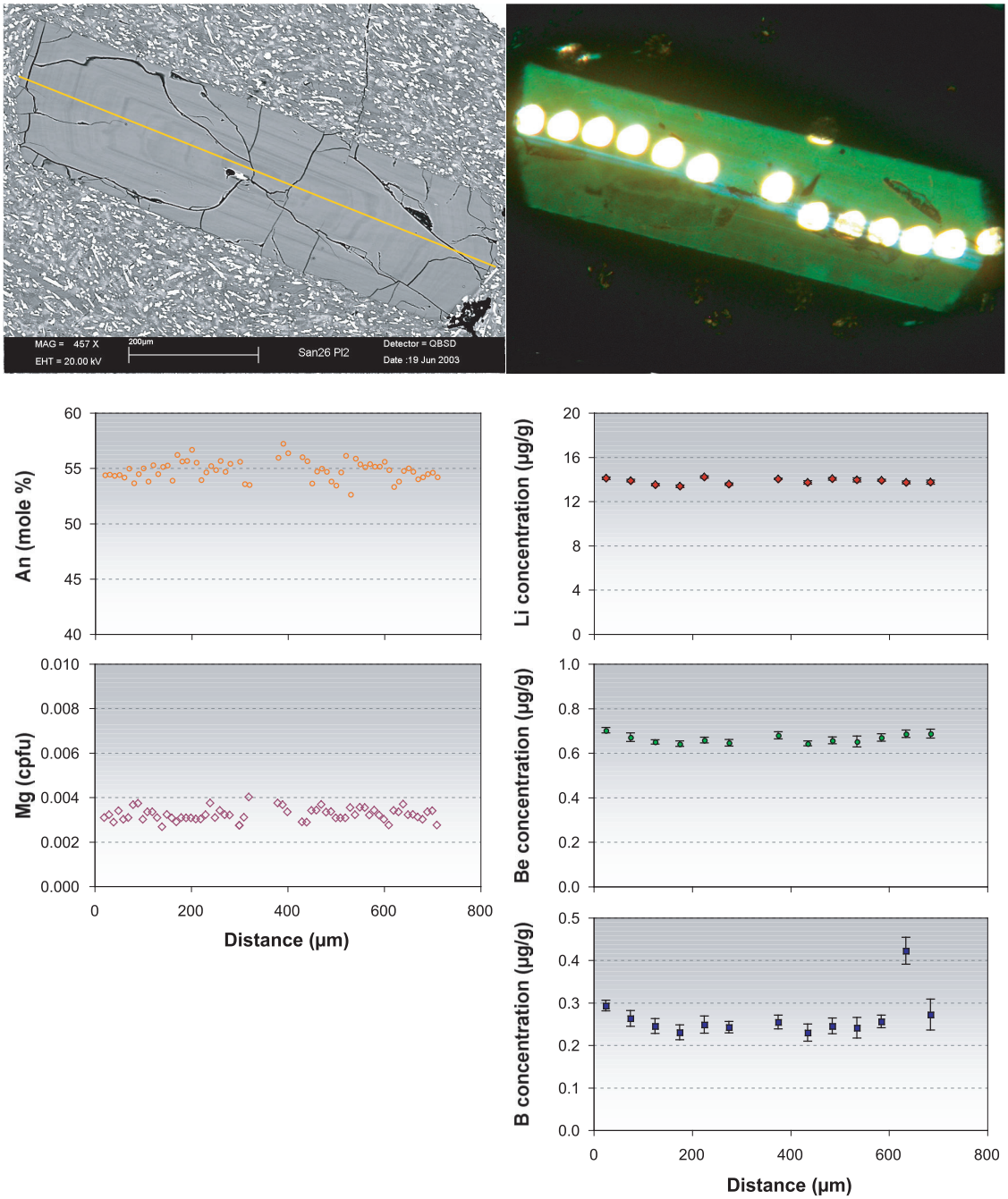

(µm)	Distance	40	90	140	190	240	300	390	450	500	550	600	650	700
(cpfu)	Si	2.470	2.474	2.464	2.461	2.455	2.452	2.446	2.478	2.476	2.447	2.463	2.449	2.471
	Al	1.507	1.504	1.522	1.519	1.529	1.532	1.535	1.503	1.507	1.532	1.517	1.532	1.504
	Mg	0.003	0.004	0.003	0.003	0.004	0.003	0.004	0.003	0.003	0.004	0.003	0.003	0.003
	Ca	0.534	0.535	0.536	0.548	0.540	0.541	0.559	0.525	0.522	0.550	0.544	0.542	0.535
	Na	0.449	0.447	0.436	0.436	0.438	0.432	0.418	0.454	0.454	0.443	0.434	0.443	0.444
	K	0.015	0.016	0.014	0.014	0.015	0.015	0.013	0.014	0.014	0.015	0.012	0.015	0.015
	Total	4.998	4.997	4.991	4.997	4.998	4.995	4.993	4.995	4.995	5.008	4.992	5.004	4.995
(mole %)	An	54.3	54.5	55.1	55.7	55.2	55.6	57.2	53.6	53.5	55.4	55.6	55.0	54.6
(µg/g)	Li	14.062	13.850	13.483	13.345	14.179	13.527	14.003	13.695	14.017	13.922	13.874	13.683	13.712
	Be	0.701	0.670	0.649	0.640	0.657	0.645	0.678	0.642	0.656	0.650	0.669	0.685	0.686
	B	0.293	0.263	0.244	0.230	0.248	0.242	0.254	0.229	0.245	0.241	0.255	0.422	0.272

Figure 5-18. *San26 Pl2* is a type-O1 plagioclase phenocryst and as such shows only oscillatory zoning. The light elements likewise show only a narrow range of variation, mostly observed as an increase in value towards the rim or near cracks, especially for Be and B.

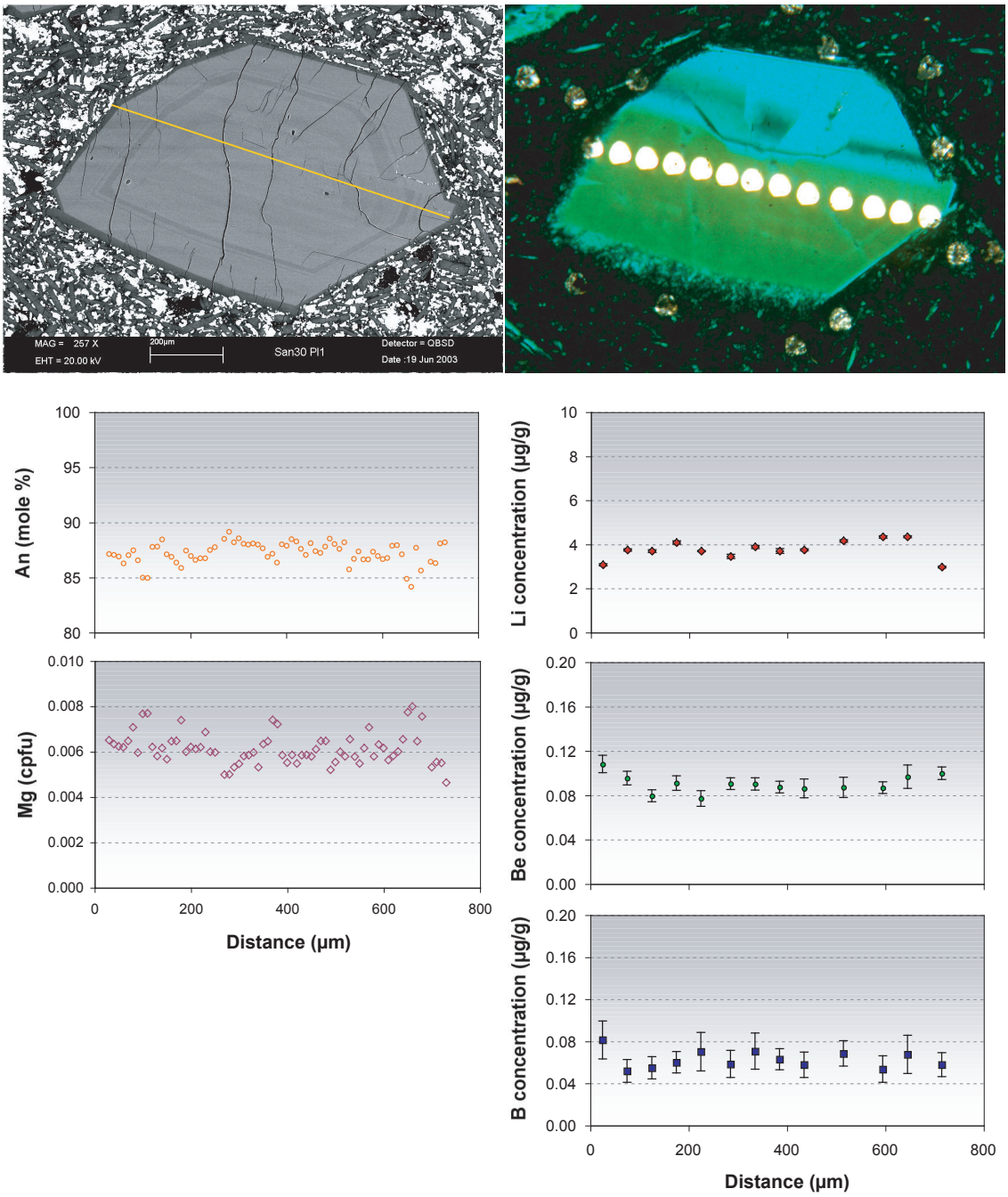

(µm)	Distance	30	80	130	180	230	290	340	390	440	520	600	650	720
(cpfu)	Si	2.124	2.127	2.113	2.128	2.124	2.106	2.117	2.116	2.120	2.116	2.125	2.155	2.109
	Al	1.855	1.848	1.870	1.854	1.861	1.875	1.866	1.875	1.867	1.864	1.855	1.820	1.865
	Mg	0.007	0.007	0.006	0.007	0.007	0.005	0.005	0.006	0.006	0.006	0.006	0.008	0.005
	Ca	0.864	0.874	0.870	0.856	0.865	0.881	0.875	0.861	0.866	0.878	0.868	0.846	0.886
	Na	0.127	0.125	0.121	0.141	0.132	0.118	0.119	0.117	0.128	0.117	0.133	0.150	0.119
	K	0.001	0.003	0.002	0.002	0.003	0.002	0.000	0.001	0.001	0.002	0.002	0.001	0.002
	Total	5.001	5.003	5.003	5.007	5.006	5.006	5.000	4.996	5.003	5.002	5.007	5.001	5.009
(mole %)	An	87.2	87.5	87.8	85.9	86.8	88.2	88.0	88.0	87.1	88.2	86.7	84.9	88.1
(µg/g)	Li	3.064	3.735	3.684	4.076	3.687	3.446	3.879	3.692	3.744	4.151	4.328	4.336	2.960
	Be	0.108	0.095	0.079	0.091	0.077	0.090	0.090	0.087	0.086	0.087	0.087	0.097	0.100
	B	0.081	0.052	0.055	0.060	0.070	0.058	0.071	0.063	0.058	0.068	0.053	0.067	0.058

Figure 5-19. *San30 Pl1* is a type-O2 phenocryst. Major and trace element composition are rather homogeneous, except that closer inspection of Li reveals a decrease towards or at the rim. The range of Li values vary between samples, and in this case is relatively low.

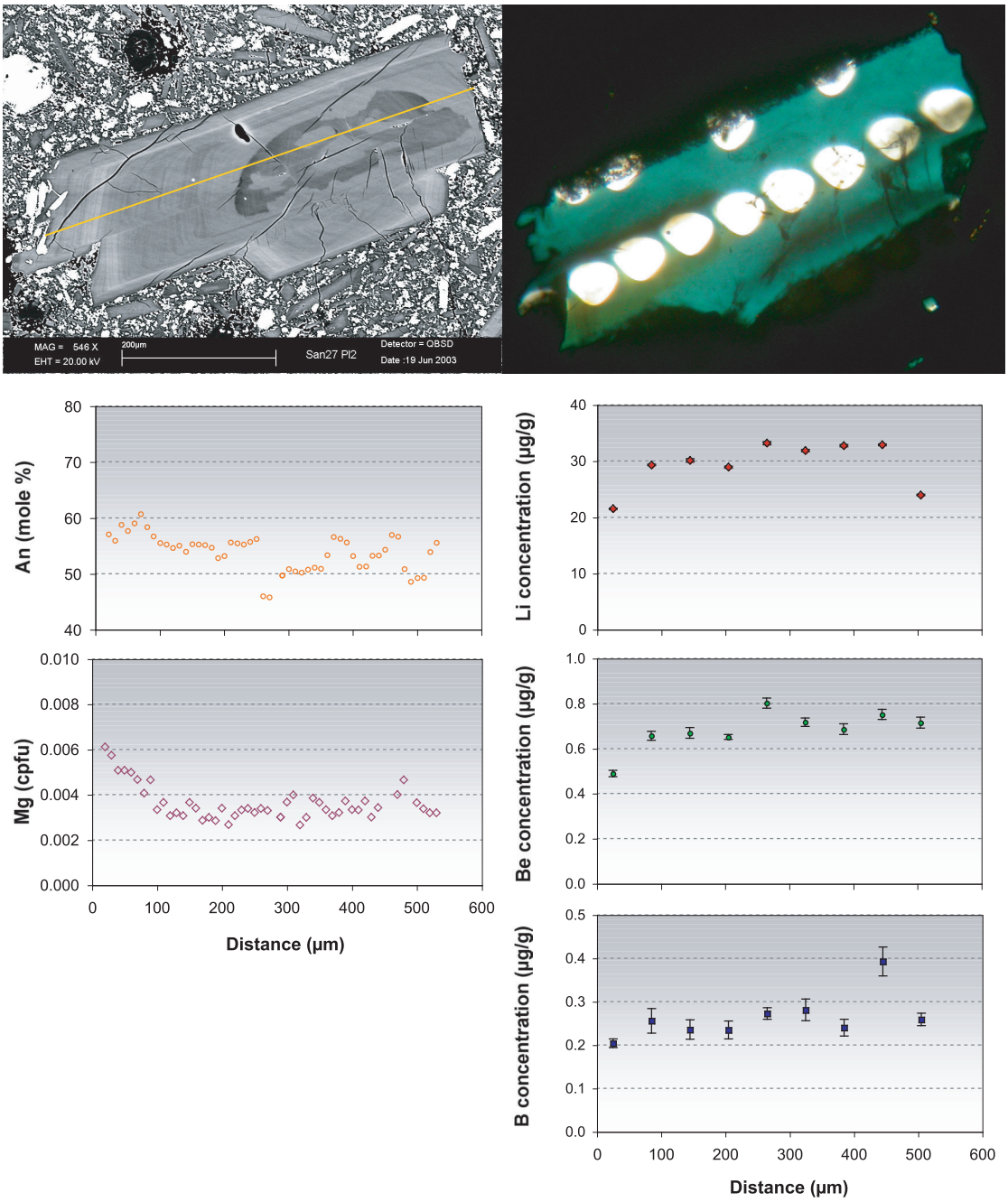

(µm)	Distance	40	100	160	220	290	340	400	460	520
(cpfu)	Si	2.430	2.455	2.456	2.460	2.521	2.516	2.482	2.475	2.463
	Al	1.541	1.526	1.526	1.522	1.465	1.465	1.498	1.428	1.520
	Mg	0.005	0.003	0.003	0.003	0.003	0.004	0.003	0.034	0.003
	Ca	0.571	0.545	0.541	0.542	0.485	0.495	0.521	0.518	0.528
	Na	0.400	0.436	0.437	0.434	0.490	0.473	0.457	0.390	0.450
	K	0.013	0.014	0.014	0.014	0.017	0.018	0.018	0.050	0.017
	Total	4.991	4.997	4.997	4.994	4.994	4.988	4.997	4.986	5.001
(mole %)	An	58.8	55.6	55.3	55.5	49.8	51.2	53.3	57.0	54.0
(µg/g)	Li	21.495	29.313	30.132	28.914	33.185	31.875	32.738	32.906	23.957
	Be	0.489	0.657	0.669	0.651	0.802	0.717	0.686	0.751	0.715
	B	0.204	0.256	0.236	0.235	0.273	0.281	0.240	0.392	0.259

Figure 5-20. *San27 Pl2* is another type-O2 phenocryst, but with a much higher range of Li concentration values than *San30 Pl1* (Fig. 5-19). The BSE image and Mg profile show that the crystal has been cut off on one end, towards the right, which implies that the nearly symmetrical Li profile does not reflect the amount of Li incorporated during crystal growth.

end is not related to crystal growth. Instead, it may have been due to the diffusion of Li towards the melt or groundmass.

Be and B profiles in the type-O2 phenocrysts have varying trends, and may not show any systematic variation. Be concentrations range from 0.071 to 1.121 μg/g and those of B from 0.048 to 0.392 μg/g (excluding one higher value with a very large error).

Type C

Five crystals from *San 22*, *San 28*, *San 31* and *San 32* were identified as type-C, having cores of An_{90-79} and rims with An_{78-48}. One crystal shows an intermediate step-like pattern in the profile with values of An_{78-73}. Mg is inversely related to An, but the range of values among cores of different crystals vary: 0.000 – 0.001 cpfu (detection limit), 0.003 – 0.004 cpfu and 0.005 – 0.007 cpfu. For these crystals, in the same order, rim values are 0.001 – 0.003 cpfu, 0.005 – 0.007 cpfu and 0.007 – 0.015 cpfu. For one crystal the pattern is not well defined, but gradually increases from 0.001 μg/g in the core to 0.009 cpfu at the rim.

Light element concentrations are likewise in different ranges of values, although these are generally inversely related to An content. Only two crystals, from samples *San 28* and *San 32*, show a marked compositional discontinuity between core and rim. The others simply exhibit profiles that increase from core to rim, or even irregular patterns.

San28 Pl2 (Fig. 5-21) is an excellent representative of type C. The core is mostly An_{88-85} in the core, and oscillating within An_{60-50} in the surrounding zone. Mg shows the reverse trend, the values within detection limit in the core, and 0.001 – 0.003 cpfu in the rim zone. Li shows a profile inverse to that of An, except for the abrupt decrease at the rim. Core values are 6.01 – 9.31 μg/g compared to rim values of 10.2 – 19.2 μg/g. Be and B, on the other hand, are more consistently inversely related with An. Be in the core is 0.214 – 0.347 μg/g compared to 0.602 – 1.311 μg/g at the rim. B concentrations amount to 0.124 – 0.183 μg/g in the core and to 0.191 – 0.272 μg/g at the rim. The distinct change in Li concentrations along the boundary between core and rim is an interesting feature, as it contradicts the expected homogenised pattern that should inevitably result from the rapid diffusion of Li, and invokes extremely fast cooling after rim growth. The decrease at the outermost rim may be due to the loss of Li in the melt in the latest stage of this crystal's growth, probably afforded by degassing. The δ^7Li profile shows neither general trend nor significant difference between the core and rim values. This may, however, simply mean that

(µm)	Distance	30	100	170	240	340	410	510	590	670	810	910	1110	1200	1300	1460	1530	1600	1680	1750	1820	1890	1960	2040
(cpfu)	Si	2.509	2.417	2.453	2.484	2.422	2.081	2.131	2.081	2.122	2.135	2.117	2.136	2.090	2.120	2.094	2.404	2.433	2.447	2.458	2.483	2.343	2.475	2.504
	Al	1.479	1.568	1.528	1.499	1.563	1.913	1.861	1.905	1.869	1.855	1.874	1.849	1.902	1.869	1.892	1.575	1.557	1.541	1.530	1.499	1.644	1.509	1.482
	Mg	0.002	0.002	0.002	0.003	0.002	0.000	0.000	0.000	0.000	0.001	0.000	0.000	0.000	0.000	0.000	0.002	0.002	0.002	0.002	0.002	0.002	0.002	0.001
	Ca	0.476	0.573	0.542	0.510	0.575	0.897	0.853	0.904	0.863	0.852	0.870	0.859	0.892	0.870	0.887	0.589	0.558	0.542	0.533	0.517	0.640	0.520	0.483
	Na	0.489	0.419	0.441	0.476	0.414	0.103	0.137	0.105	0.131	0.139	0.124	0.142	0.103	0.128	0.119	0.417	0.417	0.434	0.445	0.460	0.355	0.458	0.507
	K	0.029	0.016	0.018	0.018	0.015	0.001	0.003	0.001	0.004	0.005	0.003	0.004	0.002	0.003	0.003	0.015	0.017	0.017	0.018	0.020	0.011	0.016	0.024
	Total	5.002	5.009	5.003	5.005	5.004	5.008	5.001	5.012	5.004	5.002	5.003	5.005	5.004	5.005	5.013	5.017	4.998	5.000	5.001	4.999	5.010	4.999	5.014
(mole %)	An	51.2	55.7	58.4	50.8	58.3	82.6	87.0	88.1	86.2	85.3	86.8	86.5	89.4	86.9	85.2	59.4	57.1	55.8	55.6	52.8	61.8	53.9	75.3
(µg/g)	Li	10.225	23.692	26.740	29.165	21.033	6.020	6.503	7.264	6.015	6.905	8.749	9.307	7.436	7.187	7.431	21.585	23.126	24.231	26.145	27.748	26.686	27.909	17.453
	Be	1.176	1.081	1.060	0.962	0.602	0.227	0.229	0.268	0.214	0.246	0.347	0.322	0.254	0.271	0.309	0.670	0.725	0.808	0.944	1.012	0.952	1.153	1.311
	B	0.256	0.262	0.243	0.266	0.203	0.138	0.124	0.146	0.134	0.144	0.183	0.173	0.134	0.128	0.191	0.221	0.221	0.235	0.224	0.263	0.236	0.272	0.686
(‰)	δ^7Li	0.200	-8.079	-5.259	-6.523	-4.813	-4.990	-3.091	-2.754	-1.741	-1.545	-5.306	0.853	-5.822	-2.753	-4.059	-7.554	-8.544	-9.663	-8.310	-8.170	-8.405	-6.822	-9.779

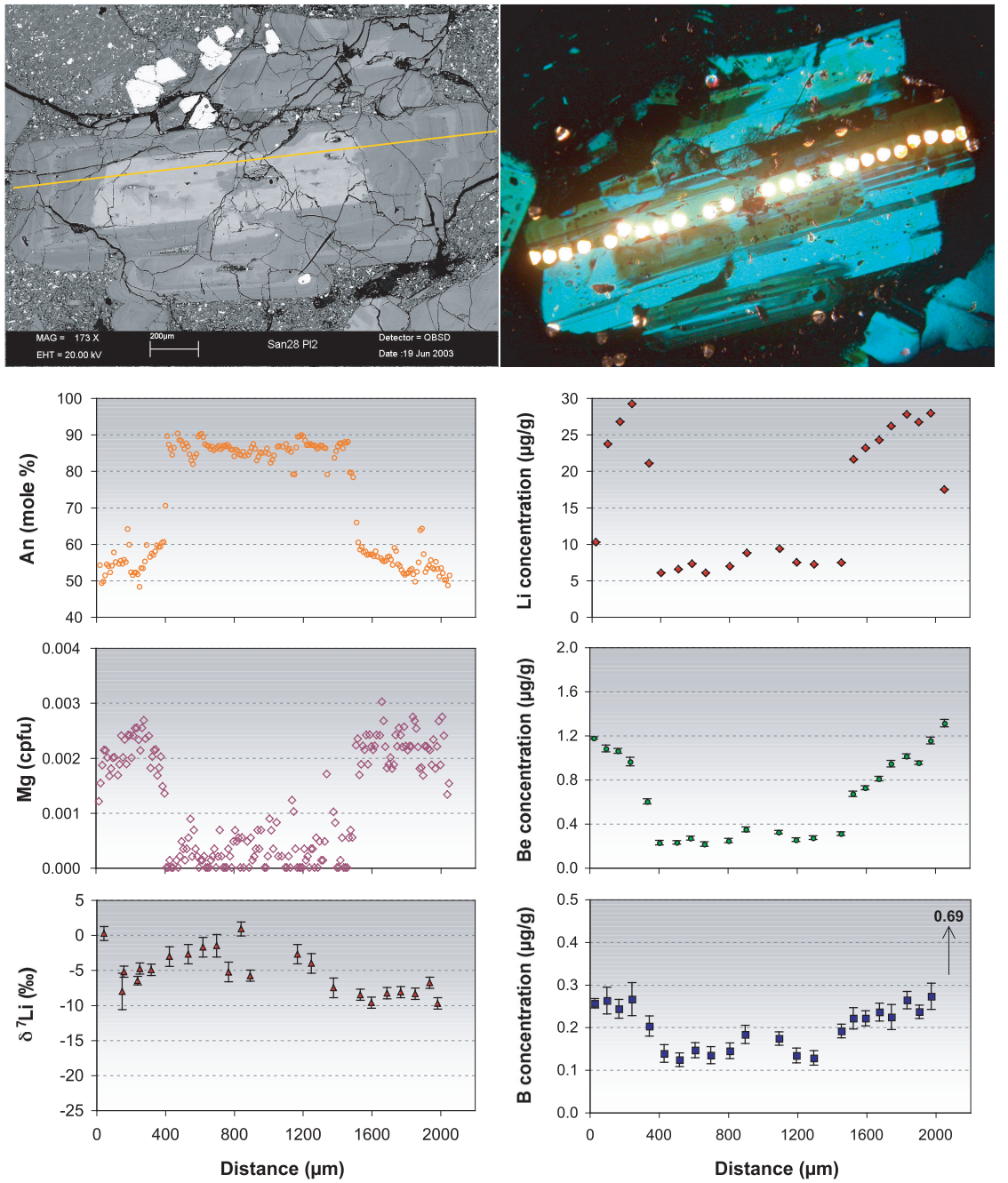

Figure 5-21. Type-C plagioclase phenocrysts have cores inherited from more mafic magma, and this is very apparent in *San28 Pl2*. An content and Mg concentration are clearly inversely related, despite Mg being at the detection limit in the core. All light elements show similar and therefore primary patterns, except for the drop in Li concentration at the rim. The high B value for the last analysis point is accompanied by a large 2σ and may be disregarded from the profile.

the two magmas that respectively formed the core and rim had similar Li isotopic compositions.

San32 Pl1 (Fig. 5-22) is also a type-C phenocryst, with a more calcic rim (An_{78-68}) than *San28 Pl2*. The concentrations of Mg and the light elements are inversely related to An. Li, Be and B concentrations in the core are 4.39 – 5.80 μg/g, 0.138 – 0.176 μg/g and 0.085 – 0.164 μg/g, respectively, as compared to 6.62 – 8.66 μg/g, 0.264 – 0.274 μg/g and 0.129 – 0.189 μg/g, respectively, at the rim.

5.2.2 Clinopyroxene

Clinopyroxene phenocrysts from Thera andesites cannot be segregated into high- and low-Mg populations, thus new types are defined for these. Type-Z clinopyroxene grains are clearly zoned, concentrically and sometimes alongside sector-zoning. Type-U grains are not zoned, or only very slightly, such that the composition remains almost the same throughout the crystals.

Type Z

Type-Z clinopyroxene phenocrysts are found in the *San 22* and *San 31* samples. The zoning patterns, although not in similar trends among all crystals of this type, exhibit a wide range of Mg# between 91 and 72. Si and Mg behave similarly, with values of 1.81 – 1.97 cpfu and 0.78 – 0.96 cpfu, respectively. Al and Ca concentrations are inversely related to these, with values of 0.06 –0.25 cpfu and 0.61 – 0.90 cpfu, respectively. Fe_{tot} is within the range 0.17 – 0.38 cpfu. Concentrations of Li (0.99 – 11.99 μg/g), Be (0.010 – 0.155 μg/g) and B (0.048 – 0.430 μg/g) generally increase from core to rim, as expected of incompatible elements, regardless of major element composition.

San22 Px2 (Fig. 5-23) is a type-Z clinopyroxene with concentric and sector zoning. The core registers as a trough in the Si and Mg profiles and as a peak in the Al profile. Such zoning is not clearly evident for Ca, Fe_{tot} and the Mg#. Rim values for Li and B are relatively high. The core value for Be is high, and B for this spot is also elevated above the surrounding crystal domains, but the larger errors for this analysis point suggest the presence of tiny inclusions of matrix material.

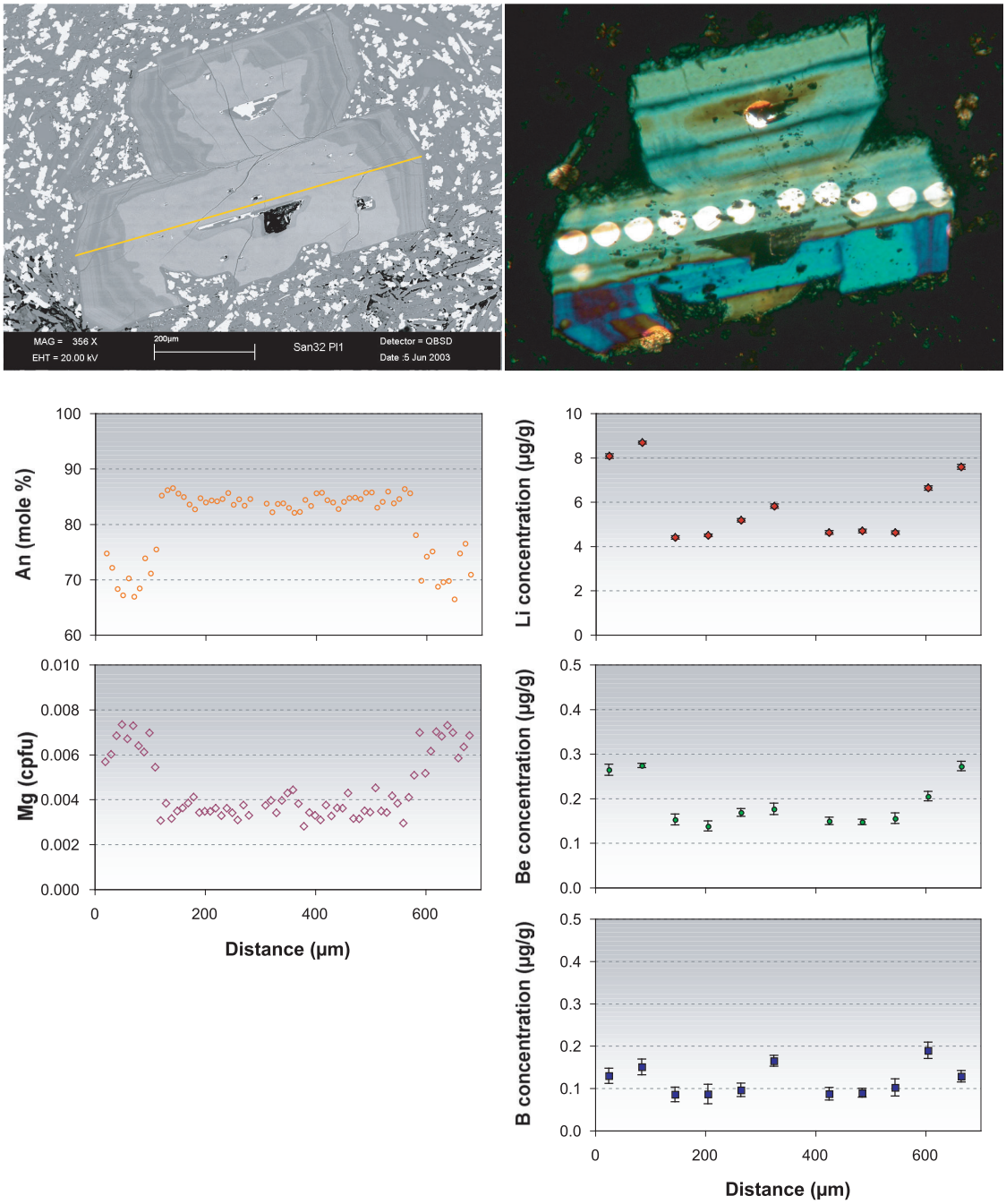

(µm)	Distance	30	90	150	210	270	330	430	490	550	610	670
(cpfu)	Si	2.272	2.248	2.138	2.149	2.155	2.154	2.138	2.145	2.147	2.246	2.218
	Al	1.700	1.721	1.831	1.831	1.816	1.815	1.838	1.832	1.834	1.723	1.757
	Mg	0.006	0.006	0.003	0.003	0.004	0.003	0.003	0.003	0.004	0.006	0.006
	Ca	0.721	0.741	0.863	0.837	0.835	0.839	0.847	0.847	0.829	0.752	0.757
	Na	0.278	0.262	0.145	0.156	0.166	0.164	0.162	0.141	0.151	0.250	0.232
	K	0.006	0.005	0.002	0.003	0.003	0.003	0.002	0.002	0.003	0.004	0.007
	Total	5.008	5.011	5.008	5.003	5.008	5.007	5.013	4.998	4.998	5.007	5.008
(mole %)	An	72.1	73.9	85.6	84.3	83.4	83.7	84.0	85.7	84.6	75.1	76.5
(µg/g)	Li	8.060	8.664	4.387	4.479	5.160	5.800	4.610	4.677	4.605	6.618	7.574
	Be	0.264	0.274	0.152	0.138	0.168	0.176	0.149	0.147	0.155	0.205	0.272
	B	0.129	0.150	0.085	0.086	0.096	0.164	0.087	0.089	0.102	0.189	0.128

Figure 5-22. Major and trace element concentration profiles for *San32 Pl1*, another type-C crystal, show the same relationships as *San28 Pl2* (Fig. 5-21). Although variations in Li and Be between the core and rim are more subtle, the striking similarity amongst the profiles suggests their primary nature.

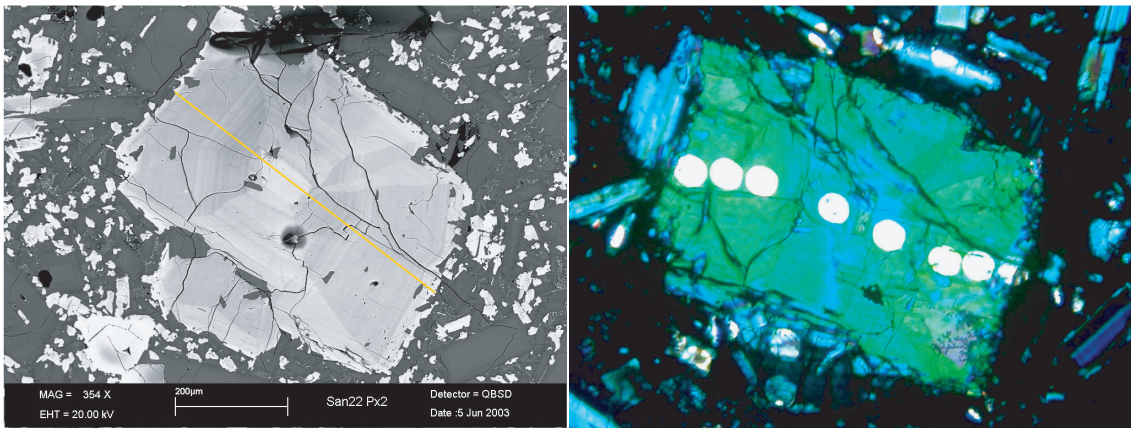

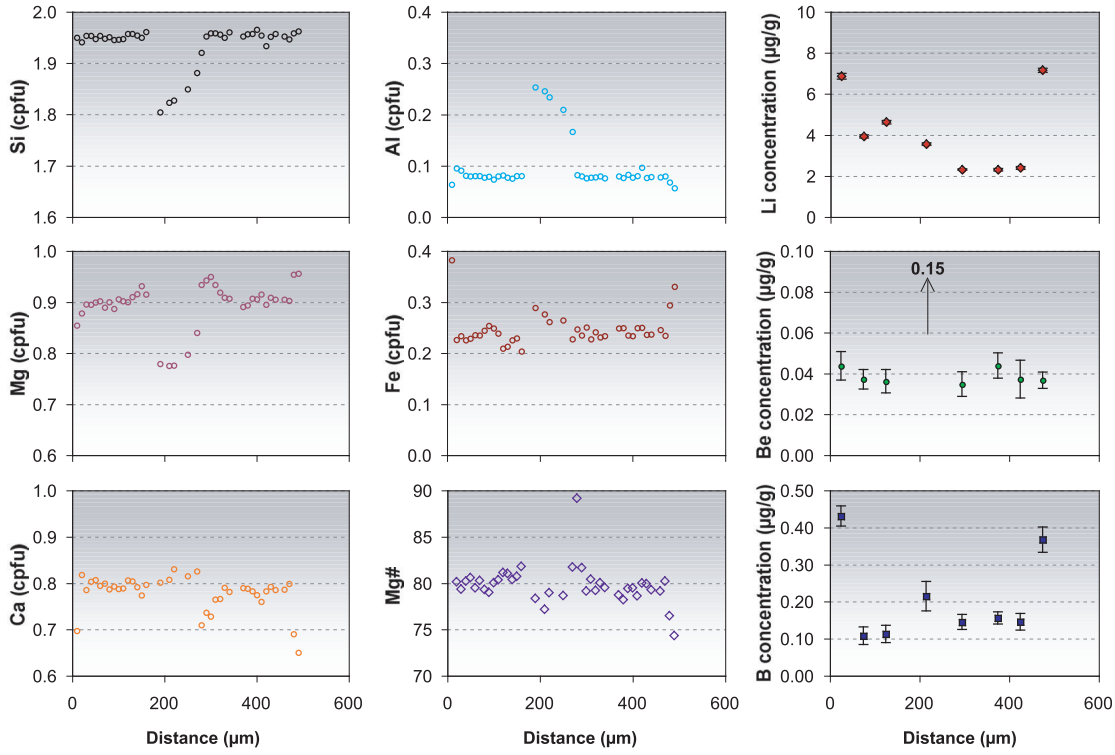

(µm)	Distance	30	80	130	220	300	380	430	480
(cpfu)	Si	1.954	1.951	1.958	1.828	1.959	1.957	1.952	1.959
	Al	0.091	0.077	0.077	0.234	0.076	0.077	0.077	0.068
	Mg	0.896	0.901	0.910	0.776	0.950	0.894	0.909	0.955
	Fe	0.234	0.244	0.213	0.262	0.251	0.249	0.236	0.294
	Ca	0.786	0.787	0.805	0.831	0.729	0.789	0.793	0.690
	Total	3.995	4.000	3.998	4.000	3.999	3.998	4.000	4.000
	Mg#	79.3	79.3	81.0	79.0	79.1	78.2	79.9	76.5
(µg/g)	Li	6.850	3.911	4.615	3.543	2.300	2.298	2.379	7.139
	Be	0.044	0.037	0.036	0.148	0.035	0.044	0.037	0.037
	B	0.430	0.107	0.112	0.214	0.145	0.156	0.145	0.367

Figure 5-23. *San22 Px2* is a type-Z clinopyroxene, showing both concentric and sector zoning, the latter apparent in the Si, Mg and Al profiles. Li and B show higher concentration values at the rim, while Be is irregular. The high Be concentration and large error values for both Be and B in the fourth analysis point may be due to inclusions.

Type U

Two type-U clinopyroxene crystals were observed in *San 32*. These phenocrysts have a narrow range of Mg# and major element composition (e.g. *San26 Px1*, Fig. 5-24). Mg# ranges from 79 to 74. Concentrations of the other components are as follows: 1.91 – 1.95 cpfu Si, 0.08 – 0.11 cpfu Al, 0.83 – 0.91 cpfu Mg, 0.28 – 0.33 cpfu Fe_{tot} and 0.61 – 0.90 cpfu Ca. The light elements behave unsystematically with concentrations of 1.86 –26.2 μg/g, 0.039 – 0.054 μg/g and 0.147 – 0.264 μg/g for Li, Be and B, respectively.

5.2.3 Orthopyroxene

Orthopyroxene phenocrysts have Mg# profiles that are flat or irregular, and are therefore not grouped into D or I types like the ones in the dacites. Values are between 61 and 70. Si, Al, Mg, Fe_{tot} and Ca are 1.93 – 1.96 cpfu, 0.02 – 0.06 cpfu, 1.14 – 1.29 cpfu, 0.60 – 0.74 cpfu and 0.06 – 0.09 cpfu, respectively. Li, Be and B follow the same flatness or irregularity in pattern, within ranges of 1.84 – 13.83 μg/g, 0.32 – 0.89 μg/g and 0.069 – 0.288 μg/g, respectively.

San26 Px1 (Fig. 5-25) is a fairly large orthopyroxene phenocryst with a narrow range of Mg#, between 61 and 63. Other components, both major and trace elements also show relatively flat profiles. The only exception to this is Li, which has elevated concentrations at the rims and near the magnetite inclusion.

5.2.4 Olivine

Mg# of olivine phenocrysts decrease from core to rim, with values of 87 – 63. Mg follows suit, within the range 1.75 – 1.23 cpfu. Fe shows the reverse trend with values between 0.24 and 0.74 cpfu. Proximity to cracks within the crystals yield concentrations that approach those of the rim. Light element concentrations increase from core to rim with 1.04 – 5.15 μg/g Li, 0.0004 – 0.0087 μg/g Be and 0.024 – 0.312 μg/g B. *San31 Ol1* (Fig. 5-26) is an olivine phenocryst with an almost skeletal texture. The profiles for the major and trace elements are uncomplicated and generally smooth, but the high Mg# in the extensive cores of these olivines point to basaltic compositions.

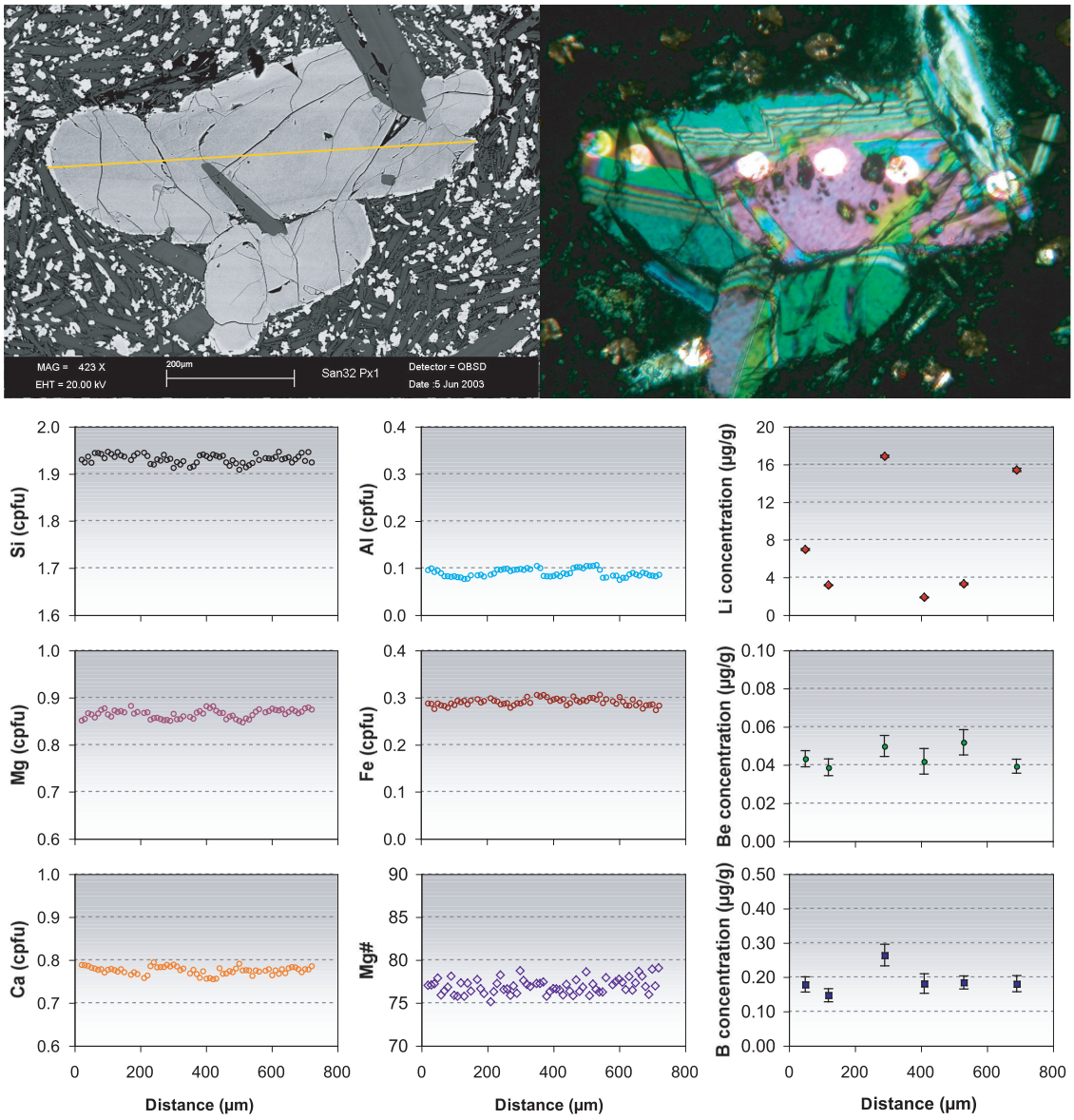

(µm)	Distance	50	120	290	410	530	690
(cpfu)	Si	1.924	1.937	1.933	1.934	1.919	1.946
	Al	0.095	0.081	0.097	0.087	0.107	0.085
	Mg	0.865	0.873	0.851	0.879	0.854	0.871
	Fe	0.288	0.291	0.289	0.298	0.296	0.285
	Ca	0.783	0.777	0.786	0.759	0.777	0.773
	Total	4.000	4.000	4.000	4.000	4.000	4.000
	Mg#	77.9	76.3	76.1	76.6	76.5	78.1
(µg/g)	Li	6.942	3.159	16.831	1.859	3.304	15.395
	Be	0.043	0.039	0.050	0.042	0.052	0.039
	B	0.178	0.147	0.264	0.181	0.184	0.180

Figure 5-24. *San32 Px1*, a type-U clinopyroxene, has nearly homogeneous major element concentrations. Light elements do not show systematic behaviour; high values may be due to inclusions of matrix material.

(µm)	Distance	30	100	170	260	350	420	540
(cpfu)	Si	1.972	1.963	1.966	1.964	1.960	1.971	1.972
	Al	0.036	0.041	0.041	0.048	0.041	0.040	0.032
	Mg	1.159	1.167	1.158	1.148	1.159	1.160	1.174
	Fe	0.717	0.720	0.730	0.727	0.728	0.715	0.717
	Ca	0.077	0.076	0.074	0.073	0.073	0.075	0.073
	Total	4.000	4.000	4.000	4.000	4.000	3.999	4.000
	Mg#	61.8	62.3	61.7	61.4	62.2	61.8	62.3
(µg/g)	Li	12.031	5.055	2.221	2.281	2.301	2.197	2.332
	Be	0.037	0.037	0.038	0.041	0.041	0.041	0.039
	B	0.153	0.173	0.149	0.178	0.167	0.172	0.133

(µm)	Distance	660	750	910	990	1070	1210	1330	1410	1530
(cpfu)	Si	1.973	1.957	1.959	1.978	1.962	1.969	1.962	1.975	1.972
	Al	0.037	0.036	0.031	0.033	0.033	0.035	0.035	0.028	0.035
	Mg	1.161	1.168	1.165	1.150	1.161	1.157	1.169	1.168	1.160
	Fe	0.717	0.728	0.735	0.725	0.735	0.721	0.725	0.717	0.723
	Ca	0.072	0.073	0.076	0.076	0.075	0.076	0.076	0.074	0.074
	Total	3.998	4.000	4.000	3.997	4.000	4.000	4.000	4.000	4.000
	Mg#	61.8	62.4	62.4	61.3	62.3	61.8	62.6	62.2	61.6
(µg/g)	Li	6.924	6.822	8.539	2.962	2.288	2.334	3.127	1.842	4.246
	Be	0.037	0.037	0.036	0.037	0.039	0.035	0.041	0.032	0.035
	B	0.151	0.148	0.148	0.141	0.133	0.144	0.134	0.114	0.144

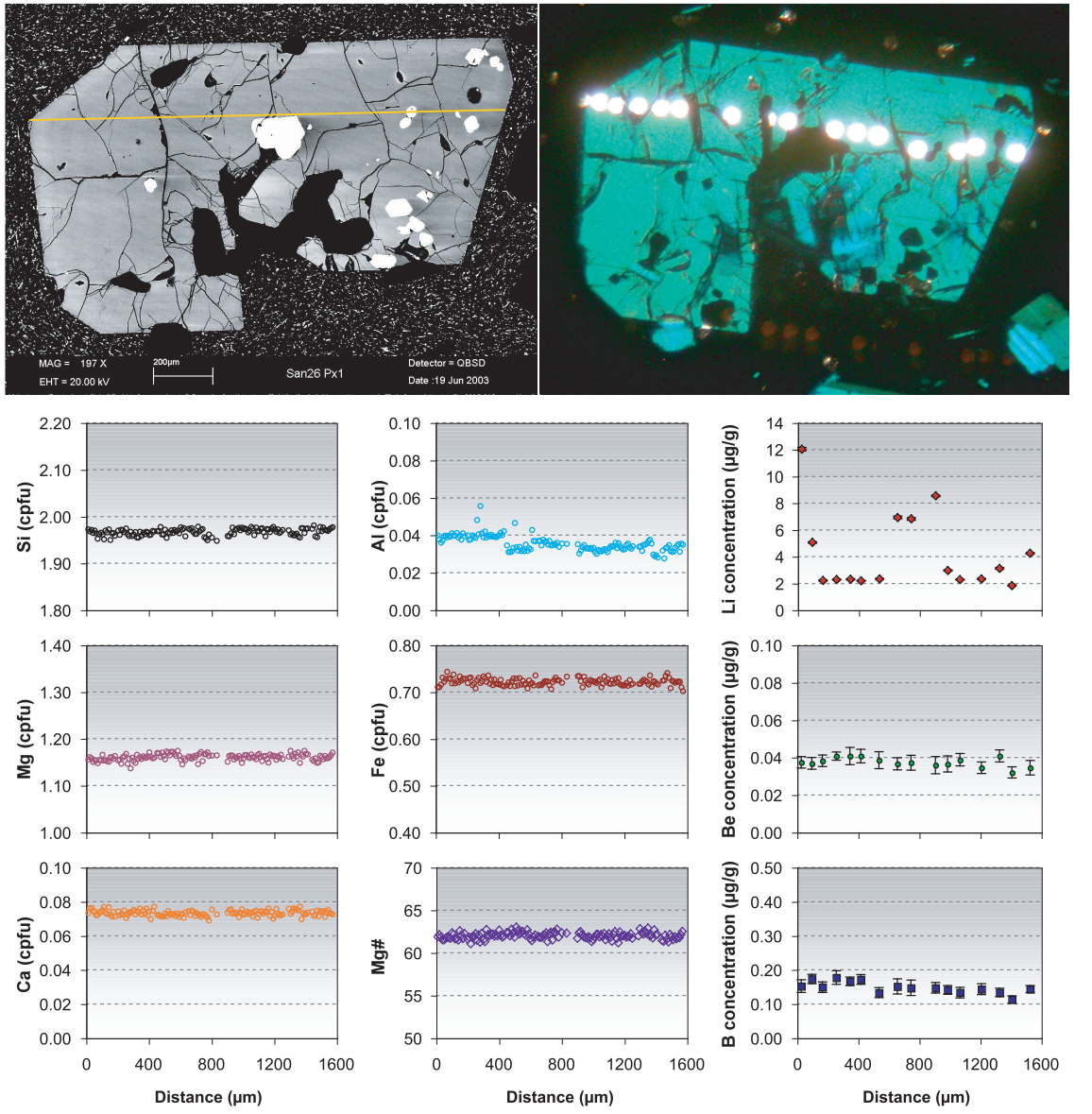

Figure 5-25. *San26 Px1* is an orthopyroxene with a fairly narrow range of major element composition, as well as Be and B concentrations. Li deviates from this trend through the elevated concentrations at the rim and near the magnetite inclusion, midway through the profile.

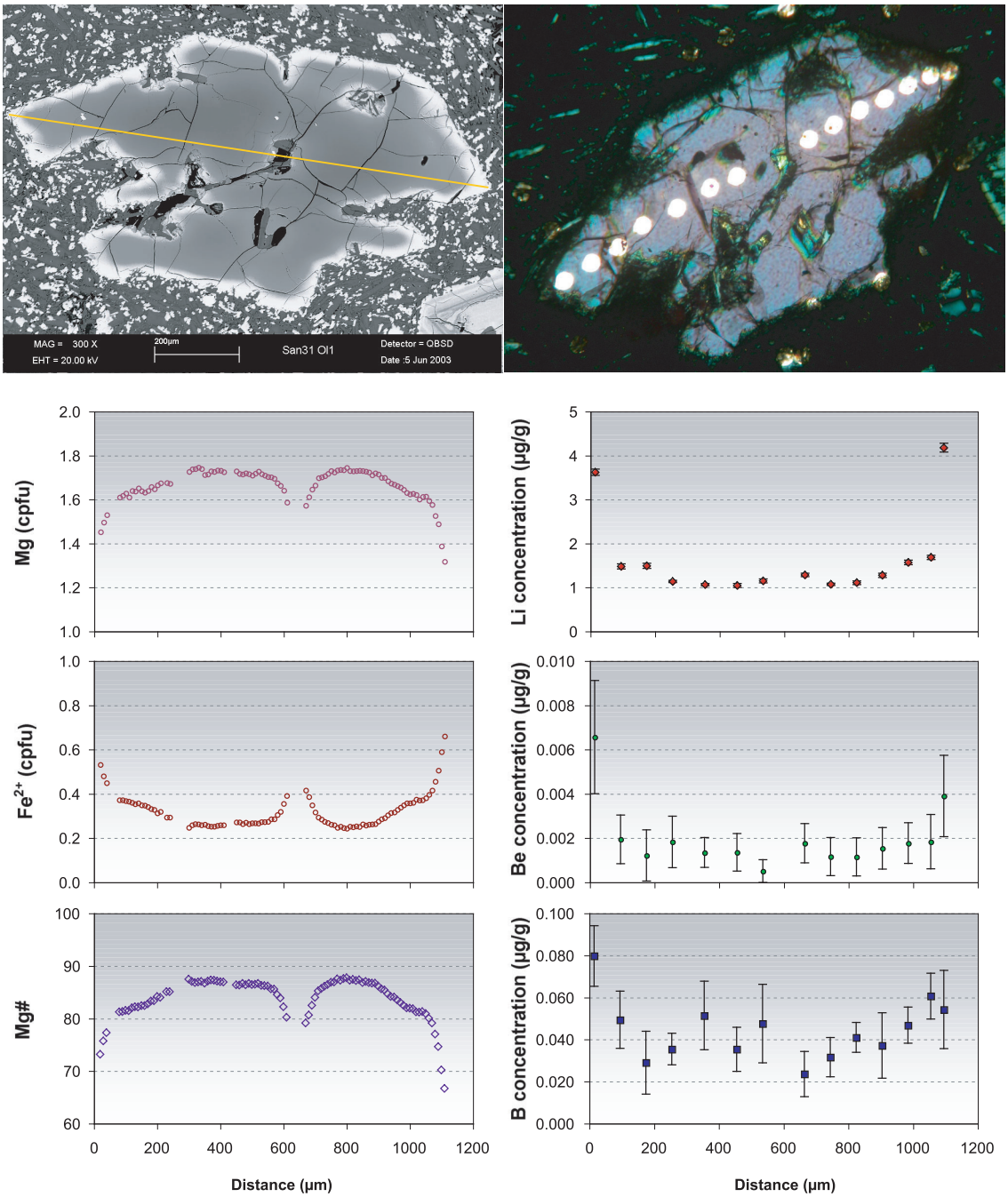

(µm)	Distance	30	110	190	310	370	470	550	680	760	840	920	1000	1070	1110
(cpfu)	Mg	1.497	1.611	1.649	1.738	1.730	1.716	1.704	1.612	1.724	1.732	1.699	1.625	1.577	1.318
	Fe2+	0.481	0.367	0.330	0.260	0.253	0.265	0.274	0.387	0.259	0.252	0.291	0.358	0.417	0.660
	Total	2.998	2.997	2.998	3.009	3.000	2.999	2.997	3.007	2.999	3.000	3.002	2.999	3.006	3.000
	Mg#	75.7	81.5	83.3	87.0	87.3	86.6	86.1	80.6	86.9	87.3	85.4	81.9	79.1	66.6
(µg/g)	Li	3.616	1.473	1.487	1.131	1.062	1.043	1.146	1.281	1.066	1.104	1.272	1.564	1.680	4.174
	Be	0.007	0.002	0.001	0.002	0.001	0.001	0.001	0.002	0.001	0.001	0.002	0.002	0.002	0.004
	B	0.080	0.049	0.029	0.035	0.051	0.035	0.047	0.024	0.032	0.041	0.037	0.047	0.061	0.054

Figure 5-26. *San31 Ol1* exhibits profiles indicative of formation in a basaltic magma and later incorporation into a more silicic composition. The high concentrations of light elements at the rim may be due to minute inclusions.

6. DISCUSSION

6.1 Nea Kameni Dacites

6.1.1 Phenocrysts and their Temporal Relations

Plagioclase

The six rock specimens taken from the 1939-1941 Nea Kameni lavas have the same phenocryst populations, such that the types and subtypes for the major mineral phases hold for all the samples. The thirty plagioclase phenocrysts analysed suggest different geneses. However, the fact that the different phenocryst types occur in both lavas imply that conditions and processes during crystal formation were not unique to a particular batch of magma, and most probably occurred repetitively, even within a single batch.

The earliest formed plagioclase identified for the 1939-1941 lava flows are the cores of **type-C** phenocrysts. These have most probably been inherited from a batch of less differentiated magma. There may have been different sources, as An contents are of at least two ranges of values. Cores of C1 crystals have $An_{58–64}$; those of C2 have $An_{73–85}$, pointing to more mafic magma. Moreover, light elements in C1 cores show trends that increase outwards, while those of C2 are mostly flat. The trend and range of values, however, are not distinct enough to allow interpretation of whether each of the core types was developed in only one batch of magma. These cores may have been entrained from more mafic parts of a convecting magma chamber, assimilated from older and more mafic instrusions that have crystallised along the walls of the chamber or conduit, or introduced by fresh mafic intrusions that mixed and mingled with the dacitic magma. It may well be possible that the cores of the sampled phenocrysts each represent a source distinct from other cores, despite similarities in the major and trace element concentrations.

Both subtypes are rimmed with zones of $An_{\sim 50}$, the typical rim composition of Nea Kameni plagioclases. Mg, in relation to the An content of both the core and rim, shows inconsistent trends. In some cases it is nearly flat (Fig. 6-1), while in others it is inversely related with An (e.g., Fig. 6-2). Mg occurs only in trace amounts in plagioclase, possibly occupying both M and T-sites (Peters et al., 1995; Hattori & Sato, 1996). Plagioclase-basalt partition experiments yield partition coefficients ($K_{Mg}^{Pl/melt}$) of 0.028 – 0.061 for An_{40-80}, with Mg partitioning only weakly dependent on plagioclase composition (Bindeman et al., 1998;

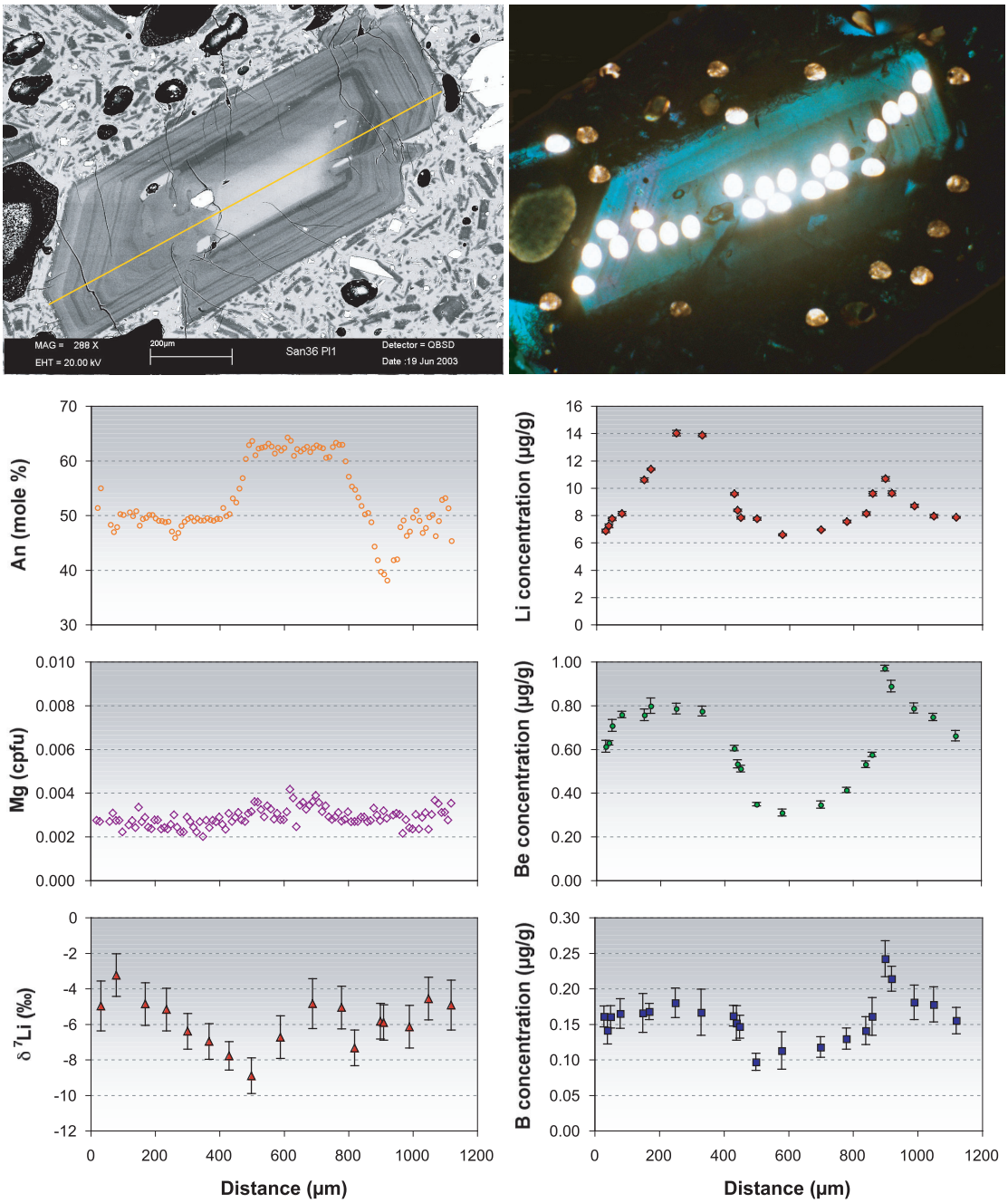

Figure 6-1. *San36a Pl1* is a type-C1 plagioclase where the three light elements show similar patterns, indicating the primary nature of the profiles. This suggests that Li has not diffused significantly. Considering the known rapid diffusion of Li in plagioclase, the data further implies that this phenocryst, or at least its rim overgrowth, crystallised very rapidly.

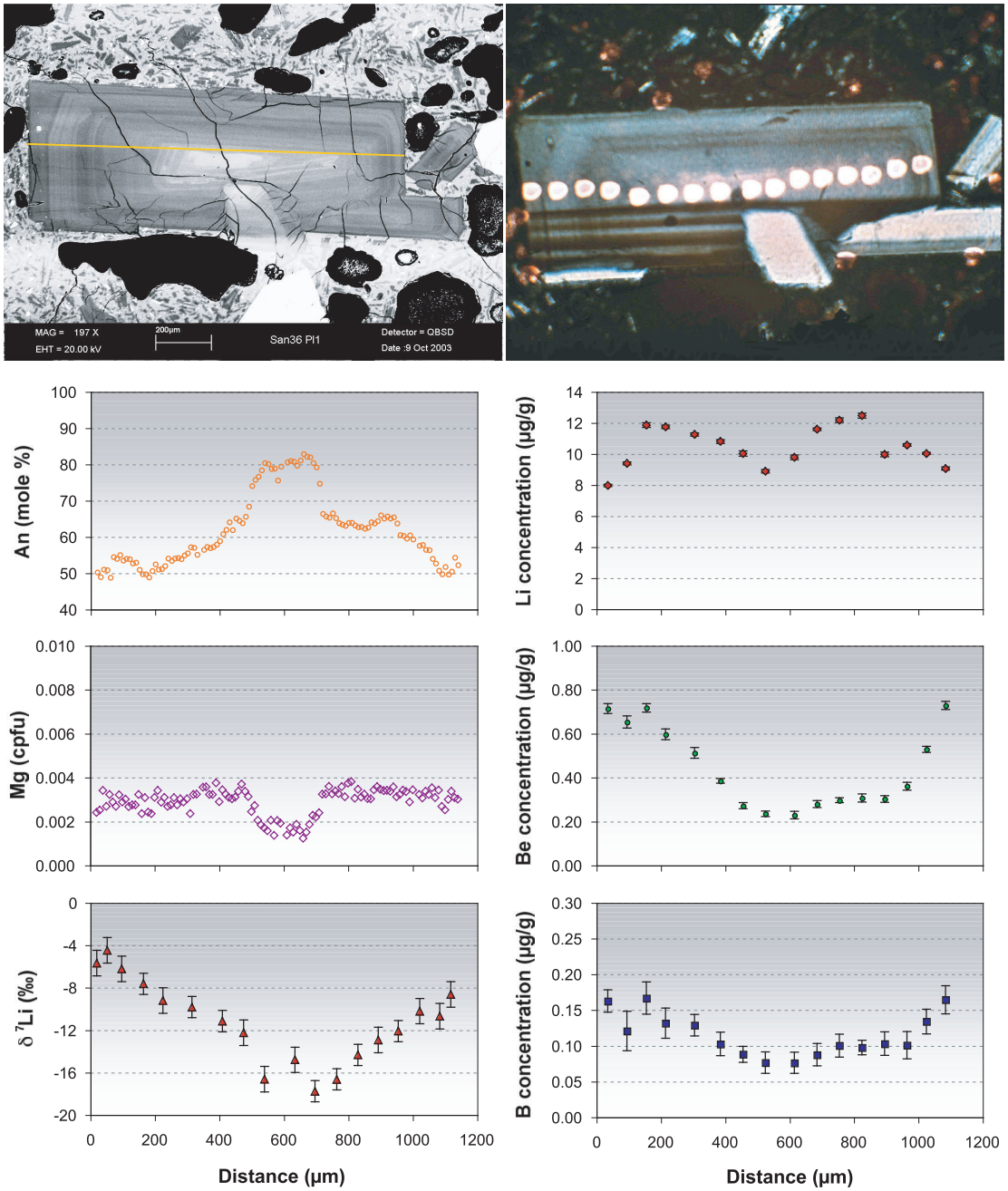

Figure 6-2. In *San36b Pl1*, a type-C2 phenocryst, the Li profile deviates from those of Be and B, showing an initial increase from the core and a decline halfway through the rim. Interpreted alongside δ^7Li data and judging from the steady increase in the heavier isotope from the core-rim boundary towards the rim, degassing may have occurred throughout the formation of the rather thick rim. The inner zone registers an increase in Li concentration simply because crystallisation and the incorporation in other growing crystals did not significantly aid the degassing process in depleting the melt of Li. Halfway through the rim, however, growth of other phases taking up Li may have significantly decreased Li concentration in the melt.

Bindeman & Davis, 2000). Previous experimental investigations of $K_{Mg}^{Pl/melt}$ show minimal decrease with decreasing temperature (Longhi et al., 1976; Weill et al., 1980; Sato, 1989; Phinney, 1992; Sisson & Grove, 1993; Blundy & Wood, 1994). Direct measurements of activity coefficients of divalent cation oxides (e.g., FeO, NiO, CoO in Holzheid et al., 1997) prove these to be relatively insensitive to compositional variations in a wide range of silicate liquids in standard states. Hence, in a diffusion model developed by Costa et al (2003), Mg flux is reckoned from the diffusion of Mg due to its own concentration gradient and the anorthite variations in plagioclase. The latter stems from the fact that the activity or chemical potential of Mg depends strongly on An content and eventually produces equilibrated concentration profiles inverse to that of An (Costa et al., 2003). The very low concentrations of Mg in the plagioclase crystals analysed for this study and the lack of systematic response to the An content amongst phenocrysts of different types hardly render further interpretation of its behaviour. In any case, the relationship between An and Mg in plagioclase is presently difficult to ascertain without a thorough knowledge of Mg diffusivities, and owing to its low abundances in plagioclase.

The abrupt change to lower An contents in type-C phenocrysts is accompanied by higher concentrations of Li, Be, B. Hence, the light elements in type-C are generally inversely related to An content, although Li to a much lesser degree, owing to its general lack of correlation with An content and its propensity to diffuse and equilibrate within the crystal (e.g., Fig. 6-2). Where the Li pattern deviates from its inverse relationship with An by means of a decline towards the rim, Li loss from the magma through degassing during crystal growth may be invoked (also in Fig. 6-2). An interesting feature of the data for type-C crystals is the crude reverse mirror image shown by δ^7Li with respect to the Li concentration pattern, whereby values decline from the central portion outwards of the core, and then increase towards the rim of the surrounding mantle (Fig. 5-7, less obvious in Fig. 6-2). Such isotopic trend probably suggests kinetic fractionation, involving the faster release of ^{6}Li from the melt during degassing. Although found in the same lava sample, the core of San *36a Pl1* (Fig. 6-1) appears to have a much heavier isotopic composition than that of *San 36b Pl1* (Fig. 6-2), adding evidence to the inference that there were different sources for the inherited crystals. Be and B exhibit more consistent trends with respect to An content, the disparity between core values of different phenocrysts simply reflecting the original Be and B concentrations of the inherited crystal.

In *San36a Pl1* (Fig. 6-1), all three light elements show a rough inverse relationship with An, which implies the primary nature of these profiles. It is known that Li, Be and B behave differently in accordance with magmatic conditions and their dependence on An content. In this case, it is too much of a coincidence for these to have been affected or even modified by different processes and still end up forming similar profiles. In particular, Be, B, and the major elements responsible for An content, are known to diffuse much slower than Li (Giletti & Shanahan 1997; Bindeman et al., 1998; Mungall et al., 1999). Moreover, the plagioclase-melt partition coefficient for Li is almost independent of An content (Bindeman et al., 1998), so all portions of the plagioclase crystal would have nearly the same Li concentration in equilibrium. The constancy of the relationship of Li data with these other elements, therefore, may be considered strong evidence for the unexpectedly fast crystallisation of this complex phenocryst. The established rapid diffusion of Li within plagioclase would have unavoidably homogenised the concentrations to create a smoother profile that deviates from those of other elements, unless arrested by the sudden cooling and solidification of the magma. This shall also be further discussed in a subsequent part of this chapter.

In *San36b Pl1* (Fig. 6-2), the Li concentration profile deviates from those of Be and B, the latter two elements being inversely related with An. Li behaviour may be understood better by considering both elemental and isotopic compositions. Within the core, Li concentration increases outwards, while δ^7Li shows the reverse pattern. Although analytical uncertainties need to be reckoned, the concentration profile may be due to the incompatible nature of Li in plagioclase. Surrounding the core, in what may be called the "mantle" to avoid confusion with the crystal's outermost rim, Li concentration increases midway, then decreases towards the rim. Within this mantle, δ^7Li increases consistently towards the rim. The isotopic data suggests that degassing of the melt occurred throughout the formation of the thick rim, progressively releasing more of the lighter isotope and leaving behind heavier isotopic compositions through kinetic fractionation. The seemingly contradictory nature of the Li concentration from the boundary with the core until halfway through the mantle, may be explained by the one other factor responsible for the amount of Li being incorporated into a growing crystal: the extent of Li uptake by the crystallising phases in the magma during a particular span of time. In this light, the initial increase in Li concentration during the mantle formation is due to the minimal uptake of Li by other crystals, or the minimal amount of crystals taking up Li in this period. Halfway during the mantle formation, however, the

ongoing loss of Li from the melt through degassing is complemented by an enhanced Li uptake of more crystals growing in the melt, thereby decreasing concentrations towards the outermost rim.

Coeval to the rims of type-C phenocrysts are **type-O** phenocrysts, which dominate the plagioclase population of the Nea Kameni dacites. These have An_{58} to An_{40}, zoning being generally oscillatory. In some cases, disruptions in the form of embayed and solution textures are evident, even occurring as multiple resorption surfaces within a single crystal. Such are probably brought about by dynamic changes in the magma chamber, including convection through compositionally disparate layers, intrusion of more mafic fractions, change in the H_2O activity which subsequently shifts the An content of the crystallising plagioclase, or some other condition that is subtle enough to effect only oscillatory zoning but significant enough to resorb existing crystal surfaces. However, it is difficult to correlate the surfaces developed by these changing conditions among different phenocrysts, as adjacent compositions and the number of occurrence differ widely from crystal to crystal.

There are also two subtypes under type-O, but in this case based on the Li concentration profiles. Lithium concentrations in the O1 subtype (see Fig. 5-3 in Chapter 5) are also flat. Amongst O2 phenocrysts, however, Li concentrations decrease from core to rim, a stark departure from the rather homogeneous major element composition, in patterns that commonly coincide with the symmetry of crystal growth (Fig. 6-3). As previously noted, this decrease may have been caused by the loss of Li from the melt. Li is a fluid-mobile element, and may therefore be easily released through degassing of the magma (Webster et al., 1989; Brenan et al., 1998; Tomascak et al., 2002; Hervig & Moore, 2003; Berlo et al., 2004; Beck et al., 2004). Furthermore, previous work on Nea Kameni dacites documents loss of water (Barton and Huijmans, 1986). δ^7Li patterns also support this conjecture. With patterns that appear like the smoothened reversals of the Li concentration profile, the trend towards heavier isotopic compositions from core to rim may be explained by kinetic fractionation during degassing-induced Li loss from the magma, wherein ^{6}Li escapes more rapidly into the volatile phase. Such is contrary to the process of equilibrium fractionation, where ^{7}Li partitions preferentially into aqueous fluids over silicate melts and minerals (e.g., Chan et al., 1992; Zhang et al., 1998; Pistiner & Henderson, 2003). The smoothness that renders a deviation from the Li concentration mirror image may then be simply due to the diffusion of Li within the crystal, which according to experiments, is believed to be very rapid (Giletti and Shanahan, 1997).

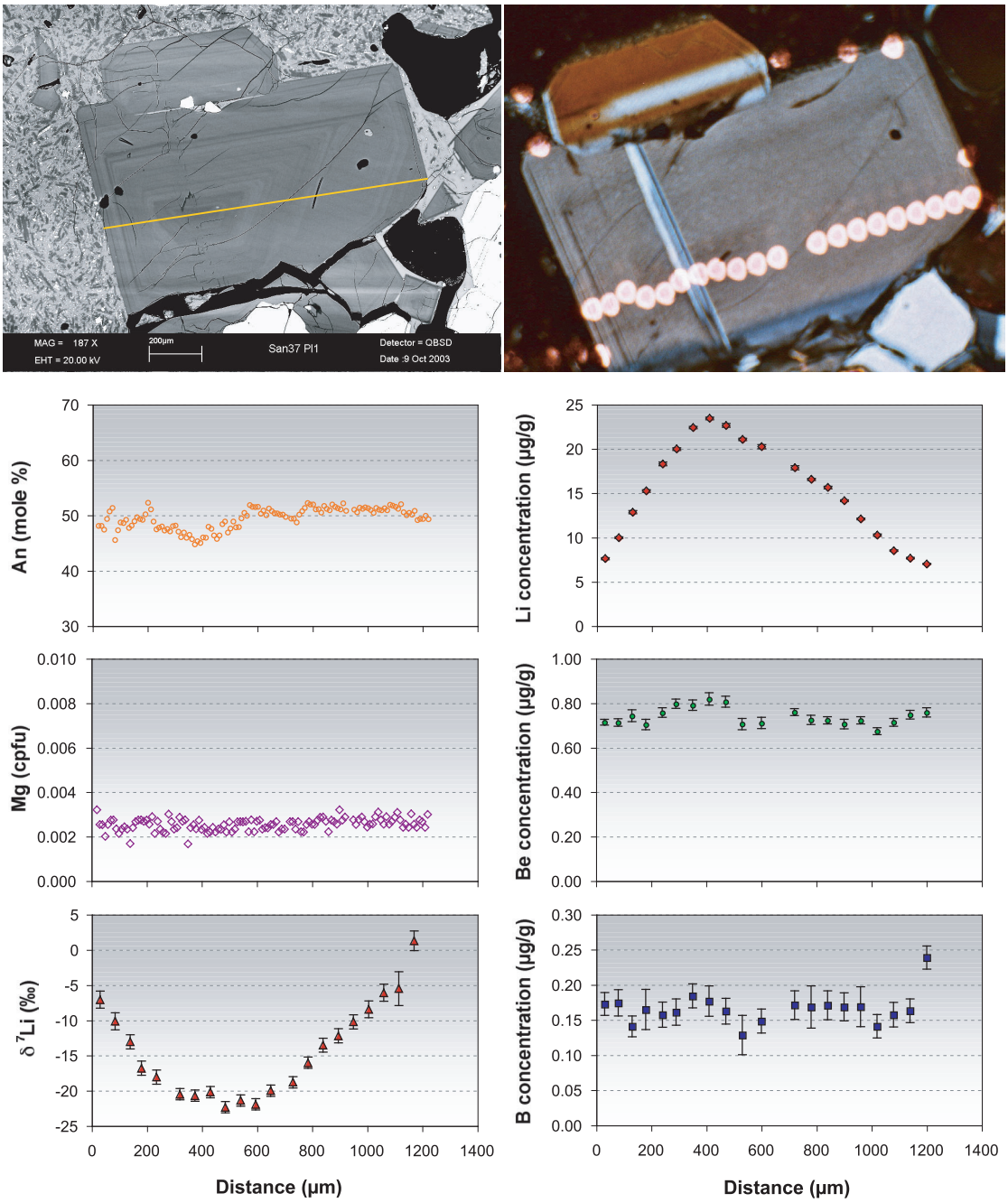

Figure 6-3. Li loss in the magma is starkly shown by *San37b Pl1*, a type-O2 plagioclase. Li decreases rather consistently from core to rim, pointing to the release of this water-soluble, light element through degassing. The shape of the profile, i.e., the presence of a sharp apex instead of a bell-shaped curve, appears to discount homogenisation through diffusion. The δ^7Li profile is smoother, but is still nearly a mirror image of the concentration trend, implying only minimal diffusion.

Despite the disparity in the Li concentration profiles of type-O phenocrysts, however, rim compositions are similar. This suggests that subtype-O2 may have formed earlier, when the magma contained more Li, and that their rims are coeval with the whole crystals of subtype-O1. The flat profiles of the latter subtype probably imply a cessation or diminution of degassing. It is significant to state at this point, that all analysed plagioclase phenocrysts, except for the xenocrystic type-A, actually have similar Li, Be and B concentrations at their rims. Furthermore, rim compositions match those of the microlites in the matrix.

The inverse relationship between An content and the light elements Be and B is generally shown by type-O plagioclase. This is to say that the core-to-rim increase assumed to be due to the progressive saturation of the melt in these incompatible elements is no longer observed. Instead, the profiles are rather flat, except for variations that reflect reverse patterns of the oscillatory zoning.

Type-N phenocrysts are normally zoned and therefore suggest 'normal' crystallisation. Cores of $An_{\sim 60}$ point to initial andesitic compositions that gradually evolved into dacitic magma, thus forming rims with $An_{\sim 30}$. Despite the expected nature of this type however, very few such phenocrysts occur in the sampled lavas. Another surprising observation is the wide range of An contents in these crystals: $An_{\sim 60}$ being the highest content amongst the entire plagioclase population with the exception of the inherited cores of type-C and the xenocrystic type-A, and $An_{\sim 30}$ being the lowest measured value at the rim of all the plagioclase phenocrysts. This seems to imply that type-N phenocrysts formed throughout the entire window of plagioclase crystallisation, but these crystals are not exceptionally large, nor affected by as much resorption as observed in type-O phenocrysts. Hence, it is difficult to ascertain the time of crystallisation of type-N phenocrysts relative to other types; on the one hand it spans the entire range of An contents of the dacitic system, but on the other hand it has preserved less of the imprints of processes that have affected other phenocrysts.

Similar trends in the An and Fe^{3+} profiles of the San 3 type-N phenocrysts are expected, as the latter substitutes for Al^{3+} in tetrahedral sites of plagioclase. The Fe^{3+} concentration pattern of *San 36b Pl2* (Fig. 6-4) may be due to a change in the oxygen fugacity in the system; this however, should not be overemphasized because of the meagre amount of this ion that goes into the plagioclase structure, and the formation of phases (e.g. magnetite) that accounts for its availability on a larger scale. Interestingly, the backscattered-electron (BSE) image shows resorption surfaces near the core of *San36b Pl2* and the neighbouring intergrown crystal. These are evident through the slight troughs in the An profile, but not in trace elements such as Fe^{3+}.

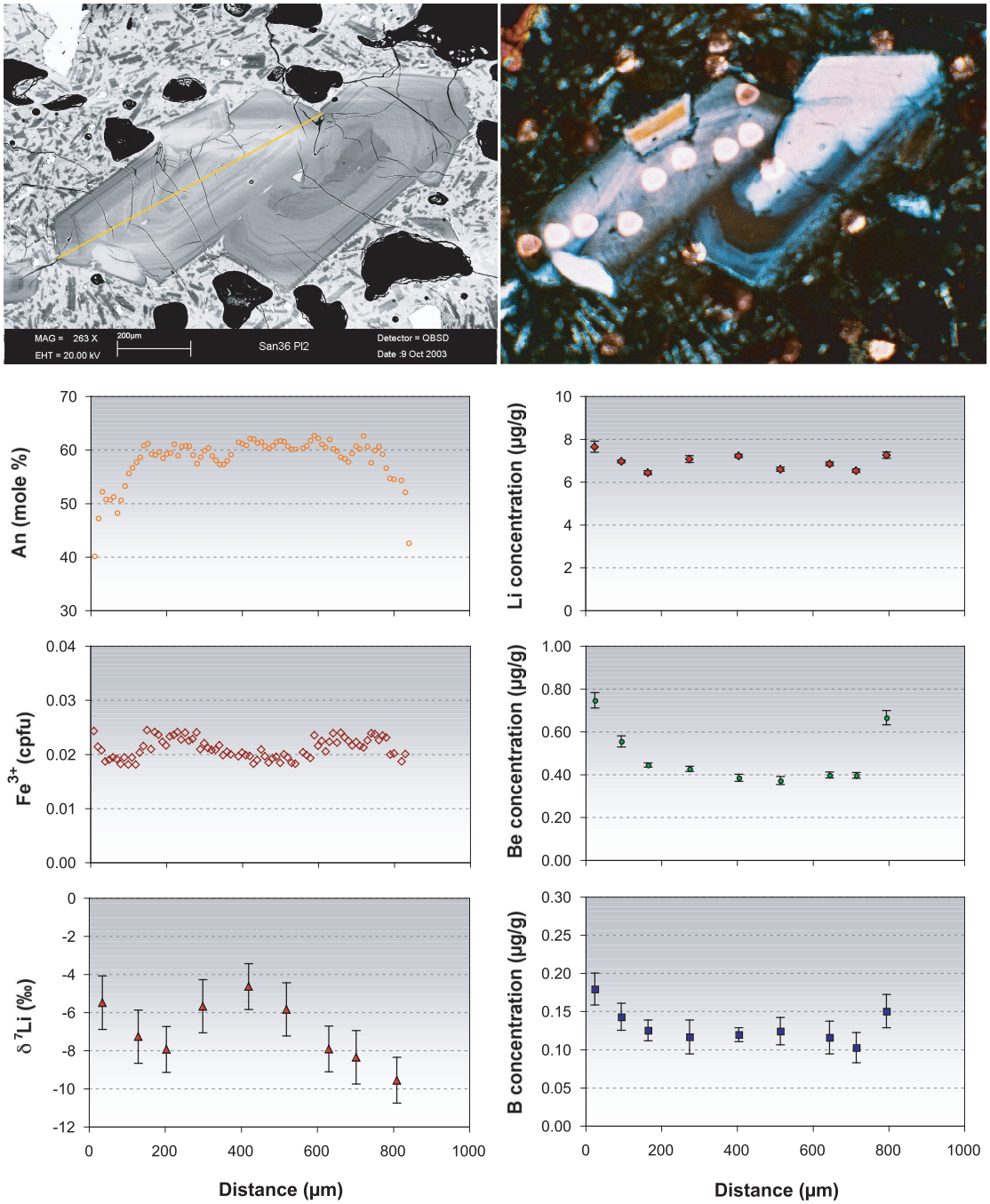

Figure 6-4. *San36b Pl2* is a type-N plagioclase with a large An range, suggesting its formation through a wide range of magma compositions, including a reversal along a resorption surface. The crystal however, is not exceptionally large, despite the fact that it covers the entire range of An contents of some inherited cores and all phenocrysts inherent to this dacitic magma.

Lithium concentrations within type-N crystals show no systematic variation and cannot be correlated with major element compositions. Also, the δ^7Li profile for *San 36b Pl2* is rather erratic. On the other hand, Be and B concentrations generally increase from core to rim. Such patterns are consistent with the assumption in the course of normal crystallisation; incompatible elements become progressively enriched in the melt and thus, are increasingly forced into the developing rims of growing crystals. The rim-ward increase in Be and B may likewise be hinged with An content; Be contents of plagioclase in granitic rocks have been found to peak at $An_{\sim 30}$ and decrease towards opposite directions from this value (Kosals et al., 1973). Such behaviour has been attributed to the strong dependence of $K_{Be}^{Pl/melt}$ on anorthite, with a maximum value for this partition coefficient for An_{30} (Evensen & London, 2002).

Type-A phenocrysts are fragments from andesitic to basaltic magmas that have not grown rims in the dacitic system, which previous work recognise as mafic enclaves (Holness et al., 2005; Martin et al., 2006). These have An contents higher than the characteristic dacitic plagioclase and even the cores of type-C phenocrysts. *San 37 Pl4* (Fig. 6-5) is such a phenocryst. Enclosed in its own matrix of mostly fine-grained pyroxene, this crystal is hardly overgrown by more albitic plagioclase, preserving the rather homogeneous $An_{\sim 90}$ composition except for the very thin outermost rim (only visible at the left end of the profile). Be and B concentrations are also within a relatively narrow range, with markedly lower concentrations than in other plagioclase types, further attesting to its xenocrystic nature.

Elemental and isotopic Li profiles, however, are comparable to those of type-O2 plagioclase. Li concentration and δ^7Li patterns are rough horizontal mirror images, although that of δ^7Li is significantly smoothened in contrast to the abruptly variable core values of Li concentration. Nonetheless, the peak concentration value corresponds to the lowest δ^7Li analysis, and the pronounced decrease in abundance towards the rim is accompanied by increasingly heavy isotopic composition. Where concentrations taper to near-zero values at the rim, δ^7Li measurements show a larger range of analytical uncertainty (Fig. 6-5). Again, loss of Li through degassing seems to be the best explanation for the profiles, but there is difficulty in determining whether this occurred during or after crystallisation. Although the sharp peak in the concentration that corresponds to the lightest isotopic composition appears to discount modification or homogenisation through diffusion, the absence of clear oscillatory concentric zoning on the crystal hampers the correlation between crystal growth and profile symmetry. Hence, the Li record may represent post-crystallisation loss through diffusion, rather than primary igneous compositions.

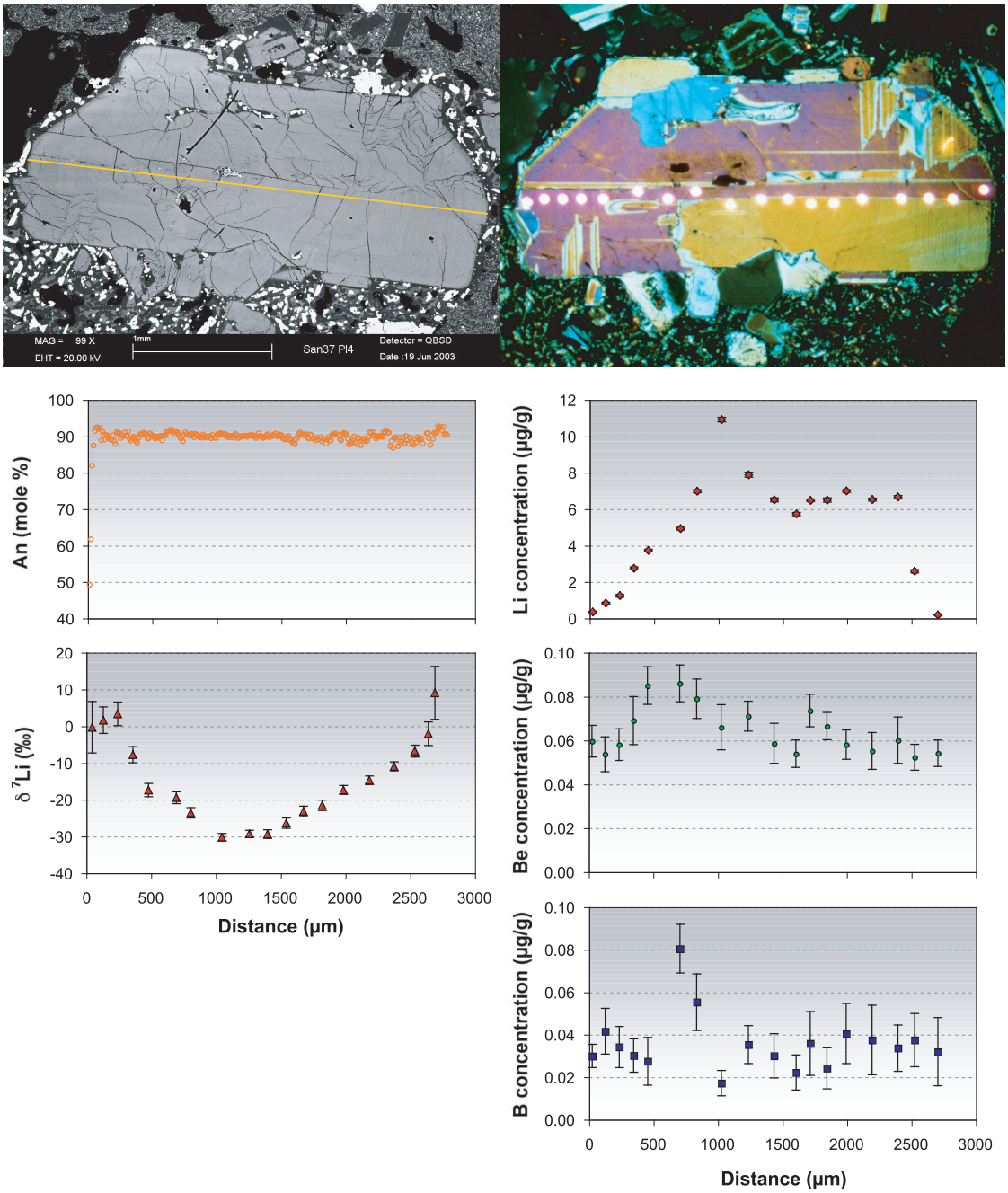

Figure 6-5. *San37a Pl4*, a xenocryst, also shows the interesting Li patterns characteristic of type-O2 phenocrysts. The rim-ward decrease in Li concentration accompanied by an increase in δ^7Li, also implies the loss of Li in the system, most probably through degassing. But the BSE image and photomicrograph do not reveal the growth zones of the crystal and whether these relate to the Li patterns. Hence, Li loss may have occurred after crystallisation and the profiles may have resulted from post-crystallisation modification through diffusion.

Pyroxene

Pyroxene phenocrysts in the Nea Kameni dacites are commonly intergrown with type-O plagioclase, and thus may be coeval with them. These intergrowths are clearly evident on scanned thin sections and photomicrographs in Chapter 4.1 figures; in Chapter 5 these are not as evident due to the disparate brightness of the two phases in BSE images and the varying extinction angles in the photomicographs.

Types D and I among the orthopyroxenes hardly vary in terms of major elements, except for the slight rim-ward decrease in Mg# in D and the opposite in I. The latter may be effected by higher oxygen fugacities in the system, or influx of more mafic magma, which would also explain the presence of high-An plagioclase and high-Mg# clinopyroxene xenocrysts in the samples. Light element concentrations and patterns are likewise similar, where Li slightly increases from core to rim, and Be and B either follow suit or vary unsystematically, all within a limited range of values. These patterns imply that light element concentrations are not dependent on major element composition.

A significant deviation from the aforementioned patterns, however, is the core-to-rim decrease in Li among type-I2 phenocryst (Fig. 6-6). As in type-O2 plagioclase phenocrysts, this may have resulted from Li loss through volatile release in the water-rich dacite. The difference in the Li concentration profiles among the various orthopyroxene phenocrysts may be explained by their relative time of formation. Type-I2 phenocrysts may have crystallised early, alongside type-O2 plagioclase, in the degassing magma. Other pyroxene and plagioclase phenocryst types subsequently developed. Through time and continued crystallisation, probably after or during a pause in the degassing, the melt may have accumulated more of the incompatible element again to account for the elevated rim values in types D and I1. The general core-to-rim decrease in δ^7Li is consistent with the assumption that degassing waned, and thus the lighter element is not preferentially released from the melt through kinetic effects. Nevertheless, this remains to be an oversimplified and very tentative explanation, which necessitates further study. In the case of clinopyroxene, for example, cooling facilitates the rapid diffusive transfer of Li from plagioclase (Coogan et al., 2005). The rate of Li exchange between these minerals is controlled by the rate of diffusion of Li within the respective crystals and the length of time for diffusion to occur at a certain temperature.

The clinopyroxene phenocrysts observed in the sample have generally flat major and trace element profiles which only slightly vary consistent with the weak zonation. The only

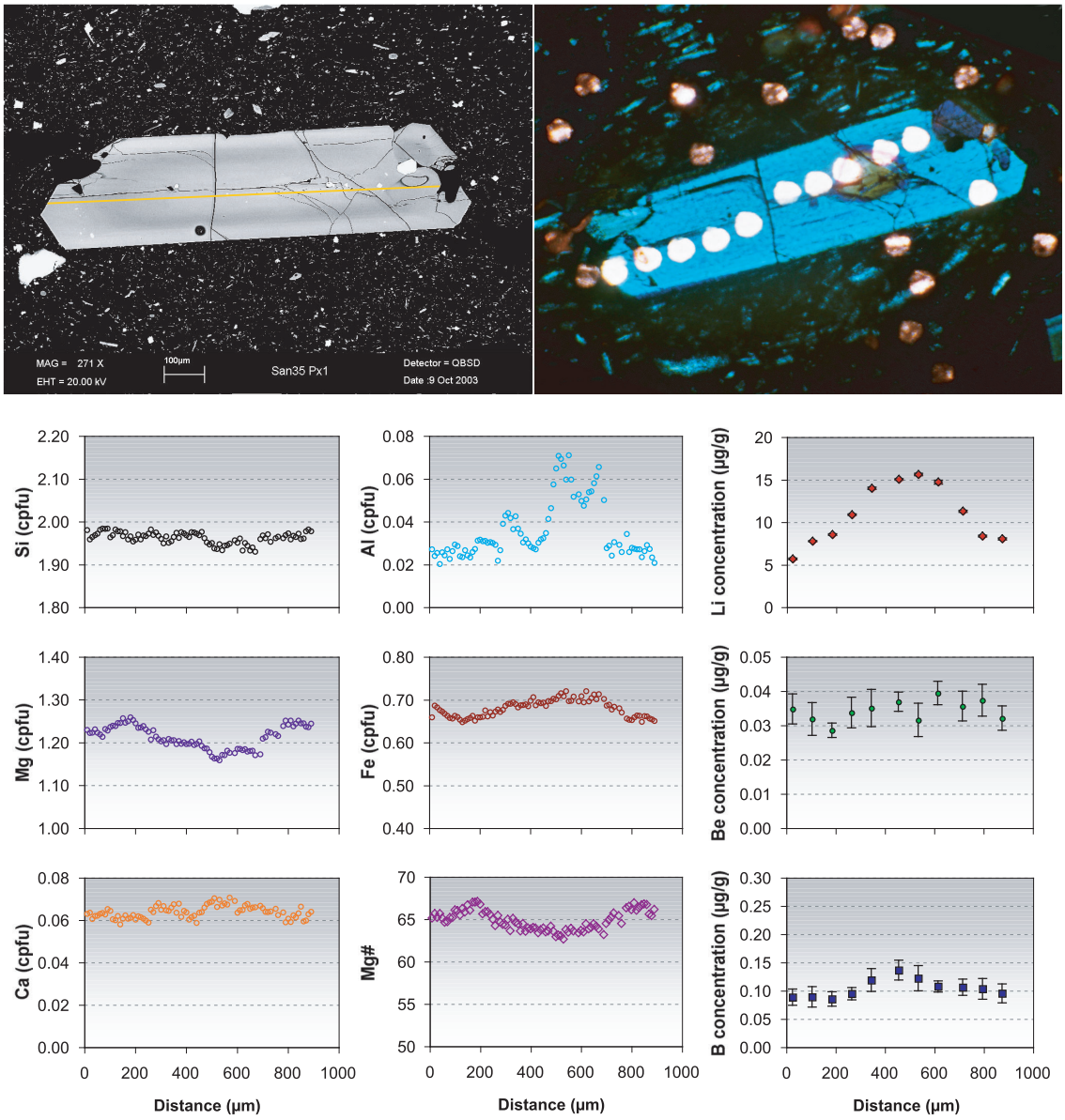

Figure 6-6. The core-to-rim decrease in Li concentration of *San35 Px1*, a type-I2 orthopyroxene, may be a product of the same process and conditions during the crystallisation of type-O2 plagioclase phenocrysts. B, being also water-soluble, may have been lost with Li through degassing.

exceptions are the elevated values for Li concentration at the rims, in contrast to the very minimal increase of this element towards the rim. *San 37 Px1* (Fig. 6-7) is different from other members of this population in that it has two zones: a relatively large core with glass inclusions and a rim with a texture quite like that of the other type-L clinopyroxene phenocrysts. The boundary between these zones is not distinct on microscopic and back-scattered electron images, although a slight discrepancy in colour coincides with the break in Mg# values. The core of this phenocryst may be from another magma fraction, although with nearly the same composition as the dacitic system where the rim developed. Li concentration appears to increase from the central portion outwards of the core, then decreases to as low as the inner core value at the inclusion-poor rim. Be and B show more chaotic profiles within the core, but this may be due to glass being included in the analysis. δ^7Li shows a profile that increases from core to rim, without apparent discontinuity across the boundary.

Type-H clinopyroxene, with its higher Mg# of 83 in the core declining to 74 at the rim, (Fig. 6-8) is probably a xenocryst from an earlier, less differentiated magma. Supporting this conjecture are its pronounced concentric and sector zoning, rare textures compared to the coexisting much less zoned clinopyroxene phenocrysts having lower Mg#. Only one such crystal was found in the thin sections, despite its readily recognizable euhedral shape and zoning. Light element analysis for this crystal does not seem to yield any significant implications, other than the increasing rim-ward Li concentrations expected during crystallisation and the slightly lower and more erratic Be and B abundances compared to other pyroxenes in the Nea Kameni dacites.

Olivine

The one olivine phenocryst (see Fig. 5-17 in chapter 5) which was large enough for detailed analysis is most likely a xenocryst from more mafic fractions. Homogenous major element composition throughout most of the crystal suggests formation in a relatively large reservoir, while the pronounced change to less mafic composition at the outermost rim signals incorporation into the more silicic magma. Li responds to this change with an increase in concentration at the rim, probably due to the higher Li content of the latter magma or the preferred incorporation of Li in the low-Mg rim. Be and B seem to increase rimwards, independent of the major element profiles, which is asymmetric for this crystal. This may be a

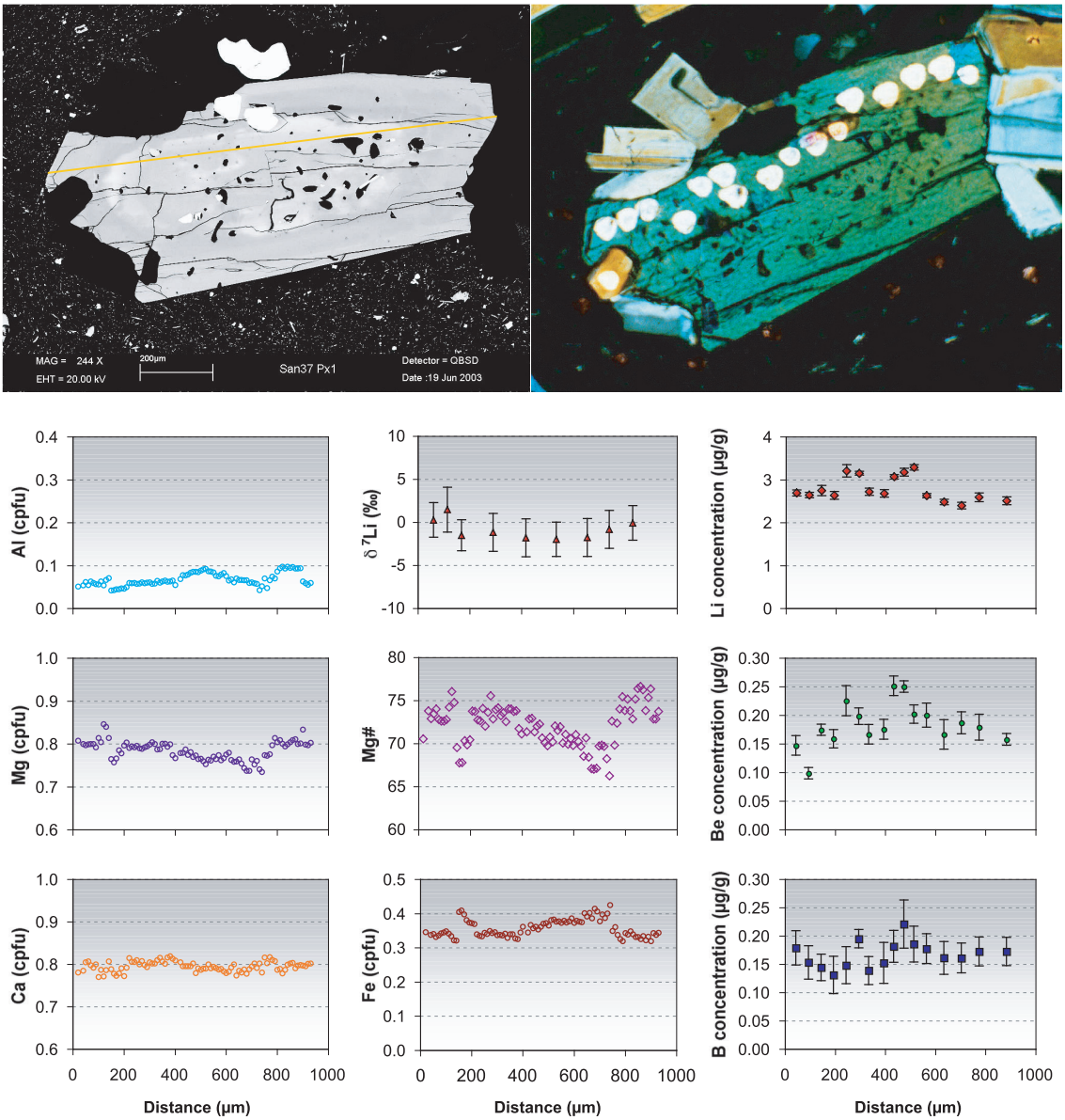

Figure 6-7. *San37a Px1* is a type-L clinopyroxene with two zones, both having formed in almost similar magmatic compositions. The crystal is larger than the typical pyroxene phenocryst in the samples and the core may thus have been inherited from an earlier magma fraction. Li seems to show an outward increase in concentration within the inner zone, but the paucity of data does not warrant much interpretation. δ^7Li surprisingly shows a smooth profile that turns up at the rim, although with relatively large analytical error.

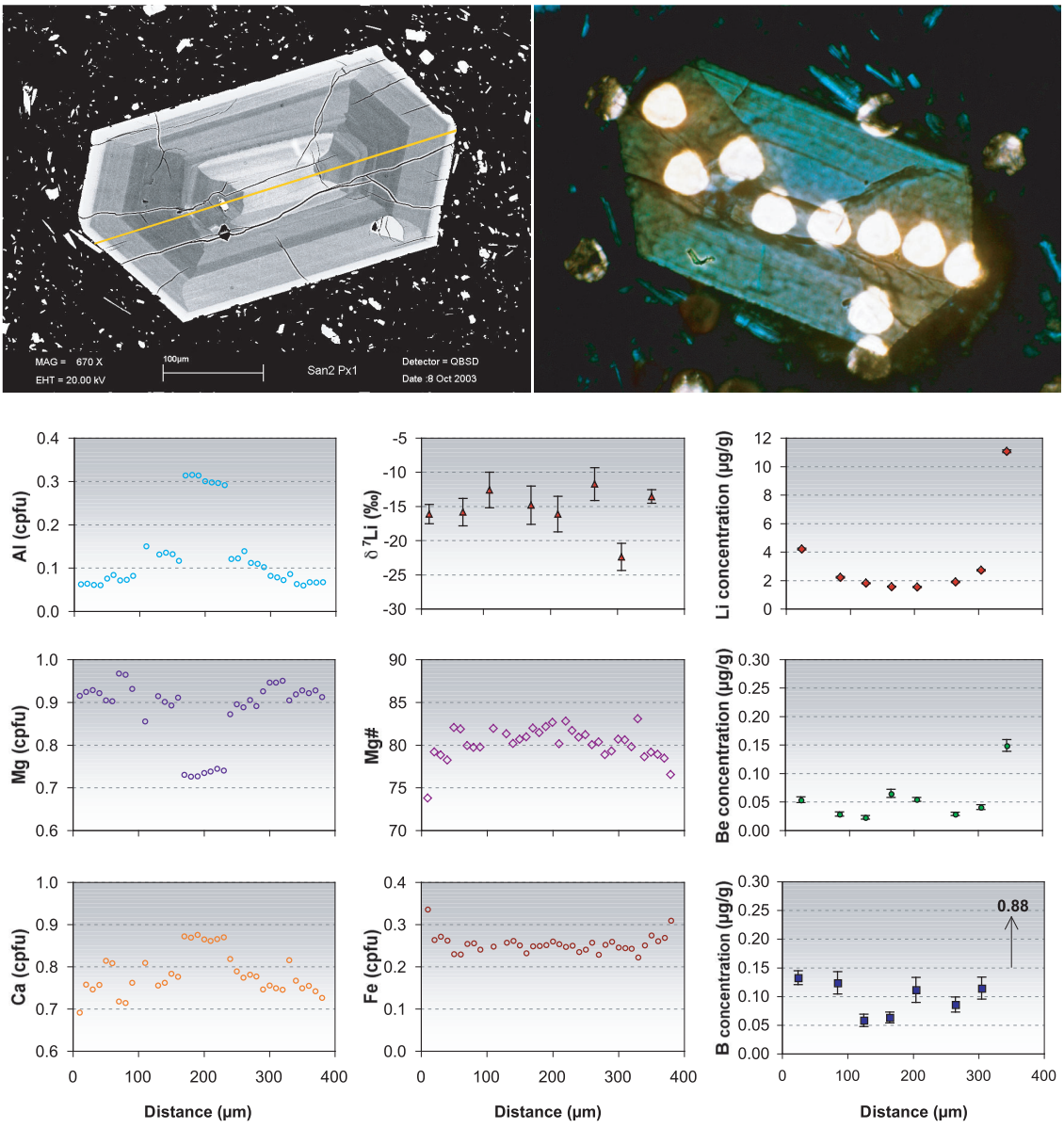

Figure 6-8. *San2b Px1*, the type-H clinopyroxene, is probably a xenocryst. Unlike all other pyroxenes in the dacites, it has higher Mg# and well defined concentric and sector zones. The light element trends, however, are similar to those of most pyroxene phenocrysts.

function of their incompatibility in olivine, but concentrations for these two elements are too low to warrant further interpretation.

6.1.2 Phenocryst Rim Compositions in relation to the Matrix

Rim compositions for all the plagioclase phenocrysts in the Nea Kameni dacites, with the exception of the xenocrystic type-A, are within the range 6.5 – 9.8 μg/g for Li, 0.60 – 0.96 μg/g for Be and 0.15 – 0.20 μg/g for B (figures 5-1 to 5-9, figures 6-1 to 6-4). The wide range of values may be due to the spatial resolution of the analysis, whereby spots cannot be effectively positioned within thin zones of the outermost rim, resulting to measurements that include neighbouring zones. Nevertheless, rim compositions generally correspond to the compositions of the microlites within the samples, suggesting that the rims formed in equilibrium with the melt. Observed matrix compositions fall within a general range of 30 – 40 μg/g for Li, 2 – 3 μg/g for Be and 15 – 25 μg/g for B (Fig. 6-9). Calculation of partition coefficients from the observed values for plagioclase yield:

$$K_{\mathrm{Li}}^{\mathrm{Pl/melt}} \approx 0.2 - 0.3$$

$$K_{\mathrm{Be}}^{\mathrm{Pl/melt}} \approx 0.3$$

$$K_{\mathrm{B}}^{\mathrm{Pl/melt}} \approx 0.01$$

The plagioclase/melt partition coefficient for Li observed in this study corresponds very well with experimental results from Bindeman et al. (1998) and Bindeman & Davies (2000), who investigated trace element partitioning between plagioclases of $An_{40\text{-}80}$ and basaltic melt. The Be plagioclase/melt partition coefficient is also similar to their result for plagioclase of $An_{\sim 40}$ but that for B is lower by at least an order of magnitude (Bindeman & Davies, 2000).

Phenocrysts of clinopyroxene and orthopyroxene are mostly much smaller than those of plagioclase. Owing to the difficulty of positioning the analysis spot within the outermost rim of these crystals, rim compositions of Li, Be and B are of an even wider range of values. Moreover, microlites of these mafic minerals are also smaller than those of plagioclase and most measurements likely include glass or other nearby microlites. Hence, the rim compositions cannot be compared with the microlite data. Despite the constraints of spatial resolution, calculations for partition coefficients for pyroxenes give:

$$K_{\mathrm{Li}}^{\mathrm{Cpx/melt}} \approx 0.1 - 0.4 \qquad K_{\mathrm{Li}}^{\mathrm{Opx/melt}} \approx 0.1 - 0.3$$

$$K_{\mathrm{Be}}^{\mathrm{Cpx/melt}} \approx 0.02 - 0.12 \qquad K_{\mathrm{Be}}^{\mathrm{Opx/melt}} \approx 0.01 - 0.02$$

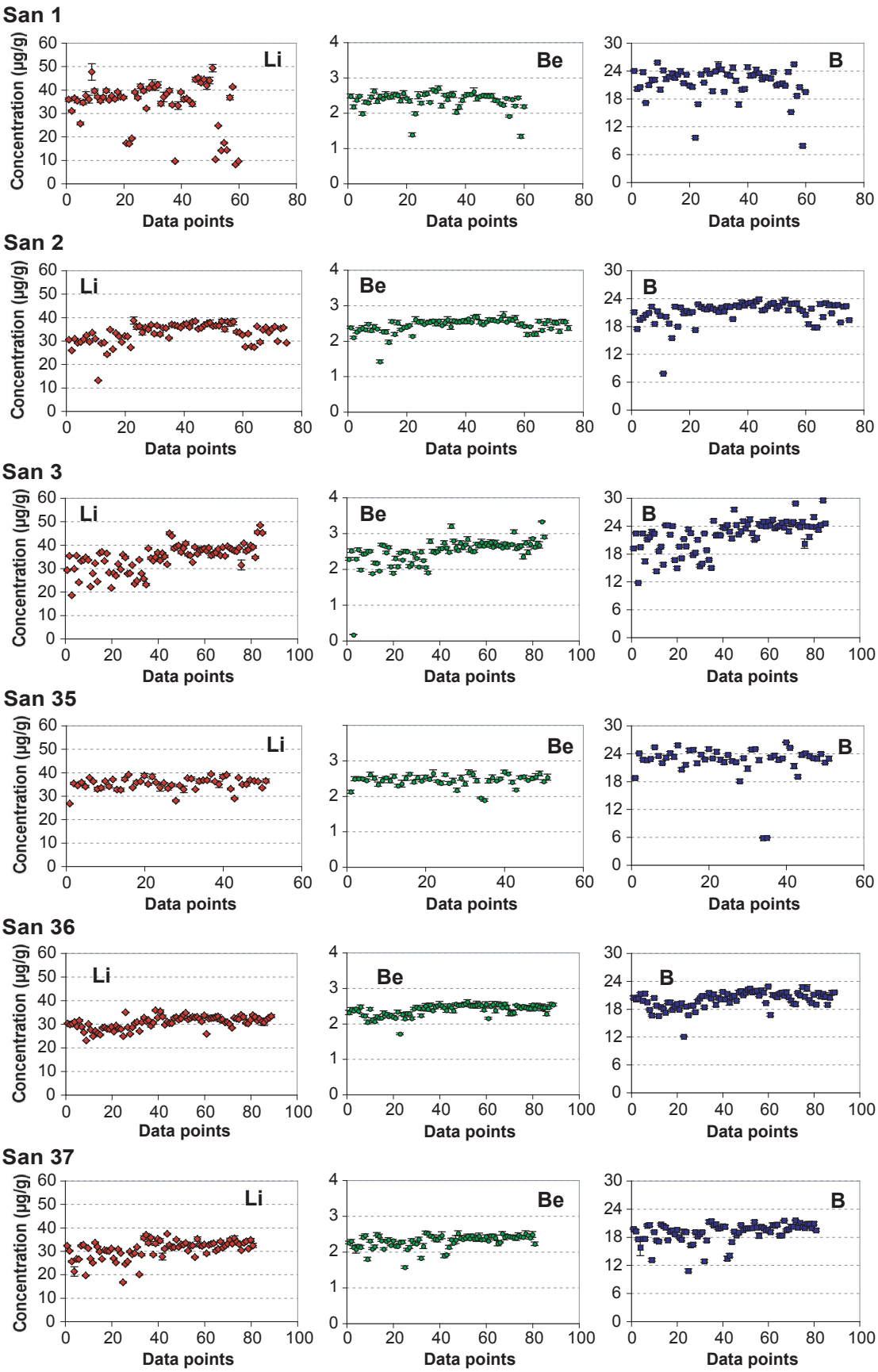

Figure 6-9. Light element analysis results for the matrix of Nea Kameni dacites show common ranges of values. Outliers are due to microlites included in the measurements, the matrix having only minimal glass.

$$K_B^{Cpx/melt} \approx 0.006 - 0.010 \qquad K_B^{Opx/melt} \approx 0.003 - 0.008$$

These values, except for the higher ends of $K_{Li}^{Px/melt}$ and $K_{Be}^{Cpx/melt}$, fall within the experimental results of Brenan et al. (1998), which among pyroxenes and olivine give crystal/melt partition coefficients of 0.1 – 0.2 for Li and 0.002 – 0.03 for Be and B. Partition coefficients derived for one crystal of olivine in this study are also consistent with their values:

$$K_{Li}^{Ol/melt} \approx 0.06 - 0.14$$

$$K_{Be}^{Ol/melt} \approx 0.002$$

$$K_B^{Ol/melt} \approx 0.003 - 0.004$$

Herd et al. (2003), modelling the partitioning of Li and B in martian basalt at 1 atm and temperatures of 1200°C and 1300°C, obtained partition coefficients of K_{Li}= 0.37 and K_B= 0.024 for plagioclase, K_{Li}= 0.20 and K_B= 0.023 for pyroxene, and K_{Li}= 0.27 and K_B= 0.007 for olivine.

6.1.3 Li, Be and B concentrations in relation to An content

Li concentrations in the plagioclase phenocrysts do not show unequivocal relationship with An content, as consistent with experiments showing only a weak dependence of Li on plagioclase composition (e.g. Bindeman et al., 1998). Although a slight decrease with increasing An content may be observed for most of the plagioclase crystals (Fig. 6-10), type-O2 crystals only show an unsystematic response to An content. These are the crystals having Li concentrations that dramatically decrease from core to rim. In such case, Li abundance in the phenocrysts may have significantly been affected by the degassing of the magma and the loss of Li from the melt during crystallisation. The pattern for Be is much more evident, and consistent for all types of plagioclase. Such inverse relationship between Be and An content has been established for compositions > An_{30} (Evensen & London, 2002). B also shows a clear inverse relationship with anorthite in type-C crystals.

Figure 6-10 further facilitates the estimation of plagioclase rim/melt partition coefficients. Most rim compositions are $An_{\sim 40}$, as one would expect in an evolving melt. Using Li, Be and B concentration values at this plagioclase composition in the graphs, estimates would understandably be consistent with partition coefficients calculated using individual rim values, while providing a more general basis and the confidence of more data points for a certain range.

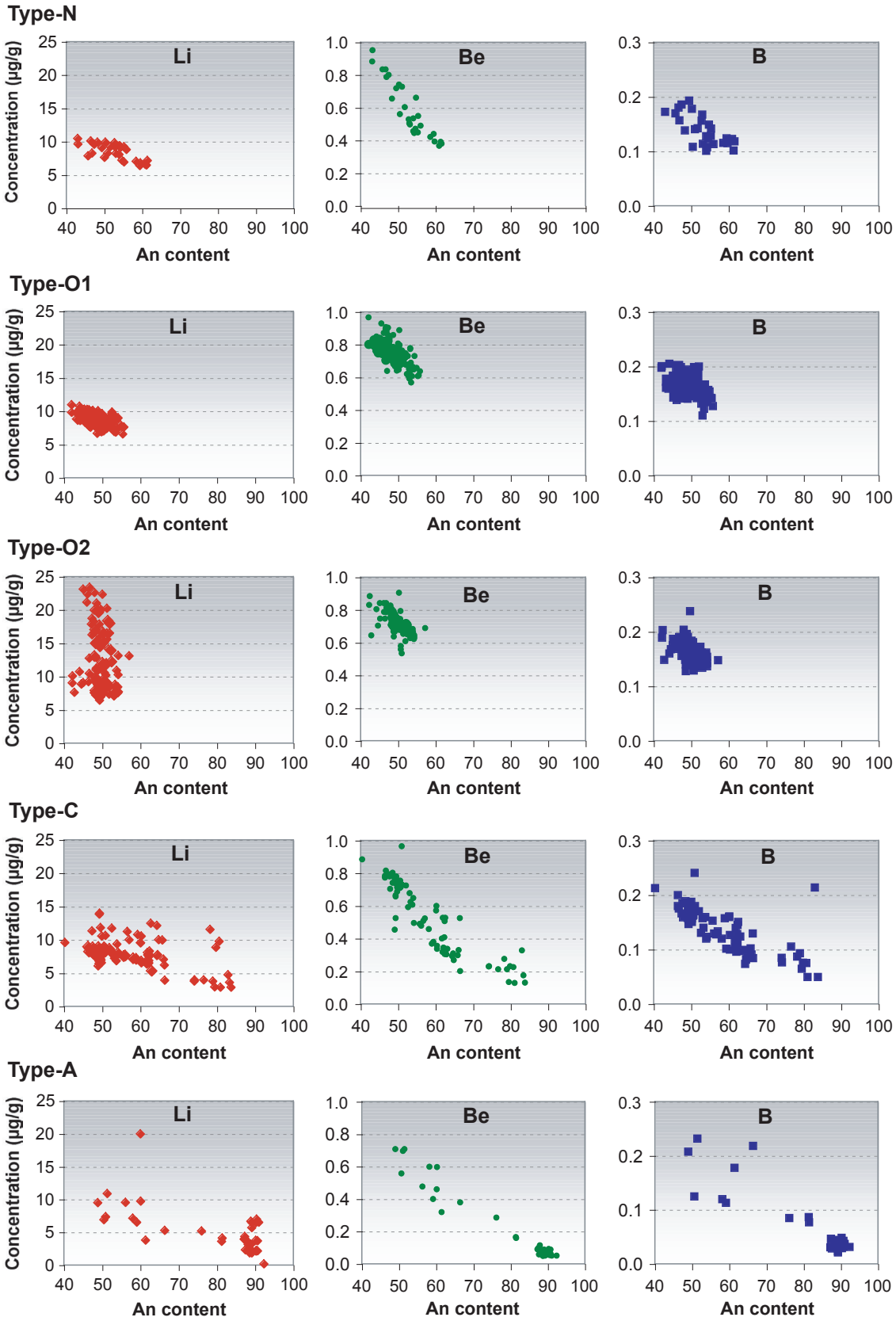

Figure 6-10. Plots of Li, Be and B concentrations against An content of the different plagioclase types show a clear inverse relationship for Be. B appears to have the same trend. Li seems to be slightly dependent on An, except in type-O2 crystals. Outliers are from measurements that included matrix material.

6.1.4 The δ^7Li Enigma

Phenocrysts and portions of the matrix in *San 36* and *San 37* were analysed for δ^7Li, the results for the phenocrysts already discussed in previous sections on phenocryst compositions and temporal relations. δ^7Li values in plagioclase phenocrysts inherent to the dacitic magma, with the lone exception of the type-N *San36b Pl2* (Fig. 6-4), generally increase from the core to the rims, with a lowest value of –24.0 ‰ in the core and a maximum value of +2.8 ‰ at the rim. The xenocrystic *San37a Pl4* also exhibits this pattern, with a minimum value of –30.2 ‰ in the core and a maximum of +9.0 ‰ at the rim. For these phenocrysts, the δ^7Li profile is explained to be a product of the degassing of magma during crystal growth, where kinetic fractionation allows the faster release of the lighter Li isotope from the magma.

Pyroxene phenocrysts show varying δ^7Li trends, possibly due to formation in different timespans, but an explanation is difficult to establish due to the limited number of crystals that were analysed for isotopic composition. Values are within the range of –22.5 ‰ to +1.4 ‰, well within the range of values for plagioclase.

A crucial, and rather puzzling, aspect of the data is the predominance of negative values for δ^7Li. A few points at the rim of plagioclase and one pyroxene crystal are only slightly positive, and although *San36b Pl2* does not show the rim-ward increase in δ^7Li, it also has low values of –5.5 ‰ to –9.6 ‰. Could degassing possibly have been so prevalent in this dacitic system? Considering the δ^7Li values for the matrix may bring insight into this enquiry. In San 36, matrix values are around –4 ‰ to 0 ‰; San 37 yields slightly lower values of –6 ‰ to –2 ‰ (Fig. 6-11). These isotopic compositions strongly suggest degassing, the significant loss of ^{6}Li from the melt during crystallisation and probably until complete solidification of the magma.

What remains of the puzzle, however, is that the subducted slab component contributes to heavy Li isotopic compositions in the magma. Indeed, current published data on subduction-related volcanic products consist mostly of positive δ^7Li values. Whole-rock analyses of arc lavas generally fall within the range of 0 to +12 ‰ (e.g. Tomascak et al., 2000; Tomascak, 2004 and references therein; Bouman et al., 2004). Melt and glass inclusion studies, however, are gaining ground in better pinpointing source materials that may not be recognised in whole-rock analyses. Plagioclase and pyroxene melt inclusions from a Plat Pays (Lesser Antilles) dacitic pumice yield a range of +4 ‰ to +15 ‰ for δ^7Li, attributed mainly to slab components derived from altered oceanic crust (Gurenko et al., 2005).

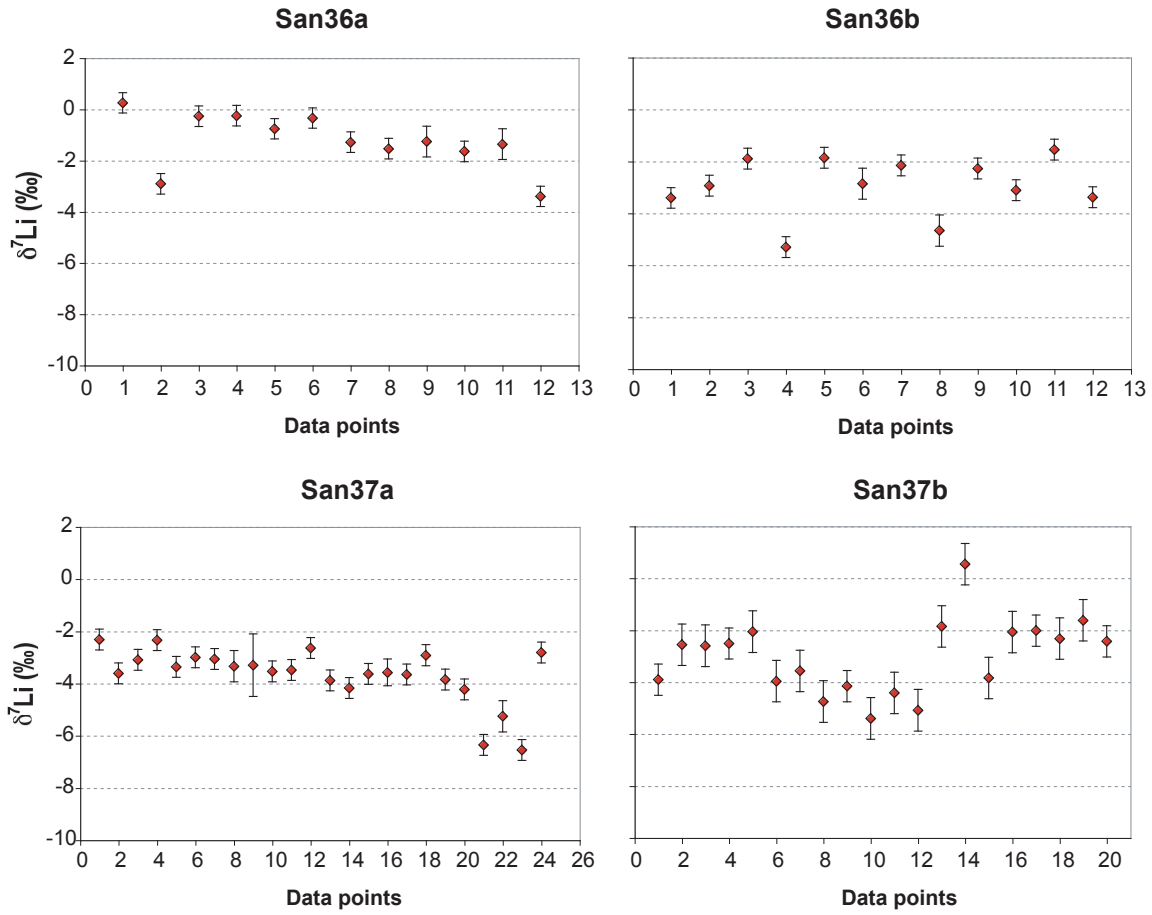

Figure 6-11. δ^7Li values of matrix material in San 36 and San 37, from Nea Kameni, are slightly negative. These are coinsistent with most phenocryst rim values for δ^7Li.

Discrepancies between the Li isotopic compositions of the Izu and northeasten Japan arc lavas are believed to arise from varying extents of Li loss and isotope fractionation, which in turn are caused by different subduction zone physical characteristics, such as thermal structure of the slab and subduction angle (Moriguti et al., 2004). Hence, not only the chemical nature of the subducting slab is of crucial importance in producing Li isotope heterogeneity in the mantle, but also the physical aspects by which it subducts into the mantle wedge. This proves the complexity of the components and processes that influence Li isotopic compositions, but more thorough studies involving particular aspects of lava samples, and not just whole-rock analyses, will definitely further our comprehension of Li fractionation and its implications on magmatic arc genesis.

6.2 Thera Andesites

6.2.1 Plagioclase

Having been collected from different units on Thera island, the different types of plagioclase phenocrysts described for the andesitic compositions do not represent common conditions or processes in a single magma chamber. Hence, the phenocryst types are discussed as isolated populations in distinct magma batches instead of related components within a single magmatic system. Although on a larger scale these units may have related geneses as they are all within the complex volcanic field of Santorini, such deduction is not justified from the scale and detail to which the Thera samples have been gathered and investigated.

Type O

Taken from a bomb within a Peristeria 3 lava flow, *San 26* has plagioclase phenocrysts belonging to type O1. These have major and trace elements within a very narrow range. Slight elevations in Be and B abundances occur in the proximity of cracks or the rims of the crystals, suggesting almost constant concentrations except where the high matrix abundances may have affected the aforementioned portions. The nearly flat profiles hint at a large magma chamber that evolved or fractionated slowly.

The more common type-O2 plagioclase phenocrysts are found in samples San 27, 28, 30 and 32 from the vicinity of Oia. As in the dacites, a general core-to-rim decrease in Li is observed, only this time within a narrower range (Fig. 6-12). The Li concentration profiles also do not show apparent correlation with crystal symmetry and growth, and may have developed through post-crystallisation diffusion. In the case of *San27 Pl2*, the rim concentrations have most probably resulted from diffusion. Notice that at the cut-off end of the crystal, Li concentration is almost the same as at the other end. Hence, as opposed to most type-O2 phenocrysts in the dacites where the coincidence between profiles and crystal symmetry suggest preserved primary concentration values, type-O2 in andesites point to post-crystallisation modification.

Type C

Type C crystals occur in *San 22*, *San 28*, *San 31* and *San 32*. Light elements are generally inversely related to An, although distinct profile discontinuities between the core and rim are hardly observable. *San 28 Pl2* (Fig. 6-13) is one of only two phenocrysts where Li, Be and B

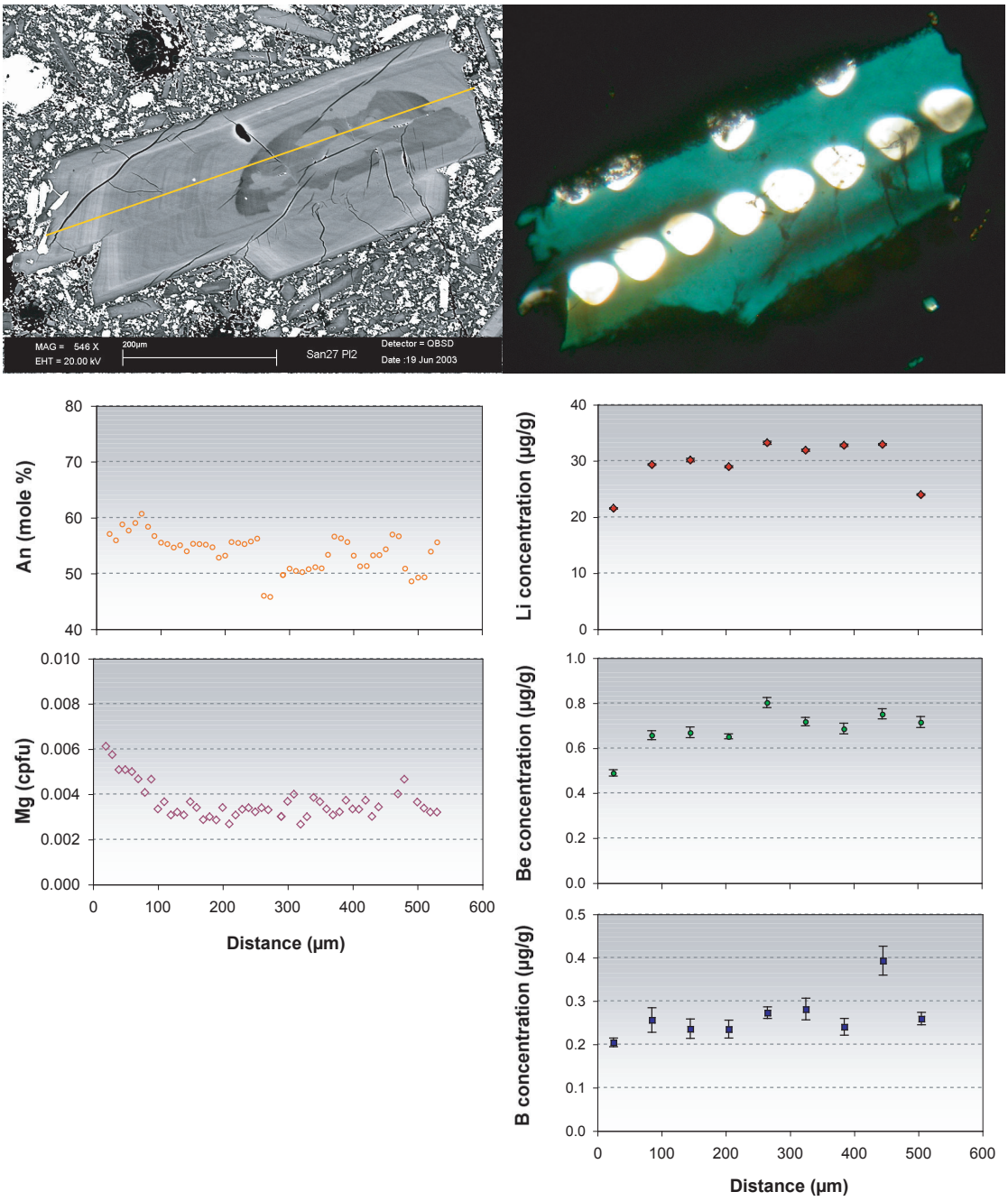

Figure 6-12. *San27 Pl2*, a type-O2 crystal, is cut-off at one end, yet shows an almost symmetrical Li concentration profile where rim values are lower than the rest of the crystal. This similarity at both ends, regardless of the portion of the crystal being represented, implies post-crystallisation diffusion of Li.

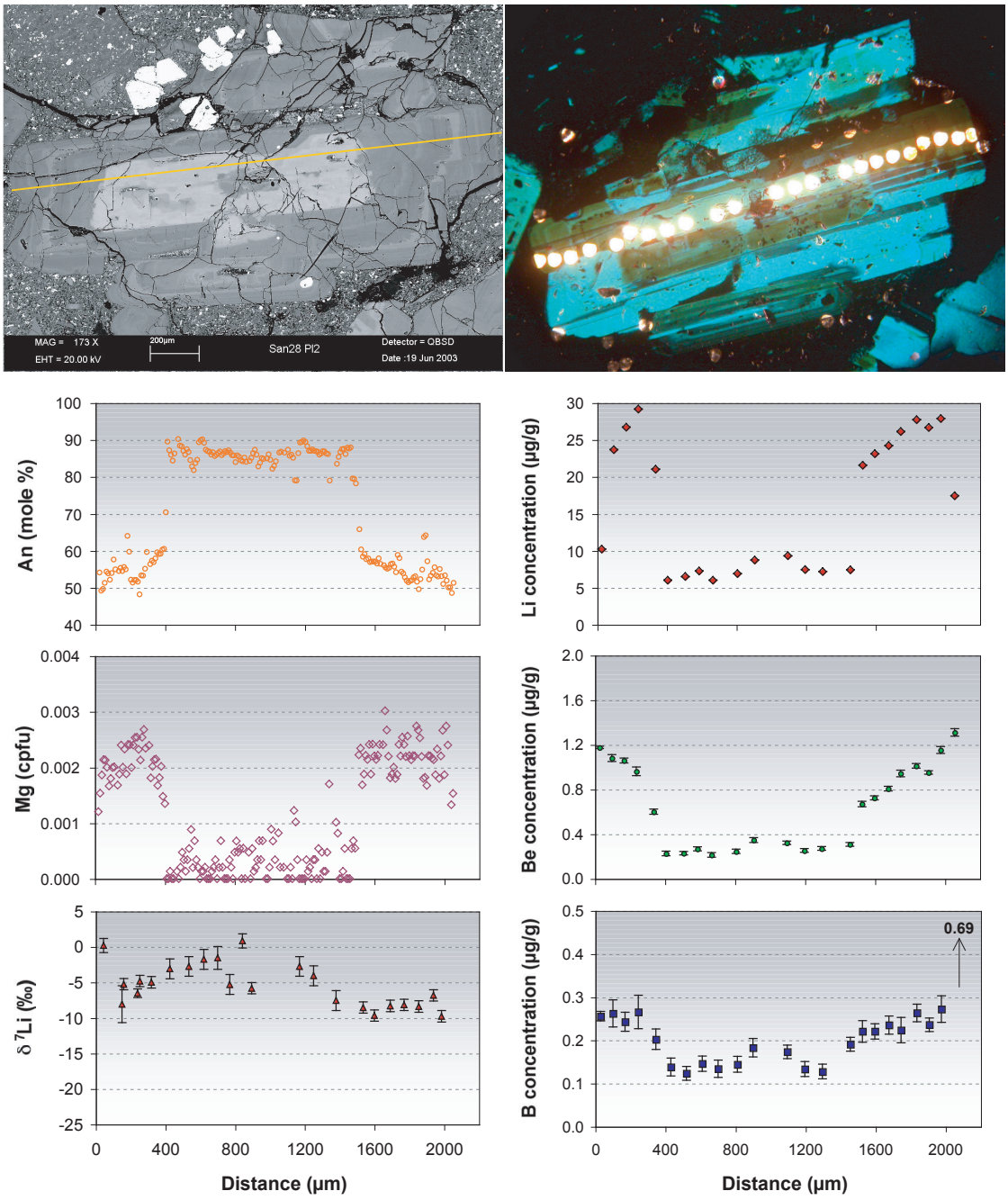

Figure 6-13. S*an28 Pl2* clearly shows the contrast between core and rim concentration values in a type-C phenocryst. Be shows a consistent inverse realtion to An content, as does B. Being known to diffuse slowly, the Be and B profiles reflect primary concenrations. Li also follows this trend, which suggests that despite its propensity to diffuse very rapidly, its original profile has been preserved. The drop in concentration at the rim may have been caused by degassing in the latter stage of crystallisation.

concentrations in the core are readily recognisable from the rim. Be and B patterns present a good mirror image of the An profile, suggesting a primary correlation in the abundances of the major and trace elements, where increasing values towards the rim have not necessarily resulted from the incompatibility of the light elements. Li displays the most pronounced inverse relation to An content, except at the rims where it decreases, again, probably due to degassing during the last stage of crystallisation. This relationship to An and the abrupt boundary between Li concentrations in the core and at the rim clearly contrast the smoothened pattern that should result from the expected rapid diffusion of Li. As discussed regarding the primary nature of the Li profile in a Nea Kameni type-C phenocrysts, such has tremendous implications either on the speed of crystallisation of phenocrysts, or the nature of Li diffusion as we know it. Using currently accepted diffusion coefficients for Li in plagioclase, a further sub-chapter will discuss estimates of magma residence time for this crystal.

Another interesting but puzzling feature of the data from the analyses of this crystal is the Mg profile, which despite the low concentrations, obviously show the expected equilibrium mirror image to An content (Costa et al., 2003). Because Li diffuses faster than Mg, we would then expect the Li profile to have already been equilibrated. But in the light of Li incorporation or diffusion kinetics not being dependent on An content in plagioclase (Giletti & Shanahan, 1997; Bindeman et al., 1998), the pronounced boundary between the core and rim values for Li would suggest non-equilibration.

6.2.2 Pyroxene

Clinopyroxenes and orthopyroxenes of the andesite are largely homogeneous, with major and trace element profiles that are rather flat, except for certain clinopyroxene phenocrysts in samples *San 22* and *San 31* where trends are disrupted by the sector zoning. The light elements either vary unsystematically or have elevated values towards the rims and near cracks. As in most other phases both in the dacites and andesites, Li shows the most variation.

6.2.3 Olivine

Analysis profiles for olivine exhibit consistent patterns. Mg# decreases from core to rim, the variations most conspicuous at the outermost portions of the crystal. The high Mg# throughout most of the olivine phenocryst point to a basaltic composition, and the abrupt drop at the rim suggest incorporation of these crystals into the andesitic melt. Hence, crystallisation in two stages is shown, although the smooth transition displayed by the profiles reflect

diffusion to a minimal extent. The light elements are consistently inversely related to Mg#, with Li displaying abrupt changes in concentration at the rims. The latter however, when considered alongside the high values and errors for Be, may be due to minute inclusions.

6.2.4 Matrix

Matrix compositions for the andesites were also analysed. However, the matrix for these samples are more coarse-grained than those of the dacite, with less glass. The resulting measurements, therefore, are rather inconsistent and are not presented here.

6.3 Estimates of Maximum Residence Time for Plagioclase

The common assumption for the subsurface structure of a volcano includes the existence of a well-defined magma chamber: a storage place underlain by feeders that deliver the molten material and an overlying conduit that serves as an escape path for the magma. Within this chamber the magma resides and nucleates to form early crystals that gradually grow – over many, many years – into phenocrysts. The long-term existence of such magma chambers, however, is difficult to prove, except beneath active volcanoes that repeatedly erupt in relatively short time spans (DePaolo, 1981; Tomiya & Takahashi, 1995; Feeley & Dungan, 1996; Clynne, 1999; Tomiya & Takahashi, 2005).

Equally difficult to prove is the concept of magma in a chamber forming crystals through most of its volume. Recent investigations of nucleation in magma reveals that crystallisation occurs only along solidification fronts (Marsh, 2006 and references therein), such as the walls of the chamber. The inner melt remains devoid of crystals, and even crystals falling from the upper solidification front are reheated and dissolved back into the magma (Marsh, 2002; Marsh, 2006). On the other hand, degassing and decompression during magma ascent significantly accelerate crystallisation (e.g. Metrich & Rutherford, 1998; Couch et al., 2003; Martel & Schmidt, 2003; Blundy & Cashman, 2005). Residence time for crystals or crystal overgrowths that formed in this manner would be very short, consisting mostly of crystal transit time through the conduit onto the earth's surface.

Where intrusion of more mafic magma into a silicic system occurs, a possible trigger for explosive eruption also exists. Amongst the strongest evidence for this are recent work on the kinetics of heterogeneous reactions in magma, which indicate that magma mingling takes place within days to weeks of the eruption (Folch & Marti, 1998; Rutherford et al., 1998, Devine et al., 1998;Venezky & Rutherford, 1999, Snyder, 2000). Seismic observations are consistent and corroborate such a timescale, as in the Pinatubo (Philippines) eruption of 1991 (White, 1996). In the light of such an eruption mechanism, estimates of maximum residence times for plagioclase phenocrysts that show magma mixing could be of great value.

6.3.1 Phenocrysts with high-An cores and low-An rims

Magma residence times may be calculated for complex plagioclase phenocrysts that suggest magma mixing. Abrupt differences in the Li concentrations between the high-An cores and low-An rims are unexpected in the light of rapid Li diffusivities in plagioclase (Giletti & Shanahan, 1997) and the negligible dependence of Li partitioning on An content (Bindeman et al., 1998). The time it takes to modify such compositional disparity through diffusion may be determined by applying the error function to Fick's second law (Fig. 6-14, a and b), thus giving this relationship for *t*, which represents the estimate for residence time:

$$t = \frac{x^2}{4D}$$

where D is the diffusion coefficient. D is calculated through the equation:

$$D = D_o \exp\left\{-\frac{E_a}{RT}\right\}$$

where $D_o = 0.000251$ m^2/s from log $D_o = -3.6$ for Albite (Giletti & Shanahan, 1997);

$E_a = 146{,}000$ J/mol also for Albite (Giletti & Shanahan, 1997);

R = 8.314 J/mol K, the ideal gas constant;

T = 1073 K, 800 °C being a conservative estimate as temperatures of 900-1200°C were established by previous work.

$$D = 0.000251 \exp\left\{-\frac{146000\text{J/mol}}{(8.314\text{J/mol})(1073\text{K})}\right\}$$

$$D = 1.23 \times 10^{-11} \text{ m}^2/\text{s}$$

Thus, for *San36a Pl1*, with a diffusion distance *x*, of ~150 μm, *t* is only about 8 min (Fig.6-15a and Appendix 2-1 for the spreadsheet showing the values used in the calculation, with examples for other temperatures over different lengths). Using D_o and E_a for anorthite would actually yield more conservative estimates (Appendix 2-1), but these were not used because of the larger uncertainties for anorthite in Giletti & Shanahan's (1997) published values for Li.

San2a Pl4 (Fig. 6-15b) is a type-C phenocryst with $An_{\sim 80}$ in the core and the usual $An_{\sim 50}$ at the rim. Mg is inversely related to An, and so are the three light elements (Fig. 5-8 in Chapter 5). The crystal is rather small and only a few points were analysed, but the data are very consistent such that Li, Be and B profiles may be taken as primary. Also, although the Li rim concentration values cannot be concluded as primary, the flat profile in the core is

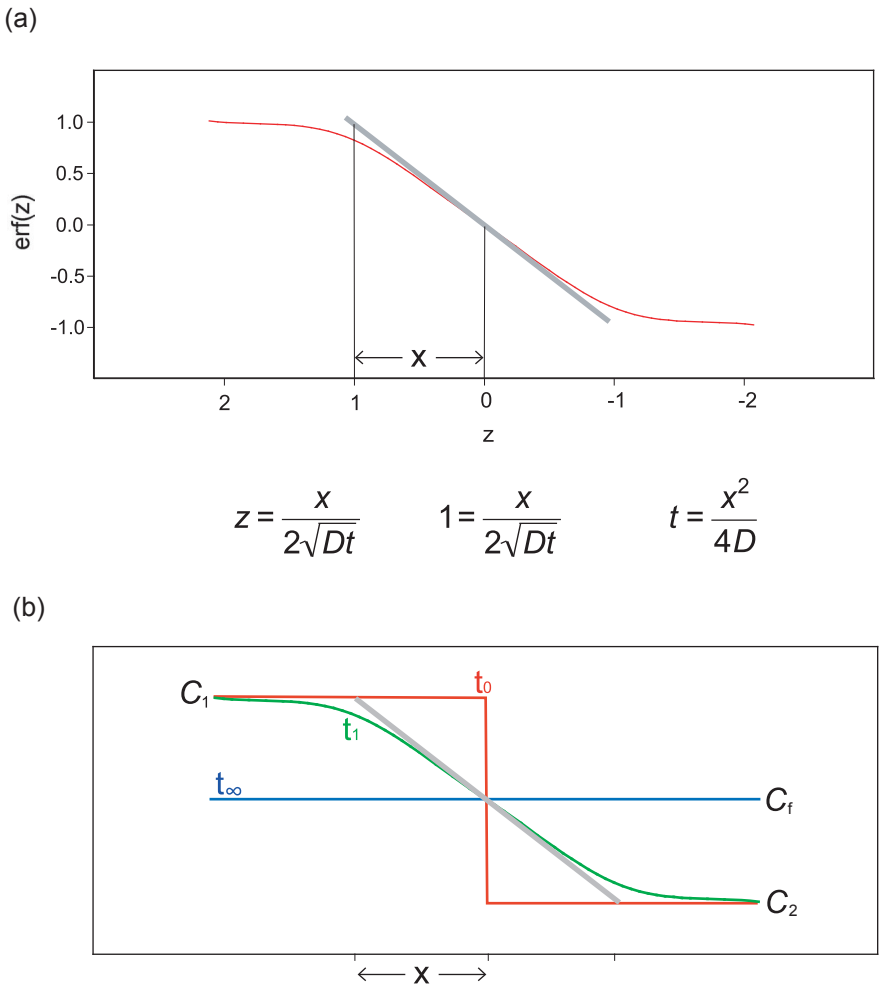

Figure 6-14. (**a**) The error function and Fick's second law may be used to derive time, *t*. The grey line is an approximation of the error function curve from -1 to 1. (**b**) At an initial time t_0, two disparate compositions C_0 and C_1 exist. Diffusion modifies the concentration through t_1 towards a homogenised profile at t_∞.

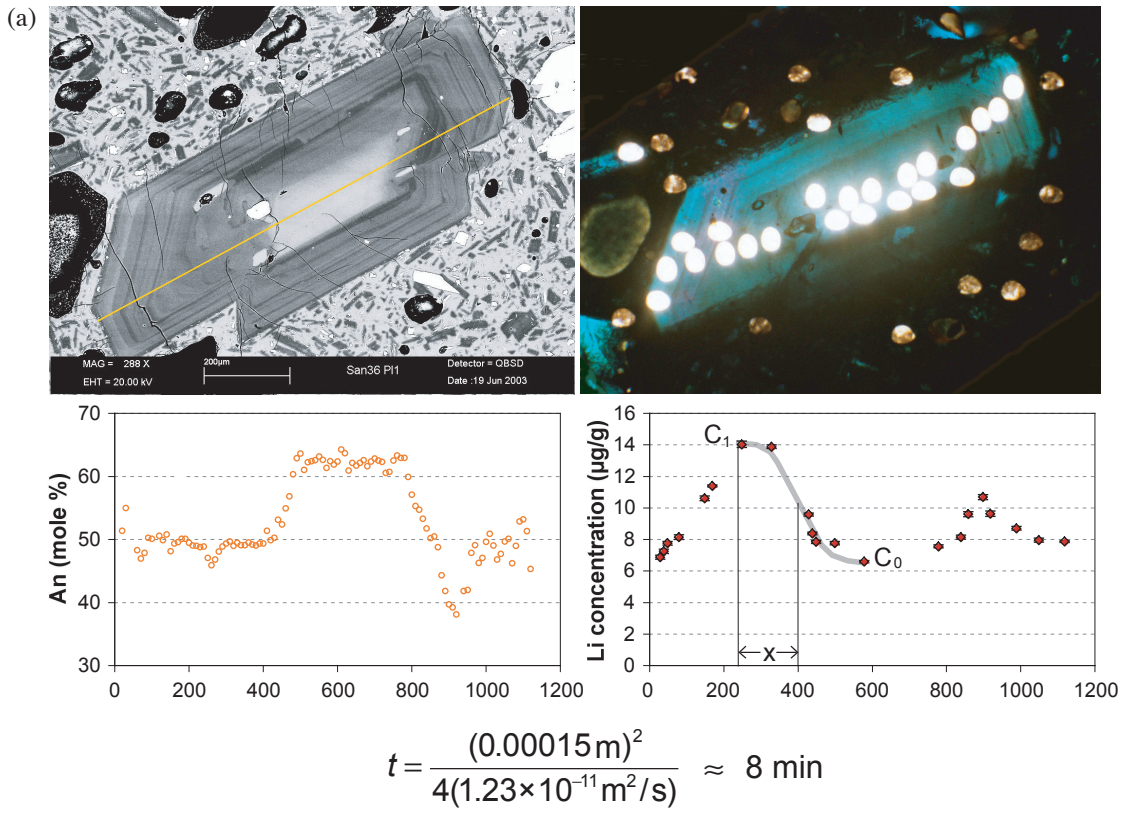

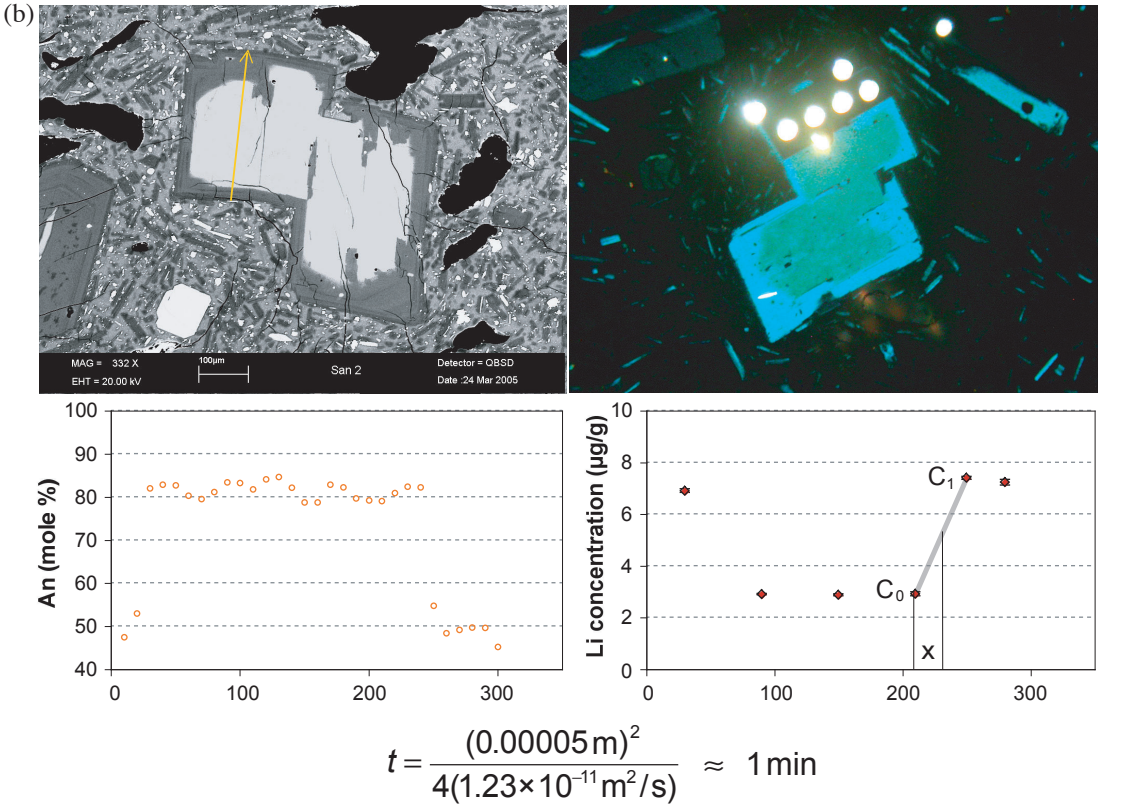

Figure 6-15. Examples of complex (type-C) phenocrysts from Nea Kameni yield maxiumum residence times of 8 minutes for *San36a Pl1* (a) and only 1 minute for *San2a Pl4* (b).

convincing evidence that no modification towards homogenisation has taken place. Had Li started to diffuse in this crystal, concentration values on the outer portions of the core would exhibit an approach to rim concentrations. Residence time, therefore, may be calculated using the horizontal distance between points of disparate values across the core-rim boundary. Notice, however, that this distance is basically controlled by how the analysis points are located. In this case, the optimum locations for analysing the rim, which was too thin to allow much choice, and the part of the core closest to the boundary, were selected so as not to jeopardize the analysis of purely core and purely rim material. The core-rim boundary on the right side is used in the calculation, the shorter distance of ~50 μm representing a closer approach to characterising the boundary. Nevertheless, this short distance yields the maximum residence time, because it is constrained by the coarse spatial resolution of the analysis.

San28 Pl2 (Fig. 6-16a) is a type-C phenocryst from an andesitic agglutinate. It is much like *San2a Pl4*, only much larger. The light elements exhibit an inverse relationship with An, except for the decreasing Li concentration values at the rim, which may be due to degassing. Again, the similarity of the Li concentration pattern with those of Be and B, and the flat profile in the core, suggest that the data reflect primary abundances. *San32 Pl1* (Fig. 6-16b) is another type-C phenocryst, from an Oia andesite flow. The core is resorbed, and rim values are higher at An_{78-68}. The profiles among the light elements are very similar, with consistent concentration levels in the core, especially towards the boundary with the rim. This apparently primary pattern again allows for the calculation of residence time.

6.3.2 Plagioclase with homogeneous An content

San37b Pl1 is a type-O2 phenocryst, 1300 μm-long, with fairly homogeneous major element compositions (Fig. 6-3). Li concentration decreases from 23.4 μg/g in the core to 7.0 μg/g at the rim. The Li concentration pattern has a distinct peak at the core of the crystal, which is asymmetrically located, and therefore suggests its primary nature. Corresponding to this peak is the lowest point on the δ^7Li trough, but this latter profile is smoothened, implying diffusion. Still, the asymmetry of both profiles, coincident with crystal growth zones, reveals that only minimal diffusion has occurred.

(a)

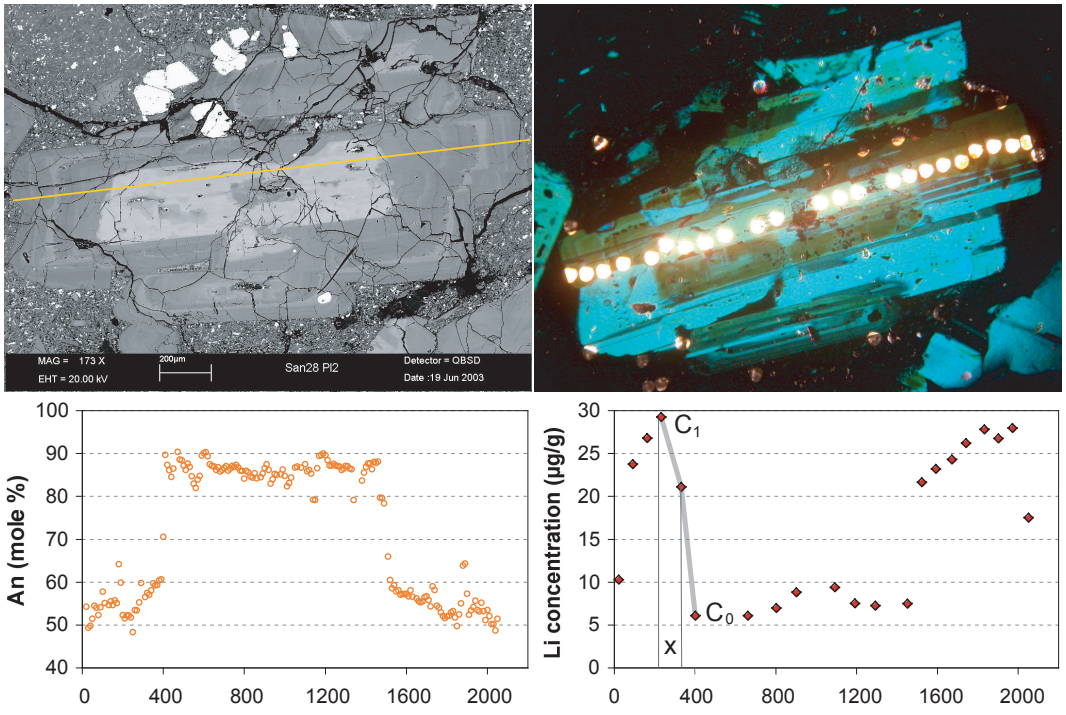

$$t = \frac{(0.0001\,\mathrm{m})^2}{4(1.23\times10^{-11}\,\mathrm{m^2/s})} \approx 3\ \mathrm{min}$$

(b)

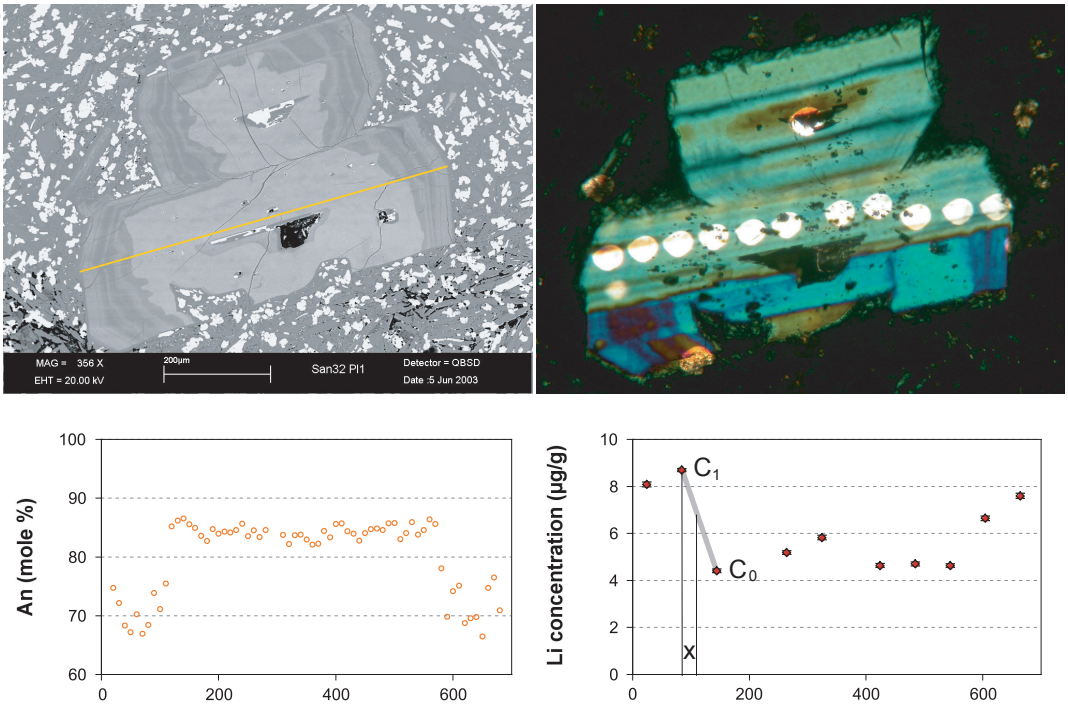

$$t = \frac{(0.00005\,\mathrm{m})^2}{4(1.23\times10^{-11}\,\mathrm{m^2/s})} \approx 1\,\mathrm{min}$$

Fig. 6-16. Type-C phenocrysts from Thera also show abrupt changes in Li composition between the core and rim. S*an28 Pl2* (a) gives approximately 3 minutes and *San32 Pl1* (b), nearly 1 minute of maximum residence time.

The Error Function and Fick's 2nd Law: Layer and Sphere methods

Different methods were used to estimate maximum residence times for *San37b Pl1*. In the first and second methods, Fick's 2nd Law and the error function are used to calculate times of layer and spherical diffusion (Crank, 1994; Ludwig, pers. comm., 2006; details of this approach are in Appendix 2-2). In both cases, the Li concentration profiles are assumed to be initially flat and at a value slightly higher than the observed maximum concentration in the crystal. This initial level of concentration is denoted as C_1. C_0, on the other hand, is assigned an initial value of 0. Given certain intervals of time, curves are generated to show the diffusion between C_0 and C_1. It is necessary to note that in reality movement of Li towards the matrix is more complex, considering the crystal/melt partition coefficient of Li, and the possible uphill diffusion due to the incompatibility of Li in this mineral phase.

Figure 6-17a shows the data set for the isotope analysis run presented separately as ^{6}Li, ^{7}Li and δ^7Li profiles. The peak concentration is made to coincide with x = 0, to aid in comparing the observed profiles with the calculated curves. The crystal is approximately 1200 μm long, shown in the layer and sphere graphs between x = – 600 μm and x = 600 μm. Beyond these boundaries, C_0 is initially 0 as earlier defined, and subsequent changes have nothing to do with the crystal being considered.

Figure 6-17b shows that the green curve, formed after 1.1 hr of diffusion through a layer of infinite area, is the nearest approximation of the ^{6}Li and ^{7}Li concentration profiles. The δ^7Li profile, however, is more similar to what would form after only 0.3 hr of diffusion. Such contradictory fits suggest that the profiles have not been developed by diffusion, but were formed during growth and were mostly preserved aftwards.

Figure 6-17c displays the most realistic approach using Fick's 2nd law and the error function, considering diffusion in three dimensions, although in the case of plagioclase such diffusion would not be isotropic. Again, the green concentration curves exhibit the most similarity to the shape of the ^{6}Li and ^{7}Li concentration profiles, except that concentration values would have to be lower than observed. Also, the deviation of the green δ^7Li curve from the observed δ^7Li profile is much more pronounced. Hence, for the concentrations and δ^7Li trend observed in this particular crystal, one would have to choose the red curves as the best fit, but this would suggest minimal departure from the primary concentrations, occurring only after 0.3 hr. Within the same short span of time, the δ^7Li profile would also be able to maintain its shape.

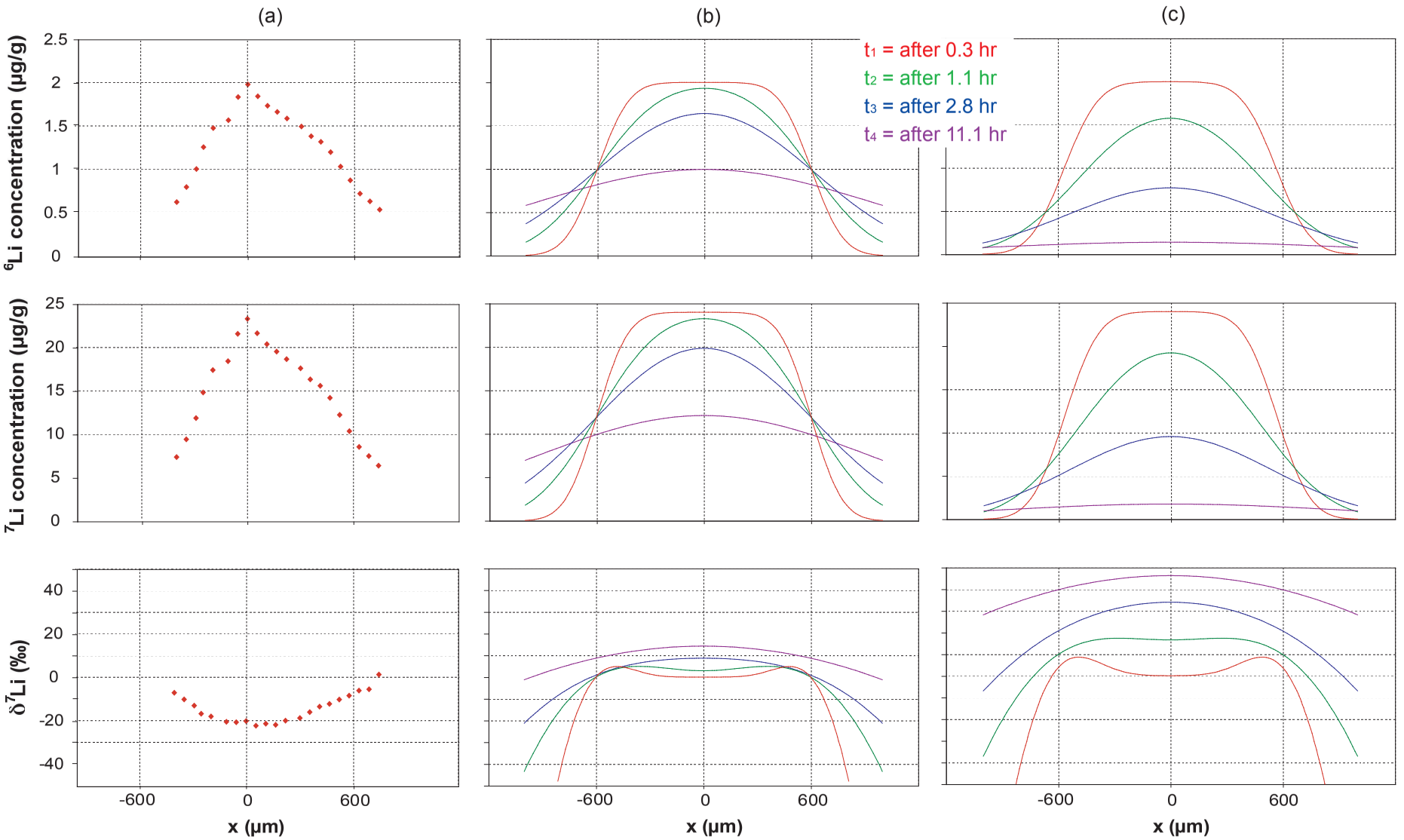

Figure 6-17. The observed Li profiles for San37b Pl1 (a) and the curves generated from the layer (b) and sphere (c) calculations using Fick's second law and the error function.

Simple Diffusion Model

We developed a simple mathematical model to determine how much time it would take to flatten out the Li concentration data for *San37b Pl1* (Fig. 6-18 and Appendix 2-3; pers. comm. with Kahl, Ludwig, Costa, Chakraborty; 2006). As earlier mentioned, this is the most direct approach to answering the question of residence time because it takes the measured Li concentration profile as a starting point, and generates the curve that should result through diffusion after a certain amount of time. The parameters used are the same for the first two approaches, with T = 1073 K and activation energy and diffusion coefficient from Giletti & Shanahan (1997).

Figure 6-18 shows how the profile would progressively deviate from the observed profile (thick grey curve) for successively longer increments of time. The red curve representing an elapsed time of 0.3 hr still fits the observed profile well, but after an hour the change would be very evident, and after 11 hrs the profile would have been flattened.

The astoundingly short residence times estimated from Li data challenge our concept of phenocryst formation. Contrary to the general and established knowledge that crystals form and reside for hundreds of years in the magma chamber, maximum residence times of minutes to hours have been derived for plagioclase phenocrysts in this study. Is it possible that what we know about Li diffusion and its speed within plagioclase crystals, are flawed? But careful experiments have been done concerning this, and even if the diffusion coefficients were off for an order of magnitude, residence time estimates of a few hours to 10 hours, or even 100 hours, are still very short compared to what we have always assumed and believed. Furthermore, experimental results on diffusion are always slower than in nature; as opposed to the gem-quality crystals used in the laboratory, natural crystals have more defect sites that facilitate diffusion.

Perhaps the solution to the great question of how phenocrysts could form so rapidly, in a matter of minutes and hours, may be answered by such driving forces as decompression and degassing. In the same way that changes in H_2O drastically affect the liquidus and solidus temperatures of plagioclase by a few hundred degrees, decompression and degassing probably cause crystallisation of phenocrysts, not slowly and gradually within the magma chamber, but extremely rapidly during ascent and eruption.

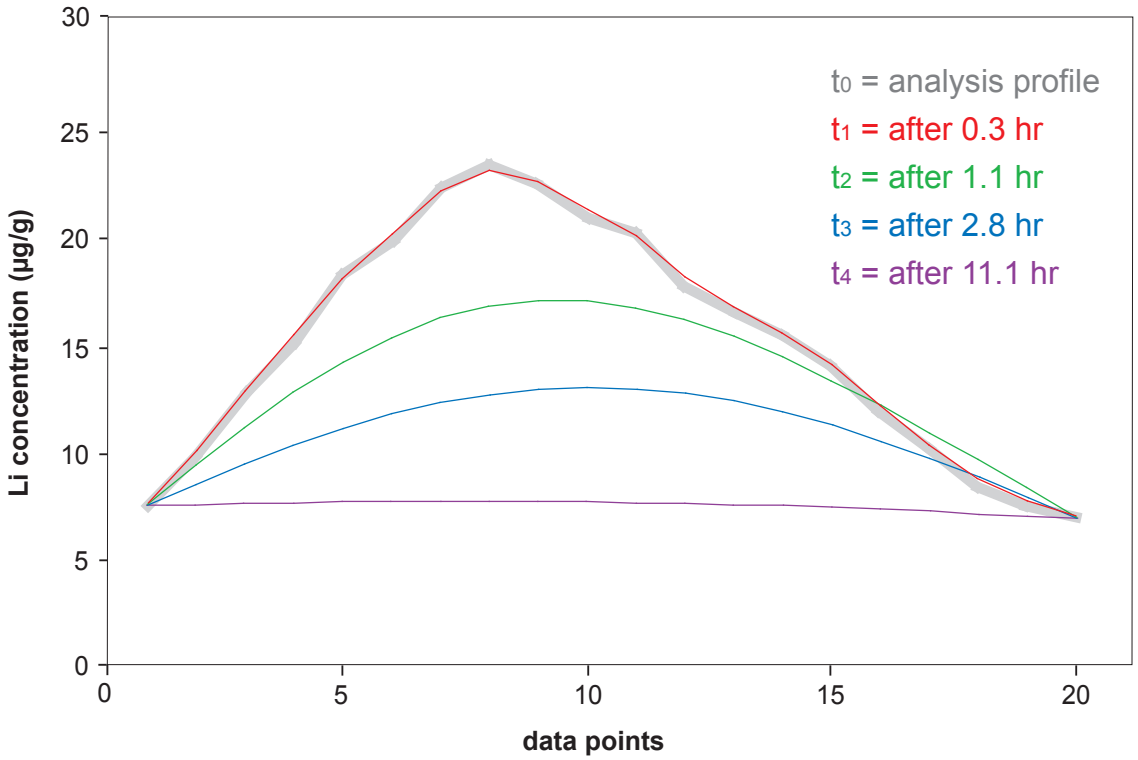

Time incerements (Δt)	Number of repetitions (n)	Total time (t)
10	100	0.28 hr
10	400	1.11 hr
10	1000	2.8 hr
10	4000	11.1 hr

Figure 6-18. The simple diffusion model developed for this study generates curves that show how the observed Li concentration profile (thick grey curve) for *San37b Pl1* would look like when given time to diffuse and homogenise. The time increments used here are the same as those in the previous layer and sphere calculations (Fig. 6-15), also depicted in the same colours.

7. CONCLUSIONS AND OUTLOOK

7. 1 Light elements in phenocrysts record magmatic histories and reveal timescales

The light elements lithium, beryllium and boron have excellent potential as tracers of source components and material recycling along subduction zones. As incompatible trace elements in the entire range of arc magma compositions, these elements provide information about (i) subtle changes of physico-chemical conditions during crystal growth and (ii) processes in the magma chamber and plumbing system of volcanoes. Particularly useful are elemental and isotopic composition profiles in phenocrysts, which yield crystallisation histories in more detail than whole-rock analyses. Subsequently, magma genesis for a particular volcanic system that may also extend to other similar volcanic centres, may be interpreted from the phenocryst archives.

Among the important processes revealed by phenocryst concentration profiles are the mixing and mingling of magmas of different compositions. In the Nea Kameni dacites these are evidenced by xenocrystic plagioclase, pyroxene and olivine phenocrysts, some of which are within mafic enclaves. High-An cores of certain plagioclase crystals also suggest early formation in andesitic to basaltic magma. Some andesitic rocks from Thera likewise have plagioclase and olivine phenocrysts that were apparently inherited from basaltic fractions. Magma mixing is an especially relevant consideration in determining volcanic eruption mechanisms. Mafic injections, in many cases, have been suspected and/or observed to trigger explosive silicic eruptions. The inevitable enquiry would then be the time span between magmatic injection and resulting eruption; thus far, this is believed to take days or weeks.

To further define such time constraints, calculation of magma residence times for certain phenocrysts in the Santorini volcanic rocks suggest very short periods – a matter of minutes to hours. This is a staggering conjecture at the least, and an astonishing discovery at the most, in the light of our current understanding of crystal formation and volcanism. However, upon the foundation of our present knowledge of partitioning and diffusivities, notably of Li in plagioclase, these short time spans are inescapable. It appears that certain phenocrysts in the magma, or at least the overgrowths on inherited cores, have formed at shallow levels during eruption, possibly as a result of degassing and decompression of the magma.

7. 2 Further detailed work using light elements should be pursued

The study of the litholphile elements Li, Be and B in individual crystals and the *in-situ* determination of δ^7Li is still in its infancy. Indeed, this detailed study of phenocrysts from Santorini Volcano is the first attempt of its kind. As expected, there remain problems with the analytical techniques and puzzles from the gathered data. But the challenge to utilise the potential of the tools and methods pioneered in this work remain as well. The existing data may be used to further develop the calculation for residence times and gain insight into late-stage occurrences in the magma, which could eventually provide insights on eruption mechanisms. It would also be worthwhile to figure out how individual crystals could exhibit a wide range of variations in the elemental and isotopic compositions of Li, and why the supposedly positive δ^7Li values for arc lavas determined by wet chemical ICP-MS techniques on whole-rock samples have not emerged from the SIMS study on Santorini samples.

Besides separate analyses on crystals and the matrix, glass inclusions representing former melt should also be investigated as they trap information on specific conditions during the course of crystallisation. Glass inclusions in plagioclase, for example, are crucial in determining the pressures and temperatures at which partial crystallisation of the magma took place, thereby unravelling magmatic pathways and evolution. Systematics of the light elements also need to be understood in more detail. Is Li entirely independent of the An content in plagioclase? Does An content control B abundances? Can we better establish the partitioning of these elements between different mineral phases and the melt or the fluid? What factors control isotopic fractionation and to which extents?

Addressing this gamut of an enquiry, on the other hand, requires procedures that would produce reliable data. As of yet, the analysis of light elements and their isotopes is a frontier being chartered with new techniques, instrumental modifications and even sample standards. These methodological enhancements too, will have to accompany the search for geochemical answers, if our knowledge of the nuances of magmatic systems and the overlying erupting volcanoes were to evolve.

8. REFERENCES

Altherr R, Schliestedt M, Okrusch M, Seidel E, Kreuzer H, Harre W, Lenz H, Wendt I, Wagner GA (1979), *Geochronology of high-pressure rocks on Sifnos (Cyclades, Greece).* Contrib, Mineral, Petrol, 70: 245-255.

Altherr R, Kreuzer H, Wendt I, Lenz H, Wagner GA, Keller J, Harre W, Höhndorf A (1982) *A late Oligocene/early Miocene high temperature belt in the Attic-Cycladic crystalline complex (SE Pelagonian, Greece).* Geol Jahrbuch E23: 97-164.

Altherr R, Kreuzer H, Lenz H, Wendt I, Harre W, Dürr S (1994) *Further evidence for a late Cretaceous low-pressure/high-temperature terrane in the Cyclades, Greece*. Chemie der Erde 54: 319-328.

Altherr R, Siebel W (2002) *I-type plutonism in a continental back-arc setting: Miocene granitoids and monzonites from the central Aegean Sea, Greece.* Contrib. Mineral. Petrol. 143: 397-415.

Angelier J, Lyberis N, Le Pichon X, Barrier E, Huchon P (1982) *The tectonic development of the Hellenic arc and the sea of Crete: a synthesis* . Tectonophysics 86: 159-196.

Arculus RJ (1994) *Aspects of magma genesis in arcs*. Lithos 33: 189-208.

Bacon CR (1986) *Magmatic inclusions in silicic and intermediate rocks*. Journal of Geophysical Research 91B: 6091-6112.

Bard E, Hamelin B, Fairbanks R, Zindler A (1990) *Calibration of the ^{14}C Timescales over the last 30 000 years using mass spectrometric U-Th ages from Barbados corals*. Nature 345: 405-410.

Barrat JA, Chaussidon M, Bohn M, Gillet Ph, Göpel C, Lesourd M (2005) *Lithium behavior during cooling of a dry basalt: An ion-microprobe study of the lunar meteorite Northwest Africa 479 (NWA 479)*. Geochimica et Cosmochimica Acta Vol. 69, No. 23, 5597-5609.

Barton M, Huijsmans JPP (1986) *Post-caldera dacites from the Santorini volcanic complex, Aegean Sea, Greece: an example of the eruption of lavas of near-constant composition over a 2,200 year period*. Contrib. Mineral. Petrol. 94: 472-495.

Beck P, Barrat JA, Chaussidon M, Gillet Ph, Bohn M (2004) *Li isotopic variations in single pyroxenes from the Northwest Africa 480 shergottite (NWA 480): a record of degassing of Martian magmas?* Geochimica et Cosmochimica Acta 68: 2925-2933.

Berlo K, Blundy J, Turner S, Cashman K, Hawkesworth C, Black S (2004) *Geochemical Precursors to Volcanic Activity at Mount St. Helens, USA*. Science Vol. 306, pp. 1167-1169.

Bindeman IN, Davis AM, Drake MJ (1998) *Ion microprobe study of plagioclase-basalt partititon experiments at natural concentration levels of trace elements*. Geochimica et Cosmochimica Acta 62: 1175-1193.

Bindeman IN, Davis AM (1999) *Convection and Redistribution of Alkalis and Trace Elements during the Mingling of Basaltic and Rhyolite Melts*. Petrology Vol.7, No. 1, pp. 99-110.

Bindeman IN, Davis AM (2000) *Trace element partitioning between plagioclase and melt: Investigation of dopant influence on partition behavior*. Geochimica et Cosmochimica Acta Vol.64, No. 16, pp. 2863-2878.

Blake MC, Bonneau M, Geyssant J, Kienast JR, Lepvrier C, Maluski H, Papanikolaou D (1981) *A geologic reconnaissance of the Cycladic blueschist belt, Greece*. Geological Soceity of American Bulletin 92: 247-254.

Blake S (1981) *Volcanism and the dynamics of open magma chambers*. Nature 289: 783-785.

Blundy JD, Shimizu N (1991) *Trace element evidence for plagioclase recycling in calc-alkaline magmas*. Earth Planetary Science Letters 102: 178-197.

Blundy JD, Wood BJ (1991) *Crystal-chemical controls on the partitioning of Sr and Ba between plagioclase feldspar, silicate melts, and hydrothermal solutions*. Geochimica et Cosmochimica Acta 55: 193-209.

Blundy JD, Wood BJ (1994) *Prediction of crystal-melt partition coefficients from elastic moduli*. Nature 372: 452-454.

Blundy J, Cashman K (2001) *Ascent-driven crystallisation of dacite magmas at Mount St. Helens, 1980-1986*. Contrib. Mineral. Petrol. 140: 631-650.

Blundy J, Cashman K (2005) *Rapid decompression-driven crystallization recorded by melt inclusions from Mount St. Helens volcano*. Geology Vol. 33, No. 10, pp. 793-796.

Bond A, Sparks RSJ 1976 *The Minoan eruption of Santorini, Greece*. Journal of the Geological Society of London, 132: 1-16.

Bouman C, Elliott T, Vroon PZ (2004*) Lithium inputs to subduction zones*. Chemical Geology 212: 59-79.

Bower SM, Woods A (1997) *Control of magma volatile content and chamber depth on the mass erupted during explosive volcanic eruptions*. Journal of Geophysical Research 102: 10273-10290.

Brenan JM, Neroda E, Lundstrom CC, Shaw HF, Ryerson FJ, Phinney DL (1998) *Behaviour of boron, beryllium, and lithium during melting and crystallization: Constraints from mineral-melt partitioning experiments*. Geochimica et Cosmochimica Acta 62: 2129-2141.

Brenan JM, Ryerson FJ, Shaw HF (1998) *The role of aqueous fluids in the slab-to-mantle transfer of boron, beryllium, and lithium during subduction: Experiments and models*. Geochimica et Cosmochimica Acta 62: 3337-3347.

Bröcker M, Enders M (1999) *U-Pb zircon geochronology and unusual eclogite-facies rocks from Syros and Tinos (Cyclades, Greece)*. Geol Mag 136: 111-118.

Bröcker M, Kreuzer H, Matthews A, Okrusch M (1993) *$^{40}Ar/^{39}Ar$ and oxygen isotope studies of polymetamorphism from Tinos island, Cycladic blueschist belt, Greece*. Journal of Metamorphic Geology 11: 223-240.

Brooker RA, James RH, Blundy JD (2004) *Trace elements and Li isotope systematics in Zabargad peridotites: evidence of ancient subduction processes in the Red Sea mantle*. Chemical Geology 212: 179-204.

Chan L-H, Edmond JM (1988) *Variation of lithium isotope composition in the marine environment: A preliminary report*. Geochimica et Cosmochimica Acta 52: 1711-1717.

Chan LH, Edmond JM, Thompson G & Gillis, K. (1992). *Lithium isotopic composition of submarine basalts: implications for the lithium cycle in the oceans*. Earth and Planetary Science Letters 108, 151-160.

Chan L-H, Gieskes JM, You C-F, Edmond JM (1994) *Lithium isotope geochemistry of sediments and hydrothermal fluids of the Guaymas Basin, Gulf of California*. Geochimica et Cosmochimica Acta 58: 4443-4454.

Chan LH, Leeman WP & You CF (1999) *Lithium isotopic composition of Central America volcanic arc lavas: implications for modification of subarc mantle by slab-derived fluids*. Chemical Geology 160, 255-280.

Chan LH, Leeman WP, You C-F (2002) *Lithium isotopic composition of Central American volcanic Arc lavas: implications for modification of subarc mantle by slab-derived fluids: correction*. Chemical Geology 182: 293-300.

Chaussidon M, Libourel G (1993) *Boron partitioning in the upper mantle: An experimental and ion probe study*. Geochimica et Cosmochimica Acta 57: 5053-5062.

Christensen JN , DePaolo DJ (1993) *Timescales of large volume silicic magma systems: Sr isotopic systematics of phenocrysts and glass from the Bishop Tuff, Long Valley, California*. Contrib. Mineral. Petrol. 113: 100-114.

Coogan LA, Kasemann S, Chakraborty S (2005) *Rates of hydrothermal cooling of new oceanic upper crust derived from lithium-geospeedometry*. Earth and Planetary Science Letters 420: 415-424.

Costa F, Chakraborty S, Dohmen R (2003) *Diffusion coupling between trace and major element and a model for calculation of magma residence times using plagioclase*. Geochimica et Cosmochimica Acta Vol. 67, No. 12, 2189-2200.

Costa F, Chakraborty S (2004) *Decadal time gaps between mafic intrusion and silicic eruption obtained from chemical zoning patterns in olivine*. Earth and Planetary Science Letters 227: 517-530.

Cottrell E, Gardner JE, Rutherford MJ (1999) *Petrologic and experimental evidence for the movement and heating of the pre-eruptive Minoan rhydacite (Santorini, Greece)*. Contrib Mineral Petrol 135: 315-331.

Couch S, Sparks RSJ & Carroll MR (2001) *Mineral disequilibrium in lavas explained by convective self-mixing in open magma chambers*. Nature, Vol. 411, pp. 1037-1039.

Couch S, Harford CL, Sparks RSJ, Caroll MR (2003) *Experimental constraints on the conditions of formation of highly calcic plagioclase microlites at the Soufrière Hills volcano, Montserrat*. Journal of Petrology 44: 1455-1475.

Crank J (1994) *The Mathematics of Diffusion, 2nd Edition*. Oxford Univ. Press, London, 414 pp.

Deer WA, Howie RA, Zussman J (1963) *Rock-Forming Minerals, Vol.4*. Longmans, Green and Co. Ltd., London, 435 pp.

DePaolo DJ (1981) *Trace element and isotoic effects of combined wallrock assimilation and fractional crystallization*. Earth and Planetary Science Letters 53: 189-202.

Devine JD, Murphy MD, Rutherford MJ, Barclay J, Sparks RSJ, Carroll MR, Young SR, Gardner JE (1998) *Petrologic evidence for pre-eruptive pressure-temperature conditions, and recent reheating, of andesitic magma erupting at the Soufriere Hills volcano, Monserrat, W.I.*. Geophysical Research Letters 25: 3669-3672.

Dominey-Howes D, Minos-Minopoulos D 2004, *Perceptions of hazard and risk on Santorini*. Journal of Volcanology and Geothermal Research 137: 285-310.

Drake MJ (1972) *The distribution of major and trace elements between plagioclase feldspar and magmatic silicate liquid: an experimental study*. Ph.D. dissertation, University of Oregon. (D1).

Drake MJ, Weill DF (1972) *New rare earth elements standards for electron microprobe analysis*. Chemical Geology 10: 179-181.

Drake MJ, Weill DF (1975) *Partition of Sr, BA* Eu^{2+} *, Eu3+, and other REE between plagioclase feldspar and magmatic liquid: an experiment study*. Geochimica et Cosmochimica Acta 39: 689-712.

Druitt TH & Francaviglia V (1992) *Caldera formation on Santorini and the physiography of the islands in the late Bronze Age*. Bulletin of Volcanology, 54: 484-493.

Druitt TH, Edwards L, Lanphere M, Sparks RSJ, Davies M (1998*) Volcanic development of Santorini revealed by field, radiometric, chemical and isotopic studies*. The European Laboratory Volcanoes. In: Casale R et al. (eds) Proceedings of the Second Workshop, Santorini, Greece, 2 to 4 May 1996, pp 37-48, European Commission.

Druitt TH, Edwards L, Mellors RM, Pyle DM, Sparks RSJ, Lanphere M, Davies M, Barreirio B (1999) *Santorini Volcano*. 165 pp. Geological Soceity, London, Memoirs 19.

Dürr S (1986) *Das Attisch-Kykladische Kristallin*. In: Jacobshagen V (ed) Geologie von Griechenland, Bornträger, Berlin, pp. 116-148

Dürr S, Altherr R, Keller J, Okrusch M & Seidel E 1978, *The median Aegean crystalline belt: stratigraphy, structure, methamorphism, magmatism, Alps, Appennines, Hellenides. Stuttgart*. In: Closs H, Roeder D & Schmidt K (eds) Inter-union Commission on Geodynamics Scientific Report 38: 537-564.

Elliot T, Jeffcoate A, Bouman C (2004) *The terrestial Li isotope cycle : light-weight constraints on mantle convection*. Earth and Planetary Science Letters 220: 231-245.

Elliot T, Thomas AL, Jeffcoate AB, Niu Y (2002) *Li isotope variation in the upper mantle*. Geochimica et Cosmochimica Acta 66, Abstr.

Evensen JM, London D (2002) *Experimental silicate mineral/melt partition coefficients for beryllium and the crustal Be cycle from migmatite to pegmatite*. Geochimica et Cosmochimica Acta 66: No.12, pp. 2239-2265.

Folch A, Marti J (1998) *The generation of overpressure in felsic magma chambers by replenishment*. Earth and Planetary Science Lettets 163: 301-314.

Francalanci L, Vougioukalakis G, Eleftheriades G, Pinarelli L, Petrone C, Manetti P, Christofides G (1998) *Petrographic chemical and isotopic variations in the intra-caldera post-Minoan rocks of the Santorini volcanic field, Greece*. In: Casale R et al. (eds) Proceedings of the second workshop, Santorini, Greece, 2 to 4 May 1996. European Commission, 175- 186.

Friedrich WL (2000) *Fire in the Sea: Volcanism and the Natural History of Santorini*. Cambridge University Press, 258 pp.

Friedrich WL, Wagner P & Tauber H (1990) *Radiocarbon dated plant remains from the Acrotiri excavation on Santorini, Greece*. In: Hardy DA (ed.) Thera and the Aegean Worls III, 3. The Thera Foundation, London. 188-196.

Fytikas M, Kolios N & Vougioukalakis G (1990a) *Post-Minoan volcanic activity of the Santorini volcano. Volcanic hazard and risk, forecasting possibilities*. In: Hardy DA (ed) Thera and the Aegean World III, 2. The Thera Foundation, London, 183-198.

Fytikas M, Karydakis G, Kavouridis TH, Kolios N & Vougioukalakis G (1990b) *Geothermal research on Santorini*. In: Hardy DA (ed) Thera and the Aegean World III, 2. The Thera Foundation, London 241-249.

Gaetani GA, Grove TL, Bryan WB (1993) *The influence of water on the petrogenesis of subduction-related rocks*. Nature 365: 332-334.

Giletti BJ, Shanahan TM (1997*) Alkali diffusion in plagioclase feldspar*. Chemical Geolology 139: 3-20.

Ginibre C, Wörner G, Kronz A (2002) *Minor-and trace-element zoning in plagioclase: Implications for magma chamber processes at parinacota volcano, northern Chile*. Contrib. Mineral. Petrol. 143: 300-315.

Grove TL & Kinzler RJ (1986) *Petrogenesis of andersites.* Annual Review of Earth Planetary Science 14: 417-454.

Grove TL, Baker MB, Kinzinger RJ (1984) *Coupled CaAl-NaSi diffusion in plagioclase feldspar: Experiments and applications to cooling rate speedometry*. Geochimica et Cosmochimica Acta 48: 2113-2121.

Gurenko AA, Trumbull RB, Thomas R, Lindsay JM (2005) *A Melt Inclusion Record of Volatiles, Trace Elements and Li-B Isotopes Variations in a Single Magma System from the Plat Pays Volcanic Complex, Dominica, Lesser Antilles*. Journal Of Petrology Vol.46 , No. 12 pp. 2495-2526.

Hammer JE, Rutherford MJ (2002*) An experimental study of the kinetics of decompression-induced crystallization in silicic melt.* Jornal Of Geophysical Research, Vol. 107, No. B1, 2021 pp. 8.1- 8.23.

Hattori K & Sato H (1996) *Magma evolution recorded in plagioclase zoning in 1991 Pinatubo eruption products.* American Mineralogist Vol. 81, pp. 982-994.

Hawkesworth C, George R, Turner S, Zellmer G (2004) *Time scales of magmatic processes.* Earth and Planetary Science Letters 218: 1-16.

Heiken G, McCoy F Jr. (1984) *Caldera development during the Minoan eruption, Thira, Cyclades, Greece.* Journal of Geophysical Research 89: 8441-8462.

Herd CDK, Treiman AH, Mckay GA, Shearer CK (2004) *The behavior of Li and B during planetary basalt crystallization.* American Mineralogist 89: 832-840.

Herd CDK, Treiman AH, Mckay GA, Shearer CK (2005) *Light lithophile elements in martian basalts: Evaluating the evidence for magmatic water degassing.* Geochimica et Cosmochimica Acta Vol. 69, No. 9, pp. 2431-2440.

Hervig RL, Moore G (2003) *Fractionation of boron (and lithium) between hydrous fluid and silicate melt: diffusion, contamination, and orphaned experiments.* EOS Trans AGU 84, Fall Meet. Suppl., Abstr.

Hervig RL, Moore GM, Williams LB, Peacock SM, Holloway JR, Roggensack K (2002) *Isotopic and elemental partitioning of boron between hydrous fluid and silicate melt.* American Mineralogist 87: 769-774.

Hess KU, Dingwell DB (1996) *Viscosities of hydrous leucogranitic melts: A non-Arrhenian model.* American Mineralogist 81: 1297-1300.

Higgins M D (1996) *Magma dynamics beneath Kameni volcano, Thera, Greece, as revealed by crystal size and shape measurements.* Journal of Volcanology and Geothermal Research 70: 37-48.

Holness MB, Martin VM, Pyle DM (2005*) Information about open-system magma chambers derived from textures in magmatic enclaves: the Kameni Islands, Santorini, Greece.* Geological Magazine 142 (6), pp. 637 -649.

Holzheid A, Palme H, Chakraborty S (1997) *The activities of NiO,CoO and FeO in silicate melts.* Chemical Geoogy 139: 21-38.

Huijsmans JPP (1985*) Calcalkaline lavas from the volcanic complex of Santorini, Aegean Sea, Greece.* Geologica Ultraiectina 41: 1- 316.

Huijsmans JPP, Barton M (1983a) *Petrographic and geochemical evidence for the role of magma mixing and fractional crystallization in zone magma chambers on Santorini, Cyclades, Greece.* IAVCEI, XVIII General Assembly, Hamburg, Programs and Abstracts: 67.

Huijsmans JPP, Barton M (1983b) *Constant composition of post-caldera lavas from Santorini, Cyclades, Greece.* EOS Trans Am Geophys Union 64: 336-337.

Huijsmans JPP, Barton M, Salters VJM (1988) *Geochemistry and evolution of the calc-alkaline volcanic complex of Santorini, Aegean Sea, Greece*. Journal of Volcanology and Geothermal Research 34: 283-306.

Humphreys MCS, Blundy JD, Stephen R, Sparks J (2006) *Magma Evolution and Open-System Processes at Shiveluch Volcano: Insights from Phenocryst Zoning*. Journal Of Petrology Vol. 47, No. 12, pp. 2303-2334.

Ishikawa T, Nakamura E (1994) *Origin of the slab component in arc lavas from across-arc variation of B and Pb isotopes*. Nature 370: 205-208

Ishikawa T, Tera F (1997) *Source, composition and distribution of the fluid in the Kurile mantle wedge: Constraints from across-arc variations of B/Nb and B isotopes*. Earth and Planetary Science Letters 152: 123-138

Ishikawa T, Tera F, Nakazawa T (2001) *Boron isotope and trace element systematics of the three volcanic zones in the Kamchatka arc*. Geochimica et Cosmochimica Acta 65: 4523-4537.

Jackson JA (1994) *Active tectonics of the Aegean region*. Annual Reviews of Earth and Planetary Sciences 22: 239-271.

Jacobsen SB, Quick JE, Wasserburg GJ (1984) *A Nd and Sr isotopic study of the Trinity Peridotite; implications for mantel evolution*. Earth and Planetary Science Letters 68: 361-378.

Jambon A, Semet MP (1978) *Lithium diffusion in silicate glasses of albite, orthoclase, and obsidian composition: an ion-microprobe determination*. Earth and Planetary Science Letters 37: 445-450.

James RJ, Palmer MR (2000) *The lithium isotope composition of international rock standards*. Chemical Geology 166: 319-326.

Jolivet L (2001) *A comparison of geodetic and finite strain pattern in the Aegean, geodynamic implications*. Earth and Planetary Science Letters 187: 95-104.

Kalogeropoulos S & Paritsis S (1990) *Geological and geochemical evolution of the Santorini volcano: a review*. In: Hardy DA (ed) Thera and the Aegean World III, 2. The Thera Foundation, London 164-171.

Kasemann SA, Jeffcoate AB, Elliot T (2005) *Lithium Isotope Composition of Basalt Glass Reference Material*. Analytical Chemistry 77:5251-5257.

Kobayashi K, Tanaka R, Moriguti T, Shimizu K, Nakamura E (2004) *Lithium, boron and lead isotope systematics on glass inclusions in olivines from Hawaiian lavas: evidence for recycled components in the Hawaiian plume*. Chemical Geology 212: 143-161.

Kosals YA, Nedashkovskiy PG, Petrov LL, Serykh VI (1973) *Beryllium distribution in granitoid plagioclase*. Geochem Int 1: 753-767.

LaTourette T, Wasserburg GJ (1998) *Mg diffusion anorthite: Implications for the formation of early solar system planetesimals*. Earth and Planetary Science Letters 158: 91-108.

Leeman WP (1996) *Boron and other fluid-mobile elements in volcanic arc lavas: implications for subduction processes*. AGU Geophysical Monograph 96.

Leeman WP, Carr MJ, Morris JD (1994) *Boron geochemistry of the central American Volcanic Arc: Constraints on the genesis of subduction-related magmas*. Geochimica et Cosmochimica Acta 58: 149-168.

Lentz RCF, McSween HY Jr, Ryan J, Riciputi LR (2001) *Water in martian magmas: Clues from light lithophile elements in shergottite and nakhlite pyroxenes*. Geochimica et Cosmochimica Acta 65: 4551-4565.

LePichon X, Lybéris N, Alvarez F (1984) *Subsidence history of the north Aegean Trough*- In Dixon JE and Robertson AHF (eds.): The geological evolution of the eastern Mediterranean, 727-741, Oxford (Backwell).

Lofgren GE, Ronaldson CH, Usselman TM (1975) *Geology, petrology and crystallization of Apollo 15 quartz-normative basalts*. Proc. 6th Lunar Sci. Conf. 79-99.

Longhi J, Walker D, Hayes JF (1976) *Fe and Mg in plagioclase,* in: Proc. 7th Lunar Planet. Sci. Conf., pp. 1281-1300.

Lundgaard KL, Tegner C (2004) *Partitioning of ferric and ferrous iron between plagioclase and silicate melt*. Contrib. Mineral. Petrol. 147: 470-483.

Lundstrom CC, Chaussidon M, Hsui AT, Kelemen P, Zimmerman M (2005) *Observations of Li isotopic variations in the Trinity Ophiolite: Evidence for isotopic fractionation by diffusion during mantle melting*. Geochimica et Cosmochimica Acta 69: 735-751.

Mann AC (1983) *Trace element geochemistry of high-alumina basalt-andesite-dacite-rhyodacite lavas of the main volcanic series of Santorini volcano, Greece*. Contrib. Mineral. Petrol. 84: 43-57.

Marsch BD (2002) *On bimodal differentiation by solidification front instability in basaltic magmas, part I: Basic mechanics*. Geochimica et Cosmochimica Acta 66: 221-2229.

Marsch BD (2006) *Dynamics of Magmatic Systems*. Elements, Vol. 2, pp. 287-292.

Marschall HR, Ludwig T (2004) *The low-boron contest: minimising surface contamination and analysing boron concentrations at the ng/g-level by secondary ion mass spectrometry*. Mineralogy and Petrology 81: 165-278.

Martel C, Schmidt BC (2003) *Decompression experiments as an insight into ascent rates of silicic magmas. Contrib. Mineral. Petrol. 144: 397-415.*

Martin VM, Holness MB & Pyle DM (2006) Textural analysis of magmatic enclaves from the Kameni Islands, Santorini, Greece. Journal of Volcanology and Geothermal Research 154: 89-102.

McKenzie D (1978) *Active tectonics of the Alpine-Himalayan belt: The Aegean Sea and surrounding regions*. Royal Astr Soc Geophys Journal 55: 217-254.

Mercier J-L, Sorel D, Vergely P, Simeakis K (1989) *Extensional tectonic regimes in the Aegean basins during the Cenozoic*. Basin Research 2: 49-71.

Metrich N, Rutherford MJ (1998) *Low pressure Crystallization paths of H2O-saturated basaltic-hawaiitic melts from Mt. Etna: implications for open-system degassing of basaltic volcanoes*. Geochimica et Cosmochemica Acta 62: 1195-1205.

Monaghan MC, Klein J, Measures CI (1988) *The origin of ^{10}Be in island-arc volcanic rocks*. Earth and Planetary Science Letters 89: 288-298.

Morgan DJ, Blake S, Roger NW, DeVivo B, Rolandi G, McDonald R, Hawkesworth CJ (2004) *Timescales of Crystal residence and magma chamber volume from modeling of diffusion profiles in phenocrysts: Vesuvius 1944*. Earth and Planetary Science Letters 222: 933-946.

Morgan GB, & London D (1996). *Optimizing the electron microprobe analysis of hydrous alkali aluminosilicate glasses*. American Mineralogist 81:1176-1185.

Moriguti T, Nakamura E (1998) *Across-arc variation of Li isotopes in lavas and implications for crust/mantle recycling at subduction zones*. Earth and Planetary Science Letters 163: 167-174.

Moriguti T, Shibata T, Nakamura E (2004) *Lithium, boron and lead isotope and trace element systematics of Quaternary basaltic volcanic rocks in northeastern Japan: mineralogical controls on slab-derived fluid composition*. Chemical Geology 212: 81-100.

Mountrakis D, Pavlides S, Chatzipetros A, Meletidis S, Tranos MM, Vougioukalakis G, Kilias A (1998) *Active deformation of Santorini. In: Casale R et al. (eds) Proceedings of the Second Workshop, Santorini, Greece,* 2 to 4 May 1996, pp. 13-22, European Commission.

Mountrakis D, Pavlides S, Zouros N, Astaras T, Chatzipetros A (1998) *Seismic fault geometry and kinematics of the 13 May 1995 Western Macedonia (Greece) earthquake*. Journal of Geodynamics 26: 175-196.

Mungall JE, Dingwell DB, Chaussidon M (1999) *Chemical diffusivities of 18 trace elements in granitoid melts*. Geochimica et Cosmochimica Acta 63: 2599-2610.

Mungall JE (2002) *Empirical models relating viscosity and tracer diffusion in magmatic silicate melts*. Geochimica et Cosmochimica Acta 66, No. 1, pp. 125-143.

Murphy MD, Sparks RSJ, Barclay MR, Carroll M, Lejeune TS, Brewer TS, McDonald R, Black S, Young S (1998) *The role of magma missing in triggering the current eruption at the Soufriere Hills volcano, Montserrat, West indies*. Geophysical Research Letters 25: 3433-3436.

NakamuraM (1995) *Continous mixing of crystal mush and replenished magma in the ongoing Unzen eruption*. Geology 23: 807-810.

Nicholls IA (1971a) *Petrology of Santorini volcano, Cyclades, Greece*. Journal of Petrology 12: 67-119.

Nicholls IA 1971b) *Santorini volcano, Greece – Tectonic and petrochemical relationships with volcanics of the Aegean region*. Tectonophysics 11: 377-385.

Okay AI, Kelley SP (1994) *Tectonic setting, petrology and geochronology of jadeite+ glaucophane and chloritoid+glaucophane schists from north-west Turkey*. Journal of Metamorphic Geology 12: 455-466.

Ottolini L, Le Fèvre B, Vannucci R (2004) *Direct assessment of mantle boron and lithium contents and distribution by SIMS analyses of peridotite minerals*. Earth and Planetary Science Letters 228: 19-36.

Peter MT, Schaffner EE, Burnett DS, Kim SS (1995) *Magnesium and titanium partitioning between anorthite and Type B CAI liquid: Dependence on oxygen fugacity and liquid composition*. Geochimica et Cosmochimica Acta 59: 2785-2796.

Pallister JS, Hoblitt RP, Meeker GP, Knight RJ Siems DF (1996) *Magma mixing at Mount Pinatubo: petrographic and chemical evidence from the 1991 deposits,* in: Newhall CG and Punongbayan RS (Eds.), Fire and Mud: Eruption and Lahar of Mount Pinatubo, Philippines PHILVOLCS, Quezon City and Univ. Washington Press, Seattle, WA, 1996, pp. 687-731.

Papazachos BC & Pangitopoulos DG (1993) *Normal faults associated with volcanic activity and deep rupture zones in the southern Aegean volcanic arc*. Tectonophysics 220: 301-308.

Pearce NJG, Perkins WT, Westgate JA, Gorton MP, Jackson SE, Neal CR, Chenery SP (1996) *A Compilation of New and Published Major and Trace Element Data for NIST SRM 610 and NIST SRM 612 Glass Reference Materials*. Geostandards Newsletter Vol. 21, No.1, pp. 115-144.

Phinney WC (1992) *Partition coeficients for iron between plagioclase and basalt as a function of oxygen fugacity; implication for Archean and lunar anorthosites*. Geochimica et Cosmochimica Acta 56: 1885- 1895.

Pichler H & Friedrich WL (1976) *Radiocarbon dates of Santorini volcanics*. Nature 262:373-374.

Pistiner JS, Henderson GM (2003) *Lithium-isotope fractionation during continental weathering processes*. Earth Planetary Science Letters 214: 327-339.

Richter FM, Davis AM, DePaolo DJ, Watson EB (2003) *Isotope fractionation by chemical diffusion between molten basalt and rhyolite*. Geochimica et Cosmochimica Acta 67: 3905-3923.

Robertson AHF, Dixon JE (1984) *Introduction: Aspects of the geological evolution of the Eastern Mediterranean*. In: Robertson AHF, Dixon JE (eds) The Geological Evolution of the Eastern Mediterranean, Geol Soc London Spec Publ 17, pp 1-74.

Rutherford MJ, Devine JD, Barclay J (1998) *Changing magma conditions and ascent rates during the Soufriere Hills eruption on Montserrat*. GSA Today, pp. 1-7.

Ryan JG (1989) *The systematics of lithium, beryllium and boron in young volcanic rocks*. PhD thesis, Columbia University, New York.

Ryan JG, Langmuir CH (1987*) The systematics of lithium abundances in young volcanic rocks*. Geochimica et Cosmochimica Acta 51: 1727-1741.

Sato H (1989) *Mg-Fe partitioning between between plagioclase and liquid in basalts of Hole 504B*, Leg 111: A study of melting at 1 atm. Proceedings of Ocean Drilling Program, Scientific Results, 111, 17-26.

Shaw HR (1972) *Viscosities of magmatic silicate liquids: an empirical method of prediction.* Am. J. Sci. 272: 870-893.

Schmidt C, Thomas R, Heinrich W (2004) *Boron speciation in aqueous fluids at 22 to 600 °C and 0.1 MPa to 2GPa*. Geochimica et Cosmochim Acta 69: 275-281.

Schmincke HU (2004) *Volcanism*. Springer-Verlag Berlin Heidelberg 324 pp.

Seyfried WE Jr, Chen X, Chan L-H (1998*) Trace element mobility and lithium isotope exchange during hydrothermal alteration of seafloor weathered basalt:* an experimental study at 350°C, 500 bars. Geochimica et Cosmochimica Acta 62: 949-960.

Seyfried WE Jr, Janecky DR, Mottl MJ (1984) *Alteration of the oceanic crust: Implications for geochemical cycles of lithium and boron*. Geochim Cosmochim Acta 48: 557-569.

Shannon RD (1976) *Revised effective ionic radii and systematic studies of interatomic distances in halides and chalcogenides*. Acta Crystallogr. A32, 751-767.

Sisson TW, Grove TL (1993) *Experimental investigations of the role of H_2O in Calc-alkaline differentiation and subduction zone magmatism*. Contrib. Mineral. Petrol.,113: 143-166.

Smith VC, Shane P, Nairn IA (2005) *Trends in rhyolite geochemistry, mineralogy, and magma storage during the last 50 kyr at Okataina and Taupo volcanic centres, Taupo Volcanic Zone, New Zealand.* Journal of Volcanology and Geothermal Research 148: 372-406.

Snyder D, *Thermal effects of the intrusion of basaltic magma into a more silicic magm chamber and implications for eruption triggering*. Earth and Planetary Science Letters 175 (2000) 257-273.

Sparks RSJ, Marshall LA (1986) *Thermal and mechanical constraints on mixing between mafic and silicic magmas*. Journal of Volcanology and Geothermal Research 29: 99-24.

Sparks RSJ, Wilson CJN 1990. *The Minoan deposits: a review of their characteristics and interpretations*. In: Hardy DA (ed) Thera and the Aegean World III,2. The Thera Foundation, London 89-99.

Sparks RSJ (2003) *Forecasting volcanic eruptions*. Earth and Planetary Science Letters 210: 1-15.

Sparks RSJ, Sigrudsson H, Wilson L (1977) *Magma mixing: mechanism of trigerring explosive acid erruption*. Nature 267: 315-318.

Stamatelopoulou-Seymour K, Vlassopoulos D, Pearce TH, Rice C (1990) *The record of magma chamber processes in phenocrysts at Thera Volcano, Aegean Volcanic Arc, Greece*. Contrib. Mineral. Petrol. 104: 73 -84.

Stix J, Layne GD, Williams SN (2003) *Mechanisms of degassing at Nevado del Ruiz volcano, Colombia*. J Geol Soc London 160: 507-521.

Sun S, McDonough WF (1989) *Chemical and isotopic systematics of ocean basalts: Implications for matle composition and processes. In Magnetism in the Ocean Basins* (eds. A. D. and Sauders MJ Norry), pp. 313-345. Blackwell Scientific.

Tait SR, Wörner G, van den Bogaard, Schminke H (1989) *Cumulate nodules as evidence for convective fractionation in a phonolite magma chamber*. Journal of Volcanology and Geothermal Research 37: 21-37.

Tarney J, Barr S, Mitropoulos P, Sideris K, Katerinopoulos A, Stouraiti C (1998*) Santorini: geochemical constraints on magma sources and eruption mechanisms*. In: Casale R et al. (eds) Proceedings of the Second Workshop, Santorini, Greece, 2 to 4 May 1996, pp 89-112, European Commission.

Teng FZ, McDonough WF, Rudnick RL, Dalpé C, Tomascak PB, Gao S, Chappell BW (2004*) Lithium isotopic composition and concentration of the upper continental crust*. Geochim Cosmochim Acta: 68: 4167-4178.

Tomascak PB, Ryan JG, Defant MJ (2000) *Lithium isotope evidence for light element decoupling in the Panama subarc mantle*. Geology 28: 507-510.

Tomascak PB, Widom E, Benton LD, Goldstein SL, Ryan JG (2002) *The control of lithium budgets in island arcs*. Earth and Planetary Science Letters 196: 227-238.

Tomascak PB (2004*) Developments in the understanding and application of lithium isotopes in the Earth and Planetary Sciences*. Review in Mineralogy & Geochemistry 55, pp. 153-195, Mineral Society of America, Washington, D.C.

Tomiya A, Takahashi E (1995) *Reconstruction of a evolving magma chambr beneath Usu volcano since 1663 eruption*. Journal of Petrology 36: 617-636.

Tomiya A, Takahashi E (2005) *Evolution of the Magma Chambe beneath USU Volcano since 1663: a Natural Laboratory for Observing Changing Phenocryst Compositions and Textures*. Journal of Petrology Vol. 46, No. 12, pp. 2395-2426.

Urey HC, *The Cosmic abundances of K, U, and Th and the heat balances of the Earth, Moon, and Mars*. Proc. Natl. Acad. Sci. USA 41 (1955) 127-144.

Venesky DY, Rutherford MH (1999) *Petrology and Fe-Ti oxide reequilibration of the 1991 Mount Unzen mixed magma*. Journal of Volcanology and Geothermal Research 89: 213-230.

Webster JD, Holloway JR, Hervig RL (1989) *Partitioning of lithophile trace elements between H_2O and H_2O + CO_2 fluids and topaz rhyolite melt*. Economic Geology 84: 116-134.

Weill DF, Hon R, Navrotsky A (1980) *The igneous system $CaMgSi_2O_6$-$CaAl_2Si_2O_8$-$NaAlSi_3O_8$: Variations on a classic theme by Bowen*. In Hargraves B, Ed., Physics of magnetic process, Princeton University Press, New Jersey pp. 49-92.

White RA (1996) *Precursory deep long-period earthquakes at Mount Pinatubo, Spatio-temporal links to a basalt trigger*. Newhall CG and Punongbayan RS (Eds). Fire and Mud: Eruptions and Lahars of Mount Pinatubo, Philippines PHILVOLCS, Quezon City, Philippines and Univ. Washington Press, Seattle, WA, pp. 307-327.

Wijbrans JR and McDougall I (1988) *Metamorphic evolution of the Attic-Cycladic metamorphic belt on Naxos (Cyclades, Greece) utilizing $^{40}Ar/^{39}Ar$ age spectrum measurements*. J Metam Geol 6: 571-594.

Woodland AB, Seitz HM, Altherr R, Olker B, Marschall H, Ludwig T (2002) *Li abundances in eclogite minerals: a clue to a crustal or mantle origin?* Contrib Mineral Petrol 143: 587-601.

Wunder B, Meixner A, Romer R, Heinrich W (2006) *Temperature-dependent isotopic fractionation of lithium between clinopyroxene and high-pressure hydrous fluids*. Contrib. Mineral. Petrol. 151: 112-120.

You C-F, Butterfield DA, Spivack AJ, Gieskes JM, Gamo T, Campbell AJ (1994) *Boron and halide systematics in submarine hydrothermal solutions*. Earth and Planetary Science Letters 123: 227-238.

Zhang L, Chan L-H, Gieskes JM (1998) *Lithium isotope geochemistry of pore waters from Ocean Drilling Program Sites 918 and 919, Irminger Basin*. Geochimica et Cosmochimica Acta 62: 2437-2450.

Zack T, Tomascak PB, Rudnick RL, Dalpe C, McDonough WF (2003) *Extremely light Li in orogenic eclogites: The role of isotope fractionation during dehydration in subducted oceanic crust*. Earth and Planetary Science Letters 208: 279-290.

Zellmer GF, Blake S,Vance D, Hawkesworth C, Turner S, (1999) *Plagioclase residence times at two island arc volcanoes (Kameni Islands, Santorini, and Soufriere, St.Vincent) determined by Sr diffusion systematics*. Contrib. Mineral. Petrol. 136: 345-357.

Zellmer GF, Sparks RSJ, Hawkesworth C, Wiedenbeck M (2003) *Magma emplacement and remobilization timescales beneath Montserrat: insights from Sr and Ba zonation in plagioclase phenocrysts*. Journal of Petrology 44: 1413-1431.

Zellmer GF, Turner S, Hawkesworth C (2000) *Timescales of destructive plate margin magmatism: New insights from Santorini, Aegean volcanic arc*. Earth and Planetary Science Letters 174:265-281.

APPENDIX 1:
ANALYTICAL PROCEDURE

A total of 40 samples were collected from the volcanic products of Santorini of the Hellenic Arc, Greece. These consist of lava flow and pyroclastic rock samples taken from different units on Nea Kameni, Thera and Therasia islands. The number of samples considered for analyses was subsequently narrowed down to sixteen, and thirteen of these are presented in this work. Among these are the six porphyritic to glomeroporphyritic dacitic lava flow fragments from Nea Kameni, the rest being andesitic lava and agglutinate samples from Thira.

Polished sections were prepared for detailed measurements. Initial examination consisted of characterising mineral phases under polarised microscopy. Further scrutiny of the thin sections were done with a Leo 440 scanning electron microscope (SEM) at the Institut für Umwelt Geochemie, Universität-Heidelberg to identify the various populations of plagioclase, clinopyroxene, orthopyroxene, and olivine phenocrysts. Such populations were identified in each of the rock samples and representative phenocrysts were chosen for further analyses. Major and trace element analyses profiles were subsequently done for 45 plagioclase, 16 clinopyroxene, 13 orthopyroxene and 4 olivine phenocrysts. Photomicrographs and back-scattered electron (BSE) images of these crystals were made to facilitate documentation and analyses.

A1.1 Major Element Analysis

Major and minor element concentrations were determined through electron probe microanalysis (EPMA) using a Cameca SX 51 at the Universität Heidelberg Mineralogisches Institut. The 50 μm–thick polished sections were thoroughly cleaned and coated with carbon. Profiles were run through phenocrysts of particular interest, whereas point analyses were done for small crystals and glassy or fine-grained portions of the matrix. The electron microprobe has five wavelength-dispersive spectrometers. An accelerating voltage of 15 kV, a beam current of 20 nA, and a 10 μm beam diameter were employed for the analysis of plagioclase. For some of these crystals, oxides of Sr, Ba, and Mg were measured besides those of Na, Ca, K, Al, Si and Fe. Counting time for each oxide is normally between 10-20 s, except for SrO and BaO that are for 40 s, and MgO for 100 s. SrO and BaO show much scatter in all of these crystals; but MgO exhibits zonation where considerable variations in anorthite content exist. The same voltage and current were used for pyroxenes and olivines, but with a 1 μm beam diameter. Besides the oxides of the major elements Mg, Fe, Ca, Na, Al and Si, analyses of Ti, K, Mn, and Cr were obtained for pyroxenes with counting times of 10 s. Olivine phenocryst

analysis included all of these elements with the addition of Ni. Matrix analysis consisted of oxide concentrations of Na, Ca, K, Fe, Mg, Al, Si, Mn, Ti and P, investigated using a 20 μm × 30 μm scanning mode (magnitude 8888), acquired with an accelerating voltage of 15 kV and a probe current of 10-20 nA.

Details of the EPMA set-up for plagioclase, pyroxene, olivine (Ni is measured only for olivine) and matrix analysis are as follows:

Plagioclase

Element	Standard	Crystal	Spectrometer	Counting time (s)	Detection limit (wt %)
Na	Albite	TAP	1	10	0.04
Mg	MgO	TAP	5	100	0.02
Al	Anorthite	TAP	1	10	0.04
Si	Wollastonite	TAP	5	10	0.03
K	Orthoclase	PET	3	10	0.03
Ca	Anorthite	PET	3	10	0.03
Sr	Celestine	PET	3	40	0.10
Ba	$BaSO_4$	PET	3	40	0.07

Pyroxene & Olivine

Element	Standard	Crystal	Spectrometer	Counting time (s)	Detection limit (wt %)
Na	Albite	TAP	1	10	0.04
Mg	MgO	TAP	5	10	0.07
Al	Al_2O_3	TAP	1	10	0.06
Si	Wollastonite	TAP	5	10	0.03
K	Orthoclase	PET	3	10	0.03
Ca	Wollastonite	PET	3	10	0.04
Ti	TiO_2	PET	2	10	0.06
Cr	Cr_2O_3	PET	2	10	0.07
Mn	Rhodonite	LIF	4	10	0.08
Fe	Fe_20_3	LIF	4	10	0.11
Ni (Ol)	NiO	LIF	4	10	0.10

Matrix

Element	Standard	Crystal	Spectrometer	Counting time (s)	Detection limit (wt %)
Na	Albite	TAP	1	10	0.05
Mg	MgO	TAP	5	10	0.07
Al	Al_2O_3	TAP	1	10	0.05
Si	Wollastonite	TAP	5	10	0.04
P	Apatite	PET	2	30	0.10
Ca	Wollastonite	PET	3	10	0.04
K	Orthoclase	PET	3	10	0.03
Mn	Rhodonite	LIF	4	10	0.08
Fe	Fe_20_3	LIF	4	10	0.12
Ti	TiO_2	PET	2	10	0.06

A1.2 Light Element Analysis

Li, Be, and B analysis was done with a modified Cameca IMS 3f ion microprobe equipped with a primary beam mass filter, also at the Universität Heidelberg Mineralogisches Institut. The same thin sections used for the EPMA were polished with 0.5 μm γ-alumina powder to remove the carbon coating, rinsed with ethanol and then with distilled water, and subjected to two successive ultrasonic baths of 15 min each in ultrapure (Millipore-filtered) water. These were then coated with gold ~50 nm thick. Analyses were done with ^{30}Si as reference isotope and NIST SRM-610 glass as standard. The same phenocrysts were considered for both major and light element analyses, so SiO_2 wt % values from the EPMA profiles were used as inner reference for each SIMS analysis point.

The set-up involves a $^{16}O^-$ primary ion beam of 14.5 keV and 20 nA with a diameter of ~30 μm. Positive secondary ions are accelerated to a nominal energy of 4.5 keV. The energy window of the mass spectrometer is set to 40 eV. Employed for the mass filtering are an offset of 75 eV and a 10% mass resolution of ~1000 (m/Δm) to suppress interefering molecules and minimise matrix effects. To reduce the effects of contamination, the intermediate field aperture FA2 (750 μm) is used, thereby reducing the diameter of the analysed area to ~12 μm in the 25 μm imaged field mode. Intensities of 10^{-1} – 10^6 can be detected by the electron multiplier, and detection limits for Li and Be were at 1 ng/g and for B at 3 ng/g. Secondary ions are counted by the electron multiplier. Each analysis consists of 10 cycles with an integration time of 2s/cycle for Si, 8s/cycle for Li, 16s/cycle for Be and B. Pre-sputtering takes ~342 s (~6 min), and each analysis spot requires a total analysis time of ~18 min. (For more details regarding the SIMS analysis please refer to Ottolini et al., 1993; Ottolini et al., 2002; Marschall & Ludwig, 2004)

A1.3 Lithium Isotope Analysis

Lithium isotope analysis was done on the samples from the Nea Kameni dacites and one sample from Thera. The same crystals that were analysed for Li, Be and B were investigated for Li isotopes, but the thin sections were re-polished to remove the holes of the previous SIMS spots. Cleaning and gold coating ensued as previously described.

The SIMS is set up with a 14.5 keV $^{16}O^-$ primary ion beam and variable primary beam currents of $I_P = 0.5 – 50$ nA. Spot diameter varies from ~5 μm to ~30 μm depending on I_P. Secondary ions are collected by a single electron multiplier, and ^7Li Count rates $i(^7Li)$ range from 2×10^4 to 3×10^6 s^{-1}. Count rates are corrected for a counting system deadtime of 35 ns.

Mass resolution ($m/\Delta m$) for Li isotope measurements is ~750 at 10 % intensity ratio. The energy window is at 100 eV and without any offset. Each analysis spot measures between N=30 and N=250 cycles, with counting times of 3.518 s and 1.003 s on ^{6}Li and ^{7}Li, respectively. Presputtering lasts for 5 min and settling time between two different masses is 200 ms, resulting to a total of approximately 10 min for one analysis with N=50. The internal precision of a single analysis is typically ≤1 ‰ (2σ), except for analyses with low count rates ($i(^{7}\text{Li}) < 5\times10^{4}$ s^{-1}) where precision is ≤2 ‰ (2σ). Synthetic basaltic glass GSD-1G (Jochum et al., 2005), analysed with I_P = 20 nA and N = 50, is used to correct the instrumental mass fractionation. The mean of the MC-ICP-MS value (+31.14‰) and the TIMS value (+31.7‰) published in Kasemann et al. (2005): δ^{7}Li(GSD-1G) = +31.42‰ are utilised. This yeilds an instrumental mass fractionation of α_{inst}(GSD-1G) = 1.0176. Reproducibility of measured isotope ratios during an analytical session (eight days) on the Heidelberg ims 3f is typically ≤1 ‰ (2σ).

Review analysis was done for the Li isotope analysis with a deadtime correction of 16 ns. In each cycle for this new set-up, the ^{6}Li signal is integrated for 1.759 s before and after the collection of the ^{7}Li signal. Such is to eliminate any bias of the measured isotope ratio, which might be caused by increasing or decreasing count rates.

APPENDIX 2:

ESTIMATES FOR PLAGIOCLASE MAXIMUM RESIDENCE TIME

$\log D_o$	D_o	E_a	T (°C)	T (K)	$-E_a/RT$	D (m^2/s)	$\log D$	x (μm)	x (m)	t (s)	t (min)	t (hr)	t (yr)
Albite													
-3.8	0.000158	146000	200	473	-37.13	1.19E-20	-19.92	400	0.00040	3.356E+12	5.593E+10	9.322E+08	1.064E+05
-3.8	0.000158	146000	300	573	-30.65	7.77E-18	-17.11	400	0.00040	5.151E+09	8.585E+07	1.431E+06	1.633E+02
-3.8	0.000158	146000	400	673	-26.09	7.38E-16	-15.13	400	0.00040	5.423E+07	9.038E+05	1.506E+04	1.719E+00
-3.8	0.000158	146000	500	773	-22.72	2.16E-14	-13.67	400	0.00040	1.854E+06	3.091E+04	5.151E+02	5.880E-02
-3.8	0.000158	146000	600	873	-20.12	2.91E-13	-12.54	400	0.00040	1.374E+05	2.290E+03	3.817E+01	4.358E-03
-3.8	0.000158	146000	700	973	-18.05	2.30E-12	-11.64	400	0.00040	1.739E+04	2.898E+02	4.830E+00	5.513E-04
-3.8	0.000158	146000	**800**	1073	-16.37	1.24E-11	-10.91	**400**	0.00040	3.234E+03	5.390E+01	8.983E-01	1.025E-04
-3.8	0.000158	146000	**800**	1073	-16.37	1.24E-11	-10.91	**300**	0.00030	1.819E+03	3.032E+01	5.053E-01	5.768E-05
-3.8	0.000158	146000	**800**	1073	-16.37	1.24E-11	-10.91	**150**	0.00015	4.548E+02	**7.580E+00**	1.263E-01	1.442E-05
-3.8	0.000158	146000	**800**	1073	-16.37	1.24E-11	-10.91	**100**	0.00010	2.021E+02	**3.369E+00**	5.614E-02	6.409E-06
-3.8	0.000158	146000	**800**	1073	-16.37	1.24E-11	-10.91	**50**	0.00005	**5.053E+01**	8.422E-01	1.404E-02	1.602E-06
-3.8	0.000158	146000	900	1173	-14.97	4.99E-11	-10.30	400	0.00040	8.013E+02	1.335E+01	2.226E-01	2.541E-05
-3.8	0.000158	146000	900	1173	-14.97	4.99E-11	-10.30	300	0.00030	4.507E+02	7.512E+00	1.252E-01	1.429E-05
-3.8	0.000158	146000	900	1173	-14.97	4.99E-11	-10.30	200	0.00020	2.003E+02	3.339E+00	5.565E-02	6.352E-06
-3.8	0.000158	146000	900	1173	-14.97	4.99E-11	-10.30	100	0.00010	5.008E+01	8.347E-01	1.391E-02	1.588E-06
-3.8	0.000158	146000	900	1173	-14.97	4.99E-11	-10.30	50	0.00005	1.252E+01	2.087E-01	3.478E-03	3.970E-07
-3.8	0.000158	146000	1000	1273	-13.79	1.62E-10	-9.79	400	0.00040	2.472E+02	4.120E+00	6.867E-02	7.839E-06
-3.8	0.000158	146000	1000	1273	-13.79	1.62E-10	-9.79	300	0.00030	1.391E+02	2.318E+00	3.863E-02	4.409E-06
-3.8	0.000158	146000	1000	1273	-13.79	1.62E-10	-9.79	200	0.00020	6.180E+01	1.030E+00	1.717E-02	1.960E-06
-3.8	0.000158	146000	1000	1273	-13.79	1.62E-10	-9.79	100	0.00010	1.545E+01	2.575E-01	4.292E-03	4.899E-07
-3.8	0.000158	146000	1000	1273	-13.79	1.62E-10	-9.79	50	0.00005	3.863E+00	6.438E-02	1.073E-03	1.225E-07
Anorthite													
-3.6	0.000251	151000	200	473	-38.40	5.30E-21	-20.28	400	0.00040	7.551E+12	1.258E+11	2.097E+09	2.394E+05
-3.6	0.000251	151000	300	573	-31.70	4.31E-18	-17.37	400	0.00040	9.283E+09	1.547E+08	2.579E+06	2.944E+02
-3.6	0.000251	151000	400	673	-26.99	4.78E-16	-15.32	400	0.00040	8.362E+07	1.394E+06	2.323E+04	2.651E+00
-3.6	0.000251	151000	500	773	-23.50	1.57E-14	-13.80	400	0.00040	2.547E+06	4.246E+04	7.076E+02	8.078E-02
-3.6	0.000251	151000	600	873	-20.80	2.32E-13	-12.64	400	0.00040	1.727E+05	2.878E+03	4.797E+01	5.476E-03
-3.6	0.000251	151000	700	973	-18.67	1.97E-12	-11.71	400	0.00040	2.035E+04	3.392E+02	5.654E+00	6.454E-04
-3.6	0.000251	151000	**800**	1073	-16.93	1.12E-11	-10.95	**400**	0.00040	3.574E+03	5.957E+01	9.928E-01	1.133E-04
-3.6	0.000251	151000	**800**	1073	-16.93	1.12E-11	-10.95	**300**	0.00030	2.010E+03	3.351E+01	5.584E-01	6.375E-05
-3.6	0.000251	151000	**800**	1073	-16.93	1.12E-11	-10.95	**150**	0.00015	5.026E+02	**8.376E+00**	1.396E-01	1.594E-05
-3.6	0.000251	151000	**800**	1073	-16.93	1.12E-11	-10.95	**100**	0.00010	2.234E+02	**3.723E+00**	6.205E-02	7.083E-06
-3.6	0.000251	151000	**800**	1073	-16.93	1.12E-11	-10.95	**50**	0.00005	**5.584E+01**	9.307E-01	1.551E-02	1.771E-06
-3.6	0.000251	151000	900	1173	-15.48	4.74E-11	-10.32	400	0.00040	8.442E+02	1.407E+01	2.345E-01	2.677E-05
-3.6	0.000251	151000	900	1173	-15.48	4.74E-11	-10.32	300	0.00030	4.749E+02	7.915E+00	1.319E-01	1.506E-05
-3.6	0.000251	151000	900	1173	-15.48	4.74E-11	-10.32	200	0.00020	2.111E+02	3.518E+00	5.863E-02	6.693E-06
-3.6	0.000251	151000	900	1173	-15.48	4.74E-11	-10.32	100	0.00010	5.276E+01	8.794E-01	1.466E-02	1.673E-06
-3.6	0.000251	151000	900	1173	-15.48	4.74E-11	-10.32	50	0.00005	1.319E+01	2.198E-01	3.664E-03	4.183E-07
-3.6	0.000251	151000	1000	1273	-14.27	1.60E-10	-9.80	400	0.00040	2.502E+02	4.169E+00	6.949E-02	7.933E-06
-3.6	0.000251	151000	1000	1273	-14.27	1.60E-10	-9.80	300	0.00030	1.407E+02	2.345E+00	3.909E-02	4.462E-06
-3.6	0.000251	151000	1000	1273	-14.27	1.60E-10	-9.80	200	0.00020	6.254E+01	1.042E+00	1.737E-02	1.983E-06
-3.6	0.000251	151000	1000	1273	-14.27	1.60E-10	-9.80	100	0.00010	1.564E+01	2.606E-01	4.343E-03	4.958E-07
-3.6	0.000251	151000	1000	1273	-14.27	1.60E-10	-9.80	50	0.00005	3.909E+00	6.515E-02	1.086E-03	1.239E-07

APPENDIX 2-1: Table for calculating diffusion times between two different compositions. D_o and E_a values are from Gilleti & Shanahan (1997). The highlighted values of time are for the examples in the discussion (Figs. 6-15 and 6-16).

APPENDIX 2-2: LAYER AND SPHERE CALCULATIONS

The layer calculation assumes the diffusion of a substance initially confined in a region $-h < x < +h$. The generated curves in Fig. 6-19 are symmetrical about $x = 0$, showing that at this point, the system may be cut in half by a plane without affecting the distribution Hence, this equation also gives the distribution for a semi-infinite system:

$$C = \frac{1}{2} C_o \left\{ \operatorname{erf} \frac{h - x}{2\sqrt{Dt}} + \operatorname{erf} \frac{h + x}{2\sqrt{Dt}} \right\}$$

The sphere computation assumes a diffusing substance initially distributed uniformly through a sphere of radius a, the concentration C at radius r, and time t is given by:

$$C = \frac{1}{2} C_o \left\{ \operatorname{erf} \frac{a - r}{2\sqrt{Dt}} + \operatorname{erf} \frac{a + r}{2\sqrt{Dt}} \right\} - \frac{C_o}{r} \sqrt{\frac{Dt}{\pi}} \left[\exp\left\{ \frac{-(a - r)^2}{4Dt} \right\} - \exp\left\{ \frac{-(a + r)^2}{4Dt} \right\} \right]$$

where C_0 is the initial uniform concentration in the sphere.

For details please refer to *The Mathematics of Diffusion* by Crank, revised 1994.
D_{Li} used for the spreadsheet is from Giletti & Shanahan, 1997 and β from Richter et al., 2003.

2-3
Simple Diffusion Model using Mathematica

```
Clear[T, Q, R, rr, r, tt, dd, a, b, D0, DLi, x^2, Δx, Δt, Cli, tlx, tld, n]
```

```
Clear::ssym : D0 is not a symbol or a string. Mehr…
```

```
Clear::ssym : x^2 is not a symbol or a string. Mehr…
```

```
T = 1073.15;
```

```
Q = -146000;
```

```
R = 8.314;
```

```
D0 = 1.58 * 10 ^ -4;
```

```
DLi = D0 * e^(Q/(R*T)) * 10^12
```

```
12.3588
```

```
Δx = 63.15789474
```

```
63.1579
```

```
tlx = 20;
```

```
tld = tlx * Δx
```

```
1263.16
```

```
tlx = tld / Δx
```

```
20.
```

```
Δx^2
```

```
3988.92
```

```
Δt = 10
```

```
10
```

$$r = DLi * \frac{\Delta t}{\Delta x^2}$$

```
0.0309829
```

$$rr = \frac{\Delta t}{\Delta x^2}$$

```
0.00250694
```

```
dd = Table[0, {tlx}]
```

```
{0, 0, 0, 0, 0, 0, 0, 0, 0, 0, 0, 0, 0, 0, 0, 0, 0, 0, 0, 0}
```

```
Do[dd[[i]] = (D0 * e^(Q/(R*T))) * 10^12, {i, 1, tlx}]; dd
```

```
{12.3588, 12.3588, 12.3588, 12.3588, 12.3588, 12.3588,
 12.3588, 12.3588, 12.3588, 12.3588, 12.3588, 12.3588, 12.3588,
 12.3588, 12.3588, 12.3588, 12.3588, 12.3588, 12.3588, 12.3588}
```

```
ListPlot[dd,  PlotJoined → True]
```

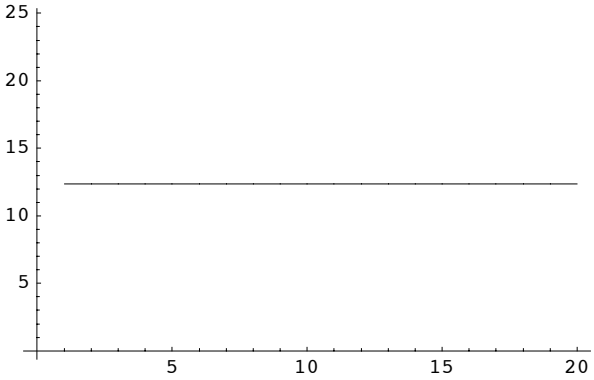

- Graphics -

```
Import["C:\data\San37bPl1-1.li.txt", "List"];
```

General::globf : Cannot open object obtained by expansion of C:\data\San37bPl1-1.li.txt. Mehr…

Import::nffil : File not found during Import[C:\data\San37bPl1-1.li.txt, List]. Mehr…

```
Cli = {7.592439861`, 9.958016617`, 12.83913057`, 15.22711601`, 18.28551326`,
   19.96085414`, 22.38133717`, 23.4173839`, 22.62999764`, 21.04498733`,
   20.24009737`, 17.8617206`, 16.53408499`, 15.62258863`, 14.12374514`,
   12.07960641`, 10.25293105`, 8.500971983`, 7.651834706`, 6.996763838`};
```

```
cle = ListPlot[Cli, PlotRange → {{0, tlx}, {1, 30}},
  PlotJoined → True, PlotStyle → RGBColor[1, 0, 1]]
```

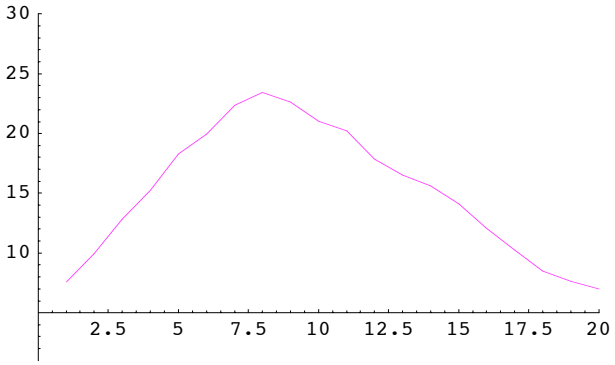

- Graphics -

```
Dimensions[Cli]
```

```
{20}
```

```
tlx
```

```
20.
```

```
a = Table[Cli]; a
```

```
{7.59244, 9.95802, 12.8391, 15.2271, 18.2855, 19.9609,
 22.3813, 23.4174, 22.63, 21.045, 20.2401, 17.8617, 16.5341,
 15.6226, 14.1237, 12.0796, 10.2529, 8.50097, 7.65183, 6.99676}
```

```
n = 4000;
```

```
Do[b = a; Do[a[[i]] = b[[i]] + rr * (dd[[i]] * (b[[i + 1]] - 2 * b[[i]] + b[[i - 1]]) +
       (b[[i + 1]] - b[[i]]) * (dd[[i + 1]] - dd[[i]])), {i, 2, tlx - 1}], {n}]; a
```

```
{7.59244, 7.63554, 7.6766, 7.71366, 7.74484, 7.76845,
 7.78298, 7.78718, 7.78009, 7.76103, 7.72968, 7.68603, 7.63042,
 7.56351, 7.48628, 7.39997, 7.30608, 7.20632, 7.10256, 6.99676}
```

```
calcprof = ListPlot[a, PlotJoined → True]; Show[cle, calcprof]
```

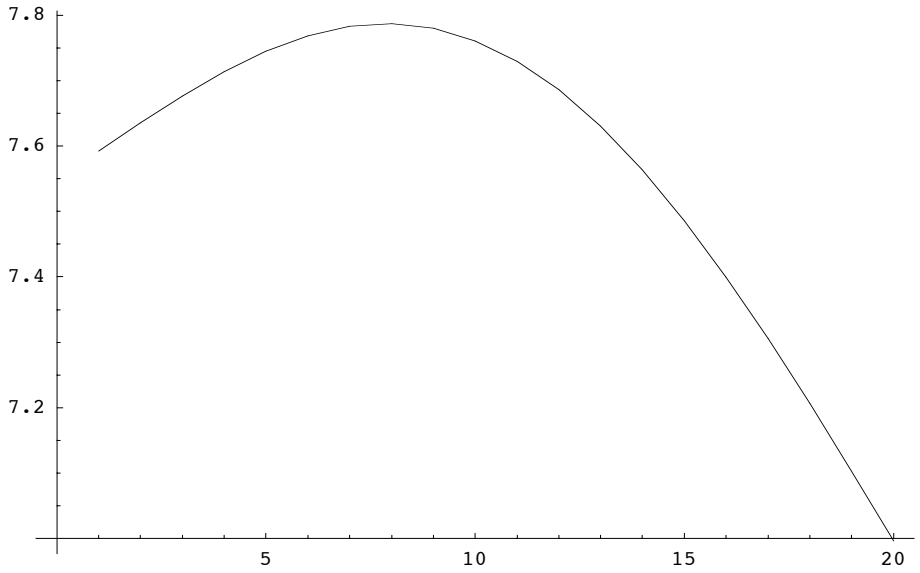

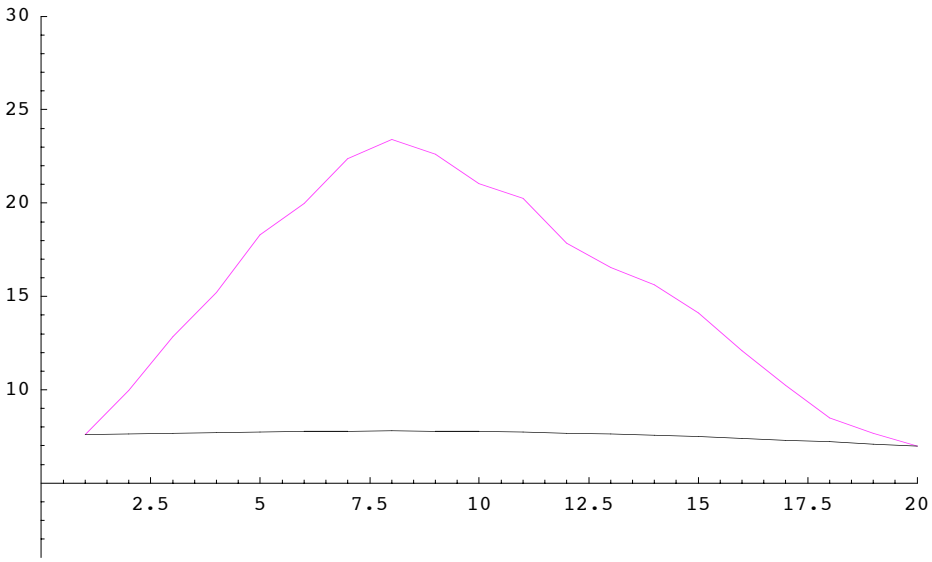


```
- Graphics -
```

```
tt = (n * Δt) / (3600.)
```

```
11.1111
```

APPENDIX 3:
REPRESENTATIVE EPMA AND SIMS DATA

3.1 NEA KAMENI DACITES

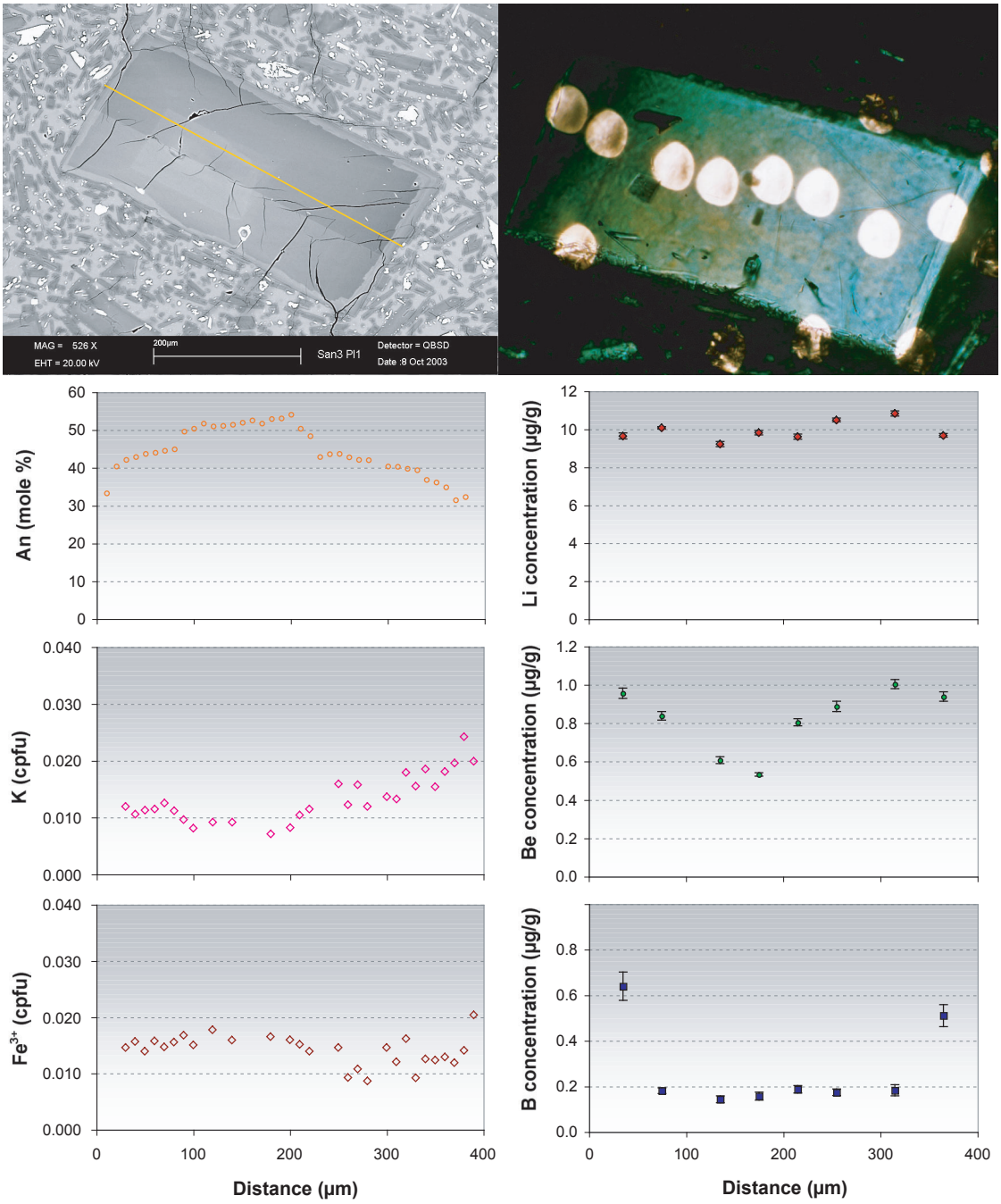

Plagioclase Type-N: *San3b Pl1*

	Data Point	4	8	14	18	22	26	32	37
	Name	San3bPl1	San3bPl1	San3bPl1	San3bPl1	San3bPl1	San3bPl1	San3bPl1	San3bPl1
	Mineral	Fsp	Fsp	Fsp	Fsp	Fsp	Fsp	Fsp	Fsp
	Distance	40	80	140	180	220	260	320	370
%	SiO2	57.949	57.217	55.598	55.288	55.720	57.125	57.838	60.529
	Al2O3	25.670	26.068	27.047	27.159	27.363	26.832	26.085	25.027
	Fe2O3	0.462	0.458	0.465	0.482	0.409	0.273	0.478	0.358
	CaO	8.836	9.162	10.396	10.851	10.067	8.686	8.248	6.640
	Na2O	6.486	6.183	5.412	5.315	5.901	6.396	6.883	7.949
	K2O	0.184	0.194	0.158	0.122	0.199	0.213	0.313	0.347
	Total	99.587	99.282	99.076	99.217	99.659	99.525	99.845	100.850
cpfu	Si	2.609	2.587	2.527	2.513	2.520	2.573	2.599	2.679
	Al	1.362	1.389	1.449	1.455	1.458	1.424	1.381	1.306
	Fe3	0.016	0.016	0.016	0.016	0.014	0.009	0.016	0.012
	Ca	0.426	0.444	0.506	0.528	0.488	0.419	0.397	0.315
	Na	0.566	0.542	0.477	0.468	0.517	0.558	0.600	0.682
	K	0.011	0.011	0.009	0.007	0.011	0.012	0.018	0.020
	Total	4.990	4.988	4.984	4.989	5.009	4.996	5.011	5.013
mole (%)	An	43.0	46.5	51.6	52.7	47.3	43.0	39.9	33.0
µg/g	Li	9.638	10.078	9.213	9.812	9.607	10.487	10.832	9.671
	Be	0.956	0.838	0.607	0.533	0.804	0.887	1.003	0.938
	B	0.639	0.181	0.143	0.157	0.187	0.173	0.183	0.510

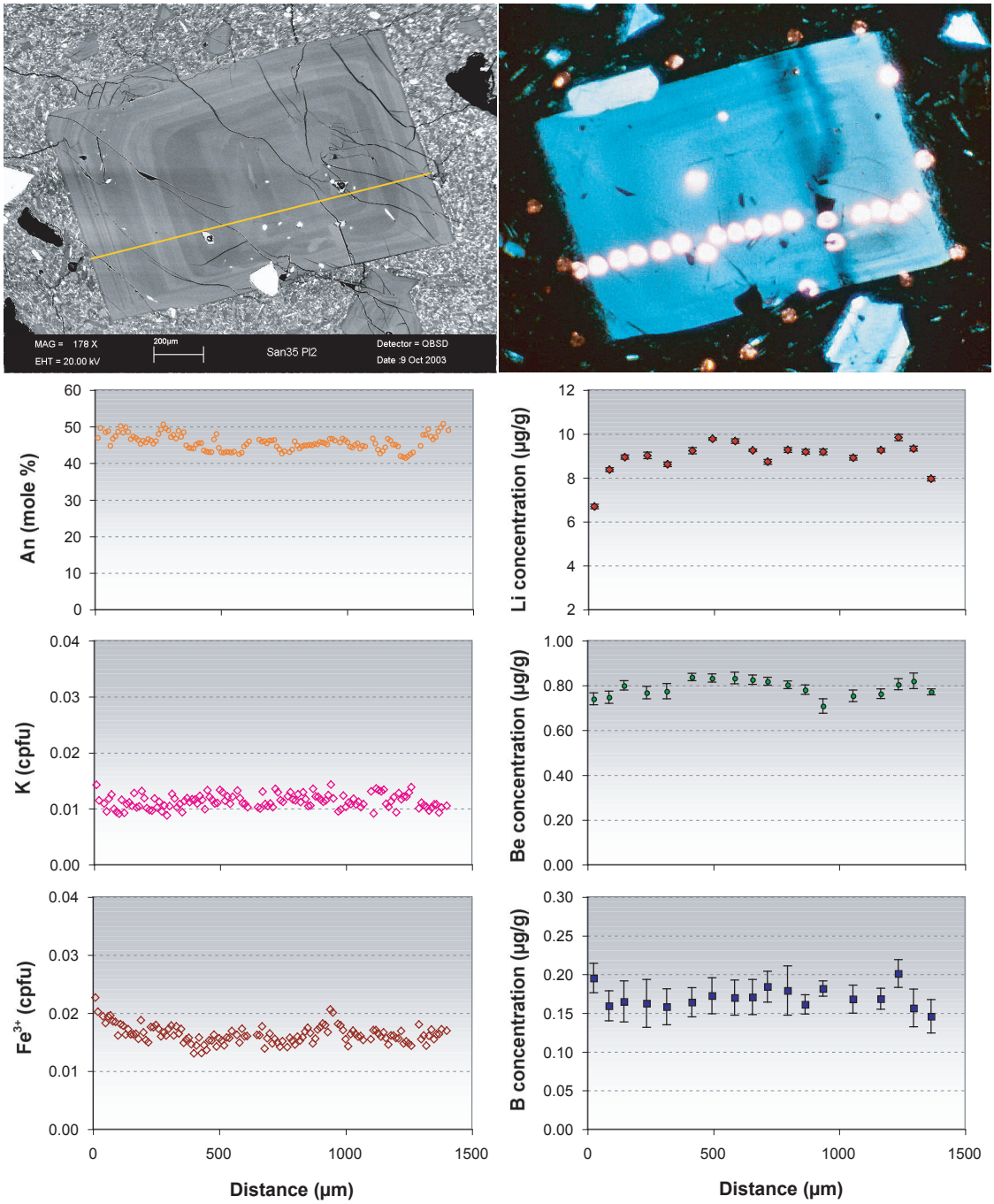

Plagioclase Type-O1: *San35 Pl2*

	Data Point	4	9	15	24	32	42	50	59	66	72	80	87	94	106	117	124	130	137
	Name	san35pl2	san35pl2	san35pl2	san35pl2	san35pl2	san35pl2	san35pl2	san35pl2	san35pl2	san35pl2	san35pl2	san35pl2	san35pl2	san35pl2	san35pl2	san35pl2	san35pl2	san35pl2
	Mineral	Fsp	Fsp	Fsp	Fsp	Fsp	Fsp	Fsp	Fsp	Fsp	Fsp	Fsp	Fsp	Fsp	Fsp	Fsp	Fsp	Fsp	Fsp
	Distance	40	90	150	240	320	420	500	590	660	720	800	870	940	1060	1170	1240	1300	1370
%	SiO2	55.805	56.045	56.612	56.272	56.736	56.561	57.329	56.762	56.244	56.481	57.140	56.971	55.793	57.157	56.618	57.893	56.422	55.037
	Al2O3	27.674	27.586	27.281	27.308	27.400	27.242	26.524	26.537	26.905	27.155	27.212	26.966	26.990	26.637	26.996	26.647	27.586	27.867
	Fe2O3	0.572	0.545	0.482	0.516	0.478	0.465	0.462	0.508	0.475	0.458	0.432	0.436	0.603	0.473	0.429	0.449	0.459	0.479
	CaO	9.801	9.895	9.650	9.338	9.758	9.237	8.903	9.110	9.471	9.173	9.221	9.225	9.621	9.214	9.482	8.694	9.787	10.298
	Na2O	5.750	5.763	5.916	6.015	6.120	6.086	6.513	6.236	6.144	6.279	6.244	6.148	6.055	6.269	6.079	6.647	5.889	5.723
	K2O	0.189	0.163	0.183	0.205	0.207	0.213	0.232	0.189	0.173	0.235	0.200	0.236	0.246	0.178	0.179	0.212	0.193	0.160
	Total	99.791	99.997	100.124	99.654	100.699	99.804	99.963	99.342	99.412	99.781	100.449	99.982	99.308	99.928	99.783	100.542	100.336	99.564
cpfu	Si	2.517	2.522	2.542	2.538	2.536	2.546	2.576	2.566	2.545	2.545	2.555	2.559	2.531	2.569	2.550	2.583	2.529	2.494
	Al	1.471	1.463	1.444	1.452	1.443	1.445	1.404	1.414	1.435	1.442	1.434	1.428	1.443	1.411	1.433	1.401	1.458	1.488
	Fe3	0.019	0.018	0.016	0.018	0.016	0.016	0.016	0.017	0.016	0.016	0.015	0.015	0.021	0.016	0.015	0.015	0.015	0.016
	Ca	0.474	0.477	0.464	0.451	0.467	0.445	0.429	0.441	0.459	0.443	0.442	0.444	0.468	0.444	0.458	0.416	0.470	0.500
	Na	0.503	0.503	0.515	0.526	0.530	0.531	0.567	0.547	0.539	0.549	0.541	0.535	0.533	0.546	0.531	0.575	0.512	0.503
	K	0.011	0.009	0.010	0.012	0.012	0.012	0.013	0.011	0.010	0.014	0.011	0.014	0.014	0.010	0.010	0.012	0.011	0.009
	Total	4.995	4.993	4.991	4.996	5.005	4.995	5.005	4.997	5.004	5.007	4.997	4.994	5.010	4.996	4.997	5.002	4.995	5.010
mole (%)	An	48.7	48.8	47.0	46.6	47.9	44.9	43.4	44.3	46.2	45.0	45.1	45.2	46.6	44.5	46.1	42.0	46.9	49.8
µg/g	Li	6.683	8.360	8.935	9.008	8.604	9.225	9.764	9.662	9.243	8.717	9.259	9.180	9.173	8.909	9.247	9.827	9.316	7.948
	Be	0.740	0.747	0.799	0.768	0.774	0.837	0.832	0.832	0.825	0.818	0.802	0.780	0.707	0.753	0.762	0.804	0.820	0.771
	B	0.195	0.159	0.165	0.162	0.158	0.164	0.172	0.170	0.170	0.184	0.179	0.161	0.181	0.168	0.168	0.201	0.156	0.146

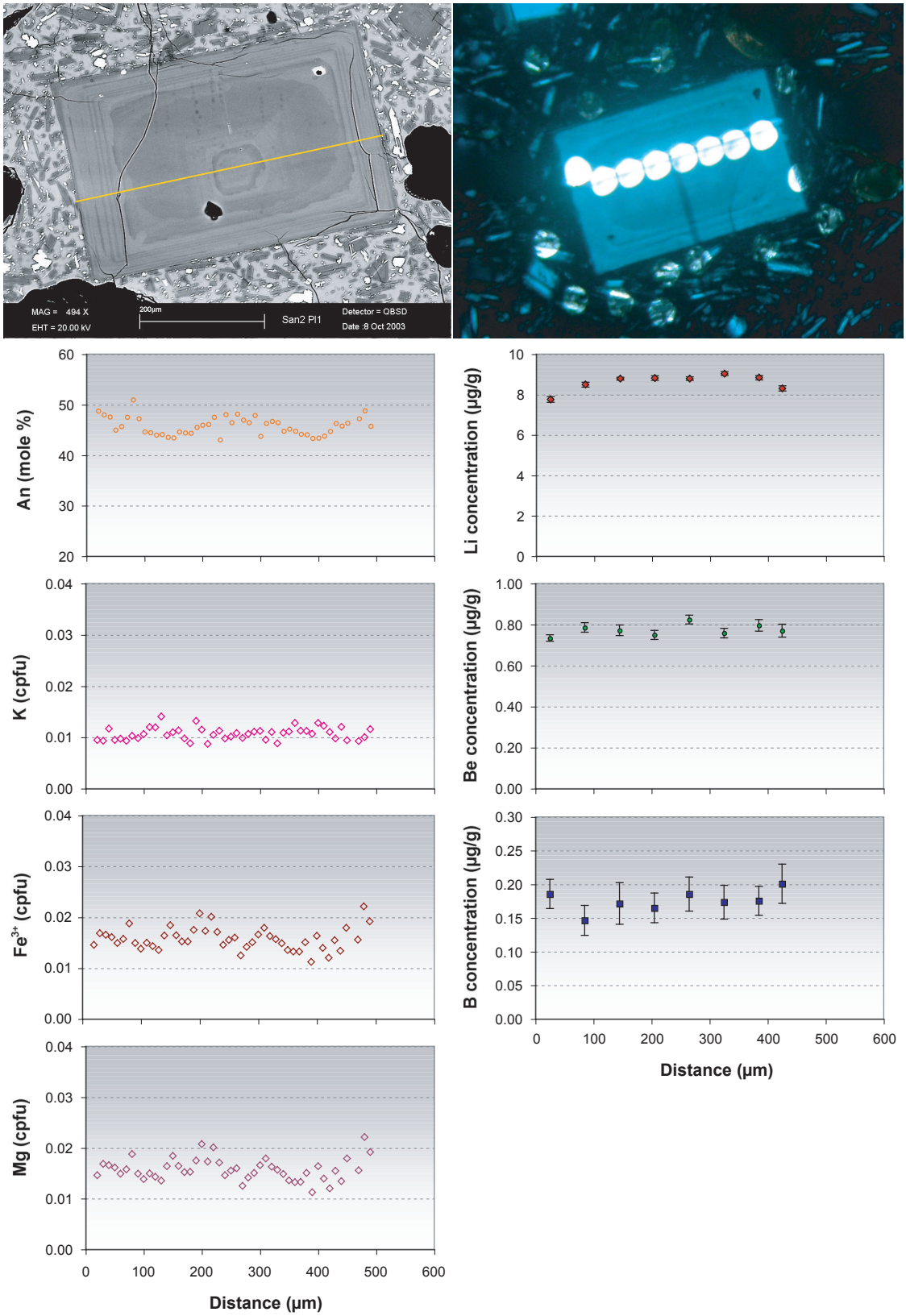

Plagioclase Type-O1: *San2b Pl1*

	Data Point	4	10	16	22	28	34	40	44
	Name	San2bpl1	San2bpl1	San2bpl1	San2bpl1	San2bpl1	San2bpl1	San2bpl1	San2bpl1
	Mineral	Fsp	Fsp	Fsp	Fsp	Fsp	Fsp	Fsp	Fsp
	Distance	40	100	160	220	280	340	400	440
%	SiO2	56.449	57.566	57.175	56.389	56.591	57.371	57.649	57.256
	Al2O3	28.268	27.623	27.423	28.041	28.096	27.695	27.442	27.096
	Fe2O3	0.495	0.415	0.489	0.598	0.422	0.445	0.490	0.399
	MgO	0.036	0.035	0.028	0.033	0.030	0.033	0.032	0.032
	CaO	9.833	9.243	9.079	9.807	9.724	9.233	9.019	9.484
	Na2O	5.974	6.330	6.210	5.970	6.178	6.276	6.488	6.186
	K2O	0.206	0.188	0.199	0.184	0.188	0.192	0.226	0.211
	Total	101.261	101.400	100.603	101.022	101.229	101.245	101.346	100.664
cpfu	Si	2.510	2.549	2.551	2.513	2.517	2.545	2.555	2.556
	Al	1.481	1.442	1.442	1.473	1.473	1.448	1.433	1.426
	Fe3	0.017	0.014	0.016	0.020	0.014	0.015	0.016	0.013
	Mg	0.002	0.002	0.002	0.002	0.002	0.002	0.002	0.002
	Ca	0.468	0.439	0.434	0.468	0.463	0.439	0.428	0.454
	Na	0.515	0.544	0.537	0.516	0.533	0.540	0.558	0.535
	K	0.012	0.011	0.011	0.010	0.011	0.011	0.013	0.012
	Total	5.005	5.000	4.994	5.003	5.012	4.999	5.005	4.998
mole (%)	An	46.9	45.5	44.2	45.6	47.2	45.5	43.6	46.2
µg/g	Li	7.753	8.491	8.783	8.812	8.789	9.036	8.834	8.304
	Be	0.734	0.785	0.771	0.749	0.824	0.758	0.796	0.770
	B	0.186	0.146	0.171	0.165	0.186	0.173	0.175	0.201

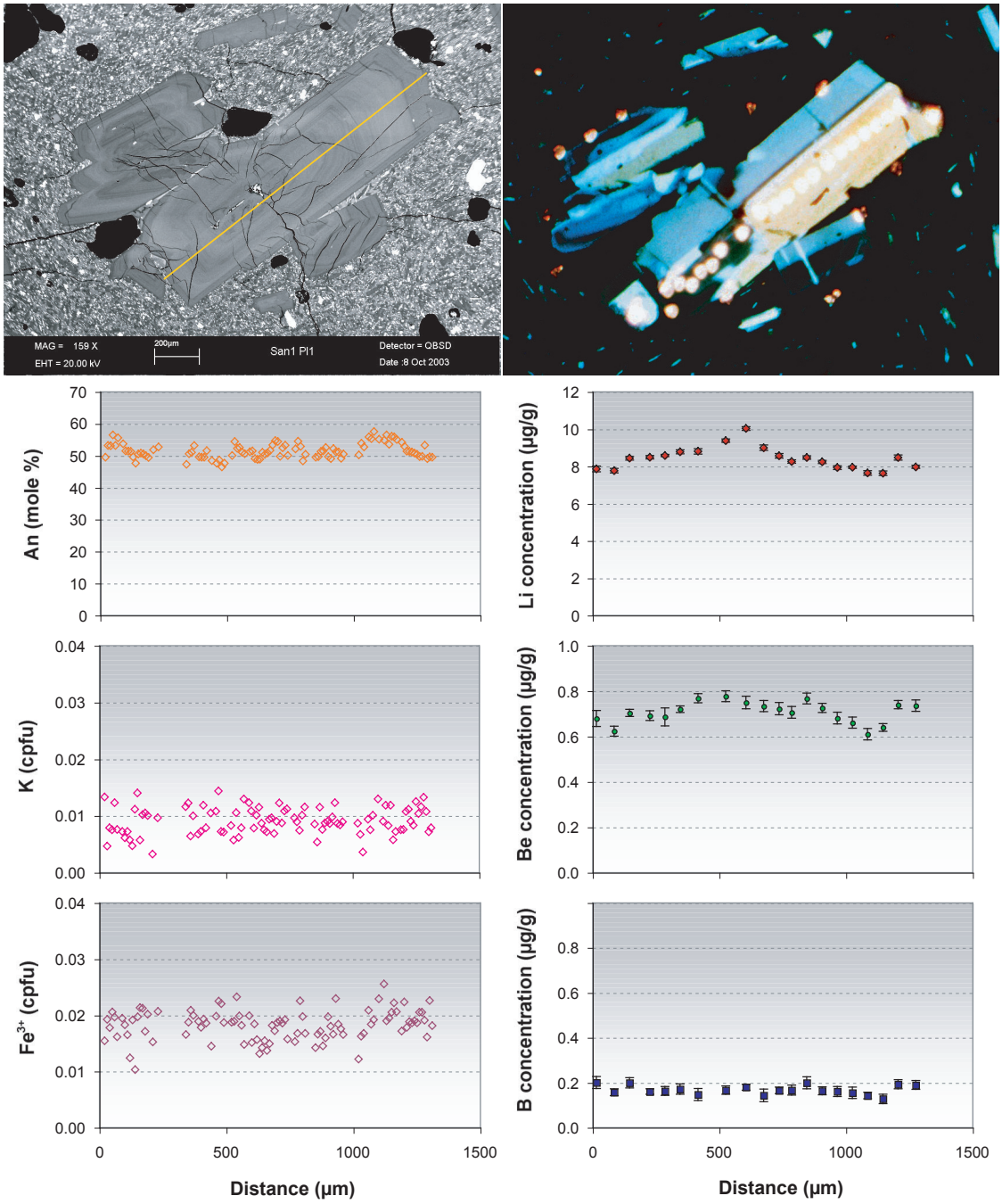

Plagioclase Type-O1: *San1b Pl1*

	Data Point	3	10	16	23	29	36	42	54	62	69	74	80	87	93	96	106	110	116	123	130
	Name	San1bPl1	San1bPl1	San1bPl1	San1bPl1	San1bPl1	San1bPl1	San1bPl1	San1bPl1	San1bPl1	San1bPl1	San1bPl1	San1bPl1	San1bPl1	San1bPl1	San1bPl1	San1bPl1	San1bPl1	San1bPl1	San1bPl1	San1bPl1
	Mineral	Fsp	Fsp	Fsp	Fsp	Fsp	Fsp	Fsp	Fsp	Fsp	Fsp	Fsp	Fsp	Fsp	Fsp	Fsp	Fsp	Fsp	Fsp	Fsp	Fsp
	Distance	30	100	160	230	290	360	420	540	620	690	740	800	870	930	960	1060	1100	1160	1230	1300
%	SiO2	55.852	54.430	55.500	55.373	55.891	55.733	55.215	54.383	55.793	53.972	55.512	56.133	55.341	55.027	55.870	53.929	53.906	53.330	54.558	55.656
	Al2O3	28.666	27.894	27.850	28.130	27.965	28.457	27.565	28.358	27.826	28.317	27.253	27.325	27.788	27.406	28.347	28.859	29.112	29.008	28.538	28.041
	Fe2O3	0.576	0.533	0.632	0.613	0.499	0.619	0.546	0.680	0.462	0.503	0.462	0.583	0.503	0.673	0.492	0.613	0.675	0.650	0.548	0.669
	CaO	10.760	10.590	10.806	10.986	10.096	10.077	10.561	10.403	9.933	11.321	10.292	9.833	10.529	10.744	10.271	11.321	11.224	11.802	10.593	10.014
	Na2O	5.237	5.509	5.785	5.430	5.250	5.347	5.473	5.234	5.760	5.176	5.676	5.799	5.517	5.643	5.562	4.939	5.051	5.153	5.585	5.625
	K2O	0.082	0.106	0.100	0.169	0.207	0.113	0.137	0.182	0.176	0.119	0.194	0.176	0.200	0.213	0.157	0.163	0.225	0.100	0.157	0.125
	Total	101.173	99.062	100.673	100.701	99.908	100.346	99.497	99.240	99.950	99.408	99.389	99.849	99.878	99.706	100.699	99.824	100.193	100.043	99.979	100.130
cpfu	Si	2.487	2.481	2.492	2.484	2.514	2.497	2.503	2.472	2.513	2.456	2.518	2.530	2.499	2.496	2.498	2.443	2.435	2.419	2.465	2.503
	Al	1.504	1.498	1.474	1.487	1.483	1.503	1.473	1.519	1.477	1.519	1.457	1.451	1.479	1.465	1.494	1.541	1.550	1.551	1.520	1.486
	Fe3	0.019	0.018	0.021	0.021	0.017	0.021	0.019	0.023	0.016	0.017	0.016	0.020	0.017	0.023	0.017	0.021	0.023	0.022	0.019	0.023
	Ca	0.513	0.517	0.520	0.528	0.487	0.484	0.513	0.507	0.479	0.552	0.500	0.475	0.509	0.522	0.492	0.549	0.543	0.574	0.513	0.482
	Na	0.452	0.487	0.504	0.472	0.458	0.465	0.481	0.461	0.503	0.457	0.499	0.507	0.483	0.496	0.482	0.434	0.442	0.453	0.489	0.490
	K	0.005	0.006	0.006	0.010	0.012	0.006	0.008	0.011	0.010	0.007	0.011	0.010	0.012	0.012	0.009	0.009	0.013	0.006	0.009	0.007
	Total	4.980	5.007	5.016	5.003	4.971	4.976	4.996	4.993	4.998	5.008	5.001	4.993	5.000	5.014	4.992	4.998	5.006	5.024	5.015	4.992
mole (%)	An	51.9	52.2	50.6	53.2	49.2	51.6	49.4	53.1	48.9	54.2	50.7	50.6	50.9	51.5	52.2	54.8	55.1	55.7	51.1	49.4
µg/g	Li	7.858	7.771	8.439	8.487	8.585	8.786	8.805	9.379	10.035	8.998	8.574	8.263	8.476	8.238	7.935	7.956	7.652	7.630	8.469	7.977
	Be	0.679	0.624	0.704	0.692	0.687	0.720	0.768	0.777	0.750	0.734	0.722	0.706	0.767	0.726	0.681	0.661	0.610	0.640	0.740	0.736
	B	0.201	0.157	0.199	0.161	0.163	0.171	0.147	0.167	0.180	0.143	0.165	0.167	0.199	0.164	0.161	0.155	0.143	0.128	0.193	0.190

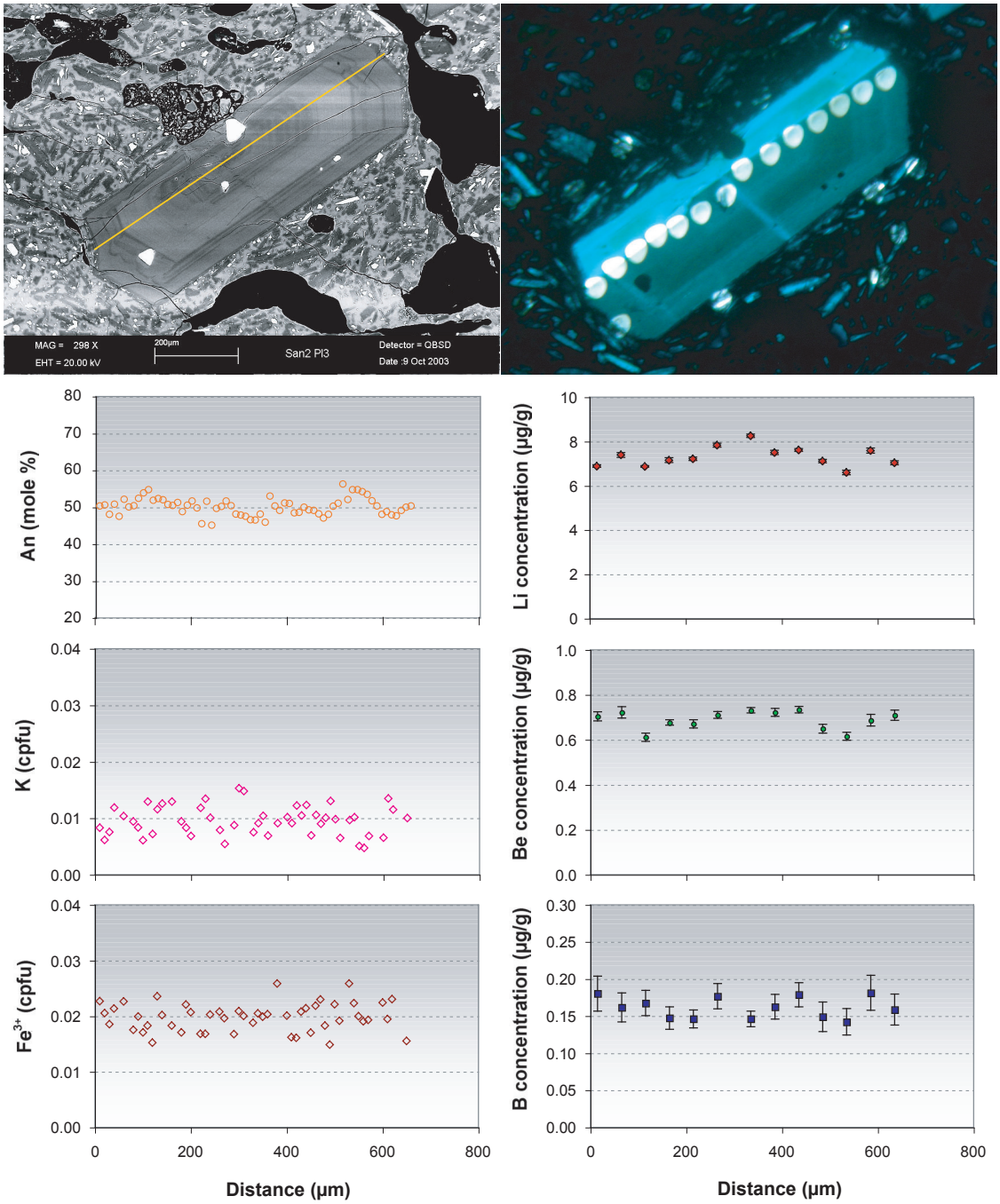

Plagioclase Type-O1: *San2b Pl4*

	Data Point	2	7	12	17	22	27	34	39	44	49	54	59	64
	Name	San2bPl4	San2bPl4	San2bPl4	San2bPl4	San2bPl4	San2bPl4	San2bPl4	San2bPl4	San2bPl4	San2bPl4	San2bPl4	San2bPl4	San2bPl4
	Mineral	Fsp	Fsp	Fsp	Fsp	Fsp	Fsp	Fsp	Fsp	Fsp	Fsp	Fsp	Fsp	Fsp
	Distance	20	70	120	170	220	270	340	390	440	490	540	590	640
%	SiO2	54.618	54.661	54.122	53.925	56.205	54.631	55.523	53.949	54.708	54.749	53.183	54.785	54.956
	Al2O3	28.060	27.079	28.891	28.290	27.308	27.999	27.264	27.676	27.572	27.901	28.874	27.563	27.601
	Fe2O3	0.603	0.562	0.448	0.448	0.496	0.573	0.599	0.453	0.623	0.435	0.652	0.616	0.436
	CaO	10.800	10.484	10.879	10.471	9.523	10.397	9.684	10.401	10.165	10.200	11.739	9.584	10.052
	Na2O	5.765	5.740	5.485	5.421	6.388	5.295	5.777	5.423	5.763	5.531	5.192	5.737	5.509
	K2O	0.106	0.149	0.125	0.118	0.206	0.094	0.157	0.163	0.212	0.225	0.175	0.137	0.075
	Total	99.952	98.675	99.950	98.673	100.126	98.989	99.004	98.065	99.043	99.041	99.815	98.422	98.629
cpfu	Si	2.472	2.503	2.448	2.466	2.529	2.487	2.524	2.483	2.494	2.492	2.419	2.506	2.507
	Al	1.497	1.461	1.540	1.525	1.448	1.502	1.461	1.501	1.481	1.497	1.548	1.486	1.484
	Fe3	0.021	0.019	0.015	0.015	0.017	0.020	0.020	0.016	0.021	0.015	0.022	0.021	0.015
	Ca	0.524	0.514	0.527	0.513	0.459	0.507	0.472	0.513	0.497	0.497	0.572	0.470	0.491
	Na	0.506	0.510	0.481	0.481	0.557	0.467	0.509	0.484	0.509	0.488	0.458	0.509	0.487
	K	0.006	0.009	0.007	0.007	0.012	0.005	0.009	0.010	0.012	0.013	0.010	0.008	0.004
	Total	5.025	5.016	5.019	5.007	5.023	4.989	4.995	5.006	5.015	5.003	5.030	4.999	4.989
mole (%)	An	49.8	51.2	53.5	50.4	49.0	51.0	46.6	50.7	49.6	49.9	55.4	49.1	50.4
µg/g	Li	6.883	7.391	6.868	7.154	7.215	7.827	8.249	7.498	7.613	7.113	6.597	7.588	7.034
	Be	0.704	0.722	0.611	0.677	0.671	0.711	0.731	0.722	0.734	0.649	0.616	0.687	0.709
	B	0.180	0.162	0.168	0.147	0.146	0.177	0.146	0.163	0.179	0.149	0.142	0.181	0.159

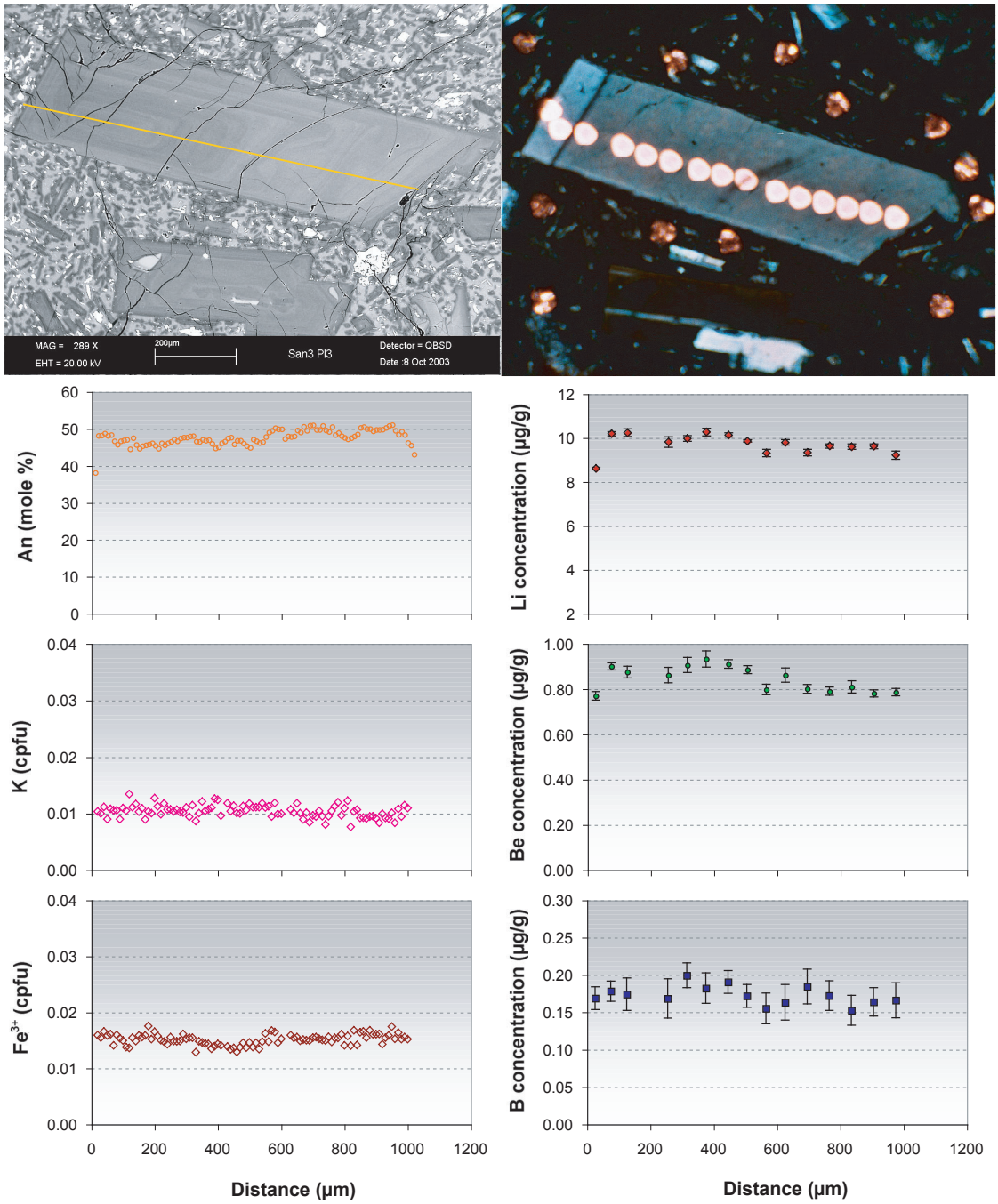

Plagioclase Type-O1: *San3b Pl3*

	Data Point	4	9	14	27	33	39	46	52	58	64	71	78	85	92	99
	Name	San3bPl3	San3bPl3	San3bPl3	San3bPl3	San3bPl3	San3bPl3	San3bPl3	San3bPl3	San3bPl3	San3bPl3	San3bPl3	San3bPl3	San3bPl3	San3bPl3	San3bPl3
	Mineral	Fsp	Fsp	Fsp	Fsp	Fsp	Fsp	Fsp	Fsp	Fsp	Fsp	Fsp	Fsp	Fsp	Fsp	Fsp
	Distance	40	90	140	270	330	390	460	520	580	640	710	780	850	920	990
%	SiO2	56.486	56.856	57.155	56.394	57.063	57.115	56.832	56.982	55.694	56.398	55.897	56.039	55.636	55.838	55.955
	Al2O3	27.829	27.725	27.678	27.882	27.901	27.546	27.952	27.907	28.411	28.179	28.300	28.149	28.219	28.528	28.190
	Fe2O3	0.493	0.458	0.445	0.439	0.386	0.416	0.386	0.435	0.488	0.460	0.462	0.458	0.486	0.426	0.462
	CaO	10.080	9.667	9.542	9.510	9.638	9.176	9.691	9.580	10.171	10.010	10.312	10.070	10.308	10.325	9.944
	Na2O	5.838	6.085	6.256	5.978	6.079	6.232	6.056	6.035	5.560	5.985	5.737	5.787	5.617	5.732	5.856
	K2O	0.196	0.159	0.206	0.187	0.153	0.222	0.177	0.196	0.208	0.178	0.166	0.210	0.161	0.175	0.201
	Total	100.922	100.950	101.282	100.390	101.220	100.707	101.094	101.135	100.532	101.210	100.874	100.713	100.427	101.024	100.608
cpfu	Si	2.520	2.533	2.538	2.525	2.533	2.547	2.528	2.532	2.495	2.510	2.497	2.506	2.496	2.491	2.505
	Al	1.463	1.455	1.448	1.471	1.460	1.448	1.465	1.462	1.500	1.478	1.490	1.484	1.492	1.500	1.487
	Fe3	0.017	0.015	0.015	0.015	0.013	0.014	0.013	0.015	0.016	0.015	0.016	0.015	0.016	0.014	0.016
	Ca	0.482	0.461	0.454	0.456	0.458	0.438	0.462	0.456	0.488	0.477	0.494	0.482	0.496	0.494	0.477
	Na	0.505	0.526	0.539	0.519	0.523	0.539	0.522	0.520	0.483	0.516	0.497	0.502	0.489	0.496	0.508
	K	0.011	0.009	0.012	0.011	0.009	0.013	0.010	0.011	0.012	0.010	0.009	0.012	0.009	0.010	0.011
	Total	4.998	4.999	5.006	4.997	4.996	4.998	5.000	4.995	4.994	5.007	5.003	5.001	4.998	5.005	5.004
mole (%)	An	48.4	46.5	46.0	47.2	47.1	45.3	46.6	46.7	50.0	48.6	50.2	48.6	49.8	50.0	48.0
µg/g	Li	8.609	10.191	10.240	9.816	9.976	10.274	10.136	9.865	9.310	9.799	9.335	9.636	9.603	9.620	9.223
	Be	0.770	0.900	0.875	0.861	0.906	0.933	0.911	0.885	0.798	0.862	0.801	0.790	0.809	0.781	0.786
	B	0.169	0.178	0.174	0.169	0.199	0.182	0.190	0.172	0.155	0.163	0.184	0.172	0.153	0.164	0.166

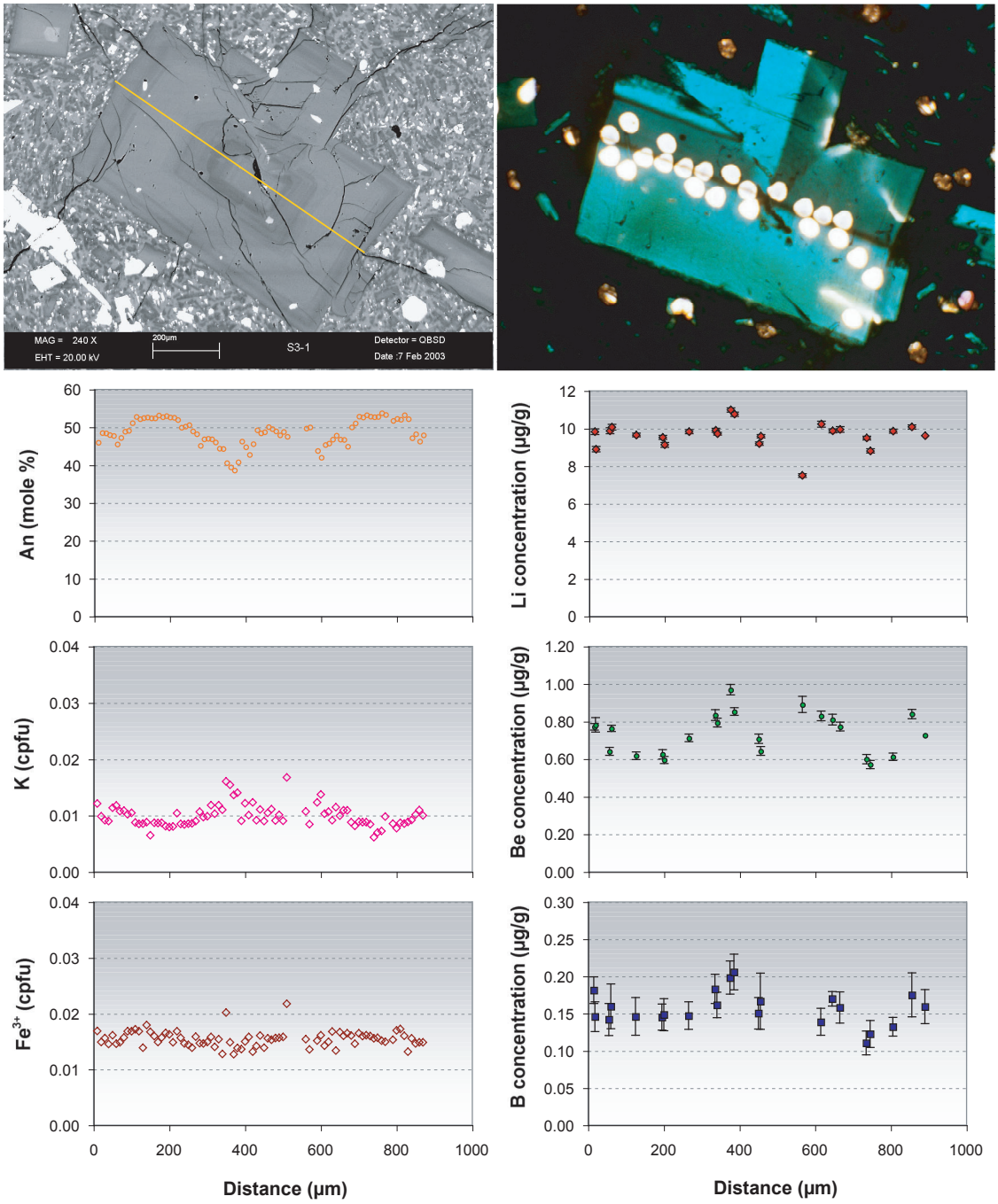

Plagioclase Type-O1: *San3a Pl1*

	Data Point	2	6	13	18	19	20	27	33	34	38	39	45	46	57	60	62	64	67	74	76	81	86	87
	Name	San3Pl1	San3Pl1	San3Pl1	San3Pl1	San3Pl1	San3Pl1	San3Pl1	San3Pl1	San3Pl1	San3Pl1	San3Pl1	San3Pl1	San3Pl1	San3Pl1	San3Pl1	San3Pl1	San3Pl1	San3Pl1	San3Pl1	San3Pl1	San3Pl1	San3Pl1	San3Pl1
	Mineral	Fsp	Fsp	Fsp	Fsp	Fsp	Fsp	Fsp	Fsp	Fsp	Fsp	Fsp	Fsp	Fsp	Fsp	Fsp	Fsp	Fsp	Fsp	Fsp	Fsp	Fsp	Fsp	Fsp
	Distance	20	60	130	180	190	200	270	330	340	380	390	450	460	570	600	620	640	670	740	760	810	860	870
%	SiO2	56.332	57.102	55.213	55.345	55.480	55.136	56.623	57.583	57.664	58.636	57.018	56.197	56.039	56.045	58.373	57.299	56.789	57.457	55.050	55.001	55.271	57.205	56.659
	Al2O3	27.844	27.332	28.462	28.417	28.464	28.517	27.589	27.068	27.045	26.314	27.357	27.941	28.011	28.028	26.375	27.272	27.429	27.208	28.493	28.653	28.462	27.397	27.722
	Fe2O3	0.443	0.435	0.410	0.465	0.490	0.482	0.470	0.460	0.380	0.413	0.405	0.412	0.462	0.402	0.480	0.446	0.398	0.492	0.460	0.448	0.510	0.442	0.442
	CaO	10.130	9.498	10.874	10.767	10.891	11.079	9.693	9.291	9.188	8.374	9.512	10.119	10.308	10.131	8.584	9.478	9.800	9.299	10.921	10.909	10.652	9.528	9.933
	Na2O	5.915	6.260	5.420	5.319	5.314	5.488	5.727	6.407	6.352	6.693	6.086	5.856	5.661	5.581	6.538	6.190	5.884	6.284	5.389	5.171	5.405	6.095	5.954
	K2O	0.173	0.207	0.149	0.152	0.142	0.139	0.158	0.208	0.194	0.247	0.159	0.158	0.183	0.148	0.242	0.188	0.201	0.192	0.107	0.126	0.152	0.193	0.176
	Total	100.837	100.834	100.528	100.465	100.781	100.841	100.260	101.017	100.823	100.677	100.537	100.683	100.664	100.335	100.592	100.873	100.501	100.932	100.420	100.308	100.452	100.860	100.886
cpfu	Si	2.516	2.546	2.479	2.484	2.483	2.471	2.536	2.562	2.567	2.608	2.548	2.513	2.508	2.512	2.600	2.552	2.540	2.557	2.474	2.473	2.482	2.548	2.527
	Al	1.466	1.437	1.506	1.503	1.501	1.506	1.457	1.419	1.419	1.379	1.441	1.473	1.477	1.481	1.385	1.432	1.446	1.427	1.509	1.518	1.506	1.438	1.457
	Fe3	0.015	0.015	0.014	0.016	0.017	0.016	0.016	0.015	0.013	0.014	0.014	0.014	0.016	0.014	0.016	0.015	0.013	0.016	0.016	0.015	0.017	0.015	0.015
	Ca	0.485	0.454	0.523	0.518	0.522	0.532	0.465	0.443	0.438	0.399	0.455	0.485	0.494	0.487	0.410	0.452	0.470	0.443	0.526	0.525	0.512	0.455	0.475
	Na	0.512	0.541	0.472	0.463	0.461	0.477	0.497	0.553	0.548	0.577	0.527	0.508	0.491	0.485	0.565	0.535	0.510	0.542	0.470	0.451	0.471	0.526	0.515
	K	0.010	0.012	0.009	0.009	0.008	0.008	0.009	0.012	0.011	0.014	0.009	0.009	0.010	0.008	0.014	0.011	0.011	0.011	0.006	0.007	0.009	0.011	0.010
	Total	5.004	5.004	5.002	4.992	4.993	5.010	4.981	5.003	4.997	4.991	4.993	5.002	4.997	4.987	4.989	4.997	4.991	4.998	5.001	4.990	4.996	4.994	4.999
mole (%)	An	47.7	46.9	52.5	53.0	52.9	52.8	47.5	45.0	43.2	42.0	44.0	49.2	49.5	50.1	43.8	46.0	47.2	47.3	52.9	53.4	52.6	47.5	47.2
µg/g	Li	9.827	9.875	9.650	8.898	9.524	9.128	9.829	9.902	9.720	10.981	10.757	9.189	9.585	7.495	10.074	10.229	9.876	9.946	9.488	8.805	9.859	10.079	9.608
	Be	0.772	0.642	0.618	0.782	0.626	0.596	0.713	0.835	0.794	0.970	0.853	0.709	0.643	0.891	0.764	0.831	0.810	0.773	0.601	0.572	0.613	0.840	0.728
	B	0.181	0.142	0.146	0.146	0.145	0.148	0.147	0.183	0.162	0.198	0.206	0.150	0.167	1.495	0.160	0.139	0.170	0.158	0.111	0.123	0.132	0.175	0.159

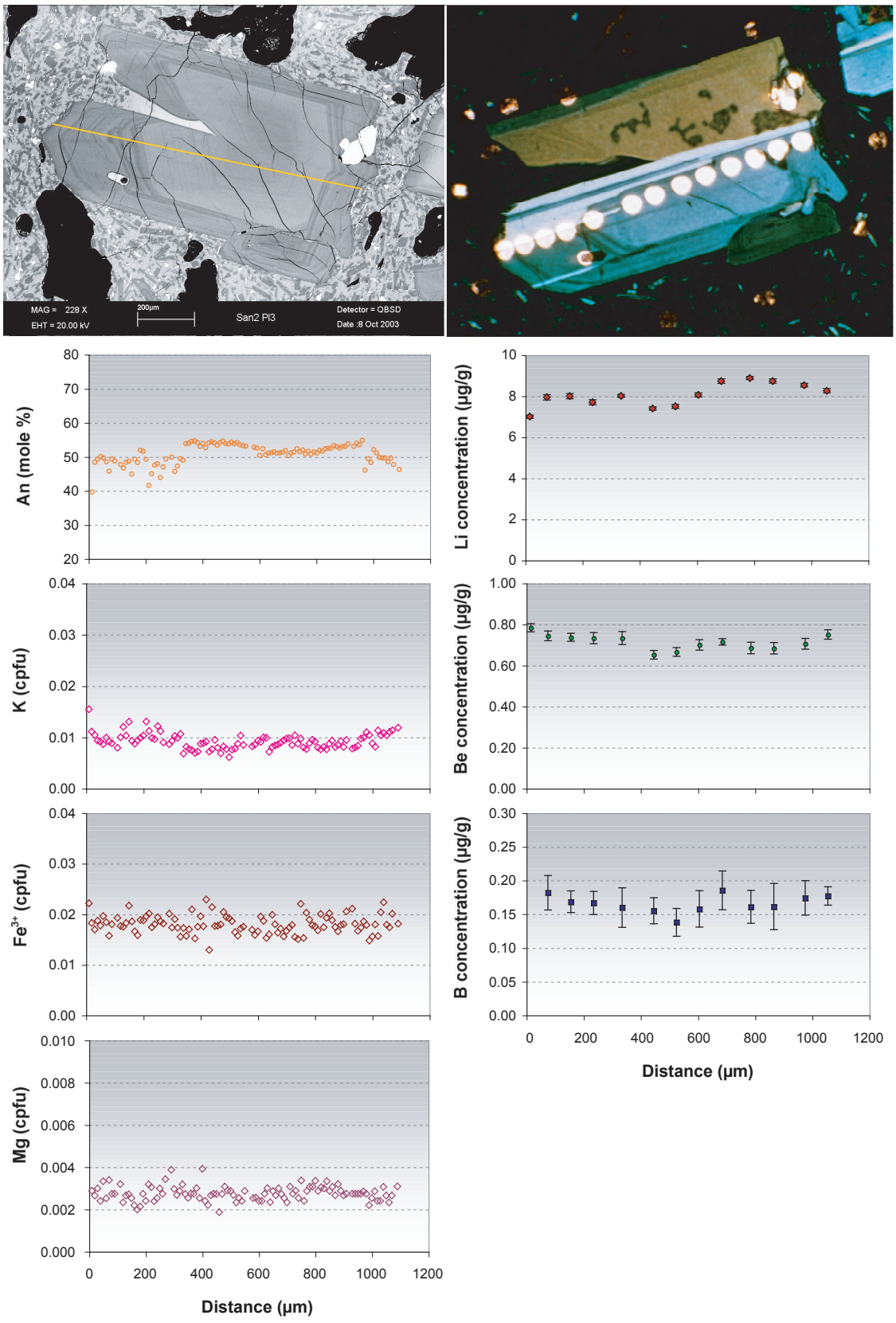

Plagioclase Type-O1: *San2b Pl3*

	Data Point	3	8	16	24	34	45	53	61	69	79	87	98	106
	Name	San2bPl3	San2bPl3	San2bPl3	San2bPl3	San2bPl3	San2bPl3	San2bPl3	San2bPl3	San2bPl3	San2bPl3	San2bPl3	San2bPl3	San2bPl3
	Mineral	Fsp	Fsp	Fsp	Fsp	Fsp	Fsp	Fsp	Fsp	Fsp	Fsp	Fsp	Fsp	Fsp
	Distance	30	80	160	240	340	450	530	610	690	790	870	980	1060
%	SiO2	56.111	56.409	56.113	56.469	54.753	55.112	54.980	55.358	55.619	55.455	55.149	55.906	56.332
	Al2O3	28.300	27.839	28.092	27.765	29.226	29.084	29.046	28.557	28.678	28.493	28.954	27.916	27.960
	Fe2O3	0.506	0.468	0.552	0.536	0.513	0.526	0.468	0.579	0.465	0.528	0.518	0.530	0.518
	MgO	0.045	0.041	0.033	0.038	0.041	0.041	0.038	0.036	0.038	0.046	0.040	0.041	0.035
	CaO	10.234	9.989	10.074	9.913	11.209	11.006	10.891	10.733	10.617	10.529	10.796	10.264	10.276
	Na2O	5.788	5.633	5.701	5.913	5.273	5.277	5.188	5.361	5.416	5.463	5.261	5.763	5.723
	K2O	0.184	0.160	0.163	0.169	0.119	0.167	0.153	0.159	0.165	0.166	0.142	0.192	0.194
	Total	101.168	100.539	100.728	100.803	101.134	101.213	100.764	100.783	100.998	100.680	100.860	100.612	101.038
cpfu	Si	2.500	2.523	2.508	2.522	2.447	2.459	2.461	2.478	2.482	2.484	2.466	2.505	2.512
	Al	1.486	1.467	1.480	1.461	1.539	1.529	1.533	1.507	1.508	1.504	1.526	1.474	1.469
	Fe3	0.017	0.016	0.019	0.018	0.017	0.018	0.016	0.020	0.016	0.018	0.017	0.018	0.017
	Mg	0.003	0.003	0.002	0.003	0.003	0.003	0.003	0.002	0.003	0.003	0.003	0.003	0.002
	Ca	0.488	0.479	0.482	0.474	0.537	0.526	0.522	0.515	0.508	0.505	0.517	0.493	0.491
	Na	0.500	0.488	0.494	0.512	0.457	0.456	0.450	0.465	0.469	0.474	0.456	0.501	0.495
	K	0.010	0.009	0.009	0.010	0.007	0.010	0.009	0.009	0.009	0.009	0.008	0.011	0.011
	Total	5.004	4.985	4.994	4.999	5.007	5.001	4.994	4.996	4.995	4.997	4.994	5.005	4.998
mole (%)	An	49.4	48.1	47.7	46.6	52.4	54.0	53.8	51.3	51.3	51.2	53.1	48.1	48.8
µg/g	Li	7.002	7.949	7.997	7.705	8.013	7.398	7.507	8.062	8.735	8.879	8.736	8.537	8.266
	Be	0.784	0.744	0.737	0.733	0.733	0.652	0.666	0.700	0.715	0.686	0.684	0.705	0.751
	B	0.582	0.182	0.169	0.167	0.160	0.155	0.138	0.158	0.185	0.161	0.161	0.174	0.177

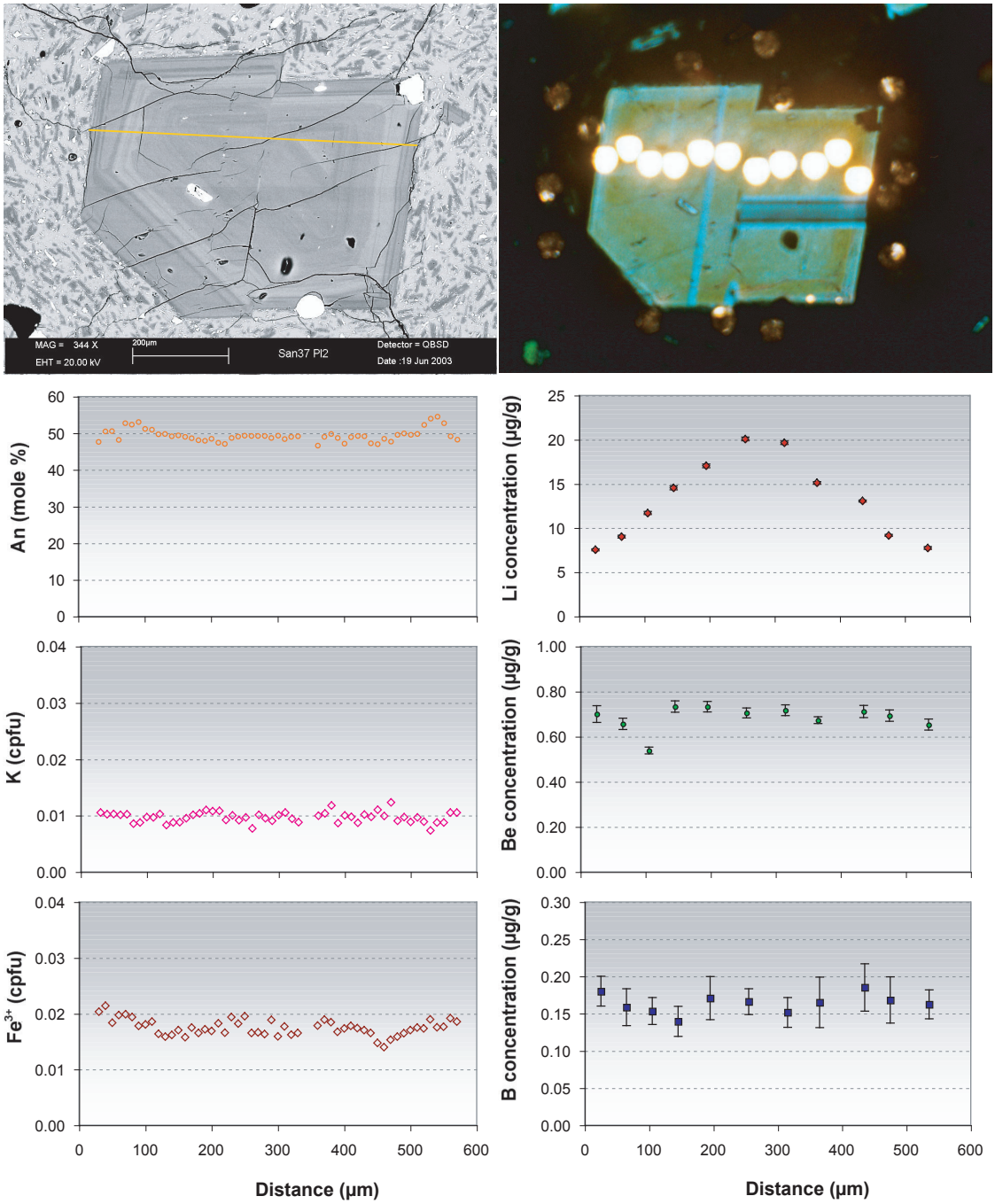

Plagioclase Type-O2: *San37a Pl2*

	Data Point	3	7	11	15	20	26	32	37	44	48	54
	Name	San37Pl2	San37Pl2	San37Pl2	San37Pl2	San37Pl2	San37Pl2	San37Pl2	San37Pl2	San37Pl2	San37Pl2	San37Pl2
	Mineral	Fsp	Fsp	Fsp	Fsp	Fsp	Fsp	Fsp	Fsp	Fsp	Fsp	Fsp
	Distance	30	70	110	150	200	260	320	370	440	480	540
%	SiO2	54.877	54.738	55.478	55.861	55.940	55.716	55.495	55.604	55.917	55.540	54.374
	Al2O3	27.584	28.778	28.202	28.096	27.903	28.088	28.190	28.050	27.814	28.237	28.963
	Fe2O3	0.593	0.589	0.550	0.506	0.500	0.490	0.479	0.560	0.488	0.470	0.518
	CaO	9.825	11.038	10.623	10.201	10.070	10.302	9.969	10.201	9.810	10.309	11.247
	Na2O	5.930	5.432	5.617	5.734	5.873	5.838	5.705	5.827	6.020	5.756	5.148
	K2O	0.181	0.178	0.169	0.154	0.188	0.135	0.164	0.181	0.170	0.158	0.152
	Total	98.990	100.753	100.639	100.552	100.474	100.569	100.002	100.423	100.219	100.470	100.402
cpfu	Si	2.500	2.457	2.488	2.503	2.509	2.498	2.499	2.497	2.513	2.493	2.448
	Al	1.481	1.522	1.491	1.484	1.475	1.484	1.496	1.485	1.473	1.494	1.537
	Fe3	0.020	0.020	0.019	0.017	0.017	0.017	0.016	0.019	0.016	0.016	0.018
	Ca	0.480	0.531	0.510	0.490	0.484	0.495	0.481	0.491	0.472	0.496	0.543
	Na	0.524	0.473	0.488	0.498	0.511	0.508	0.498	0.507	0.525	0.501	0.449
	K	0.011	0.010	0.010	0.009	0.011	0.008	0.009	0.010	0.010	0.009	0.009
	Total	5.016	5.013	5.006	5.000	5.006	5.009	4.999	5.010	5.009	5.008	5.004
mole (%)	An	48.9	51.2	50.8	49.4	48.1	49.4	49.0	48.6	48.0	49.2	53.9
µg/g	Li	7.526	9.017	11.695	14.536	17.033	20.070	19.642	15.101	13.051	9.152	7.736
	Be	0.700	0.657	0.538	0.733	0.733	0.705	0.717	0.673	0.712	0.693	0.653
	B	0.180	0.159	0.153	0.139	0.171	0.166	0.152	0.165	0.185	0.168	0.163

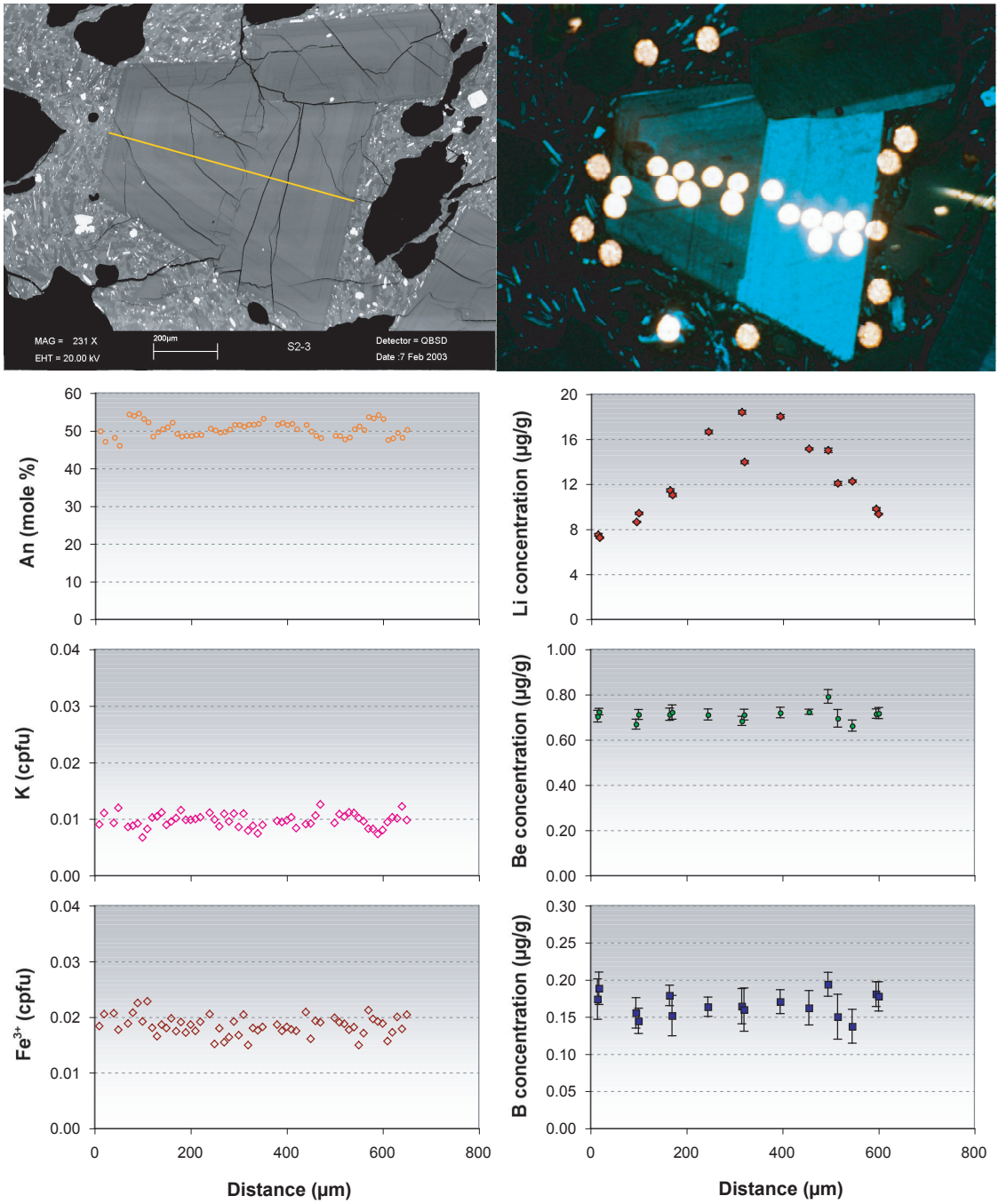

Plagioclase Type-O2: *San2a Pl3*

	Data Point	1	2	10	12	17	19	25	32	34	40	46	52	54	57	62	63
	Name	San2Pl3	San2Pl3	San2Pl3	San2Pl3	San2Pl3	San2Pl3	San2Pl3	San2Pl3	San2Pl3	San2Pl3	San2Pl3	San2Pl3	San2Pl3	San2Pl3	San2Pl3	San2Pl3
	Mineral	Fsp	Fsp	Fsp	Fsp	Fsp	Fsp	Fsp	Fsp	Fsp	Fsp	Fsp	Fsp	Fsp	Fsp	Fsp	Fsp
	Distance	10	20	100	120	170	190	250	320	340	400	460	520	540	570	620	630
%	SiO2	55.739	56.043	54.436	55.878	55.476	56.015	55.707	54.727	54.577	55.059	55.506	55.360	55.410	54.421	56.047	55.514
	Al2O3	28.041	27.589	28.504	27.952	27.867	27.827	27.759	28.536	28.470	28.164	27.933	27.580	28.071	28.587	27.691	27.788
	Fe2O3	0.543	0.606	0.562	0.533	0.513	0.509	0.446	0.439	0.516	0.536	0.569	0.549	0.536	0.625	0.509	0.589
	CaO	10.337	9.768	10.846	9.996	10.278	10.008	10.130	10.693	10.691	10.568	10.092	9.710	10.375	11.130	9.780	10.218
	Na2O	5.726	6.037	5.273	5.866	5.851	5.818	5.555	5.525	5.466	5.465	5.858	5.872	5.621	5.291	5.830	5.767
	K2O	0.157	0.192	0.116	0.178	0.176	0.171	0.171	0.137	0.128	0.169	0.184	0.179	0.192	0.143	0.179	0.175
	Total	100.543	100.235	99.737	100.403	100.161	100.348	99.768	100.057	99.848	99.961	100.142	99.250	100.205	100.197	100.036	100.051
cpfu	Si	2.500	2.519	2.465	2.507	2.499	2.514	2.513	2.469	2.468	2.485	2.500	2.512	2.494	2.457	2.521	2.502
	Al	1.482	1.462	1.521	1.478	1.479	1.472	1.476	1.518	1.517	1.498	1.483	1.475	1.489	1.521	1.468	1.476
	Fe3	0.018	0.020	0.019	0.018	0.017	0.017	0.015	0.015	0.018	0.018	0.019	0.019	0.018	0.021	0.017	0.020
	Ca	0.497	0.470	0.526	0.481	0.496	0.481	0.490	0.517	0.518	0.511	0.487	0.472	0.500	0.538	0.471	0.494
	Na	0.498	0.526	0.463	0.510	0.511	0.506	0.486	0.483	0.479	0.478	0.511	0.517	0.491	0.463	0.508	0.504
	K	0.009	0.011	0.007	0.010	0.010	0.010	0.010	0.008	0.007	0.010	0.011	0.010	0.011	0.008	0.010	0.010
	Total	5.004	5.009	5.000	5.005	5.013	5.000	4.989	5.010	5.008	5.001	5.010	5.005	5.003	5.008	4.996	5.006
mole (%)	An	48.6	48.6	53.4	50.2	50.0	48.7	50.1	51.5	52.3	51.9	48.9	48.2	50.0	52.4	48.4	48.6
µg/g	Li	7.239	7.487	8.632	9.396	11.434	11.021	16.630	18.370	13.945	17.994	15.125	14.998	12.053	12.248	9.780	9.331
	Be	0.724	0.703	0.669	0.711	0.712	0.722	0.711	0.683	0.711	0.720	0.723	0.791	0.694	0.662	0.715	0.717
	B	0.189	0.174	0.156	0.145	0.179	0.152	0.164	0.164	0.160	0.170	0.162	0.194	0.150	0.137	0.181	0.178

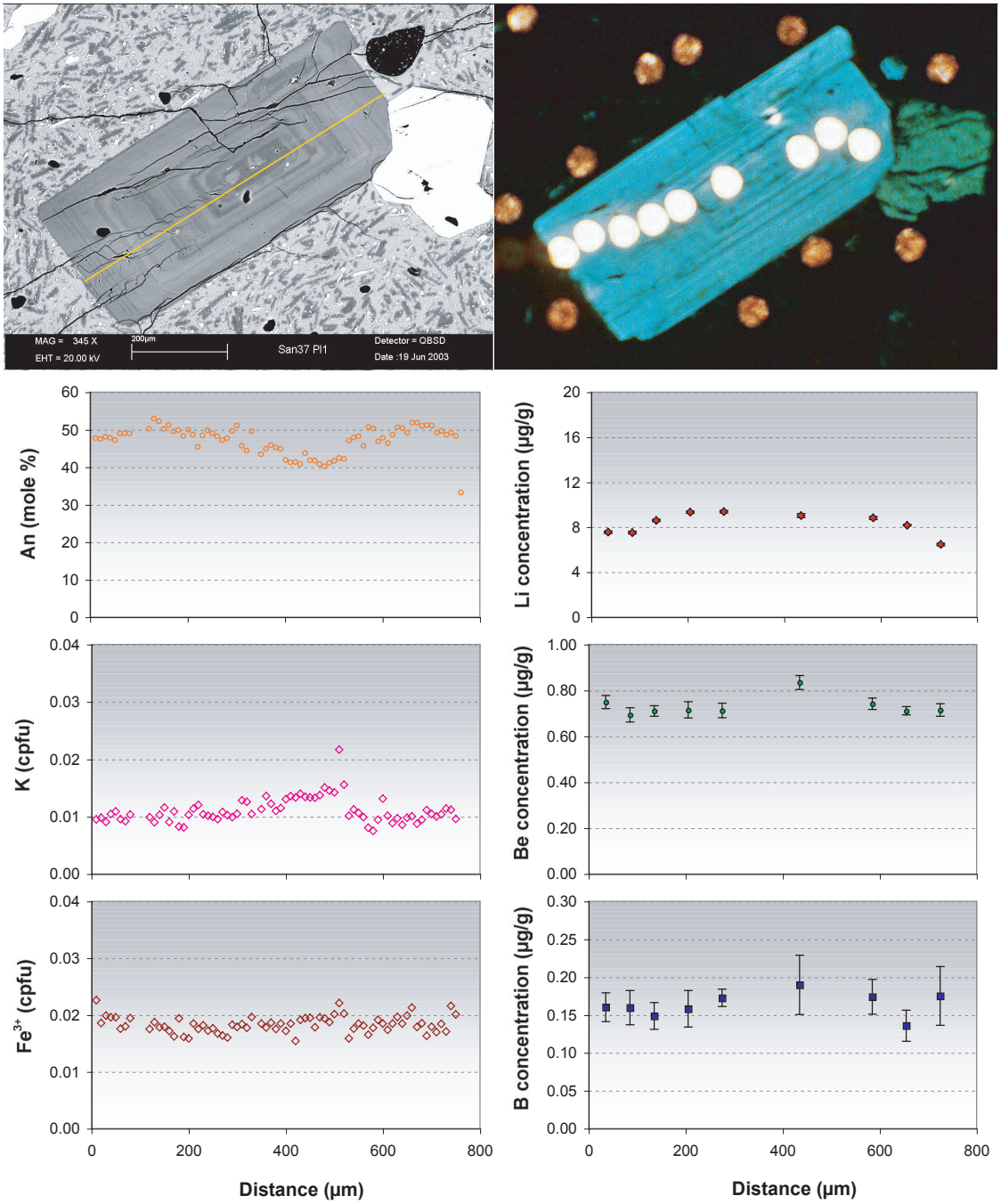

Plagioclase Type-O2: *San37a Pl1*

	Data Point	3	8	13	20	27	43	58	65	72
	Name	San37Pl1	San37Pl1	San37Pl1	San37Pl1	San37Pl1	San37Pl1	San37Pl1	San37Pl1	San37Pl1
	Mineral	Fsp	Fsp	Fsp	Fsp	Fsp	Fsp	Fsp	Fsp	Fsp
	Distance	30	80	130	200	270	430	580	650	720
%	SiO2	55.795	53.745	54.635	55.420	55.891	57.953	55.403	55.525	55.585
	Al2O3	27.875	28.700	28.901	28.033	27.701	26.486	28.353	28.171	28.292
	Fe2O3	0.588	0.566	0.555	0.468	0.482	0.569	0.525	0.588	0.546
	CaO	10.024	10.127	11.035	10.262	9.747	8.438	10.487	10.179	10.269
	Na2O	5.950	5.795	5.385	5.651	5.975	6.709	5.684	5.765	5.718
	K2O	0.158	0.178	0.157	0.179	0.188	0.245	0.131	0.171	0.182
	Total	100.390	99.111	100.668	100.013	99.984	100.400	100.583	100.399	100.592
cpfu	Si	2.506	2.451	2.454	2.498	2.517	2.589	2.485	2.494	2.492
	Al	1.475	1.542	1.530	1.489	1.470	1.395	1.499	1.491	1.495
	Fe3	0.020	0.019	0.019	0.016	0.016	0.019	0.018	0.020	0.018
	Ca	0.482	0.495	0.531	0.496	0.470	0.404	0.504	0.490	0.493
	Na	0.518	0.512	0.469	0.494	0.522	0.581	0.494	0.502	0.497
	K	0.009	0.010	0.009	0.010	0.011	0.014	0.007	0.010	0.010
	Total	5.010	5.030	5.011	5.002	5.006	5.002	5.008	5.007	5.005
mole (%)	An	48.0	50.3	52.0	49.1	47.9	42.1	49.4	50.7	49.3
µg/g	Li	7.547	7.513	8.591	9.332	9.366	9.028	8.809	8.173	6.454
	Be	0.749	0.693	0.710	0.715	0.712	0.834	0.742	0.711	0.714
	B	0.160	0.160	0.149	0.158	0.173	0.190	0.174	0.136	0.175

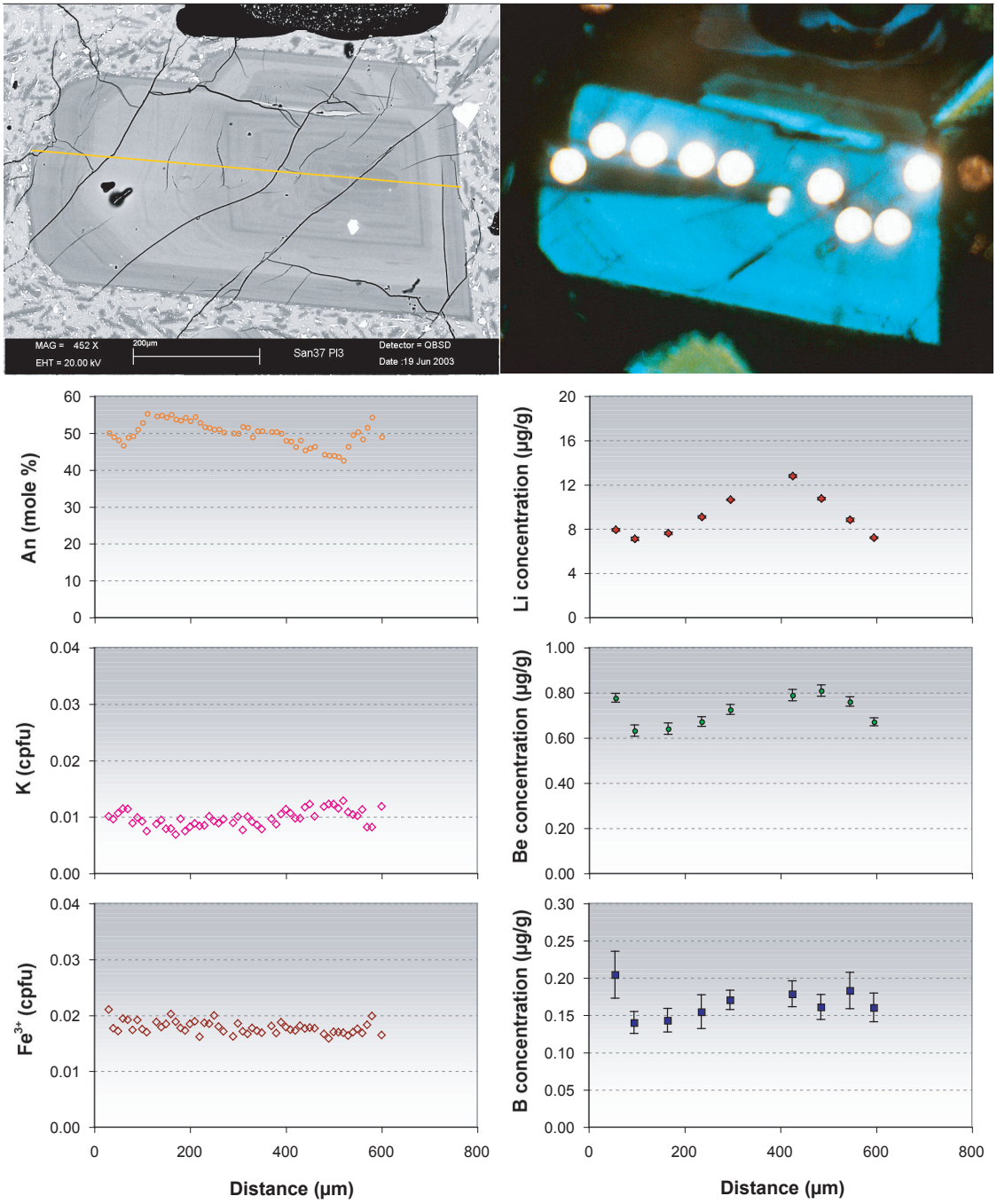

Plagioclase Type-O2: *San37a Pl3*

	Data Point	6	10	17	24	30	43	49	55	60
	Name	San37Pl3	San37Pl3	San37Pl3	San37Pl3	San37Pl3	San37Pl3	San37Pl3	San37Pl3	San37Pl3
	Mineral	Fsp	Fsp	Fsp	Fsp	Fsp	Fsp	Fsp	Fsp	Fsp
	Distance	60	100	170	240	300	430	490	550	600
%	SiO2	56.710	54.494	54.165	54.738	55.609	55.731	56.849	55.427	55.838
	Al2O3	27.467	28.831	28.971	28.593	28.143	27.907	27.178	28.226	27.843
	Fe2O3	0.575	0.515	0.553	0.543	0.548	0.536	0.468	0.519	0.485
	CaO	9.558	10.816	11.040	10.663	10.283	10.008	9.085	10.445	10.047
	Na2O	6.039	5.341	5.242	5.558	5.696	5.970	6.391	5.692	5.789
	K2O	0.200	0.159	0.119	0.175	0.175	0.169	0.214	0.177	0.206
	Total	100.549	100.156	100.090	100.270	100.454	100.321	100.185	100.486	100.208
cpfu	Si	2.537	2.457	2.446	2.466	2.496	2.504	2.550	2.489	2.510
	Al	1.448	1.532	1.542	1.518	1.489	1.478	1.437	1.494	1.475
	Fe3	0.019	0.017	0.019	0.018	0.019	0.018	0.016	0.018	0.016
	Ca	0.458	0.523	0.534	0.515	0.494	0.482	0.437	0.503	0.484
	Na	0.524	0.467	0.459	0.486	0.496	0.520	0.556	0.496	0.505
	K	0.011	0.009	0.007	0.010	0.010	0.010	0.012	0.010	0.012
	Total	4.997	5.006	5.007	5.013	5.003	5.012	5.008	5.008	5.002
mole (%)	An	47.9	53.0	54.1	51.4	50.6	46.6	44.0	49.4	49.0
µg/g	Li	7.897	7.092	7.594	9.059	10.618	12.756	10.725	8.812	7.196
	Be	0.777	0.632	0.640	0.672	0.725	0.789	0.809	0.760	0.671
	B	0.204	0.140	0.143	0.155	0.170	0.179	0.161	0.183	0.160

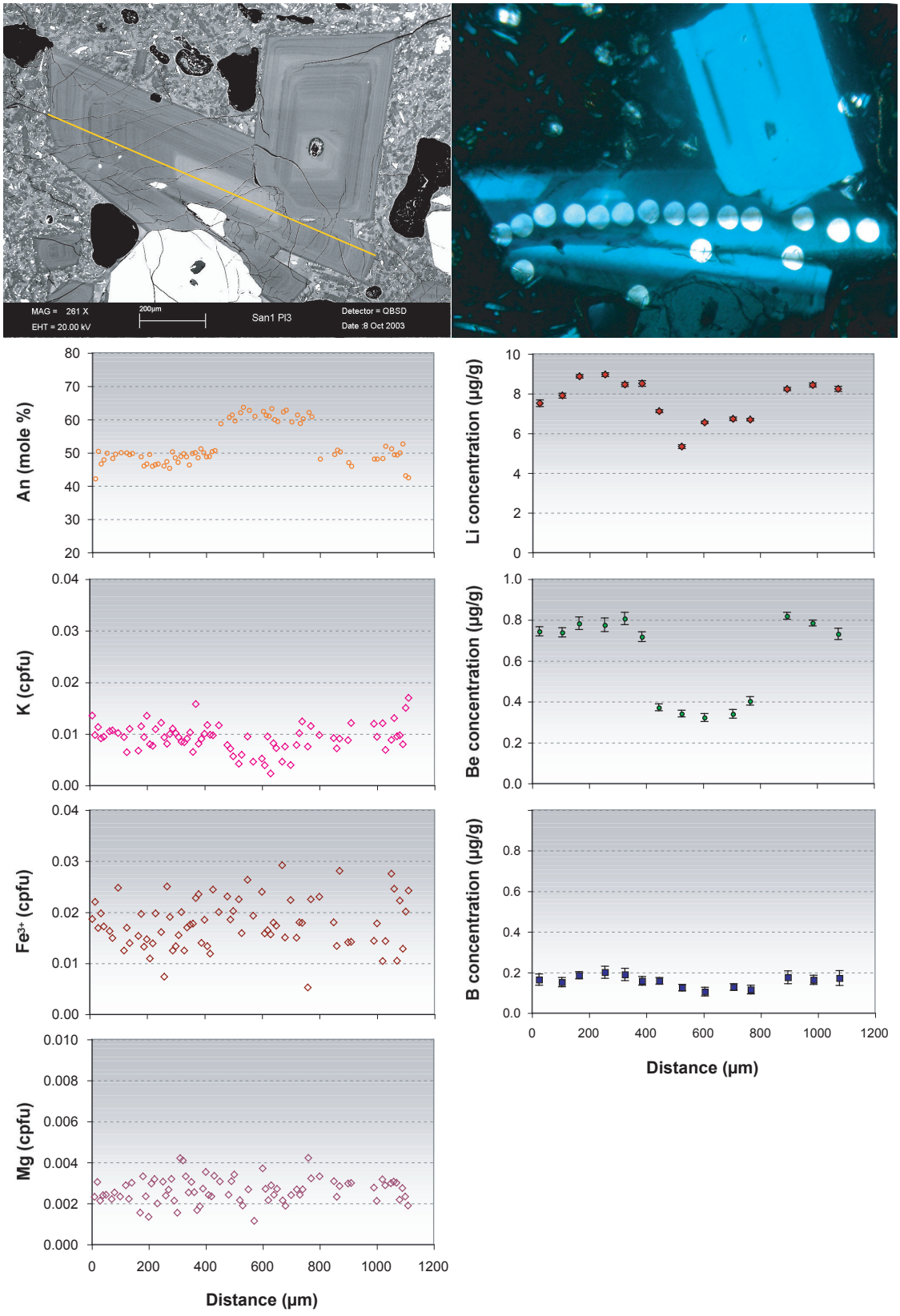

Plagioclase Type-C: *San1b Pl3*

	Data Point	3	12	17	26	33	39	45	53	61	72	77	90	99	108
	Name	San1bPl3	San1bPl3	San1bPl3	San1bPl3	San1bPl3	San1bPl3	San1bPl3	San1bPl3	San1bPl3	San1bPl3	San1bPl3	San1bPl3	San1bPl3	San1bPl3
	Mineral	Fsp	Fsp	Fsp	Fsp	Fsp	Fsp	Fsp	Fsp	Fsp	Fsp	Fsp	Fsp	Fsp	Fsp
	Distance	30	120	170	260	330	390	450	530	610	720	770	900	990	1080
%	SiO2	57.110	56.631	56.377	57.012	56.486	56.976	53.401	52.442	52.387	53.403	53.797	57.513	56.156	57.016
	Al2O3	27.669	27.741	27.929	28.134	28.394	27.967	30.376	30.612	30.206	30.025	29.413	27.758	27.482	28.149
	Fe2O3	0.503	0.369	0.456	0.219	0.371	0.418	0.593	0.466	0.463	0.443	0.665	0.422	0.422	0.668
	MgO	0.032	0.043	0.023	0.036	0.050	0.041	0.046	0.028	0.040	0.040	0.048	0.045	0.041	0.033
	CaO	9.388	9.661	9.980	9.728	9.763	10.159	12.148	12.429	12.730	12.742	12.289	9.626	9.468	9.983
	Na2O	5.907	5.334	5.765	5.957	5.647	5.589	4.695	3.912	4.432	4.419	4.363	5.978	5.622	5.501
	K2O	0.199	0.163	0.118	0.164	0.147	0.159	0.204	0.102	0.067	0.136	0.200	0.155	0.207	0.172
	Total	100.808	99.942	100.648	101.250	100.858	101.309	101.463	99.991	100.325	101.208	100.775	101.497	99.398	101.522
cpfu	Si	2.543	2.539	2.519	2.529	2.515	2.528	2.387	2.374	2.371	2.394	2.419	2.544	2.536	2.524
	Al	1.452	1.466	1.471	1.471	1.490	1.462	1.601	1.633	1.611	1.586	1.559	1.447	1.463	1.468
	Fe3	0.017	0.012	0.015	0.007	0.012	0.014	0.020	0.016	0.016	0.015	0.022	0.014	0.014	0.022
	Mg	0.002	0.003	0.002	0.002	0.003	0.003	0.003	0.002	0.003	0.003	0.003	0.003	0.003	0.002
	Ca	0.448	0.464	0.478	0.462	0.466	0.483	0.582	0.603	0.617	0.612	0.592	0.456	0.458	0.473
	Na	0.510	0.464	0.499	0.512	0.487	0.481	0.407	0.343	0.389	0.384	0.380	0.513	0.492	0.472
	K	0.011	0.009	0.007	0.009	0.008	0.009	0.012	0.006	0.004	0.008	0.011	0.009	0.012	0.010
	Total	4.983	4.958	4.991	4.993	4.982	4.979	5.012	4.976	5.011	5.001	4.987	4.986	4.978	4.972
mole (%)	An	48.398	50.060	47.518	46.325	48.362	50.093	58.845	62.938	61.642	60.180	61.544	46.565	48.194	50.760
µg/g	Li	7.509	7.892	8.864	8.950	8.457	8.503	7.112	5.328	6.543	6.727	6.683	8.223	8.427	8.234
	Be	0.744	0.739	0.783	0.776	0.807	0.718	0.372	0.341	0.322	0.340	0.403	0.820	0.785	0.732
	B	0.164	0.151	0.185	0.200	0.189	0.158	0.158	0.125	0.105	0.128	0.115	0.176	0.162	0.171

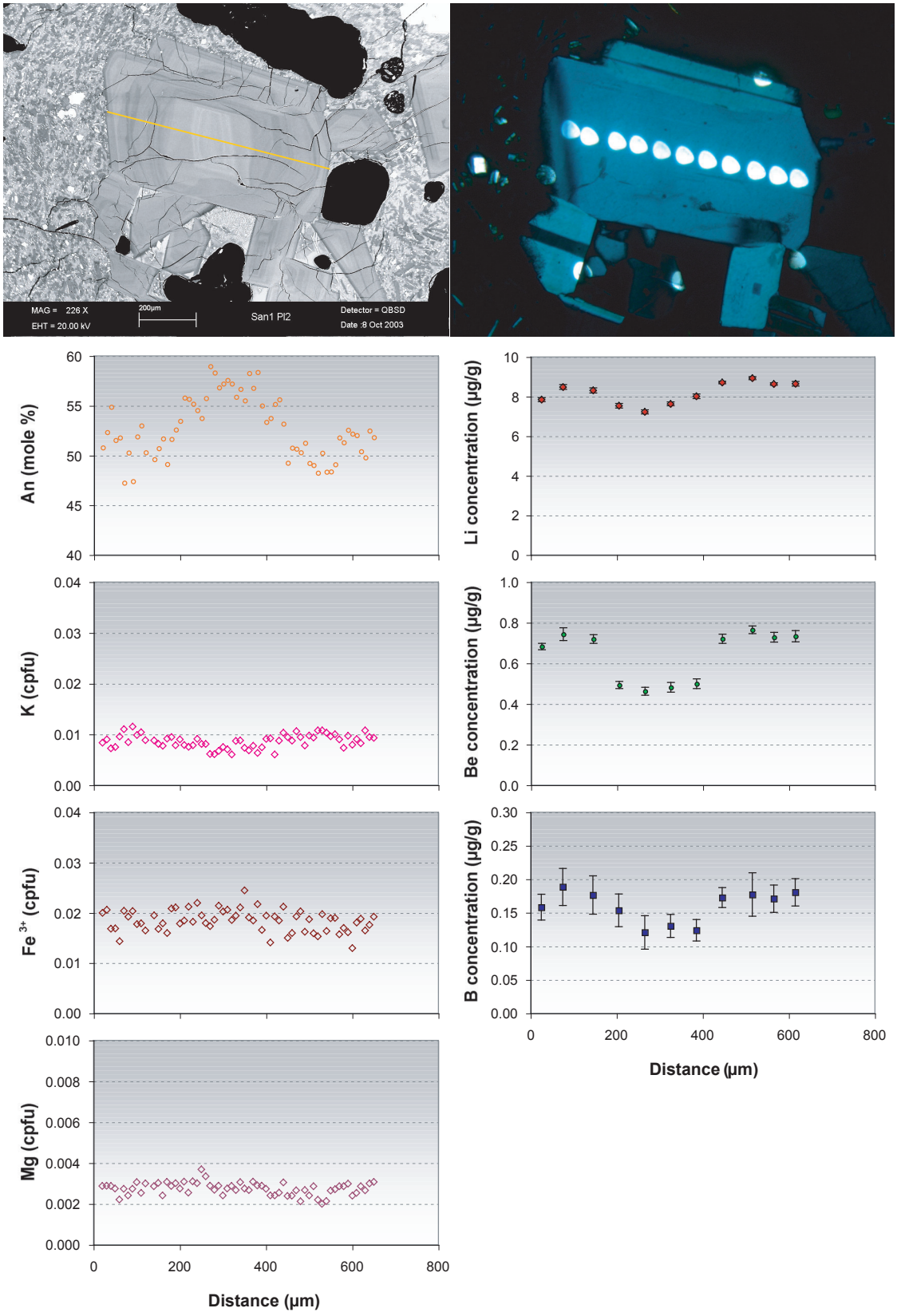

Plagioclase Type-C: *San1b Pl2*

	Data point	4	9	16	22	28	34	40	46	53	58	63
	Name	San1bPl2	San1bPl2	San1bPl2	San1bPl2	San1bPl2	San1bPl2	San1bPl2	San1bPl2	San1bPl2	San1bPl2	San1bPl2
	Mineral	Fsp	Fsp	Fsp	Fsp	Fsp	Fsp	Fsp	Fsp	Fsp	Fsp	Fsp
	Distance	40	90	160	220	280	340	400	460	530	580	630
%	SiO2	54.785	56.749	55.551	54.398	53.880	54.708	55.328	56.257	56.049	56.056	55.880
	Al2O3	28.827	27.412	28.101	28.797	29.554	29.318	28.710	28.228	28.166	28.332	28.379
	Fe2O3	0.498	0.602	0.528	0.625	0.550	0.625	0.576	0.476	0.586	0.506	0.490
	MgO	0.043	0.041	0.036	0.038	0.040	0.046	0.041	0.036	0.030	0.043	0.040
	CaO	11.086	9.359	10.193	11.214	11.770	11.310	10.623	10.117	10.075	10.334	10.122
	Na2O	5.035	5.732	5.258	4.932	4.646	4.777	5.130	5.419	5.506	5.417	5.634
	K2O	0.126	0.201	0.135	0.131	0.106	0.154	0.159	0.154	0.189	0.129	0.189
	Total	100.400	100.096	99.802	100.135	100.546	100.938	100.567	100.687	100.601	100.817	100.734
cpfu	Si	2.462	2.545	2.503	2.454	2.423	2.447	2.479	2.511	2.507	2.502	2.498
	Al	1.527	1.449	1.492	1.531	1.567	1.545	1.516	1.485	1.485	1.490	1.495
	Fe3	0.017	0.020	0.018	0.021	0.019	0.021	0.019	0.016	0.020	0.017	0.016
	Mg	0.003	0.003	0.002	0.003	0.003	0.003	0.003	0.002	0.002	0.003	0.003
	Ca	0.534	0.450	0.492	0.542	0.567	0.542	0.510	0.484	0.483	0.494	0.485
	Na	0.439	0.498	0.459	0.431	0.405	0.414	0.446	0.469	0.478	0.469	0.488
	K	0.007	0.011	0.008	0.008	0.006	0.009	0.009	0.009	0.011	0.007	0.011
	Total	4.989	4.976	4.975	4.989	4.990	4.981	4.981	4.977	4.985	4.982	4.996
mole (%)	An	52.9	49.9	50.5	55.6	58.0	56.0	54.0	50.2	49.0	51.9	50.9
µg/g	Li	7.839	8.484	8.307	7.535	7.228	7.631	8.015	8.706	8.930	8.635	8.644
	Be	0.682	0.744	0.719	0.493	0.463	0.482	0.500	0.721	0.765	0.729	0.733
	B	0.158	0.189	0.176	0.154	0.121	0.130	0.124	0.173	0.177	0.171	0.181

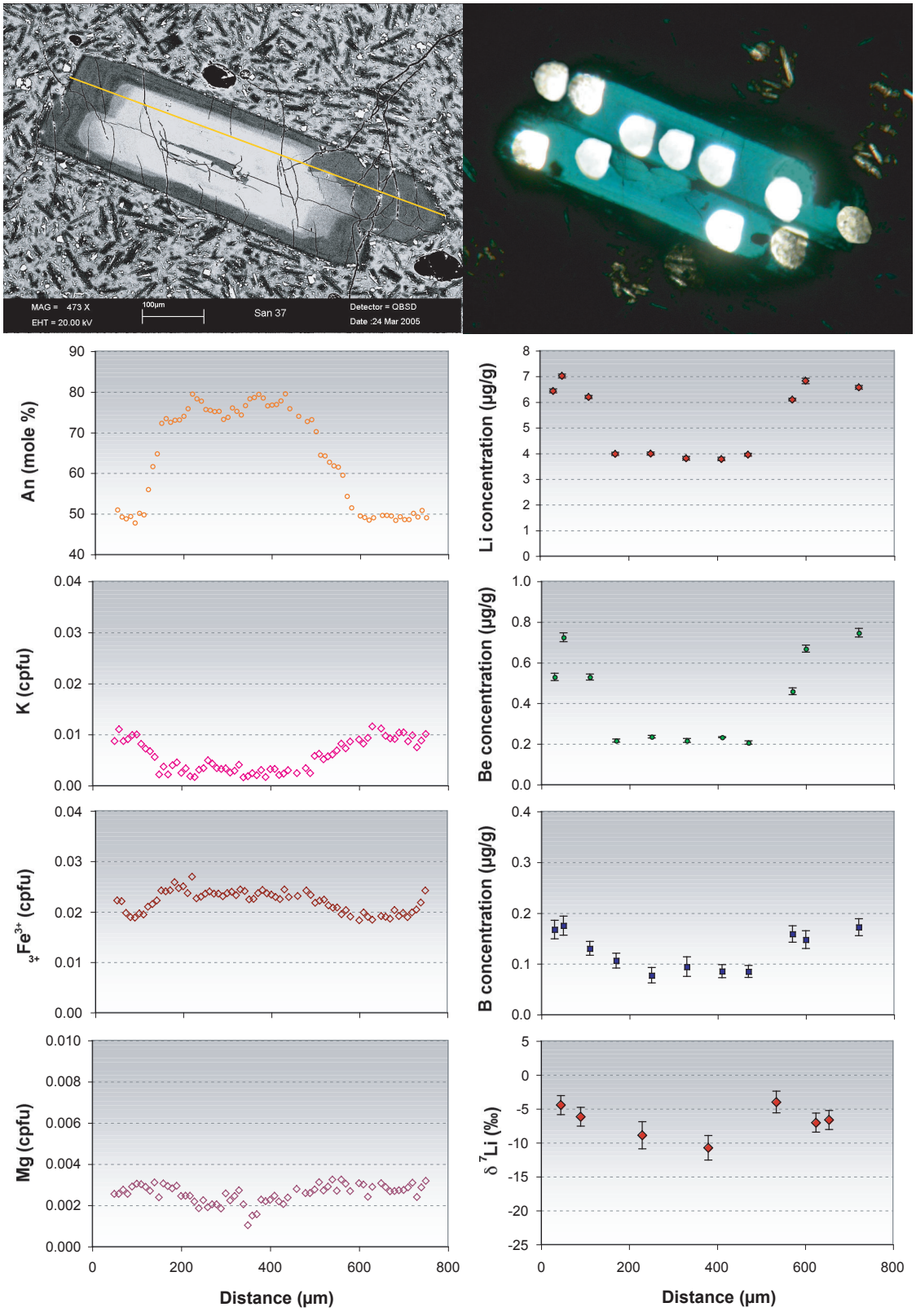

Plagioclase Type-C: *San37a Pl5*

	Data Point	6	9	14	21	29	37	46	51	62	71	74
	Name	San37cPl	San37cPl	San37cPl	San37cPl	San37cPl	San37cPl	San37cPl	San37cPl	San37cPl	San37cPl	San37cPl
	Mineral	Fsp	Fsp	Fsp	Fsp	Fsp	Fsp	Fsp	Fsp	Fsp	Fsp	Fsp
	Distance	60	90	140	210	290	370	460	510	620	710	740
%	SiO2	55.68	55.57	51.90	48.72	49.44	48.31	49.30	51.34	56.01	56.23	55.74
	Al2O3	27.93	27.77	30.59	32.77	32.18	33.48	32.35	30.76	28.01	28.09	28.40
	Fe2O3	0.65	0.55	0.65	0.69	0.67	0.69	0.67	0.65	0.56	0.56	0.65
	MgO	0.04	0.04	0.05	0.04	0.03	0.02	0.04	0.05	0.04	0.04	0.04
	CaO	10.26	9.61	13.23	15.32	15.09	16.14	15.06	13.40	10.15	10.03	10.68
	Na2O	5.82	5.79	3.97	2.68	3.04	2.31	2.92	4.08	5.95	5.85	5.69
	K2O	0.19	0.17	0.10	0.06	0.06	0.03	0.04	0.11	0.16	0.15	0.16
	Total	100.57	99.50	100.48	100.27	100.50	100.99	100.38	100.38	100.88	100.95	101.36
cpfu	Si	2.498	2.513	2.349	2.224	2.251	2.194	2.246	2.331	2.504	2.508	2.484
	Al	1.477	1.480	1.632	1.763	1.727	1.792	1.737	1.646	1.475	1.477	1.491
	Fe3	0.022	0.019	0.022	0.024	0.023	0.024	0.023	0.022	0.019	0.019	0.022
	Mg	0.003	0.003	0.003	0.002	0.002	0.002	0.003	0.003	0.002	0.003	0.003
	Ca	0.493	0.465	0.642	0.749	0.736	0.785	0.735	0.652	0.486	0.480	0.510
	Na	0.507	0.507	0.348	0.237	0.268	0.203	0.258	0.359	0.516	0.506	0.492
	K	0.011	0.010	0.006	0.003	0.003	0.002	0.002	0.006	0.009	0.009	0.009
	Total	5.011	4.997	5.001	5.003	5.010	5.001	5.004	5.018	5.012	5.001	5.010
mole (%)	An	49.7	49.2	66.3	76.5	74.1	78.9	74.1	66.4	48.9	49.2	49.8
µg/g	Li	7.010	6.428	6.195	3.975	3.986	3.804	3.774	3.942	6.088	6.819	6.565
	Be	0.724	0.529	0.529	0.216	0.235	0.216	0.232	0.206	0.458	0.668	0.746
	B	0.175	0.167	0.130	0.106	0.077	0.094	0.085	0.085	0.159	0.147	0.172

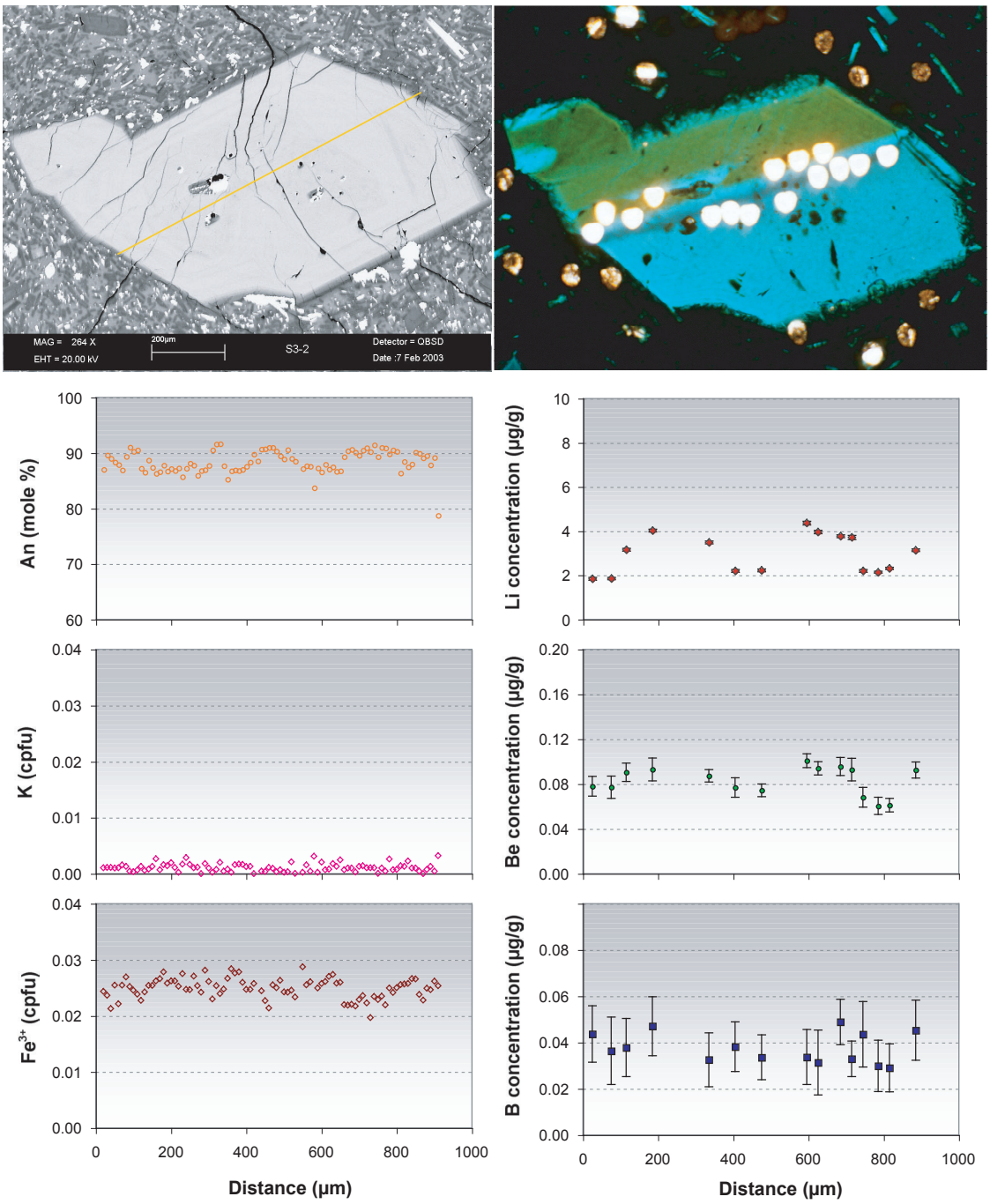

Plagioclase Type-A: *San3a Pl2*

	Data Point	3	8	12	19	34	41	48	60	63	69	72	75	79	82	89
	Name	San3Pl2	San3Pl2	San3Pl2	San3Pl2	San3Pl2	San3Pl2	San3Pl2	San3Pl2	San3Pl2	San3Pl2	San3Pl2	San3Pl2	San3Pl2	San3Pl2	San3Pl2
	Mineral	Fsp	Fsp	Fsp	Fsp	Fsp	Fsp	Fsp	Fsp	Fsp	Fsp	Fsp	Fsp	Fsp	Fsp	Fsp
	Distance	30	80	120	190	340	410	480	600	630	690	720	750	790	820	890
%	SiO2	45.702	45.973	46.294	46.341	45.911	45.836	44.805	46.459	46.450	45.486	45.445	45.661	45.361	46.080	45.509
	Al2O3	34.705	34.524	34.433	34.221	34.146	34.486	34.597	34.168	34.191	34.901	34.998	34.975	34.890	34.559	33.915
	Fe2O3	0.683	0.779	0.660	0.748	0.712	0.715	0.715	0.747	0.795	0.630	0.646	0.663	0.697	0.743	0.705
	CaO	18.173	17.995	17.827	17.747	17.778	17.956	18.070	17.504	17.805	18.549	18.413	18.167	18.321	17.751	17.777
	Na2O	1.161	1.185	1.440	1.499	1.378	1.308	1.068	1.502	1.405	1.120	1.012	1.202	1.059	1.279	1.356
	K2O	0.019	0.022	0.022	0.024	0.008	0.022	0.006	0.035	0.031	0.005	0.018	0.001	0.012	0.022	0.022
	Total	100.443	100.478	100.676	100.580	99.933	100.323	99.261	100.415	100.677	100.691	100.532	100.669	100.340	100.434	99.284
cpfu	Si	2.100	2.110	2.120	2.124	2.118	2.108	2.084	2.131	2.127	2.087	2.087	2.093	2.087	2.114	2.115
	Al	1.879	1.868	1.858	1.849	1.857	1.869	1.897	1.847	1.845	1.887	1.894	1.889	1.892	1.869	1.858
	Fe3	0.024	0.027	0.023	0.026	0.025	0.025	0.025	0.026	0.027	0.022	0.022	0.023	0.024	0.026	0.025
	Ca	0.895	0.885	0.875	0.872	0.879	0.885	0.901	0.860	0.874	0.912	0.906	0.892	0.903	0.873	0.885
	Na	0.103	0.105	0.128	0.133	0.123	0.117	0.096	0.134	0.125	0.100	0.090	0.107	0.094	0.114	0.122
	K	0.001	0.001	0.001	0.001	0.000	0.001	0.000	0.002	0.002	0.000	0.001	0.000	0.001	0.001	0.001
	Total	5.001	4.996	5.004	5.006	5.003	5.004	5.003	5.000	5.000	5.008	5.000	5.004	5.002	4.996	5.006
mole (%)	An	88.6	89.1	88.1	87.2	88.2	88.6	90.3	87.3	87.1	90.1	90.6	90.6	90.2	87.5	88.9
µg/g	Li	1.839	1.849	3.153	4.019	3.484	2.194	2.222	4.361	3.962	3.767	3.712	2.198	2.138	2.306	3.133
	Be	0.078	0.077	0.091	0.093	0.087	0.077	0.074	0.101	0.094	0.096	0.093	0.068	0.060	0.061	0.093
	B	0.044	0.036	0.038	0.047	0.033	0.038	0.034	0.034	0.031	0.049	0.033	0.044	0.030	0.029	0.045

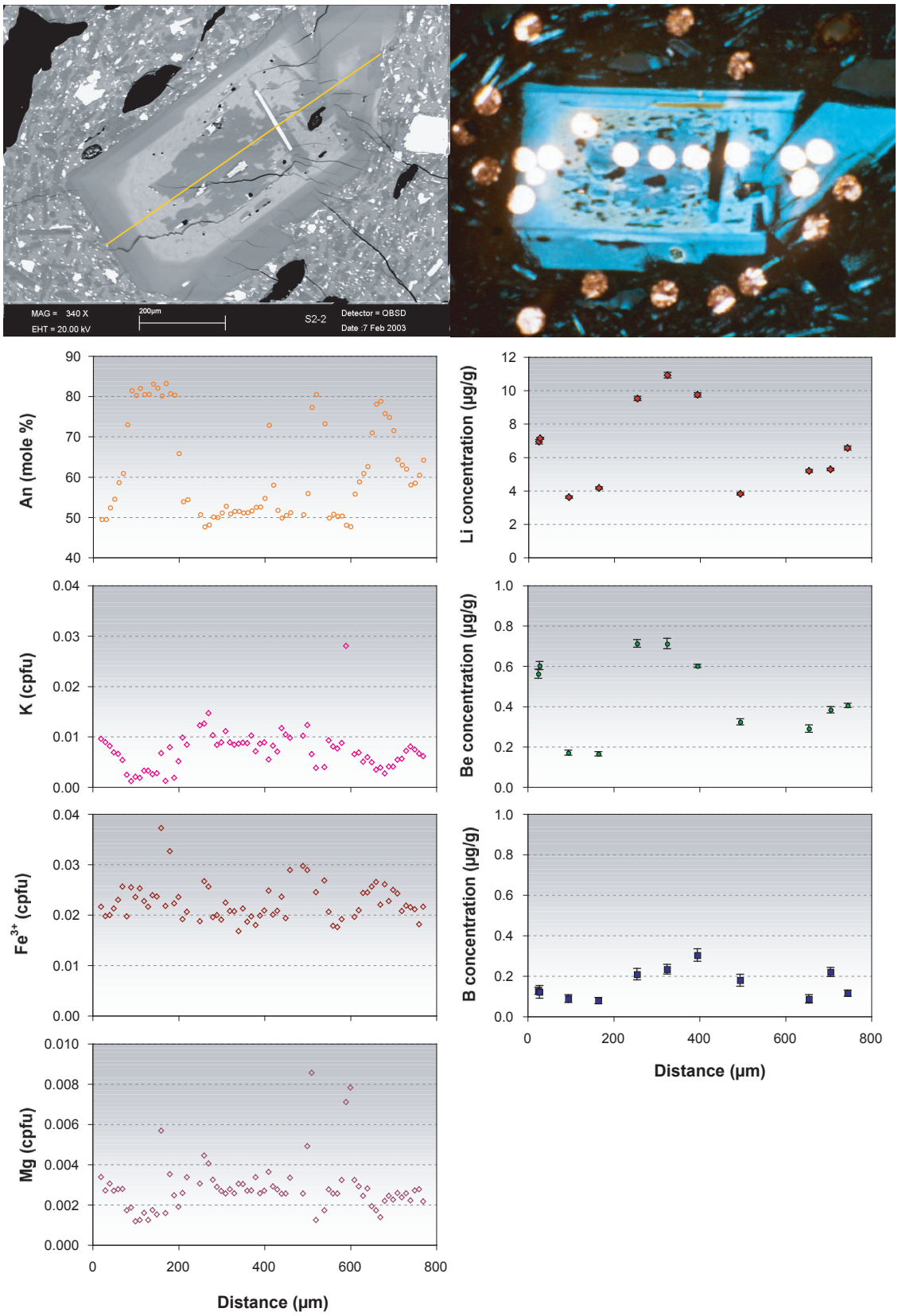

Plagioclase Type-A: *San2a Pl2*

	Data Point	3	6	10	17	26	33	40	50	66	71	75
	Name	San2Pl2	San2Pl3	San2Pl4	San2Pl5	San2Pl6	San2Pl7	San2Pl8	San2Pl9	San2Pl10	San2Pl11	San2Pl12
	Mineral	Fsp	Fsp	Fsp	Fsp	Fsp	Fsp	Fsp	Fsp	Fsp	Fsp	Fsp
	Distance	30	60	100	170	260	330	400	500	660	710	750
%	SiO2	55.422	53.206	47.484	46.983	56.111	55.211	54.678	54.006	48.183	52.184	53.444
	Al2O3	27.514	29.653	33.125	33.662	27.128	28.086	28.525	28.999	32.670	30.044	29.426
	Fe2O3	0.578	0.675	0.678	0.629	0.785	0.610	0.613	0.852	0.768	0.710	0.619
	MgO	0.040	0.041	0.017	0.023	0.066	0.038	0.040	0.073	0.025	0.038	0.040
	CaO	10.165	11.952	16.237	16.965	9.794	10.621	11.121	11.589	16.057	13.378	11.834
	Na2O	5.736	4.663	2.207	1.888	5.947	5.520	5.086	5.052	2.482	4.103	4.632
	K2O	0.153	0.113	0.034	0.020	0.218	0.145	0.153	0.213	0.058	0.093	0.128
	Total	99.608	100.303	99.782	100.170	100.049	100.231	100.216	100.784	100.243	100.550	100.123
cpfu	Si	2.509	2.404	2.185	2.157	2.528	2.486	2.465	2.430	2.207	2.362	2.417
	Al	1.468	1.579	1.796	1.822	1.440	1.491	1.515	1.538	1.763	1.603	1.568
	Fe3	0.020	0.023	0.023	0.022	0.027	0.021	0.021	0.029	0.026	0.024	0.021
	Mg	0.003	0.003	0.001	0.002	0.004	0.003	0.003	0.005	0.002	0.003	0.003
	Ca	0.493	0.579	0.800	0.835	0.473	0.512	0.537	0.559	0.788	0.649	0.573
	Na	0.503	0.409	0.197	0.168	0.519	0.482	0.444	0.441	0.220	0.360	0.406
	K	0.009	0.007	0.002	0.001	0.013	0.008	0.009	0.012	0.003	0.005	0.007
	Total	5.004	5.002	5.005	5.006	5.004	5.003	4.994	5.013	5.010	5.007	4.995
mole (%)	An	50.5	58.0	81.3	81.4	48.8	51.3	60.1	61.3	76.0	66.3	59.0
µg/g	Li	6.918	7.121	3.602	4.148	9.505	10.904	9.721	3.800	5.173	5.266	6.548
	Be	0.561	0.602	0.169	0.164	0.711	0.711	0.600	0.323	0.289	0.383	0.404
	B	0.126	0.121	0.088	0.078	0.208	0.232	0.302	0.178	0.086	0.219	0.114

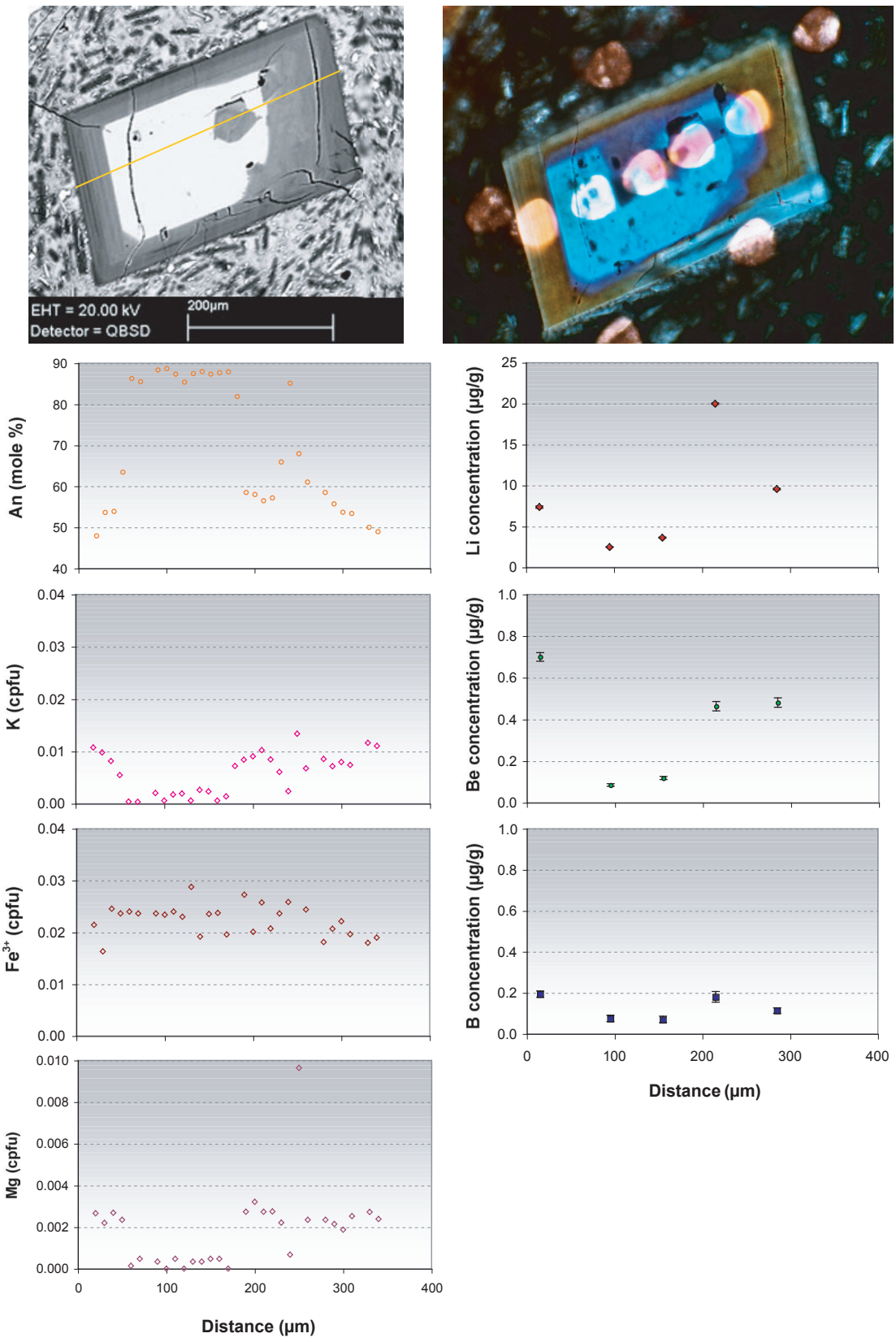

Plagioclase Type-A: *San37b Pl3*

	Data Point	2	10	16	22	29
	Name	San37bPl3	San37bPl3	San37bPl3	San37bPl3	San37bPl3
	Mineral	Fsp	Fsp	Fsp	Fsp	Fsp
	Distance	20	100	160	220	290
%	SiO2	56.659	45.794	46.040	54.011	54.391
	Al2O3	27.714	34.985	34.869	29.441	29.101
	Fe2O3	0.638	0.678	0.688	0.613	0.612
	MgO	0.040	0.000	0.007	0.041	0.032
	CaO	9.775	17.965	17.493	11.817	11.483
	Na2O	5.842	1.250	1.344	4.870	5.017
	K2O	0.189	0.010	0.010	0.148	0.125
	Total	100.857	100.682	100.451	100.941	100.761
cpfu	Si	2.527	2.097	2.110	2.423	2.442
	Al	1.457	1.888	1.883	1.557	1.540
	Fe3	0.021	0.023	0.024	0.021	0.021
	Mg	0.003	0.000	0.000	0.003	0.002
	Ca	0.467	0.882	0.859	0.568	0.552
	Na	0.505	0.111	0.119	0.424	0.437
	K	0.011	0.001	0.001	0.008	0.007
	Total	4.991	5.002	4.996	5.004	5.000
mole (%)	An	50.9	88.2	87.8	60.0	56.1
µg/g	Li	7.355	2.485	3.626	19.989	9.563
	Be	0.700	0.085	0.118	0.463	0.481
	B	0.194	0.075	0.070	0.180	0.114

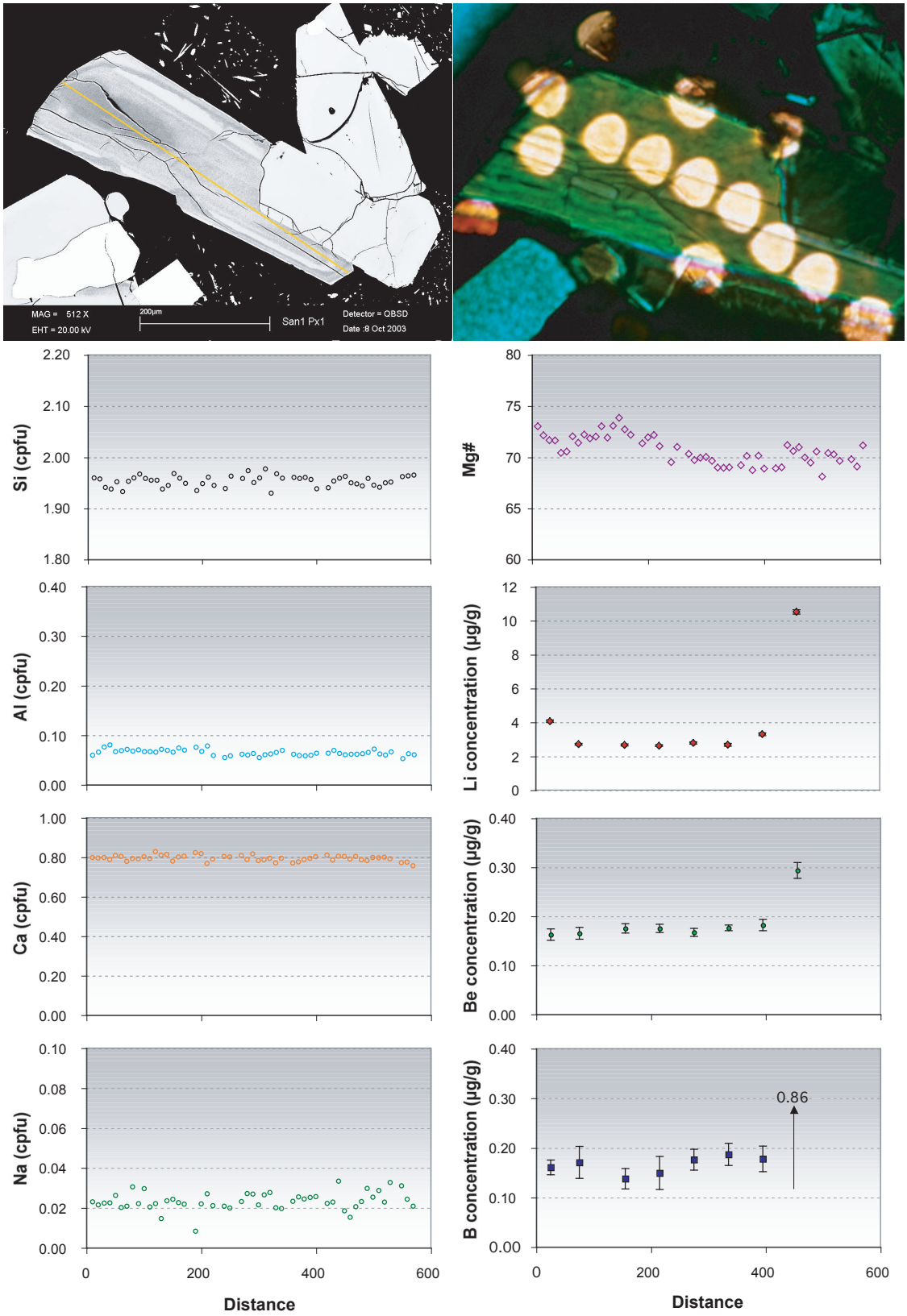

Clinopyroxene Type-L1: *San1b Cpx1*

	Data Point	3	8	16	22	28	34	40	52
	Name	San1bCpx1	San1bCpx1	San1bCpx1	San1bCpx1	San1bCpx1	San1bCpx1	San1bCpx1	San1bCpx1
	Mineral	Cpx	Cpx	Cpx	Cpx	Cpx	Cpx	Cpx	Cpx
	Distance	30	80	160	220	280	340	400	520
%	SiO2	52.517	53.245	52.417	52.216	52.766	52.267	51.824	52.22
	TiO2	0.539	0.459	0.405	0.499	0.492	0.61	0.515	0.515
	Al2O3	1.761	1.58	1.699	1.362	1.381	1.589	1.461	1.387
	Cr2O3	0	0	0.102	0.126	0.079	0	0.007	0.246
	FeO	10.4	10.42	9.661	10.791	10.71	10.967	11.493	10.719
	MnO	0.611	0.393	0.438	0.436	0.416	0.634	0.546	0.678
	MgO	14.754	14.601	14.432	14.871	13.828	13.691	14.261	14.203
	CaO	20.362	20.312	20.203	19.993	19.84	19.972	20.201	20.193
	Na2O	0.301	0.418	0.301	0.28	0.363	0.26	0.342	0.305
	Total	101.245	101.428	99.658	100.574	99.875	99.99	100.656	100.466
cpfu	Si	1.942	1.960	1.960	1.946	1.975	1.960	1.939	1.951
	Ti	0.015	0.013	0.011	0.014	0.014	0.017	0.014	0.014
	Al	0.077	0.069	0.075	0.060	0.061	0.070	0.064	0.061
	Cr	0.000	0.000	0.003	0.004	0.002	0.000	0.000	0.007
	Fe2	0.322	0.321	0.302	0.336	0.335	0.344	0.360	0.335
	Mn	0.019	0.012	0.014	0.014	0.013	0.020	0.017	0.021
	Mg	0.813	0.801	0.804	0.826	0.771	0.765	0.796	0.791
	Ca	0.807	0.801	0.809	0.798	0.795	0.802	0.810	0.808
	Na	0.022	0.030	0.022	0.020	0.026	0.019	0.025	0.022
	Total	4.016	4.007	4.001	4.018	3.993	3.997	4.026	4.011
	Mg#	71.7	71.4	72.7	71.1	69.7	69.0	68.9	70.3
µg/g	Li	4.070	2.706	2.664	2.623	2.782	2.674	3.299	10.520
	Be	0.163	0.165	0.175	0.175	0.167	0.176	0.182	0.293
	B	0.160	0.171	0.138	0.149	0.176	0.187	0.178	0.857

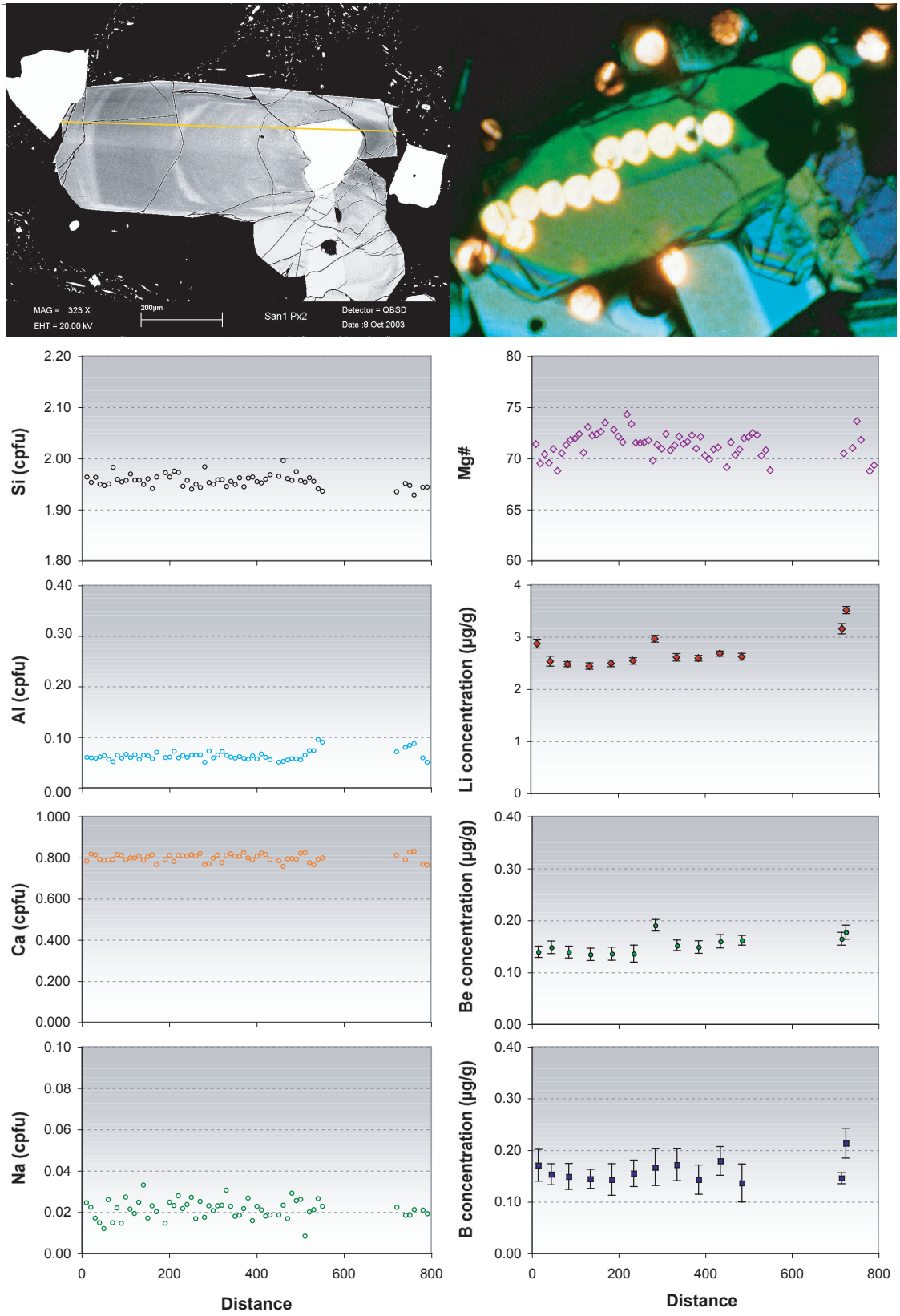

Clinopyroxene Type-L1: *San1b Cpx2*

	Data Point	4	8	11	16	21	26	31	36	41	46	51	74	78
	Name	San1bCpx2	San1bCpx2	San1bCpx2	San1bCpx2	San1bCpx2	San1bCpx2	San1bCpx2	San1bCpx2	San1bCpx2	San1bCpx2	San1bCpx2	San1bCpx2	San1bCpx2
	Mineral	Cpx	Cpx	Cpx	Cpx	Cpx	Cpx	Cpx	Cpx	Cpx	Cpx	Cpx	Cpx	Cpx
	Distance	40	80	110	160	210	260	310	360	410	460	510	740	780
%	SiO2	52.449	52.872	53.221	52.641	53.116	52.616	52.92	52.997	52.821	53.452	52.502	52.524	51.833
	TiO2	0.555	0.27	0.574	0.669	0.542	0.399	0.462	0.462	0.454	0.39	0.671	0.662	0.492
	Al2O3	1.404	1.483	1.381	1.326	1.653	1.491	1.495	1.427	1.54	1.192	1.479	1.833	1.351
	Cr2O3	0	0	0	0.143	0	0.007	0.039	0	0	0.032	0.023	0	0
	FeO	11.187	10.375	9.826	10.206	10.132	10.484	9.988	10.249	10.94	10.216	9.844	10.44	11.827
	MnO	1.028	0.679	0.767	0.351	0.22	0.615	0.395	0.659	0.351	0.417	0.417	0.593	0.832
	MgO	14.332	14.455	14.435	15.171	14.303	14.793	14.679	14.511	14.235	14.407	14.546	14.336	14.584
	CaO	19.916	20.553	20.19	20.629	19.635	20.366	20.529	20.326	20.818	18.987	20.695	19.882	19.131
	Na2O	0.209	0.31	0.302	0.324	0.324	0.237	0.324	0.259	0.297	0.324	0.119	0.259	0.291
	K2O	0.034	0	0.072	0	0	0.017	0	0	0.023	0	0	0.055	0.078
	Total	101.114	100.997	100.768	101.46	99.925	101.025	100.831	100.89	101.479	99.417	100.296	100.584	100.419
cpfu	Si	1.950	1.960	1.970	1.942	1.976	1.950	1.959	1.963	1.952	1.996	1.954	1.952	1.944
	Ti	0.016	0.008	0.016	0.019	0.015	0.011	0.013	0.013	0.013	0.011	0.019	0.018	0.014
	Al	0.062	0.065	0.060	0.058	0.072	0.065	0.065	0.062	0.067	0.052	0.065	0.080	0.060
	Cr	0.000	0.000	0.000	0.004	0.000	0.000	0.001	0.000	0.000	0.001	0.001	0.000	0.000
	Fe2	0.348	0.322	0.304	0.315	0.315	0.325	0.309	0.317	0.338	0.319	0.306	0.324	0.371
	Mn	0.032	0.021	0.024	0.011	0.007	0.019	0.012	0.021	0.011	0.013	0.013	0.019	0.026
	Mg	0.794	0.799	0.796	0.834	0.793	0.817	0.810	0.801	0.784	0.802	0.807	0.794	0.816
	Ca	0.793	0.816	0.801	0.815	0.783	0.809	0.814	0.807	0.824	0.760	0.825	0.792	0.769
	Na	0.015	0.022	0.022	0.023	0.023	0.017	0.023	0.019	0.021	0.023	0.009	0.019	0.021
	K	0.002	0.000	0.003	0.000	0.000	0.001	0.000	0.000	0.001	0.000	0.000	0.003	0.004
	Total	4.012	4.012	3.997	4.020	3.985	4.015	4.007	4.002	4.013	3.978	3.999	4.000	4.024
	Mg#	69.5	71.3	72.4	72.6	71.6	71.6	72.4	71.6	69.9	71.5	72.5	71.0	68.7
µg/g	Li	2.870	2.530	2.474	2.438	2.489	2.538	2.961	2.606	2.588	2.675	2.619	3.154	3.513
	Be	0.139	0.148	0.139	0.134	0.136	0.136	0.190	0.152	0.149	0.159	0.161	0.164	0.177
	B	0.170	0.153	0.149	0.144	0.143	0.155	0.167	0.171	0.143	0.179	0.136	0.145	0.213

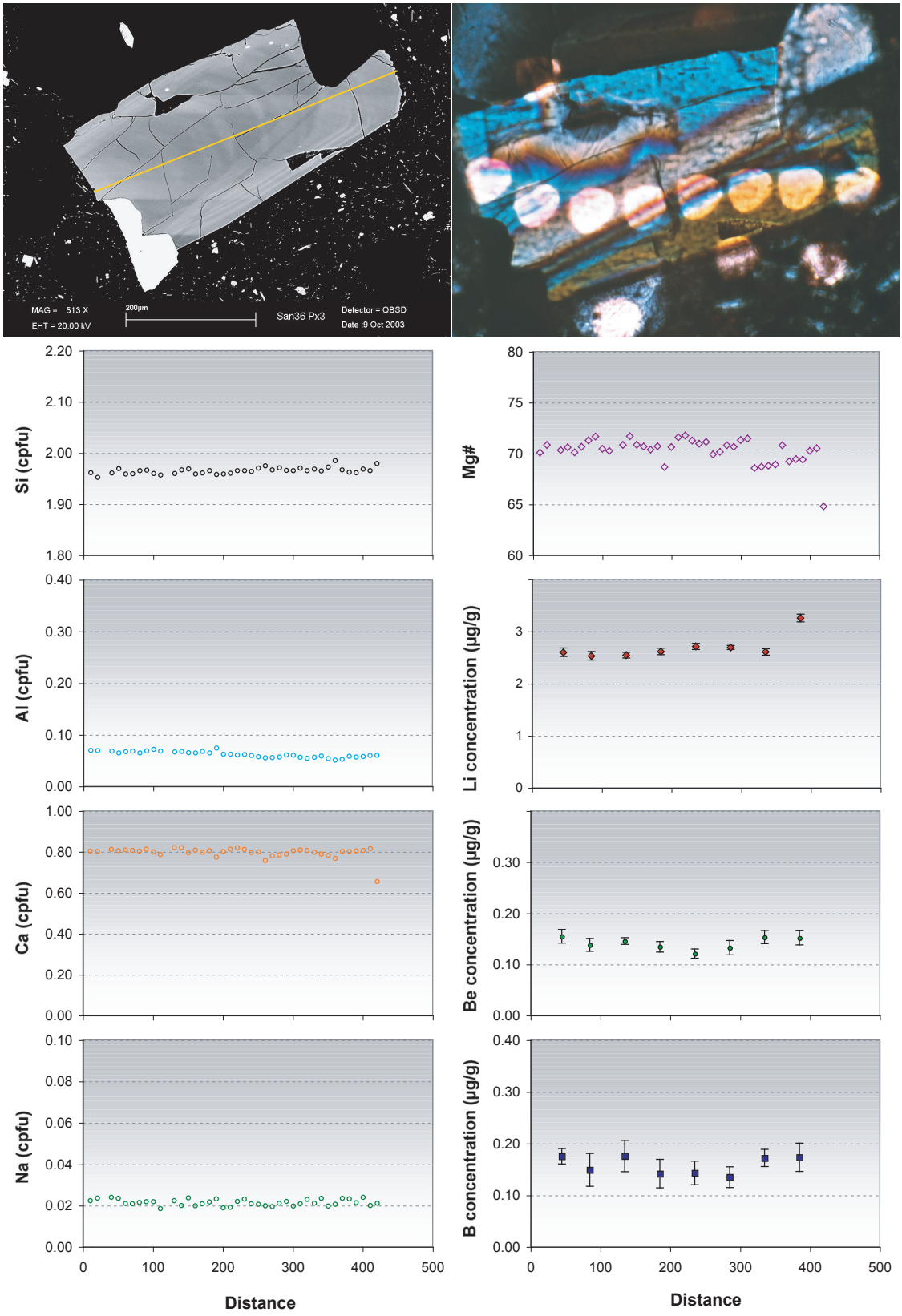

Clinopyroxene Type-L2: *San36b Cpx3*

	Data Point	5	9	14	19	24	29	34	39
	Name	San36bCpx3	san36px3	san36px3	san36px3	san36px3	san36px3	san36px3	san36px3
	Mineral	Cpx	Cpx	Cpx	Cpx	Cpx	Cpx	Cpx	Cpx
	Distance	50	90	140	190	240	290	340	390
%	SiO2	52.629	52.263	52.359	51.792	52.269	52.509	52.231	52.419
	TiO2	0.504	0.445	0.465	0.5	0.417	0.442	0.417	0.49
	Al2O3	1.489	1.563	1.553	1.683	1.364	1.398	1.341	1.309
	Cr2O3	0	0.035	0	0.031	0	0	0	0
	FeO	10.28	9.845	9.768	11.254	10.441	10.55	11.239	11.019
	MnO	0.595	0.491	0.545	0.54	0.554	0.664	0.585	0.563
	MgO	13.848	13.956	13.868	13.828	14.294	14.24	13.89	14.002
	CaO	20.143	20.228	20.439	19.163	19.835	19.728	19.65	20.117
	Na2O	0.326	0.303	0.278	0.319	0.29	0.306	0.324	0.298
	K2O	0	0	0.016	0	0.001	0.004	0.004	0.019
	Total	99.814	99.129	99.291	99.11	99.465	99.841	99.681	100.236
cpfu	Si	1.970	1.967	1.968	1.958	1.965	1.967	1.966	1.962
	Ti	0.014	0.013	0.013	0.014	0.012	0.012	0.012	0.014
	Al	0.066	0.069	0.069	0.075	0.060	0.062	0.059	0.058
	Cr	0.000	0.001	0.000	0.001	0.000	0.000	0.000	0.000
	Fe2	0.322	0.310	0.307	0.356	0.328	0.330	0.354	0.345
	Mn	0.019	0.016	0.017	0.017	0.018	0.021	0.019	0.018
	Mg	0.773	0.783	0.777	0.780	0.801	0.795	0.779	0.781
	Ca	0.808	0.816	0.823	0.776	0.799	0.792	0.792	0.807
	Na	0.024	0.022	0.020	0.023	0.021	0.022	0.024	0.022
	K	0.000	0.000	0.001	0.000	0.000	0.000	0.000	0.001
	Total	3.995	3.996	3.995	4.001	4.004	4.001	4.005	4.007
	Mg#	70.6	71.6	71.7	68.7	70.9	70.6	68.8	69.4
µg/g	Li	2.598	2.530	2.543	2.614	2.709	2.691	2.605	3.257
	Be	0.155	0.138	0.146	0.134	0.121	0.133	0.153	0.152
	B	0.175	0.149	0.175	0.142	0.143	0.135	0.172	0.173

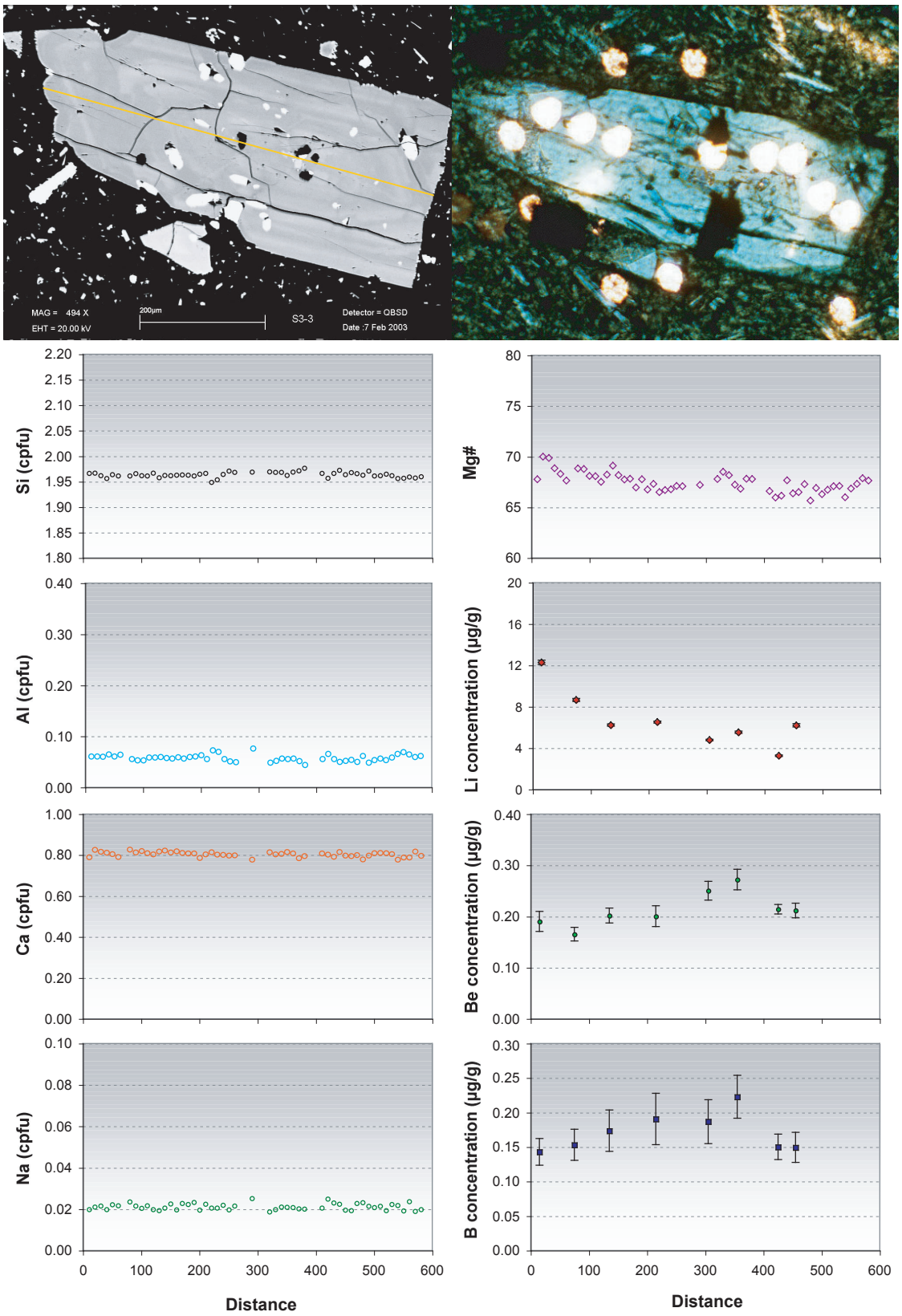

Clinopyroxene Type-L2: *San3a Cpx3*

	Data Point	2	8	14	32	41	46	53	56
	Name	San3Cpx3	San3Cpx3	San3Cpx3	San3Cpx3	San3Cpx3	San3Cpx3	San3Cpx3	San3Cpx3
	Mineral	Cpx	Cpx	Cpx	Cpx	Cpx	Cpx	Cpx	Cpx
	Distance	20	80	140	320	410	460	530	560
%	SiO2	52.37	52.124	52.036	52.614	52.267	51.983	51.923	51.82
	TiO2	0.397	0.352	0.435	0.379	0.404	0.389	0.434	0.495
	Al2O3	1.389	1.266	1.307	1.119	1.266	1.224	1.338	1.47
	Cr2O3	0	0	0.023	0.01	0	0	0	0
	FeO	10.435	11.017	10.86	11.501	11.875	11.989	11.685	11.695
	MnO	0.578	0.549	0.518	0.644	0.573	0.618	0.64	0.662
	MgO	13.654	13.636	13.623	13.571	13.283	13.338	13.372	13.505
	CaO	20.592	20.594	20.413	20.361	20.105	19.63	19.91	19.464
	Na2O	0.291	0.325	0.284	0.26	0.284	0.266	0.306	0.325
	K2O	0.014	0.013	0	0.011	0.018	0	0.008	0.006
	Total	99.72	99.876	99.499	100.47	100.075	99.437	99.616	99.442
%	Si	1.967	1.962	1.963	1.970	1.967	1.969	1.962	1.960
	Ti	0.011	0.010	0.012	0.011	0.011	0.011	0.012	0.014
	Al	0.061	0.056	0.058	0.049	0.056	0.055	0.060	0.066
	Cr	0.000	0.000	0.001	0.000	0.000	0.000	0.000	0.000
	Fe2	0.328	0.347	0.343	0.360	0.374	0.380	0.369	0.370
	Mn	0.018	0.018	0.017	0.020	0.018	0.020	0.020	0.021
	Mg	0.765	0.765	0.766	0.757	0.745	0.753	0.753	0.761
	Ca	0.829	0.830	0.825	0.817	0.811	0.796	0.806	0.789
	Na	0.021	0.024	0.021	0.019	0.021	0.020	0.022	0.024
	K	0.001	0.001	0.000	0.001	0.001	0.000	0.000	0.000
	Total	4.002	4.012	4.006	4.004	4.004	4.003	4.007	4.005
	Mg#	69.992	68.812	69.099	67.778	66.599	66.479	67.105	67.304
µg/g	Li	12.285	8.641	6.217	6.508	4.768	5.527	3.255	6.197
	Be	0.190	0.165	0.202	0.200	0.250	0.272	0.214	0.212
	B	0.143	0.153	0.174	0.191	0.187	0.223	0.150	0.149

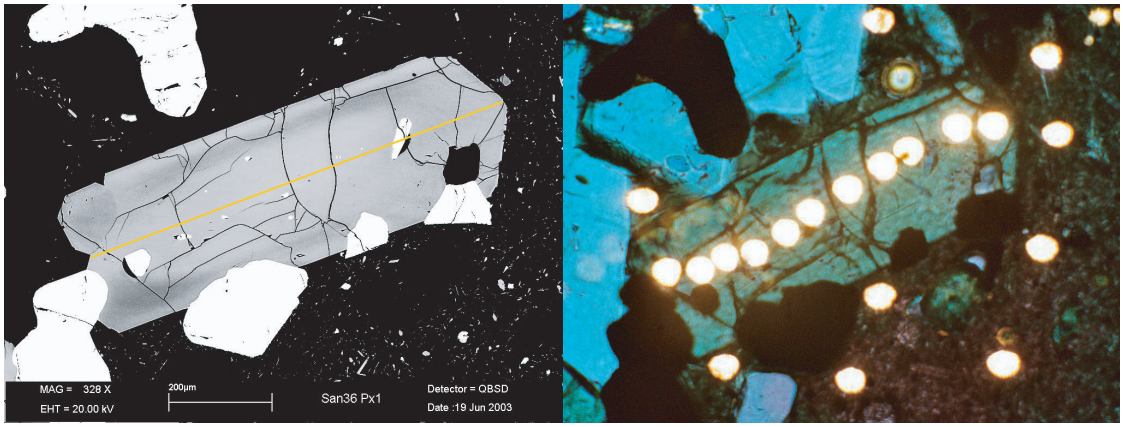

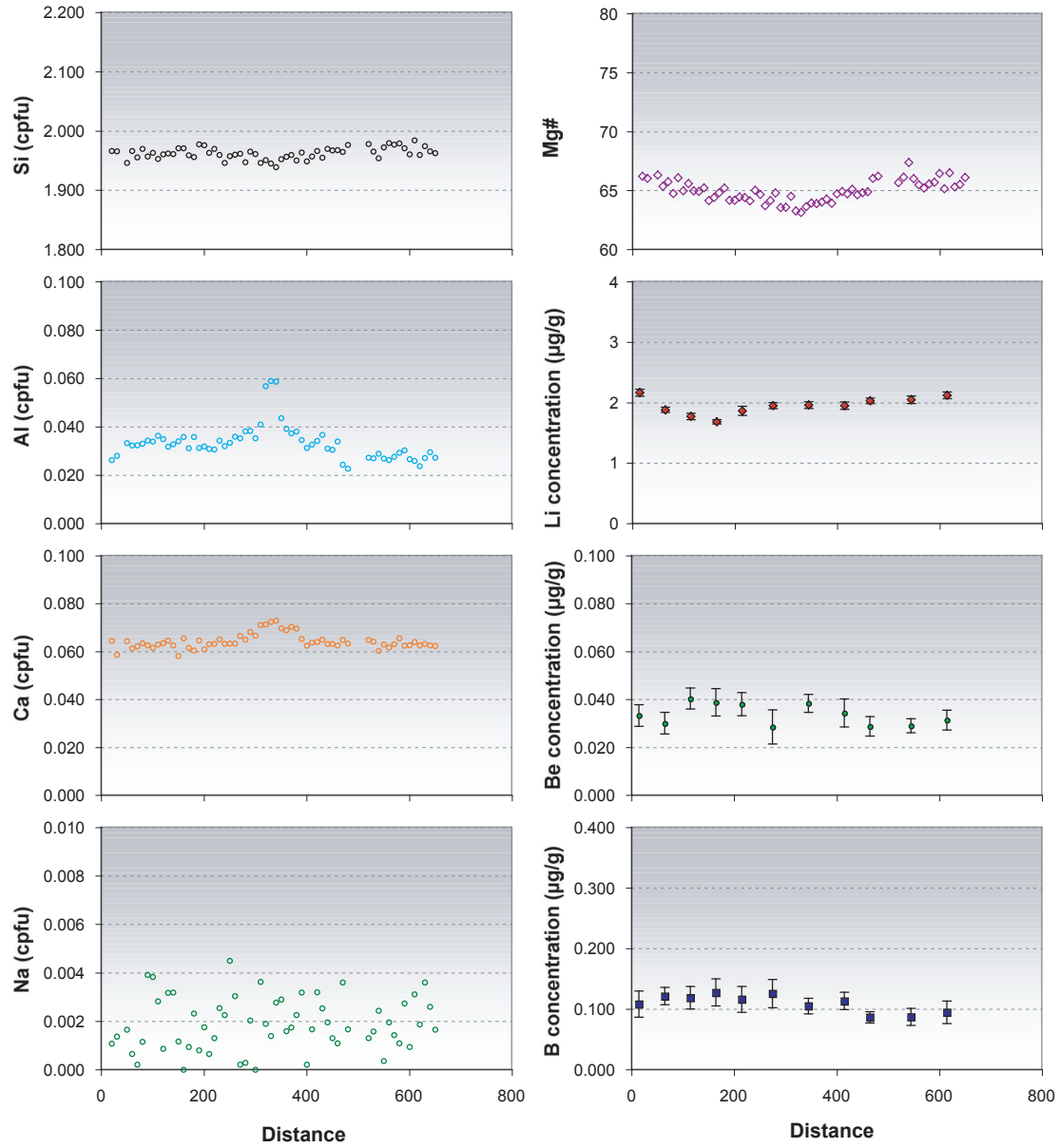

Orthopyroxene Type-I1: *San36a Opx1*

	Data Point	3	8	13	18	23	29	36	43	48	56	63
	Name	San36Opx1	San36Opx1	San36Opx1	San36Opx1	San36Opx1	San36Opx1	San36Opx1	San36Opx1	San36Opx1	San36Opx1	San36Opx1
	Mineral	Opx	Opx	Opx	Opx	Opx	Opx	Opx	Opx	Opx	Opx	Opx
	Distance	30	80	130	180	230	290	360	430	480	560	630
%	SiO2	52.748	52.744	52.674	52.233	52.269	52.541	52.130	52.237	52.701	53.046	53.104
	TiO2	0.232	0.444	0.310	0.307	0.275	0.224	0.277	0.312	0.175	0.249	0.260
	Al2O3	0.639	0.752	0.726	0.811	0.778	0.869	0.886	0.833	0.514	0.599	0.620
	Cr2O3	0.000	0.000	0.010	0.000	0.000	0.007	0.047	0.000	0.000	0.001	0.023
	Fe2O3	1.023	0.131	1.047	1.325	1.193	0.713	1.156	1.372	0.578	0.129	0.442
	FeO	20.517	21.313	21.067	20.766	21.380	21.777	21.391	20.808	20.289	20.915	21.009
	MnO	0.986	0.908	1.007	1.042	0.988	1.014	1.113	0.952	1.029	0.940	0.984
	MgO	22.324	21.918	21.820	21.785	21.389	21.268	21.185	21.724	22.263	22.221	22.137
	CaO	1.471	1.589	1.619	1.507	1.622	1.703	1.717	1.624	1.577	1.546	1.588
	Na2O	0.019	0.016	0.044	0.032	0.035	0.028	0.022	0.035	0.023	0.027	0.050
	K2O	0.000	0.018	0.001	0.000	0.000	0.000	0.000	0.001	0.010	0.023	0.000
	Total	99.958	99.833	100.325	99.808	99.929	100.144	99.924	99.898	99.160	99.696	100.217
cpfu	Si	1.966	1.970	1.962	1.956	1.960	1.965	1.956	1.955	1.977	1.980	1.974
	Ti	0.007	0.012	0.009	0.009	0.008	0.006	0.008	0.009	0.005	0.007	0.007
	Al	0.028	0.033	0.032	0.036	0.034	0.038	0.039	0.037	0.023	0.026	0.027
	Cr	0.000	0.000	0.000	0.000	0.000	0.000	0.001	0.000	0.000	0.000	0.001
	Fe3	0.029	0.004	0.029	0.037	0.034	0.020	0.033	0.039	0.016	0.004	0.012
	Fe2	0.639	0.666	0.656	0.650	0.670	0.681	0.671	0.651	0.636	0.653	0.653
	Mn	0.031	0.029	0.032	0.033	0.031	0.032	0.035	0.030	0.033	0.030	0.031
	Mg	1.240	1.220	1.212	1.216	1.195	1.186	1.185	1.212	1.245	1.236	1.227
	Ca	0.059	0.064	0.065	0.060	0.065	0.068	0.069	0.065	0.063	0.062	0.063
	Na	0.001	0.001	0.003	0.002	0.003	0.002	0.002	0.003	0.002	0.002	0.004
	K	0.000	0.001	0.000	0.000	0.000	0.000	0.000	0.000	0.000	0.001	0.000
	Total	4	4	4	4	4	4	4	4	4	4	4
	Mg#	66.0	64.7	64.9	65.2	64.1	63.5	63.8	65.0	66.2	65.4	65.3
µg/g	Li	2.156	1.874	1.766	1.675	1.856	1.942	1.952	1.942	2.021	2.040	2.112
	Be	0.033	0.030	0.040	0.039	0.038	0.028	0.038	0.034	0.029	0.029	0.031
	B	0.107	0.121	0.118	0.127	0.115	0.125	0.104	0.113	0.086	0.087	0.094

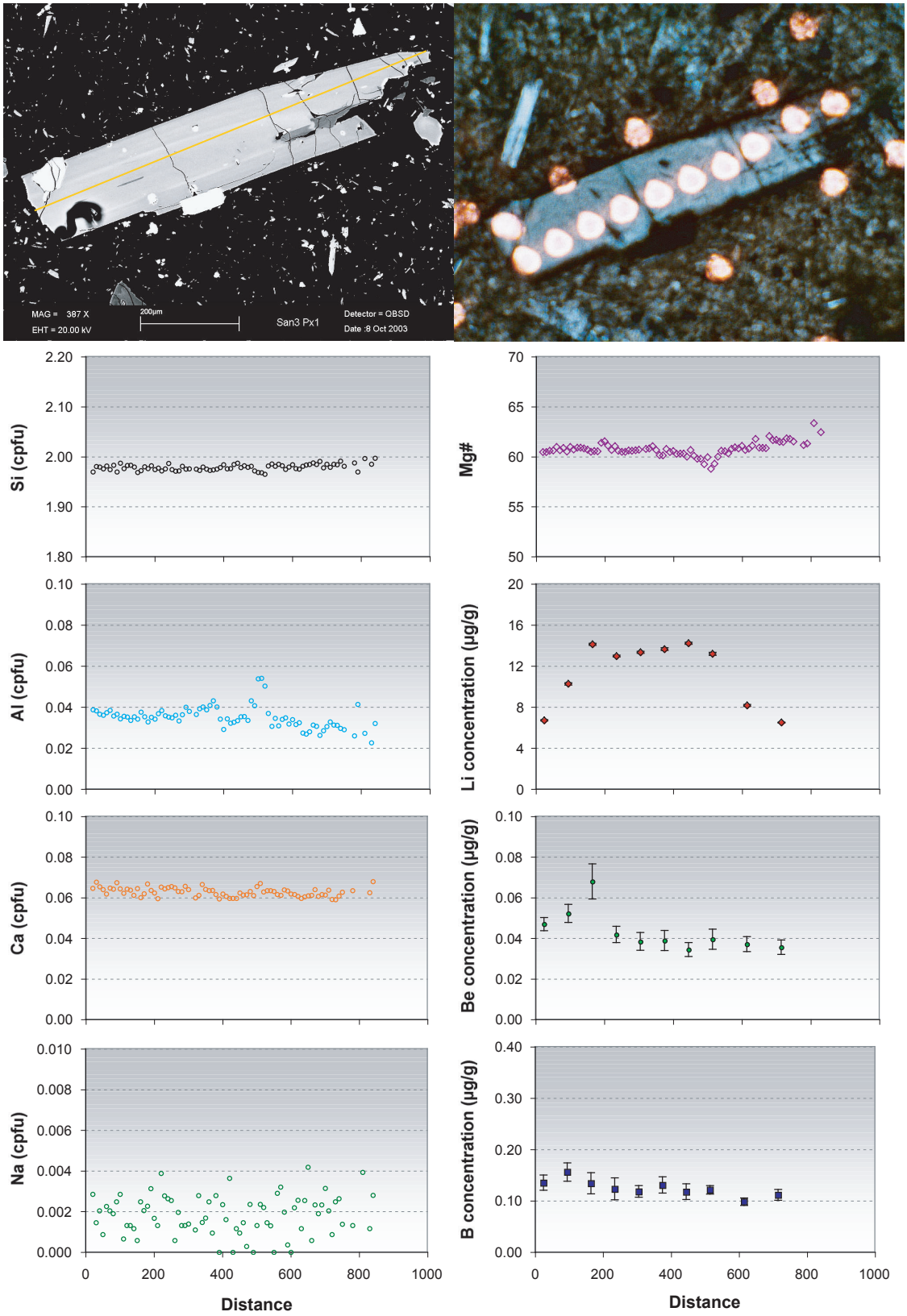

Orthopyroxene Type-I2: *San3b Opx1*

	Data Point	4	11	18	25	32	39	46	53	63	73
	Name	San3bOpx1	San3bOpx1	San3bOpx1	San3bOpx1	San3bOpx1	San3bOpx1	San3bOpx1	San3bOpx1	San3bOpx1	San3bOpx1
	Mineral	Opx	Opx	Opx	Opx	Opx	Opx	Opx	Opx	Opx	Opx
	Distance	40	110	180	250	320	390	460	530	630	730
µg/g	SiO2	52.547	52.594	52.421	52.43	52.216	52.365	52.693	52.43	52.783	52.505
	TiO2	0.272	0.327	0.302	0.289	0.347	0.24	0.279	0.314	0.239	0.22
	Al2O3	0.824	0.805	0.739	0.784	0.818	0.769	0.801	0.829	0.62	0.701
	Cr2O3	0	0	0.025	0.01	0	0	0.013	0	0.015	0.025
	FeO	23.424	23.505	23.514	23.642	23.297	23.58	23.755	23.606	23.398	22.674
	MnO	1.03	1.055	1.081	1.033	1.136	1.122	1.028	1.104	1.099	1.109
	MgO	20.167	20.359	20.202	20.267	20.207	20.189	20.044	19.839	20.587	20.565
	CaO	1.62	1.545	1.654	1.626	1.48	1.468	1.524	1.568	1.485	1.459
	Na2O	0.028	0.009	0.031	0.035	0.015	0	0.02	0.02	0.016	0.034
	K2O	0	0.005	0.011	0	0.007	0.008	0.01	0	0	0.013
	Total	99.912	100.204	99.98	100.116	99.523	99.741	100.167	99.71	100.242	99.305
cpfu	Si	1.980	1.976	1.976	1.974	1.976	1.979	1.982	1.982	1.981	1.984
	Ti	0.008	0.009	0.009	0.008	0.010	0.007	0.008	0.009	0.007	0.006
	Al	0.037	0.036	0.033	0.035	0.036	0.034	0.036	0.037	0.027	0.031
	Cr	0.000	0.000	0.001	0.000	0.000	0.000	0.000	0.000	0.000	0.001
	Fe2	0.738	0.739	0.741	0.745	0.737	0.745	0.747	0.746	0.735	0.717
	Mn	0.033	0.034	0.035	0.033	0.036	0.036	0.033	0.035	0.035	0.035
	Mg	1.133	1.140	1.135	1.138	1.140	1.137	1.124	1.118	1.152	1.159
	Ca	0.065	0.062	0.067	0.066	0.060	0.059	0.061	0.063	0.060	0.059
	Na	0.002	0.001	0.002	0.003	0.001	0.000	0.001	0.001	0.001	0.002
	K	0.000	0.000	0.001	0.000	0.000	0.000	0.000	0.000	0.000	0.001
	Total	3.995	3.997	4.000	4.001	3.997	3.998	3.993	3.992	3.998	3.995
	Mg#	60.5	60.7	60.5	60.4	60.7	60.4	60.1	60.0	61.1	61.8
µg/g	Li	6.677	10.234	14.095	12.942	13.312	13.616	14.181	13.150	8.127	6.457
	Be	0.047	0.052	0.068	0.042	0.038	0.039	0.034	0.039	0.037	0.035
	B	0.135	0.156	0.134	0.123	0.118	0.130	0.117	0.121	0.098	0.111

	Data Point	3	10	16	23	29	36	42	54	62	69	74	80	87	93	96	106	110	116	123	130
	Name	San1bPl1	San1bPl1	San1bPl1	San1bPl1	San1bPl1	San1bPl1	San1bPl1	San1bPl1	San1bPl1	San1bPl1	San1bPl1	San1bPl1	San1bPl1	San1bPl1	San1bPl1	San1bPl1	San1bPl1	San1bPl1	San1bPl1	San1bPl1
	Mineral	Fsp	Fsp	Fsp	Fsp	Fsp	Fsp	Fsp	Fsp	Fsp	Fsp	Fsp	Fsp	Fsp	Fsp	Fsp	Fsp	Fsp	Fsp	Fsp	Fsp
	Distance	30	100	160	230	290	360	420	540	620	690	740	800	870	930	960	1060	1100	1160	1230	1300
%	SiO2	55.852	54.430	55.500	55.373	55.891	55.733	55.215	54.383	55.793	53.972	55.512	56.133	55.341	55.027	55.870	53.929	53.906	53.330	54.558	55.656
	Al2O3	28.666	27.894	27.850	28.130	27.965	28.457	27.565	28.358	27.826	28.317	27.253	27.325	27.788	27.406	28.347	28.859	29.112	29.008	28.538	28.041
	Fe2O3	0.576	0.533	0.632	0.613	0.499	0.619	0.546	0.680	0.462	0.503	0.462	0.583	0.503	0.673	0.492	0.613	0.675	0.650	0.548	0.669
	CaO	10.760	10.590	10.806	10.986	10.096	10.077	10.561	10.403	9.933	11.321	10.292	9.833	10.529	10.744	10.271	11.321	11.224	11.802	10.593	10.014
	Na2O	5.237	5.509	5.785	5.430	5.250	5.347	5.473	5.234	5.760	5.176	5.676	5.799	5.517	5.643	5.562	4.939	5.051	5.153	5.585	5.625
	K2O	0.082	0.106	0.100	0.169	0.207	0.113	0.137	0.182	0.176	0.119	0.194	0.176	0.200	0.213	0.157	0.163	0.225	0.100	0.157	0.125
	Total	101.173	99.062	100.673	100.701	99.908	100.346	99.497	99.240	99.950	99.408	99.389	99.849	99.878	99.706	100.699	99.824	100.193	100.043	99.979	100.130
cpfu	Si	2.487	2.481	2.492	2.484	2.514	2.497	2.503	2.472	2.513	2.456	2.518	2.530	2.499	2.496	2.498	2.443	2.435	2.419	2.465	2.503
	Al	1.504	1.498	1.474	1.487	1.483	1.503	1.473	1.519	1.477	1.519	1.457	1.451	1.479	1.465	1.494	1.541	1.550	1.551	1.520	1.486
	Fe3	0.019	0.018	0.021	0.021	0.017	0.021	0.019	0.023	0.016	0.017	0.016	0.020	0.017	0.023	0.017	0.021	0.023	0.022	0.019	0.023
	Ca	0.513	0.517	0.520	0.528	0.487	0.484	0.513	0.507	0.479	0.552	0.500	0.475	0.509	0.522	0.492	0.549	0.543	0.574	0.513	0.482
	Na	0.452	0.487	0.504	0.472	0.458	0.465	0.481	0.461	0.503	0.457	0.499	0.507	0.483	0.496	0.482	0.434	0.442	0.453	0.489	0.490
	K	0.005	0.006	0.006	0.010	0.012	0.006	0.008	0.011	0.010	0.007	0.011	0.010	0.012	0.012	0.009	0.009	0.013	0.006	0.009	0.007
	Total	4.980	5.007	5.016	5.003	4.971	4.976	4.996	4.993	4.998	5.008	5.001	4.993	5.000	5.014	4.992	4.998	5.006	5.024	5.015	4.992
mole (%)	An	51.9	52.2	50.6	53.2	49.2	51.6	49.4	53.1	48.9	54.2	50.7	50.6	50.9	51.5	52.2	54.8	55.1	55.7	51.1	49.4
µg/g	Li	7.858	7.771	8.439	8.487	8.585	8.786	8.805	9.379	10.035	8.998	8.574	8.263	8.476	8.238	7.935	7.956	7.652	7.630	8.469	7.977
	Be	0.679	0.624	0.704	0.692	0.687	0.720	0.768	0.777	0.750	0.734	0.722	0.706	0.767	0.726	0.681	0.661	0.610	0.640	0.740	0.736
	B	0.201	0.157	0.199	0.161	0.163	0.171	0.147	0.167	0.180	0.143	0.165	0.167	0.199	0.164	0.161	0.155	0.143	0.128	0.193	0.190

	Data Point	4	10	16	22	28	34	40	44
	Name	San2bpl1	San2bpl1	San2bpl1	San2bpl1	San2bpl1	San2bpl1	San2bpl1	San2bpl1
	Mineral	Fsp	Fsp	Fsp	Fsp	Fsp	Fsp	Fsp	Fsp
	Distance	40	100	160	220	280	340	400	440
%	SiO2	56.449	57.566	57.175	56.389	56.591	57.371	57.649	57.256
	Al2O3	28.268	27.623	27.423	28.041	28.096	27.695	27.442	27.096
	Fe2O3	0.495	0.415	0.489	0.598	0.422	0.445	0.490	0.399
	MgO	0.036	0.035	0.028	0.033	0.030	0.033	0.032	0.032
	CaO	9.833	9.243	9.079	9.807	9.724	9.233	9.019	9.484
	Na2O	5.974	6.330	6.210	5.970	6.178	6.276	6.488	6.186
	K2O	0.206	0.188	0.199	0.184	0.188	0.192	0.226	0.211
	Total	101.261	101.400	100.603	101.022	101.229	101.245	101.346	100.664
cpfu	Si	2.510	2.549	2.551	2.513	2.517	2.545	2.555	2.556
	Al	1.481	1.442	1.442	1.473	1.473	1.448	1.433	1.426
	Fe3	0.017	0.014	0.016	0.020	0.014	0.015	0.016	0.013
	Mg	0.002	0.002	0.002	0.002	0.002	0.002	0.002	0.002
	Ca	0.468	0.439	0.434	0.468	0.463	0.439	0.428	0.454
	Na	0.515	0.544	0.537	0.516	0.533	0.540	0.558	0.535
	K	0.012	0.011	0.011	0.010	0.011	0.011	0.013	0.012
	Total	5.005	5.000	4.994	5.003	5.012	4.999	5.005	4.998
mole (%)	An	46.9	45.5	44.2	45.6	47.2	45.5	43.6	46.2
µg/g	Li	7.753	8.491	8.783	8.812	8.789	9.036	8.834	8.304
	Be	0.734	0.785	0.771	0.749	0.824	0.758	0.796	0.770
	B	0.186	0.146	0.171	0.165	0.186	0.173	0.175	0.201

	Data point	4	9	16	22	28	34	40	46	53	58	63
	Name	San1bPl2	San1bPl2	San1bPl2	San1bPl2	San1bPl2	San1bPl2	San1bPl2	San1bPl2	San1bPl2	San1bPl2	San1bPl2
	Mineral	Fsp	Fsp	Fsp	Fsp	Fsp	Fsp	Fsp	Fsp	Fsp	Fsp	Fsp
	Distance	40	90	160	220	280	340	400	460	530	580	630
%	SiO2	54.785	56.749	55.551	54.398	53.880	54.708	55.328	56.257	56.049	56.056	55.880
	Al2O3	28.827	27.412	28.101	28.797	29.554	29.318	28.710	28.228	28.166	28.332	28.379
	Fe2O3	0.498	0.602	0.528	0.625	0.550	0.625	0.576	0.476	0.586	0.506	0.490
	MgO	0.043	0.041	0.036	0.038	0.040	0.046	0.041	0.036	0.030	0.043	0.040
	CaO	11.086	9.359	10.193	11.214	11.770	11.310	10.623	10.117	10.075	10.334	10.122
	Na2O	5.035	5.732	5.258	4.932	4.646	4.777	5.130	5.419	5.506	5.417	5.634
	K2O	0.126	0.201	0.135	0.131	0.106	0.154	0.159	0.154	0.189	0.129	0.189
	Total	100.400	100.096	99.802	100.135	100.546	100.938	100.567	100.687	100.601	100.817	100.734
cpfu	Si	2.462	2.545	2.503	2.454	2.423	2.447	2.479	2.511	2.507	2.502	2.498
	Al	1.527	1.449	1.492	1.531	1.567	1.545	1.516	1.485	1.485	1.490	1.495
	Fe3	0.017	0.020	0.018	0.021	0.019	0.021	0.019	0.016	0.020	0.017	0.016
	Mg	0.003	0.003	0.002	0.003	0.003	0.003	0.003	0.002	0.002	0.003	0.003
	Ca	0.534	0.450	0.492	0.542	0.567	0.542	0.510	0.484	0.483	0.494	0.485
	Na	0.439	0.498	0.459	0.431	0.405	0.414	0.446	0.469	0.478	0.469	0.488
	K	0.007	0.011	0.008	0.008	0.006	0.009	0.009	0.009	0.011	0.007	0.011
	Total	4.989	4.976	4.975	4.989	4.990	4.981	4.981	4.977	4.985	4.982	4.996
mole (%)	An	52.9	49.9	50.5	55.6	58.0	56.0	54.0	50.2	49.0	51.9	50.9
µg/g	Li	7.839	8.484	8.307	7.535	7.228	7.631	8.015	8.706	8.930	8.635	8.644
	Be	0.682	0.744	0.719	0.493	0.463	0.482	0.500	0.721	0.765	0.729	0.733
	B	0.158	0.189	0.176	0.154	0.121	0.130	0.124	0.173	0.177	0.171	0.181

	Data Point	2	6	13	18	19	20	27	33	34	38	39	45	46	57	60	62	64	67	74	76	81	86	87
	Name	San3Pl1	San3Pl1	San3Pl1	San3Pl1	San3Pl1	San3Pl1	San3Pl1	San3Pl1	San3Pl1	San3Pl1	San3Pl1	San3Pl1	San3Pl1	San3Pl1	San3Pl1	San3Pl1	San3Pl1	San3Pl1	San3Pl1	San3Pl1	San3Pl1	San3Pl1	San3Pl1
	Mineral	Fsp	Fsp	Fsp	Fsp	Fsp	Fsp	Fsp	Fsp	Fsp	Fsp	Fsp	Fsp	Fsp	Fsp	Fsp	Fsp	Fsp	Fsp	Fsp	Fsp	Fsp	Fsp	Fsp
	Distance	20	60	130	180	190	200	270	330	340	380	390	450	460	570	600	620	640	670	740	760	810	860	870
%	SiO2	56.332	57.102	55.213	55.345	55.480	55.136	56.623	57.583	57.664	58.636	57.018	56.197	56.039	56.045	58.373	57.299	56.789	57.457	55.050	55.001	55.271	57.205	56.659
	Al2O3	27.844	27.332	28.462	28.417	28.464	28.517	27.589	27.068	27.045	26.314	27.357	27.941	28.011	28.028	26.375	27.272	27.429	27.208	28.493	28.653	28.462	27.397	27.722
	Fe2O3	0.443	0.435	0.410	0.465	0.490	0.482	0.470	0.460	0.380	0.413	0.405	0.412	0.462	0.402	0.480	0.446	0.398	0.492	0.460	0.448	0.510	0.442	0.442
	CaO	10.130	9.498	10.874	10.767	10.891	11.079	9.693	9.291	9.188	8.374	9.512	10.119	10.308	10.131	8.584	9.478	9.800	9.299	10.921	10.909	10.652	9.528	9.933
	Na2O	5.915	6.260	5.420	5.319	5.314	5.488	5.727	6.407	6.352	6.693	6.086	5.856	5.661	5.581	6.538	6.190	5.884	6.284	5.389	5.171	5.405	6.095	5.954
	K2O	0.173	0.207	0.149	0.152	0.142	0.139	0.158	0.208	0.194	0.247	0.159	0.158	0.183	0.148	0.242	0.188	0.201	0.192	0.107	0.126	0.152	0.193	0.176
	Total	100.837	100.834	100.528	100.465	100.781	100.841	100.260	101.017	100.823	100.677	100.537	100.683	100.664	100.335	100.592	100.873	100.501	100.932	100.420	100.308	100.452	100.860	100.886
cpfu	Si	2.516	2.546	2.479	2.484	2.483	2.471	2.536	2.562	2.567	2.608	2.548	2.513	2.508	2.512	2.600	2.552	2.540	2.557	2.474	2.473	2.482	2.548	2.527
	Al	1.466	1.437	1.506	1.503	1.501	1.506	1.457	1.419	1.419	1.379	1.441	1.473	1.477	1.481	1.385	1.432	1.446	1.427	1.509	1.518	1.506	1.438	1.457
	Fe3	0.015	0.015	0.014	0.016	0.017	0.016	0.016	0.015	0.013	0.014	0.014	0.014	0.016	0.014	0.016	0.015	0.013	0.016	0.016	0.015	0.017	0.015	0.015
	Ca	0.485	0.454	0.523	0.518	0.522	0.532	0.465	0.443	0.438	0.399	0.455	0.485	0.494	0.487	0.410	0.452	0.470	0.443	0.526	0.525	0.512	0.455	0.475
	Na	0.512	0.541	0.472	0.463	0.461	0.477	0.497	0.553	0.548	0.577	0.527	0.508	0.491	0.485	0.565	0.535	0.510	0.542	0.470	0.451	0.471	0.526	0.515
	K	0.010	0.012	0.009	0.009	0.008	0.008	0.009	0.012	0.011	0.014	0.009	0.009	0.010	0.008	0.014	0.011	0.011	0.011	0.006	0.007	0.009	0.011	0.010
	Total	5.004	5.004	5.002	4.992	4.993	5.010	4.981	5.003	4.997	4.991	4.993	5.002	4.997	4.987	4.989	4.997	4.991	4.998	5.001	4.990	4.996	4.994	4.999
mole (%)	An	47.7	46.9	52.5	53.0	52.9	52.8	47.5	45.0	43.2	42.0	44.0	49.2	49.5	50.1	43.8	46.0	47.2	47.3	52.9	53.4	52.6	47.5	47.2
µg/g	Li	9.827	9.875	9.650	8.898	9.524	9.128	9.829	9.902	9.720	10.981	10.757	9.189	9.585	7.495	10.074	10.229	9.876	9.946	9.488	8.805	9.859	10.079	9.608
	Be	0.772	0.642	0.618	0.782	0.626	0.596	0.713	0.835	0.794	0.970	0.853	0.709	0.643	0.891	0.764	0.831	0.810	0.773	0.601	0.572	0.613	0.840	0.728
	B	0.181	0.142	0.146	0.146	0.145	0.148	0.147	0.183	0.162	0.198	0.206	0.150	0.167	1.495	0.160	0.139	0.170	0.158	0.111	0.123	0.132	0.175	0.159

	Data Point	4	10	16	22
	Name	San3bPl4	San3bPl4	San3bPl4	San3bPl4
	Mineral	Fsp	Fsp	Fsp	Fsp
	Distance	40	100	160	220
%	SiO2	50.915	47.103	46.808	51.580
	Al2O3	31.671	34.189	34.219	30.783
	Fe2O3	0.679	0.708	0.779	0.822
	MgO	0.103	0.083	0.080	0.116
	CaO	14.288	17.046	17.263	13.429
	Na2O	3.280	1.832	1.649	3.735
	K2O	0.046	0.047	0.007	0.090
	Total	100.982	101.008	100.805	100.555
cpfu	Si	2.298	2.145	2.137	2.335
	Al	1.685	1.835	1.841	1.642
	Fe3	0.023	0.024	0.027	0.028
	Mg	0.007	0.006	0.005	0.008
	Ca	0.691	0.832	0.845	0.651
	Na	0.287	0.162	0.146	0.328
	K	0.003	0.003	0.000	0.005
	Total	4.993	5.007	5.002	4.997
mole (%)	An	72.8	84.7	85.5	64.2
µg/g	Li	5.528	3.466	2.777	3.427
	Be	0.286	0.093	0.074	0.108
	B	0.195	0.044	0.031	0.042

	Data Point	3	6	10	17	26	33	40	50	66	71	75
	Name	San2Pl2	San2Pl3	San2Pl4	San2Pl5	San2Pl6	San2Pl7	San2Pl8	San2Pl9	San2Pl10	San2Pl11	San2Pl12
	Mineral	Fsp	Fsp	Fsp	Fsp	Fsp	Fsp	Fsp	Fsp	Fsp	Fsp	Fsp
	Distance	30	60	100	170	260	330	400	500	660	710	750
%	SiO2	55.422	53.206	47.484	46.983	56.111	55.211	54.678	54.006	48.183	52.184	53.444
	Al2O3	27.514	29.653	33.125	33.662	27.128	28.086	28.525	28.999	32.670	30.044	29.426
	Fe2O3	0.578	0.675	0.678	0.629	0.785	0.610	0.613	0.852	0.768	0.710	0.619
	MgO	0.040	0.041	0.017	0.023	0.066	0.038	0.040	0.073	0.025	0.038	0.040
	CaO	10.165	11.952	16.237	16.965	9.794	10.621	11.121	11.589	16.057	13.378	11.834
	Na2O	5.736	4.663	2.207	1.888	5.947	5.520	5.086	5.052	2.482	4.103	4.632
	K2O	0.153	0.113	0.034	0.020	0.218	0.145	0.153	0.213	0.058	0.093	0.128
	Total	99.608	100.303	99.782	100.170	100.049	100.231	100.216	100.784	100.243	100.550	100.123
cpfu	Si	2.509	2.404	2.185	2.157	2.528	2.486	2.465	2.430	2.207	2.362	2.417
	Al	1.468	1.579	1.796	1.822	1.440	1.491	1.515	1.538	1.763	1.603	1.568
	Fe3	0.020	0.023	0.023	0.022	0.027	0.021	0.021	0.029	0.026	0.024	0.021
	Mg	0.003	0.003	0.001	0.002	0.004	0.003	0.003	0.005	0.002	0.003	0.003
	Ca	0.493	0.579	0.800	0.835	0.473	0.512	0.537	0.559	0.788	0.649	0.573
	Na	0.503	0.409	0.197	0.168	0.519	0.482	0.444	0.441	0.220	0.360	0.406
	K	0.009	0.007	0.002	0.001	0.013	0.008	0.009	0.012	0.003	0.005	0.007
	Total	5.004	5.002	5.005	5.006	5.004	5.003	4.994	5.013	5.010	5.007	4.995
mole (%)	An	50.5	58.0	81.3	81.4	48.8	51.3	60.1	61.3	76.0	66.3	59.0
µg/g	Li	6.918	7.121	3.602	4.148	9.505	10.904	9.721	3.800	5.173	5.266	6.548
	Be	0.561	0.602	0.169	0.164	0.711	0.711	0.600	0.323	0.289	0.383	0.404
	B	0.126	0.121	0.088	0.078	0.208	0.232	0.302	0.178	0.086	0.219	0.114

	Data Point	1	2	10	12	17	19	25	32	34	40	46	52	54	57	62	63
	Name	San2Pl3	San2Pl3	San2Pl3	San2Pl3	San2Pl3	San2Pl3	San2Pl3	San2Pl3	San2Pl3	San2Pl3	San2Pl3	San2Pl3	San2Pl3	San2Pl3	San2Pl3	San2Pl3
	Mineral	Fsp	Fsp	Fsp	Fsp	Fsp	Fsp	Fsp	Fsp	Fsp	Fsp	Fsp	Fsp	Fsp	Fsp	Fsp	Fsp
	Distance	10	20	100	120	170	190	250	320	340	400	460	520	540	570	620	630
%	SiO2	55.739	56.043	54.436	55.878	55.476	56.015	55.707	54.727	54.577	55.059	55.506	55.360	55.410	54.421	56.047	55.514
	Al2O3	28.041	27.589	28.504	27.952	27.867	27.827	27.759	28.536	28.470	28.164	27.933	27.580	28.071	28.587	27.691	27.788
	Fe2O3	0.543	0.606	0.562	0.533	0.513	0.509	0.446	0.439	0.516	0.536	0.569	0.549	0.536	0.625	0.509	0.589
	CaO	10.337	9.768	10.846	9.996	10.278	10.008	10.130	10.693	10.691	10.568	10.092	9.710	10.375	11.130	9.780	10.218
	Na2O	5.726	6.037	5.273	5.866	5.851	5.818	5.555	5.525	5.466	5.465	5.858	5.872	5.621	5.291	5.830	5.767
	K2O	0.157	0.192	0.116	0.178	0.176	0.171	0.171	0.137	0.128	0.169	0.184	0.179	0.192	0.143	0.179	0.175
	Total	100.543	100.235	99.737	100.403	100.161	100.348	99.768	100.057	99.848	99.961	100.142	99.250	100.205	100.197	100.036	100.051
cpfu	Si	2.500	2.519	2.465	2.507	2.499	2.514	2.513	2.469	2.468	2.485	2.500	2.512	2.494	2.457	2.521	2.502
	Al	1.482	1.462	1.521	1.478	1.479	1.472	1.476	1.518	1.517	1.498	1.483	1.475	1.489	1.521	1.468	1.476
	Fe3	0.018	0.020	0.019	0.018	0.017	0.017	0.015	0.015	0.018	0.018	0.019	0.019	0.018	0.021	0.017	0.020
	Ca	0.497	0.470	0.526	0.481	0.496	0.481	0.490	0.517	0.518	0.511	0.487	0.472	0.500	0.538	0.471	0.494
	Na	0.498	0.526	0.463	0.510	0.511	0.506	0.486	0.483	0.479	0.478	0.511	0.517	0.491	0.463	0.508	0.504
	K	0.009	0.011	0.007	0.010	0.010	0.010	0.010	0.008	0.007	0.010	0.011	0.010	0.011	0.008	0.010	0.010
	Total	5.004	5.009	5.000	5.005	5.013	5.000	4.989	5.010	5.008	5.001	5.010	5.005	5.003	5.008	4.996	5.006
mole (%)	An	48.6	48.6	53.4	50.2	50.0	48.7	50.1	51.5	52.3	51.9	48.9	48.2	50.0	52.4	48.4	48.6
µg/g	Li	7.239	7.487	8.632	9.396	11.434	11.021	16.630	18.370	13.945	17.994	15.125	14.998	12.053	12.248	9.780	9.331
	Be	0.724	0.703	0.669	0.711	0.712	0.722	0.711	0.683	0.711	0.720	0.723	0.791	0.694	0.662	0.715	0.717
	B	0.189	0.174	0.156	0.145	0.179	0.152	0.164	0.164	0.160	0.170	0.162	0.194	0.150	0.137	0.181	0.178

	Data Point	3	8	12	19	34	41	48	60	63	69	72	75	79	82	89
	Name	San3Pl2	San3Pl2	San3Pl2	San3Pl2	San3Pl2	San3Pl2	San3Pl2	San3Pl2	San3Pl2	San3Pl2	San3Pl2	San3Pl2	San3Pl2	San3Pl2	San3Pl2
	Mineral	Fsp	Fsp	Fsp	Fsp	Fsp	Fsp	Fsp	Fsp	Fsp	Fsp	Fsp	Fsp	Fsp	Fsp	Fsp
	Distance	30	80	120	190	340	410	480	600	630	690	720	750	790	820	890
%	SiO2	45.702	45.973	46.294	46.341	45.911	45.836	44.805	46.459	46.450	45.486	45.445	45.661	45.361	46.080	45.509
	Al2O3	34.705	34.524	34.433	34.221	34.146	34.486	34.597	34.168	34.191	34.901	34.998	34.975	34.890	34.559	33.915
	Fe2O3	0.683	0.779	0.660	0.748	0.712	0.715	0.715	0.747	0.795	0.630	0.646	0.663	0.697	0.743	0.705
	CaO	18.173	17.995	17.827	17.747	17.778	17.956	18.070	17.504	17.805	18.549	18.413	18.167	18.321	17.751	17.777
	Na2O	1.161	1.185	1.440	1.499	1.378	1.308	1.068	1.502	1.405	1.120	1.012	1.202	1.059	1.279	1.356
	K2O	0.019	0.022	0.022	0.024	0.008	0.022	0.006	0.035	0.031	0.005	0.018	0.001	0.012	0.022	0.022
	Total	100.443	100.478	100.676	100.580	99.933	100.323	99.261	100.415	100.677	100.691	100.532	100.669	100.340	100.434	99.284
cpfu	Si	2.100	2.110	2.120	2.124	2.118	2.108	2.084	2.131	2.127	2.087	2.087	2.093	2.087	2.114	2.115
	Al	1.879	1.868	1.858	1.849	1.857	1.869	1.897	1.847	1.845	1.887	1.894	1.889	1.892	1.869	1.858
	Fe3	0.024	0.027	0.023	0.026	0.025	0.025	0.025	0.026	0.027	0.022	0.022	0.023	0.024	0.026	0.025
	Ca	0.895	0.885	0.875	0.872	0.879	0.885	0.901	0.860	0.874	0.912	0.906	0.892	0.903	0.873	0.885
	Na	0.103	0.105	0.128	0.133	0.123	0.117	0.096	0.134	0.125	0.100	0.090	0.107	0.094	0.114	0.122
	K	0.001	0.001	0.001	0.001	0.000	0.001	0.000	0.002	0.002	0.000	0.001	0.000	0.001	0.001	0.001
	Total	5.001	4.996	5.004	5.006	5.003	5.004	5.003	5.000	5.000	5.008	5.000	5.004	5.002	4.996	5.006
mole (%)	An	88.6	89.1	88.1	87.2	88.2	88.6	90.3	87.3	87.1	90.1	90.6	90.6	90.2	87.5	88.9
µg/g	Li	1.839	1.849	3.153	4.019	3.484	2.194	2.222	4.361	3.962	3.767	3.712	2.198	2.138	2.306	3.133
	Be	0.078	0.077	0.091	0.093	0.087	0.077	0.074	0.101	0.094	0.096	0.093	0.068	0.060	0.061	0.093
	B	0.044	0.036	0.038	0.047	0.033	0.038	0.034	0.034	0.031	0.049	0.033	0.044	0.030	0.029	0.045

	Data Point	4	8	14	18	22	26	32	37
	Name	San3bPl1	San3bPl1	San3bPl1	San3bPl1	San3bPl1	San3bPl1	San3bPl1	San3bPl1
	Mineral	Fsp	Fsp	Fsp	Fsp	Fsp	Fsp	Fsp	Fsp
	Distance	40	80	140	180	220	260	320	370
%	SiO2	57.949	57.217	55.598	55.288	55.720	57.125	57.838	60.529
	Al2O3	25.670	26.068	27.047	27.159	27.363	26.832	26.085	25.027
	Fe2O3	0.462	0.458	0.465	0.482	0.409	0.273	0.478	0.358
	CaO	8.836	9.162	10.396	10.851	10.067	8.686	8.248	6.640
	Na2O	6.486	6.183	5.412	5.315	5.901	6.396	6.883	7.949
	K2O	0.184	0.194	0.158	0.122	0.199	0.213	0.313	0.347
	Total	99.587	99.282	99.076	99.217	99.659	99.525	99.845	100.850
cpfu	Si	2.609	2.587	2.527	2.513	2.520	2.573	2.599	2.679
	Al	1.362	1.389	1.449	1.455	1.458	1.424	1.381	1.306
	Fe3	0.016	0.016	0.016	0.016	0.014	0.009	0.016	0.012
	Ca	0.426	0.444	0.506	0.528	0.488	0.419	0.397	0.315
	Na	0.566	0.542	0.477	0.468	0.517	0.558	0.600	0.682
	K	0.011	0.011	0.009	0.007	0.011	0.012	0.018	0.020
	Total	4.990	4.988	4.984	4.989	5.009	4.996	5.011	5.013
mole (%)	An	43.0	46.5	51.6	52.7	47.3	43.0	39.9	33.0
µg/g	Li	9.638	10.078	9.213	9.812	9.607	10.487	10.832	9.671
	Be	0.956	0.838	0.607	0.533	0.804	0.887	1.003	0.938
	B	0.639	0.181	0.143	0.157	0.187	0.173	0.183	0.510

	Data Point	4	9	14	27	33	39	46	52	58	64	71	78	85	92	99
	Name	San3bPl3	San3bPl3	San3bPl3	San3bPl3	San3bPl3	San3bPl3	San3bPl3	San3bPl3	San3bPl3	San3bPl3	San3bPl3	San3bPl3	San3bPl3	San3bPl3	San3bPl3
	Mineral	Fsp	Fsp	Fsp	Fsp	Fsp	Fsp	Fsp	Fsp	Fsp	Fsp	Fsp	Fsp	Fsp	Fsp	Fsp
	Distance	40	90	140	270	330	390	460	520	580	640	710	780	850	920	990
%	SiO2	56.486	56.856	57.155	56.394	57.063	57.115	56.832	56.982	55.694	56.398	55.897	56.039	55.636	55.838	55.955
	Al2O3	27.829	27.725	27.678	27.882	27.901	27.546	27.952	27.907	28.411	28.179	28.300	28.149	28.219	28.528	28.190
	Fe2O3	0.493	0.458	0.445	0.439	0.386	0.416	0.386	0.435	0.488	0.460	0.462	0.458	0.486	0.426	0.462
	CaO	10.080	9.667	9.542	9.510	9.638	9.176	9.691	9.580	10.171	10.010	10.312	10.070	10.308	10.325	9.944
	Na2O	5.838	6.085	6.256	5.978	6.079	6.232	6.056	6.035	5.560	5.985	5.737	5.787	5.617	5.732	5.856
	K2O	0.196	0.159	0.206	0.187	0.153	0.222	0.177	0.196	0.208	0.178	0.166	0.210	0.161	0.175	0.201
	Total	100.922	100.950	101.282	100.390	101.220	100.707	101.094	101.135	100.532	101.210	100.874	100.713	100.427	101.024	100.608
cpfu	Si	2.520	2.533	2.538	2.525	2.533	2.547	2.528	2.532	2.495	2.510	2.497	2.506	2.496	2.491	2.505
	Al	1.463	1.455	1.448	1.471	1.460	1.448	1.465	1.462	1.500	1.478	1.490	1.484	1.492	1.500	1.487
	Fe3	0.017	0.015	0.015	0.015	0.013	0.014	0.013	0.015	0.016	0.015	0.016	0.015	0.016	0.014	0.016
	Ca	0.482	0.461	0.454	0.456	0.458	0.438	0.462	0.456	0.488	0.477	0.494	0.482	0.496	0.494	0.477
	Na	0.505	0.526	0.539	0.519	0.523	0.539	0.522	0.520	0.483	0.516	0.497	0.502	0.489	0.496	0.508
	K	0.011	0.009	0.012	0.011	0.009	0.013	0.010	0.011	0.012	0.010	0.009	0.012	0.009	0.010	0.011
	Total	4.998	4.999	5.006	4.997	4.996	4.998	5.000	4.995	4.994	5.007	5.003	5.001	4.998	5.005	5.004
mole (%)	An	48.4	46.5	46.0	47.2	47.1	45.3	46.6	46.7	50.0	48.6	50.2	48.6	49.8	50.0	48.0
µg/g	Li	8.609	10.191	10.240	9.816	9.976	10.274	10.136	9.865	9.310	9.799	9.335	9.636	9.603	9.620	9.223
	Be	0.770	0.900	0.875	0.861	0.906	0.933	0.911	0.885	0.798	0.862	0.801	0.790	0.809	0.781	0.786
	B	0.169	0.178	0.174	0.169	0.199	0.182	0.190	0.172	0.155	0.163	0.184	0.172	0.153	0.164	0.166

	Data point	4	12	16	27	33	39	43	49
	Name	San35bPl1	San35bPl1	San35bPl1	San35bPl1	San35bPl1	San35bPl1	San35bPl1	San35bPl1
	Mineral	Fsp	Fsp	Fsp	Fsp	Fsp	Fsp	Fsp	Fsp
	Distance	40	120	160	270	330	390	430	490
%	SiO2	56.253	57.896	57.050	56.434	57.639	54.984	55.070	56.131
	Al2O3	27.348	26.579	26.879	27.334	26.452	28.011	28.101	27.278
	Fe2O3	0.562	0.503	0.432	0.470	0.428	0.509	0.519	0.610
	MgO	0.038	0.038	0.043	0.040	0.030	0.036	0.040	0.045
	CaO	9.547	8.511	9.307	9.600	8.822	10.341	10.698	9.794
	Na2O	5.837	6.540	6.188	5.978	6.465	5.498	5.408	5.777
	K2O	0.193	0.220	0.222	0.166	0.212	0.171	0.146	0.178
	Total	99.778	100.287	100.121	100.022	100.048	99.550	99.982	99.813
cpfu	Si	2.535	2.587	2.560	2.537	2.584	2.490	2.485	2.531
	Al	1.452	1.400	1.422	1.448	1.398	1.495	1.495	1.449
	Fe3	0.019	0.017	0.015	0.016	0.014	0.017	0.018	0.021
	Mg	0.003	0.003	0.003	0.003	0.002	0.002	0.003	0.003
	Ca	0.461	0.408	0.447	0.462	0.424	0.502	0.517	0.473
	Na	0.510	0.567	0.538	0.521	0.562	0.483	0.473	0.505
	K	0.011	0.013	0.013	0.010	0.012	0.010	0.008	0.010
	Total	4.990	4.994	4.997	4.996	4.997	5.000	4.999	4.992
mole (%)	An	48.7	42.7	45.1	46.4	44.5	50.2	52.8	48.2
µg/g	Li	7.027	7.640	9.074	9.247	8.851	8.703	7.731	7.562
	Be	0.641	0.648	0.750	0.750	0.707	0.738	0.675	0.707
	B	0.151	0.149	0.188	0.186	0.168	0.172	0.154	0.181

	Data Point	4	9	15	24	32	42	50	59	66	72	80	87	94	106	117	124	130	137
	Name	san35pl2	san35pl2	san35pl2	san35pl2	san35pl2	san35pl2	san35pl2	san35pl2	san35pl2	san35pl2	san35pl2	san35pl2	san35pl2	san35pl2	san35pl2	san35pl2	san35pl2	san35pl2
	Mineral	Fsp	Fsp	Fsp	Fsp	Fsp	Fsp	Fsp	Fsp	Fsp	Fsp	Fsp	Fsp	Fsp	Fsp	Fsp	Fsp	Fsp	Fsp
	Distance	40	90	150	240	320	420	500	590	660	720	800	870	940	1060	1170	1240	1300	1370
%	SiO2	55.805	56.045	56.612	56.272	56.736	56.561	57.329	56.762	56.244	56.481	57.140	56.971	55.793	57.157	56.618	57.893	56.422	55.037
	Al2O3	27.674	27.586	27.281	27.308	27.400	27.242	26.524	26.537	26.905	27.155	27.212	26.966	26.990	26.637	26.996	26.647	27.586	27.867
	Fe2O3	0.572	0.545	0.482	0.516	0.478	0.465	0.462	0.508	0.475	0.458	0.432	0.436	0.603	0.473	0.429	0.449	0.459	0.479
	CaO	9.801	9.895	9.650	9.338	9.758	9.237	8.903	9.110	9.471	9.173	9.221	9.225	9.621	9.214	9.482	8.694	9.787	10.298
	Na2O	5.750	5.763	5.916	6.015	6.120	6.086	6.513	6.236	6.144	6.279	6.244	6.148	6.055	6.269	6.079	6.647	5.889	5.723
	K2O	0.189	0.163	0.183	0.205	0.207	0.213	0.232	0.189	0.173	0.235	0.200	0.236	0.246	0.178	0.179	0.212	0.193	0.160
	Total	99.791	99.997	100.124	99.654	100.699	99.804	99.963	99.342	99.412	99.781	100.449	99.982	99.308	99.928	99.783	100.542	100.336	99.564
cpfu	Si	2.517	2.522	2.542	2.538	2.536	2.546	2.576	2.566	2.545	2.545	2.555	2.559	2.531	2.569	2.550	2.583	2.529	2.494
	Al	1.471	1.463	1.444	1.452	1.443	1.445	1.404	1.414	1.435	1.442	1.434	1.428	1.443	1.411	1.433	1.401	1.458	1.488
	Fe3	0.019	0.018	0.016	0.018	0.016	0.016	0.016	0.017	0.016	0.016	0.015	0.015	0.021	0.016	0.015	0.015	0.015	0.016
	Ca	0.474	0.477	0.464	0.451	0.467	0.445	0.429	0.441	0.459	0.443	0.442	0.444	0.468	0.444	0.458	0.416	0.470	0.500
	Na	0.503	0.503	0.515	0.526	0.530	0.531	0.567	0.547	0.539	0.549	0.541	0.535	0.533	0.546	0.531	0.575	0.512	0.503
	K	0.011	0.009	0.010	0.012	0.012	0.012	0.013	0.011	0.010	0.014	0.011	0.014	0.014	0.010	0.010	0.012	0.011	0.009
	Total	4.995	4.993	4.991	4.996	5.005	4.995	5.005	4.997	5.004	5.007	4.997	4.994	5.010	4.996	4.997	5.002	4.995	5.010
mole (%)	An	48.7	48.8	47.0	46.6	47.9	44.9	43.4	44.3	46.2	45.0	45.1	45.2	46.6	44.5	46.1	42.0	46.9	49.8
µg/g	Li	6.683	8.360	8.935	9.008	8.604	9.225	9.764	9.662	9.243	8.717	9.259	9.180	9.173	8.909	9.247	9.827	9.316	7.948
	Be	0.740	0.747	0.799	0.768	0.774	0.837	0.832	0.832	0.825	0.818	0.802	0.780	0.707	0.753	0.762	0.804	0.820	0.771
	B	0.195	0.159	0.165	0.162	0.158	0.164	0.172	0.170	0.170	0.184	0.179	0.161	0.181	0.168	0.168	0.201	0.156	0.146

	Data Point	2	7	12	17	22	27	34	39	44	49	54	59	64
	Name	San2bPl4	San2bPl4	San2bPl4	San2bPl4	San2bPl4	San2bPl4	San2bPl4	San2bPl4	San2bPl4	San2bPl4	San2bPl4	San2bPl4	San2bPl4
	Mineral	Fsp	Fsp	Fsp	Fsp	Fsp	Fsp	Fsp	Fsp	Fsp	Fsp	Fsp	Fsp	Fsp
	Distance	20	70	120	170	220	270	340	390	440	490	540	590	640
%	SiO2	54.618	54.661	54.122	53.925	56.205	54.631	55.523	53.949	54.708	54.749	53.183	54.785	54.956
	Al2O3	28.060	27.079	28.891	28.290	27.308	27.999	27.264	27.676	27.572	27.901	28.874	27.563	27.601
	Fe2O3	0.603	0.562	0.448	0.448	0.496	0.573	0.599	0.453	0.623	0.435	0.652	0.616	0.436
	CaO	10.800	10.484	10.879	10.471	9.523	10.397	9.684	10.401	10.165	10.200	11.739	9.584	10.052
	Na2O	5.765	5.740	5.485	5.421	6.388	5.295	5.777	5.423	5.763	5.531	5.192	5.737	5.509
	K2O	0.106	0.149	0.125	0.118	0.206	0.094	0.157	0.163	0.212	0.225	0.175	0.137	0.075
	Total	99.952	98.675	99.950	98.673	100.126	98.989	99.004	98.065	99.043	99.041	99.815	98.422	98.629
cpfu	Si	2.472	2.503	2.448	2.466	2.529	2.487	2.524	2.483	2.494	2.492	2.419	2.506	2.507
	Al	1.497	1.461	1.540	1.525	1.448	1.502	1.461	1.501	1.481	1.497	1.548	1.486	1.484
	Fe3	0.021	0.019	0.015	0.015	0.017	0.020	0.020	0.016	0.021	0.015	0.022	0.021	0.015
	Ca	0.524	0.514	0.527	0.513	0.459	0.507	0.472	0.513	0.497	0.497	0.572	0.470	0.491
	Na	0.506	0.510	0.481	0.481	0.557	0.467	0.509	0.484	0.509	0.488	0.458	0.509	0.487
	K	0.006	0.009	0.007	0.007	0.012	0.005	0.009	0.010	0.012	0.013	0.010	0.008	0.004
	Total	5.025	5.016	5.019	5.007	5.023	4.989	4.995	5.006	5.015	5.003	5.030	4.999	4.989
mole (%)	An	49.8	51.2	53.5	50.4	49.0	51.0	46.6	50.7	49.6	49.9	55.4	49.1	50.4
µg/g	Li	6.883	7.391	6.868	7.154	7.215	7.827	8.249	7.498	7.613	7.113	6.597	7.588	7.034
	Be	0.704	0.722	0.611	0.677	0.671	0.711	0.731	0.722	0.734	0.649	0.616	0.687	0.709
	B	0.180	0.162	0.168	0.147	0.146	0.177	0.146	0.163	0.179	0.149	0.142	0.181	0.159

	Data Point	3	8	16	24	34	45	53	61	69	79	87	98	106
	Name	San2bPl3	San2bPl3	San2bPl3	San2bPl3	San2bPl3	San2bPl3	San2bPl3	San2bPl3	San2bPl3	San2bPl3	San2bPl3	San2bPl3	San2bPl3
	Mineral	Fsp	Fsp	Fsp	Fsp	Fsp	Fsp	Fsp	Fsp	Fsp	Fsp	Fsp	Fsp	Fsp
	Distance	30	80	160	240	340	450	530	610	690	790	870	980	1060
%	SiO2	56.111	56.409	56.113	56.469	54.753	55.112	54.980	55.358	55.619	55.455	55.149	55.906	56.332
	Al2O3	28.300	27.839	28.092	27.765	29.226	29.084	29.046	28.557	28.678	28.493	28.954	27.916	27.960
	Fe2O3	0.506	0.468	0.552	0.536	0.513	0.526	0.468	0.579	0.465	0.528	0.518	0.530	0.518
	MgO	0.045	0.041	0.033	0.038	0.041	0.041	0.038	0.036	0.038	0.046	0.040	0.041	0.035
	CaO	10.234	9.989	10.074	9.913	11.209	11.006	10.891	10.733	10.617	10.529	10.796	10.264	10.276
	Na2O	5.788	5.633	5.701	5.913	5.273	5.277	5.188	5.361	5.416	5.463	5.261	5.763	5.723
	K2O	0.184	0.160	0.163	0.169	0.119	0.167	0.153	0.159	0.165	0.166	0.142	0.192	0.194
	Total	101.168	100.539	100.728	100.803	101.134	101.213	100.764	100.783	100.998	100.680	100.860	100.612	101.038
cpfu	Si	2.500	2.523	2.508	2.522	2.447	2.459	2.461	2.478	2.482	2.484	2.466	2.505	2.512
	Al	1.486	1.467	1.480	1.461	1.539	1.529	1.533	1.507	1.508	1.504	1.526	1.474	1.469
	Fe3	0.017	0.016	0.019	0.018	0.017	0.018	0.016	0.020	0.016	0.018	0.017	0.018	0.017
	Mg	0.003	0.003	0.002	0.003	0.003	0.003	0.003	0.002	0.003	0.003	0.003	0.003	0.002
	Ca	0.488	0.479	0.482	0.474	0.537	0.526	0.522	0.515	0.508	0.505	0.517	0.493	0.491
	Na	0.500	0.488	0.494	0.512	0.457	0.456	0.450	0.465	0.469	0.474	0.456	0.501	0.495
	K	0.010	0.009	0.009	0.010	0.007	0.010	0.009	0.009	0.009	0.009	0.008	0.011	0.011
	Total	5.004	4.985	4.994	4.999	5.007	5.001	4.994	4.996	4.995	4.997	4.994	5.005	4.998
mole (%)	An	49.4	48.1	47.7	46.6	52.4	54.0	53.8	51.3	51.3	51.2	53.1	48.1	48.8
µg/g	Li	7.002	7.949	7.997	7.705	8.013	7.398	7.507	8.062	8.735	8.879	8.736	8.537	8.266
	Be	0.784	0.744	0.737	0.733	0.733	0.652	0.666	0.700	0.715	0.686	0.684	0.705	0.751
	B	0.582	0.182	0.169	0.167	0.160	0.155	0.138	0.158	0.185	0.161	0.161	0.174	0.177

	Data Point	3	8	13	20	27	43	58	65	72
	Name	San37Pl1	San37Pl1	San37Pl1	San37Pl1	San37Pl1	San37Pl1	San37Pl1	San37Pl1	San37Pl1
	Mineral	Fsp	Fsp	Fsp	Fsp	Fsp	Fsp	Fsp	Fsp	Fsp
	Distance	30	80	130	200	270	430	580	650	720
%	SiO2	55.795	53.745	54.635	55.420	55.891	57.953	55.403	55.525	55.585
	Al2O3	27.875	28.700	28.901	28.033	27.701	26.486	28.353	28.171	28.292
	Fe2O3	0.588	0.566	0.555	0.468	0.482	0.569	0.525	0.588	0.546
	CaO	10.024	10.127	11.035	10.262	9.747	8.438	10.487	10.179	10.269
	Na2O	5.950	5.795	5.385	5.651	5.975	6.709	5.684	5.765	5.718
	K2O	0.158	0.178	0.157	0.179	0.188	0.245	0.131	0.171	0.182
	Total	100.390	99.111	100.668	100.013	99.984	100.400	100.583	100.399	100.592
cpfu	Si	2.506	2.451	2.454	2.498	2.517	2.589	2.485	2.494	2.492
	Al	1.475	1.542	1.530	1.489	1.470	1.395	1.499	1.491	1.495
	Fe3	0.020	0.019	0.019	0.016	0.016	0.019	0.018	0.020	0.018
	Ca	0.482	0.495	0.531	0.496	0.470	0.404	0.504	0.490	0.493
	Na	0.518	0.512	0.469	0.494	0.522	0.581	0.494	0.502	0.497
	K	0.009	0.010	0.009	0.010	0.011	0.014	0.007	0.010	0.010
	Total	5.010	5.030	5.011	5.002	5.006	5.002	5.008	5.007	5.005
mole (%)	An	48.0	50.3	52.0	49.1	47.9	42.1	49.4	50.7	49.3
µg/g	Li	7.547	7.513	8.591	9.332	9.366	9.028	8.809	8.173	6.454
	Be	0.749	0.693	0.710	0.715	0.712	0.834	0.742	0.711	0.714
	B	0.160	0.160	0.149	0.158	0.173	0.190	0.174	0.136	0.175

	Data Point	3	7	11	15	20	26	32	37	44	48	54
	Name	San37Pl2	San37Pl2	San37Pl2	San37Pl2	San37Pl2	San37Pl2	San37Pl2	San37Pl2	San37Pl2	San37Pl2	San37Pl2
	Mineral	Fsp	Fsp	Fsp	Fsp	Fsp	Fsp	Fsp	Fsp	Fsp	Fsp	Fsp
	Distance	30	70	110	150	200	260	320	370	440	480	540
%	SiO2	54.877	54.738	55.478	55.861	55.940	55.716	55.495	55.604	55.917	55.540	54.374
	Al2O3	27.584	28.778	28.202	28.096	27.903	28.088	28.190	28.050	27.814	28.237	28.963
	Fe2O3	0.593	0.589	0.550	0.506	0.500	0.490	0.479	0.560	0.488	0.470	0.518
	CaO	9.825	11.038	10.623	10.201	10.070	10.302	9.969	10.201	9.810	10.309	11.247
	Na2O	5.930	5.432	5.617	5.734	5.873	5.838	5.705	5.827	6.020	5.756	5.148
	K2O	0.181	0.178	0.169	0.154	0.188	0.135	0.164	0.181	0.170	0.158	0.152
	Total	98.990	100.753	100.639	100.552	100.474	100.569	100.002	100.423	100.219	100.470	100.402
cpfu	Si	2.500	2.457	2.488	2.503	2.509	2.498	2.499	2.497	2.513	2.493	2.448
	Al	1.481	1.522	1.491	1.484	1.475	1.484	1.496	1.485	1.473	1.494	1.537
	Fe3	0.020	0.020	0.019	0.017	0.017	0.017	0.016	0.019	0.016	0.016	0.018
	Ca	0.480	0.531	0.510	0.490	0.484	0.495	0.481	0.491	0.472	0.496	0.543
	Na	0.524	0.473	0.488	0.498	0.511	0.508	0.498	0.507	0.525	0.501	0.449
	K	0.011	0.010	0.010	0.009	0.011	0.008	0.009	0.010	0.010	0.009	0.009
	Total	5.016	5.013	5.006	5.000	5.006	5.009	4.999	5.010	5.009	5.008	5.004
mole (%)	An	48.9	51.2	50.8	49.4	48.1	49.4	49.0	48.6	48.0	49.2	53.9
µg/g	Li	7.526	9.017	11.695	14.536	17.033	20.070	19.642	15.101	13.051	9.152	7.736
	Be	0.700	0.657	0.538	0.733	0.733	0.705	0.717	0.673	0.712	0.693	0.653
	B	0.180	0.159	0.153	0.139	0.171	0.166	0.152	0.165	0.185	0.168	0.163

	Data Point	6	10	17	24	30	43	49	55	60
	Name	San37Pl3	San37Pl3	San37Pl3	San37Pl3	San37Pl3	San37Pl3	San37Pl3	San37Pl3	San37Pl3
	Mineral	Fsp	Fsp	Fsp	Fsp	Fsp	Fsp	Fsp	Fsp	Fsp
	Distance	60	100	170	240	300	430	490	550	600
%	SiO2	56.710	54.494	54.165	54.738	55.609	55.731	56.849	55.427	55.838
	Al2O3	27.467	28.831	28.971	28.593	28.143	27.907	27.178	28.226	27.843
	Fe2O3	0.575	0.515	0.553	0.543	0.548	0.536	0.468	0.519	0.485
	CaO	9.558	10.816	11.040	10.663	10.283	10.008	9.085	10.445	10.047
	Na2O	6.039	5.341	5.242	5.558	5.696	5.970	6.391	5.692	5.789
	K2O	0.200	0.159	0.119	0.175	0.175	0.169	0.214	0.177	0.206
	Total	100.549	100.156	100.090	100.270	100.454	100.321	100.185	100.486	100.208
cpfu	Si	2.537	2.457	2.446	2.466	2.496	2.504	2.550	2.489	2.510
	Al	1.448	1.532	1.542	1.518	1.489	1.478	1.437	1.494	1.475
	Fe3	0.019	0.017	0.019	0.018	0.019	0.018	0.016	0.018	0.016
	Ca	0.458	0.523	0.534	0.515	0.494	0.482	0.437	0.503	0.484
	Na	0.524	0.467	0.459	0.486	0.496	0.520	0.556	0.496	0.505
	K	0.011	0.009	0.007	0.010	0.010	0.010	0.012	0.010	0.012
	Total	4.997	5.006	5.007	5.013	5.003	5.012	5.008	5.008	5.002
mole (%)	An	47.9	53.0	54.1	51.4	50.6	46.6	44.0	49.4	49.0
µg/g	Li	7.897	7.092	7.594	9.059	10.618	12.756	10.725	8.812	7.196
	Be	0.777	0.632	0.640	0.672	0.725	0.789	0.809	0.760	0.671
	B	0.204	0.140	0.143	0.155	0.170	0.179	0.161	0.183	0.160

	Data Point	3	12	17	26	33	39	45	53	61	72	77	90	99	108
	Name	San1bPl3	San1bPl3	San1bPl3	San1bPl3	San1bPl3	San1bPl3	San1bPl3	San1bPl3	San1bPl3	San1bPl3	San1bPl3	San1bPl3	San1bPl3	San1bPl3
	Mineral	Fsp	Fsp	Fsp	Fsp	Fsp	Fsp	Fsp	Fsp	Fsp	Fsp	Fsp	Fsp	Fsp	Fsp
	Distance	30	120	170	260	330	390	450	530	610	720	770	900	990	1080
%	SiO2	57.110	56.631	56.377	57.012	56.486	56.976	53.401	52.442	52.387	53.403	53.797	57.513	56.156	57.016
	Al2O3	27.669	27.741	27.929	28.134	28.394	27.967	30.376	30.612	30.206	30.025	29.413	27.758	27.482	28.149
	Fe2O3	0.503	0.369	0.456	0.219	0.371	0.418	0.593	0.466	0.463	0.443	0.665	0.422	0.422	0.668
	MgO	0.032	0.043	0.023	0.036	0.050	0.041	0.046	0.028	0.040	0.040	0.048	0.045	0.041	0.033
	CaO	9.388	9.661	9.980	9.728	9.763	10.159	12.148	12.429	12.730	12.742	12.289	9.626	9.468	9.983
	Na2O	5.907	5.334	5.765	5.957	5.647	5.589	4.695	3.912	4.432	4.419	4.363	5.978	5.622	5.501
	K2O	0.199	0.163	0.118	0.164	0.147	0.159	0.204	0.102	0.067	0.136	0.200	0.155	0.207	0.172
	Total	100.808	99.942	100.648	101.250	100.858	101.309	101.463	99.991	100.325	101.208	100.775	101.497	99.398	101.522
cpfu	Si	2.543	2.539	2.519	2.529	2.515	2.528	2.387	2.374	2.371	2.394	2.419	2.544	2.536	2.524
	Al	1.452	1.466	1.471	1.471	1.490	1.462	1.601	1.633	1.611	1.586	1.559	1.447	1.463	1.468
	Fe3	0.017	0.012	0.015	0.007	0.012	0.014	0.020	0.016	0.016	0.015	0.022	0.014	0.014	0.022
	Mg	0.002	0.003	0.002	0.002	0.003	0.003	0.003	0.002	0.003	0.003	0.003	0.003	0.003	0.002
	Ca	0.448	0.464	0.478	0.462	0.466	0.483	0.582	0.603	0.617	0.612	0.592	0.456	0.458	0.473
	Na	0.510	0.464	0.499	0.512	0.487	0.481	0.407	0.343	0.389	0.384	0.380	0.513	0.492	0.472
	K	0.011	0.009	0.007	0.009	0.008	0.009	0.012	0.006	0.004	0.008	0.011	0.009	0.012	0.010
	Total	4.983	4.958	4.991	4.993	4.982	4.979	5.012	4.976	5.011	5.001	4.987	4.986	4.978	4.972
mole (%)	An	48.398	50.060	47.518	46.325	48.362	50.093	58.845	62.938	61.642	60.180	61.544	46.565	48.194	50.760
µg/g	Li	7.509	7.892	8.864	8.950	8.457	8.503	7.112	5.328	6.543	6.727	6.683	8.223	8.427	8.234
	Be	0.744	0.739	0.783	0.776	0.807	0.718	0.372	0.341	0.322	0.340	0.403	0.820	0.785	0.732
	B	0.164	0.151	0.185	0.200	0.189	0.158	0.158	0.125	0.105	0.128	0.115	0.176	0.162	0.171

	Data Point	2	10	16	22	29
	Name	San37bPl3	San37bPl3	San37bPl3	San37bPl3	San37bPl3
	Mineral	Fsp	Fsp	Fsp	Fsp	Fsp
	Distance	20	100	160	220	290
%	SiO2	56.659	45.794	46.040	54.011	54.391
	Al2O3	27.714	34.985	34.869	29.441	29.101
	Fe2O3	0.638	0.678	0.688	0.613	0.612
	MgO	0.040	0.000	0.007	0.041	0.032
	CaO	9.775	17.965	17.493	11.817	11.483
	Na2O	5.842	1.250	1.344	4.870	5.017
	K2O	0.189	0.010	0.010	0.148	0.125
	Total	100.857	100.682	100.451	100.941	100.761
cpfu	Si	2.527	2.097	2.110	2.423	2.442
	Al	1.457	1.888	1.883	1.557	1.540
	Fe3	0.021	0.023	0.024	0.021	0.021
	Mg	0.003	0.000	0.000	0.003	0.002
	Ca	0.467	0.882	0.859	0.568	0.552
	Na	0.505	0.111	0.119	0.424	0.437
	K	0.011	0.001	0.001	0.008	0.007
	Total	4.991	5.002	4.996	5.004	5.000
mole (%)	An	50.9	88.2	87.8	60.0	56.1
µg/g	Li	7.355	2.485	3.626	19.989	9.563
	Be	0.700	0.085	0.118	0.463	0.481
	B	0.194	0.075	0.070	0.180	0.114

	Data Point	6	9	14	21	29	37	46	51	62	71	74
	Name	San37cPl	San37cPl	San37cPl	San37cPl	San37cPl	San37cPl	San37cPl	San37cPl	San37cPl	San37cPl	San37cPl
	Mineral	Fsp	Fsp	Fsp	Fsp	Fsp	Fsp	Fsp	Fsp	Fsp	Fsp	Fsp
	Distance	60	90	140	210	290	370	460	510	620	710	740
%	SiO2	55.68	55.57	51.90	48.72	49.44	48.31	49.30	51.34	56.01	56.23	55.74
	Al2O3	27.93	27.77	30.59	32.77	32.18	33.48	32.35	30.76	28.01	28.09	28.40
	Fe2O3	0.65	0.55	0.65	0.69	0.67	0.69	0.67	0.65	0.56	0.56	0.65
	MgO	0.04	0.04	0.05	0.04	0.03	0.02	0.04	0.05	0.04	0.04	0.04
	CaO	10.26	9.61	13.23	15.32	15.09	16.14	15.06	13.40	10.15	10.03	10.68
	Na2O	5.82	5.79	3.97	2.68	3.04	2.31	2.92	4.08	5.95	5.85	5.69
	K2O	0.19	0.17	0.10	0.06	0.06	0.03	0.04	0.11	0.16	0.15	0.16
	Total	100.57	99.50	100.48	100.27	100.50	100.99	100.38	100.38	100.88	100.95	101.36
cpfu	Si	2.498	2.513	2.349	2.224	2.251	2.194	2.246	2.331	2.504	2.508	2.484
	Al	1.477	1.480	1.632	1.763	1.727	1.792	1.737	1.646	1.475	1.477	1.491
	Fe3	0.022	0.019	0.022	0.024	0.023	0.024	0.023	0.022	0.019	0.019	0.022
	Mg	0.003	0.003	0.003	0.002	0.002	0.002	0.003	0.003	0.002	0.003	0.003
	Ca	0.493	0.465	0.642	0.749	0.736	0.785	0.735	0.652	0.486	0.480	0.510
	Na	0.507	0.507	0.348	0.237	0.268	0.203	0.258	0.359	0.516	0.506	0.492
	K	0.011	0.010	0.006	0.003	0.003	0.002	0.002	0.006	0.009	0.009	0.009
	Total	5.011	4.997	5.001	5.003	5.010	5.001	5.004	5.018	5.012	5.001	5.010
mole (%)	An	49.7	49.2	66.3	76.5	74.1	78.9	74.1	66.4	48.9	49.2	49.8
µg/g	Li	7.010	6.428	6.195	3.975	3.986	3.804	3.774	3.942	6.088	6.819	6.565
	Be	0.724	0.529	0.529	0.216	0.235	0.216	0.232	0.206	0.458	0.668	0.746
	B	0.175	0.167	0.130	0.106	0.077	0.094	0.085	0.085	0.159	0.147	0.172

	Data Point	3	8	15	20	25	30	35	42	49
	Name	San37Cpx2a	San37Cpx2a	San37Cpx2a	San37Cpx2a	San37Cpx2a	San37Cpx2a	San37Cpx2a	San37Cpx2a	San37Cpx2a
	Mineral	Cpx	Cpx	Cpx	Cpx	Cpx	Cpx	Cpx	Cpx	Cpx
	Distance	30	80	150	200	250	300	350	420	490
%	SiO2	51.518	51.657	52.025	52.094	51.756	51.431	51.689	51.805	51.942
	TiO2	0.509	0.509	0.455	0.776	0.514	0.515	0.514	0.545	0.515
	Al2O3	1.421	1.600	1.283	1.330	1.396	1.617	1.309	1.411	1.445
	Cr2O3	0.051	0.000	0.000	0.009	0.025	0.061	0.000	0.012	0.004
	Fe2O3	1.472	1.815	1.428	2.037	1.315	1.769	1.146	1.130	1.728
	FeO	9.709	8.515	9.861	9.380	9.674	9.804	9.718	9.781	8.968
	MnO	0.511	0.519	0.678	0.550	0.518	0.588	0.598	0.591	0.511
	MgO	14.036	14.392	14.205	14.367	14.095	14.120	14.150	14.057	14.268
	CaO	19.763	20.281	19.791	20.312	20.154	19.381	19.917	19.956	20.364
	Na2O	0.311	0.318	0.294	0.306	0.252	0.337	0.260	0.305	0.332
	K2O	0.017	0.024	0.010	0.000	0.012	0.000	0.000	0.006	0.008
	Total	99.318	99.631	100.030	101.161	99.711	99.623	99.301	99.598	100.085
cpfu	Si	1.944	1.937	1.950	1.932	1.945	1.936	1.950	1.948	1.942
	Ti	0.014	0.014	0.013	0.022	0.015	0.015	0.015	0.015	0.014
	Al	0.063	0.071	0.057	0.058	0.062	0.072	0.058	0.063	0.064
	Cr	0.002	0.000	0.000	0.000	0.001	0.002	0.000	0.000	0.000
	Fe3	0.042	0.051	0.040	0.057	0.037	0.050	0.033	0.032	0.049
	Fe2	0.306	0.267	0.309	0.291	0.304	0.309	0.307	0.308	0.280
	Mn	0.016	0.016	0.022	0.017	0.016	0.019	0.019	0.019	0.016
	Mg	0.790	0.804	0.794	0.794	0.790	0.792	0.796	0.788	0.795
	Ca	0.799	0.815	0.795	0.807	0.812	0.782	0.805	0.804	0.816
	Na	0.023	0.023	0.021	0.022	0.018	0.025	0.019	0.022	0.024
	K	0.001	0.001	0.000	0.000	0.001	0.000	0.000	0.000	0.000
	Total	4	4	4	4	4	4	4	4	4
	Mg#	72.0	75.1	72.0	73.2	72.2	72.0	72.2	71.9	73.9
µg/g	Li	2.720	2.473	2.696	2.697	2.839	2.669	2.643	2.787	2.472
	Be	0.152	0.154	0.155	0.143	0.180	0.117	0.158	0.175	0.144
	B	0.159	0.145	0.166	0.148	0.213	0.137	0.146	0.162	0.123

	Data Point	3	7	11	15	24	32
	Name	San36bCpx2	san36px2	san36px2	san36px2	san36px2	san36px2
	Mineral	Cpx	Cpx	Cpx	Cpx	Cpx	Cpx
	Distance	30	70	110	150	240	320
%	SiO2	52.241	52.139	52.269	52.265	52.233	52.098
	TiO2	0.517	0.505	0.482	0.392	0.442	0.567
	Al2O3	1.285	1.328	1.381	1.226	1.262	1.561
	Cr2O3	0	0.035	0.013	0.006	0.003	0
	FeO	10.791	10.951	11.064	11.61	11.515	11.096
	MnO	0.609	0.581	0.664	0.666	0.697	0.575
	MgO	13.946	13.805	13.706	13.672	13.818	13.74
	CaO	19.784	20.187	20.028	19.968	19.349	19.927
	Na2O	0.306	0.317	0.309	0.293	0.314	0.306
	K2O	0	0.01	0	0.011	0	0.002
	Total	99.479	99.858	99.916	100.109	99.633	99.872
		30	70	110	150	240	320
cpfu	Si	1.9670	1.9601	1.9635	1.9644	1.9683	1.9573
	Ti	0.0146	0.0143	0.0136	0.0111	0.0125	0.0160
	Al	0.0570	0.0588	0.0611	0.0543	0.0560	0.0691
	Cr	0.0000	0.0010	0.0004	0.0002	0.0001	0.0000
	Fe2	0.3398	0.3443	0.3476	0.3649	0.3629	0.3486
	Mn	0.0194	0.0185	0.0211	0.0212	0.0222	0.0183
	Mg	0.7828	0.7737	0.7675	0.7661	0.7763	0.7695
	Ca	0.7981	0.8131	0.8061	0.8041	0.7812	0.8021
	Na	0.0223	0.0231	0.0225	0.0214	0.0229	0.0223
	K	0.0000	0.0005	0.0000	0.0005	0.0000	0.0001
	Total	4.0011	4.0075	4.0034	4.0082	4.0025	4.0033
	Mg#	69.7	69.2	68.8	67.7	68.1	68.8
µg/g	Li	3.4172	2.7501	2.8322	2.8053	3.0302	3.0248
	Be	0.1390	0.1419	0.1409	0.1547	0.1343	0.1671
	B	0.1721	0.1405	0.1525	0.1565	0.1398	0.1634

	Data Point	2	8	14	32	41	46	53	56
	Name	San3Cpx3	San3Cpx3	San3Cpx3	San3Cpx3	San3Cpx3	San3Cpx3	San3Cpx3	San3Cpx3
	Mineral	Cpx	Cpx	Cpx	Cpx	Cpx	Cpx	Cpx	Cpx
	Distance	20	80	140	320	410	460	530	560
%	SiO2	52.37	52.124	52.036	52.614	52.267	51.983	51.923	51.82
	TiO2	0.397	0.352	0.435	0.379	0.404	0.389	0.434	0.495
	Al2O3	1.389	1.266	1.307	1.119	1.266	1.224	1.338	1.47
	Cr2O3	0	0	0.023	0.01	0	0	0	0
	FeO	10.435	11.017	10.86	11.501	11.875	11.989	11.685	11.695
	MnO	0.578	0.549	0.518	0.644	0.573	0.618	0.64	0.662
	MgO	13.654	13.636	13.623	13.571	13.283	13.338	13.372	13.505
	CaO	20.592	20.594	20.413	20.361	20.105	19.63	19.91	19.464
	Na2O	0.291	0.325	0.284	0.26	0.284	0.266	0.306	0.325
	K2O	0.014	0.013	0	0.011	0.018	0	0.008	0.006
	Total	99.72	99.876	99.499	100.47	100.075	99.437	99.616	99.442
%	Si	1.967	1.962	1.963	1.970	1.967	1.969	1.962	1.960
	Ti	0.011	0.010	0.012	0.011	0.011	0.011	0.012	0.014
	Al	0.061	0.056	0.058	0.049	0.056	0.055	0.060	0.066
	Cr	0.000	0.000	0.001	0.000	0.000	0.000	0.000	0.000
	Fe2	0.328	0.347	0.343	0.360	0.374	0.380	0.369	0.370
	Mn	0.018	0.018	0.017	0.020	0.018	0.020	0.020	0.021
	Mg	0.765	0.765	0.766	0.757	0.745	0.753	0.753	0.761
	Ca	0.829	0.830	0.825	0.817	0.811	0.796	0.806	0.789
	Na	0.021	0.024	0.021	0.019	0.021	0.020	0.022	0.024
	K	0.001	0.001	0.000	0.001	0.001	0.000	0.000	0.000
	Total	4.002	4.012	4.006	4.004	4.004	4.003	4.007	4.005
	Mg#	69.992	68.812	69.099	67.778	66.599	66.479	67.105	67.304
µg/g	Li	12.285	8.641	6.217	6.508	4.768	5.527	3.255	6.197
	Be	0.190	0.165	0.202	0.200	0.250	0.272	0.214	0.212
	B	0.143	0.153	0.174	0.191	0.187	0.223	0.150	0.149

	Data Point	5	9	14	19	24	29	34	39
	Name	San36bCpx3	san36px3	san36px3	san36px3	san36px3	san36px3	san36px3	san36px3
	Mineral	Cpx	Cpx	Cpx	Cpx	Cpx	Cpx	Cpx	Cpx
	Distance	50	90	140	190	240	290	340	390
%	SiO2	52.629	52.263	52.359	51.792	52.269	52.509	52.231	52.419
	TiO2	0.504	0.445	0.465	0.5	0.417	0.442	0.417	0.49
	Al2O3	1.489	1.563	1.553	1.683	1.364	1.398	1.341	1.309
	Cr2O3	0	0.035	0	0.031	0	0	0	0
	FeO	10.28	9.845	9.768	11.254	10.441	10.55	11.239	11.019
	MnO	0.595	0.491	0.545	0.54	0.554	0.664	0.585	0.563
	MgO	13.848	13.956	13.868	13.828	14.294	14.24	13.89	14.002
	CaO	20.143	20.228	20.439	19.163	19.835	19.728	19.65	20.117
	Na2O	0.326	0.303	0.278	0.319	0.29	0.306	0.324	0.298
	K2O	0	0	0.016	0	0.001	0.004	0.004	0.019
	Total	99.814	99.129	99.291	99.11	99.465	99.841	99.681	100.236
cpfu	Si	1.970	1.967	1.968	1.958	1.965	1.967	1.966	1.962
	Ti	0.014	0.013	0.013	0.014	0.012	0.012	0.012	0.014
	Al	0.066	0.069	0.069	0.075	0.060	0.062	0.059	0.058
	Cr	0.000	0.001	0.000	0.001	0.000	0.000	0.000	0.000
	Fe2	0.322	0.310	0.307	0.356	0.328	0.330	0.354	0.345
	Mn	0.019	0.016	0.017	0.017	0.018	0.021	0.019	0.018
	Mg	0.773	0.783	0.777	0.780	0.801	0.795	0.779	0.781
	Ca	0.808	0.816	0.823	0.776	0.799	0.792	0.792	0.807
	Na	0.024	0.022	0.020	0.023	0.021	0.022	0.024	0.022
	K	0.000	0.000	0.001	0.000	0.000	0.000	0.000	0.001
	Total	3.995	3.996	3.995	4.001	4.004	4.001	4.005	4.007
	Mg#	70.6	71.6	71.7	68.7	70.9	70.6	68.8	69.4
µg/g	Li	2.598	2.530	2.543	2.614	2.709	2.691	2.605	3.257
	Be	0.155	0.138	0.146	0.134	0.121	0.133	0.153	0.152
	B	0.175	0.149	0.175	0.142	0.143	0.135	0.172	0.173

	Data Point	4	8	11	16	21	26	31	36	41	46	51	74	78
	Name	San1bCpx2	San1bCpx2	San1bCpx2	San1bCpx2	San1bCpx2	San1bCpx2	San1bCpx2	San1bCpx2	San1bCpx2	San1bCpx2	San1bCpx2	San1bCpx2	San1bCpx2
	Mineral	Cpx	Cpx	Cpx	Cpx	Cpx	Cpx	Cpx	Cpx	Cpx	Cpx	Cpx	Cpx	Cpx
	Distance	40	80	110	160	210	260	310	360	410	460	510	740	780
%	SiO2	52.449	52.872	53.221	52.641	53.116	52.616	52.92	52.997	52.821	53.452	52.502	52.524	51.833
	TiO2	0.555	0.27	0.574	0.669	0.542	0.399	0.462	0.462	0.454	0.39	0.671	0.662	0.492
	Al2O3	1.404	1.483	1.381	1.326	1.653	1.491	1.495	1.427	1.54	1.192	1.479	1.833	1.351
	Cr2O3	0	0	0	0.143	0	0.007	0.039	0	0	0.032	0.023	0	0
	FeO	11.187	10.375	9.826	10.206	10.132	10.484	9.988	10.249	10.94	10.216	9.844	10.44	11.827
	MnO	1.028	0.679	0.767	0.351	0.22	0.615	0.395	0.659	0.351	0.417	0.417	0.593	0.832
	MgO	14.332	14.455	14.435	15.171	14.303	14.793	14.679	14.511	14.235	14.407	14.546	14.336	14.584
	CaO	19.916	20.553	20.19	20.629	19.635	20.366	20.529	20.326	20.818	18.987	20.695	19.882	19.131
	Na2O	0.209	0.31	0.302	0.324	0.324	0.237	0.324	0.259	0.297	0.324	0.119	0.259	0.291
	K2O	0.034	0	0.072	0	0	0.017	0	0	0.023	0	0	0.055	0.078
	Total	101.114	100.997	100.768	101.46	99.925	101.025	100.831	100.89	101.479	99.417	100.296	100.584	100.419
cpfu	Si	1.950	1.960	1.970	1.942	1.976	1.950	1.959	1.963	1.952	1.996	1.954	1.952	1.944
	Ti	0.016	0.008	0.016	0.019	0.015	0.011	0.013	0.013	0.013	0.011	0.019	0.018	0.014
	Al	0.062	0.065	0.060	0.058	0.072	0.065	0.065	0.062	0.067	0.052	0.065	0.080	0.060
	Cr	0.000	0.000	0.000	0.004	0.000	0.000	0.001	0.000	0.000	0.001	0.001	0.000	0.000
	Fe2	0.348	0.322	0.304	0.315	0.315	0.325	0.309	0.317	0.338	0.319	0.306	0.324	0.371
	Mn	0.032	0.021	0.024	0.011	0.007	0.019	0.012	0.021	0.011	0.013	0.013	0.019	0.026
	Mg	0.794	0.799	0.796	0.834	0.793	0.817	0.810	0.801	0.784	0.802	0.807	0.794	0.816
	Ca	0.793	0.816	0.801	0.815	0.783	0.809	0.814	0.807	0.824	0.760	0.825	0.792	0.769
	Na	0.015	0.022	0.022	0.023	0.023	0.017	0.023	0.019	0.021	0.023	0.009	0.019	0.021
	K	0.002	0.000	0.003	0.000	0.000	0.001	0.000	0.000	0.001	0.000	0.000	0.003	0.004
	Total	4.012	4.012	3.997	4.020	3.985	4.015	4.007	4.002	4.013	3.978	3.999	4.000	4.024
	Mg#	69.5	71.3	72.4	72.6	71.6	71.6	72.4	71.6	69.9	71.5	72.5	71.0	68.7
µg/g	Li	2.870	2.530	2.474	2.438	2.489	2.538	2.961	2.606	2.588	2.675	2.619	3.154	3.513
	Be	0.139	0.148	0.139	0.134	0.136	0.136	0.190	0.152	0.149	0.159	0.161	0.164	0.177
	B	0.170	0.153	0.149	0.144	0.143	0.155	0.167	0.171	0.143	0.179	0.136	0.145	0.213

	Data Point	3	8	16	22	28	34	40	52
	Name	San1bCpx1	San1bCpx1	San1bCpx1	San1bCpx1	San1bCpx1	San1bCpx1	San1bCpx1	San1bCpx1
	Mineral	Cpx	Cpx	Cpx	Cpx	Cpx	Cpx	Cpx	Cpx
	Distance	30	80	160	220	280	340	400	520
%	SiO2	52.517	53.245	52.417	52.216	52.766	52.267	51.824	52.22
	TiO2	0.539	0.459	0.405	0.499	0.492	0.61	0.515	0.515
	Al2O3	1.761	1.58	1.699	1.362	1.381	1.589	1.461	1.387
	Cr2O3	0	0	0.102	0.126	0.079	0	0.007	0.246
	FeO	10.4	10.42	9.661	10.791	10.71	10.967	11.493	10.719
	MnO	0.611	0.393	0.438	0.436	0.416	0.634	0.546	0.678
	MgO	14.754	14.601	14.432	14.871	13.828	13.691	14.261	14.203
	CaO	20.362	20.312	20.203	19.993	19.84	19.972	20.201	20.193
	Na2O	0.301	0.418	0.301	0.28	0.363	0.26	0.342	0.305
	Total	101.245	101.428	99.658	100.574	99.875	99.99	100.656	100.466
cpfu	Si	1.942	1.960	1.960	1.946	1.975	1.960	1.939	1.951
	Ti	0.015	0.013	0.011	0.014	0.014	0.017	0.014	0.014
	Al	0.077	0.069	0.075	0.060	0.061	0.070	0.064	0.061
	Cr	0.000	0.000	0.003	0.004	0.002	0.000	0.000	0.007
	Fe2	0.322	0.321	0.302	0.336	0.335	0.344	0.360	0.335
	Mn	0.019	0.012	0.014	0.014	0.013	0.020	0.017	0.021
	Mg	0.813	0.801	0.804	0.826	0.771	0.765	0.796	0.791
	Ca	0.807	0.801	0.809	0.798	0.795	0.802	0.810	0.808
	Na	0.022	0.030	0.022	0.020	0.026	0.019	0.025	0.022
	Total	4.016	4.007	4.001	4.018	3.993	3.997	4.026	4.011
	Mg#	71.7	71.4	72.7	71.1	69.7	69.0	68.9	70.3
µg/g	Li	4.070	2.706	2.664	2.623	2.782	2.674	3.299	10.520
	Be	0.163	0.165	0.175	0.175	0.167	0.176	0.182	0.293
	B	0.160	0.171	0.138	0.149	0.176	0.187	0.178	0.857

	DataPoint	6	16	26	35	47
	Name	San37bOpx2	San37bOpx2	San37bOpx2	San37bOpx2	San37bOpx2
	Mineral	Opx	Opx	Opx	Opx	Opx
	Distance	60	160	260	350	470
%	SiO2	54.56	53.313	53.071	52.947	52.986
	TiO2	0.225	0.269	0.295	0.297	0.324
	Al2O3	0.586	0.648	0.701	0.697	0.741
	Cr2O3	0.032	0.009	0	0.019	0.006
	FeO	21.326	21.998	22.097	22.566	22.349
	MnO	0.996	0.935	0.981	0.922	1.06
	MgO	22.152	21.427	21.27	20.873	21.009
	CaO	1.546	1.601	1.647	1.536	1.584
	Na2O	0.051	0.03	0.028	0.038	0.023
	K2O	0.005	0	0	0.004	0
	Total	101.479	100.23	100.09	99.899	100.082
cpfu	Si	1.997	1.986	1.982	1.985	1.982
	Ti	0.006	0.008	0.008	0.008	0.009
	Al	0.025	0.028	0.031	0.031	0.033
	Cr	0.001	0.000	0.000	0.001	0.000
	Fe2	0.653	0.685	0.690	0.707	0.699
	Mn	0.031	0.030	0.031	0.029	0.034
	Mg	1.209	1.190	1.184	1.167	1.172
	Ca	0.061	0.064	0.066	0.062	0.063
	Na	0.004	0.002	0.002	0.003	0.002
	K	0.000	0.000	0.000	0.000	0.000
	Total	3.986	3.993	3.995	3.993	3.993
	Mg#	64.9	63.5	63.2	62.2	62.6
µg/g	Li	2.068	2.874	1.868	2.278	3.300
	Be	0.039	0.035	0.038	0.039	0.041
	B	0.108	0.103	0.102	0.114	0.114

	Data Point	4	10	16	24	39	49
	Name	San3Opx4	San3Opx4	San3Opx4	San3Opx4	San3Opx4	San3Opx4
	Mineral	Opx	Opx	Opx	Opx	Opx	Opx
	Distance	40	100	160	240	390	490
%	SiO2	52.699	52.511	52.646	52.267	52.626	52.902
	TiO2	0.259	0.294	0.240	0.259	0.305	0.260
	Al2O3	0.707	0.724	0.569	0.699	0.699	0.756
	Cr2O3	0.000	0.000	0.029	0.000	0.010	0.023
	Fe2O3	0.000	0.207	0.000	0.497	0.000	0.000
	FeO	22.812	23.035	24.025	24.590	23.258	23.136
	MnO	1.077	1.051	1.099	1.109	1.079	0.971
	MgO	20.585	20.610	19.902	19.622	20.369	20.583
	CaO	1.513	1.545	1.564	1.524	1.473	1.466
	Na2O	0.009	0.051	0.038	0.015	0.022	0.031
	K2O	0.010	0.000	0.000	0.006	0.008	0.016
	Total	99.671	100.029	100.112	100.588	99.849	100.144
cpfu	Si	1.984	1.975	1.985	1.971	1.982	1.984
	Ti	0.007	0.008	0.007	0.007	0.009	0.007
	Al	0.031	0.032	0.025	0.031	0.031	0.033
	Cr	0.000	0.000	0.001	0.000	0.000	0.001
	Fe3	0.000	0.006	0.000	0.014	0.000	0.000
	Fe2	0.718	0.724	0.758	0.775	0.733	0.725
	Mn	0.034	0.033	0.035	0.035	0.034	0.031
	Mg	1.155	1.155	1.119	1.103	1.144	1.150
	Ca	0.061	0.062	0.063	0.062	0.059	0.059
	Na	0.001	0.004	0.003	0.001	0.002	0.002
	K	0.000	0.000	0.000	0.000	0.000	0.001
	Total	3.993	4.000	3.996	4.000	3.994	3.994
	Mg#	61.7	61.5	59.6	58.7	61.0	61.3
µg/g	Li	8.612	8.966	8.513	10.011	9.022	7.752
	Be	0.031	0.035	0.039	0.041	0.038	0.034
	B	0.133	0.111	0.129	0.134	0.139	0.119

	Data Point	2	11	19	27	35	42	49
	Name	San37bOpx1	San37bOpx1	San37bOpx1	San37bOpx1	San37bOpx1	San37bOpx1	San37bOpx1
	Mineral	Opx	Opx	Opx	Opx	Opx	Opx	Opx
	Distance	20	110	190	270	350	420	490
%	SiO2	53.091	53.660	52.828	52.815	53.519	52.900	53.668
	TiO2	0.314	0.260	0.254	0.245	0.264	0.282	0.234
	Al2O3	0.773	0.831	0.956	1.119	0.642	1.228	0.501
	Cr2O3	0.013	0.006	0.023	0.000	0.000	0.000	0.028
	FeO	21.183	19.921	21.073	21.238	21.056	21.327	21.043
	MnO	1.051	0.789	0.943	0.988	0.965	0.808	0.967
	MgO	21.633	23.168	21.850	21.608	22.044	21.681	21.704
	CaO	1.550	1.510	1.623	1.616	1.592	1.561	1.620
	Na2O	0.053	0.032	0.022	0.019	0.011	0.030	0.019
	K2O	0.000	0.007	0.031	0.004	0.000	0.020	0.035
	Total	99.661	100.184	99.603	99.652	100.093	99.837	99.819
cpfu	Si	1.983	1.979	1.975	1.974	1.987	1.972	1.998
	Ti	0.009	0.007	0.007	0.007	0.007	0.008	0.007
	Al	0.034	0.036	0.042	0.049	0.028	0.054	0.022
	Cr	0.000	0.000	0.001	0.000	0.000	0.000	0.001
	Fe2	0.662	0.614	0.659	0.664	0.654	0.665	0.655
	Mn	0.033	0.025	0.030	0.031	0.030	0.026	0.030
	Mg	1.205	1.274	1.217	1.204	1.220	1.205	1.205
	Ca	0.062	0.060	0.065	0.065	0.063	0.062	0.065
	Na	0.004	0.002	0.002	0.001	0.001	0.002	0.001
	K	0.000	0.000	0.001	0.000	0.000	0.001	0.002
	Total	3.992	3.997	3.998	3.995	3.992	3.995	3.985
	Mg#	64.5	67.5	64.9	64.5	65.1	64.4	64.8
µg/g	Li	2.704	2.386	2.745	3.025	4.011	4.665	4.292
	Be	0.053	0.034	0.039	0.038	0.038	0.034	0.031
	B	0.156	0.069	0.089	0.120	0.105	0.099	0.095

	Data Point	4	11	18	25	32	39	46	53	63	73
	Name	San3bOpx1	San3bOpx1	San3bOpx1	San3bOpx1	San3bOpx1	San3bOpx1	San3bOpx1	San3bOpx1	San3bOpx1	San3bOpx1
	Mineral	Opx	Opx	Opx	Opx	Opx	Opx	Opx	Opx	Opx	Opx
	Distance	40	110	180	250	320	390	460	530	630	730
µg/g	SiO2	52.547	52.594	52.421	52.43	52.216	52.365	52.693	52.43	52.783	52.505
	TiO2	0.272	0.327	0.302	0.289	0.347	0.24	0.279	0.314	0.239	0.22
	Al2O3	0.824	0.805	0.739	0.784	0.818	0.769	0.801	0.829	0.62	0.701
	Cr2O3	0	0	0.025	0.01	0	0	0.013	0	0.015	0.025
	FeO	23.424	23.505	23.514	23.642	23.297	23.58	23.755	23.606	23.398	22.674
	MnO	1.03	1.055	1.081	1.033	1.136	1.122	1.028	1.104	1.099	1.109
	MgO	20.167	20.359	20.202	20.267	20.207	20.189	20.044	19.839	20.587	20.565
	CaO	1.62	1.545	1.654	1.626	1.48	1.468	1.524	1.568	1.485	1.459
	Na2O	0.028	0.009	0.031	0.035	0.015	0	0.02	0.02	0.016	0.034
	K2O	0	0.005	0.011	0	0.007	0.008	0.01	0	0	0.013
	Total	99.912	100.204	99.98	100.116	99.523	99.741	100.167	99.71	100.242	99.305
cpfu	Si	1.980	1.976	1.976	1.974	1.976	1.979	1.982	1.982	1.981	1.984
	Ti	0.008	0.009	0.009	0.008	0.010	0.007	0.008	0.009	0.007	0.006
	Al	0.037	0.036	0.033	0.035	0.036	0.034	0.036	0.037	0.027	0.031
	Cr	0.000	0.000	0.001	0.000	0.000	0.000	0.000	0.000	0.000	0.001
	Fe2	0.738	0.739	0.741	0.745	0.737	0.745	0.747	0.746	0.735	0.717
	Mn	0.033	0.034	0.035	0.033	0.036	0.036	0.033	0.035	0.035	0.035
	Mg	1.133	1.140	1.135	1.138	1.140	1.137	1.124	1.118	1.152	1.159
	Ca	0.065	0.062	0.067	0.066	0.060	0.059	0.061	0.063	0.060	0.059
	Na	0.002	0.001	0.002	0.003	0.001	0.000	0.001	0.001	0.001	0.002
	K	0.000	0.000	0.001	0.000	0.000	0.000	0.000	0.000	0.000	0.001
	Total	3.995	3.997	4.000	4.001	3.997	3.998	3.993	3.992	3.998	3.995
	Mg#	60.5	60.7	60.5	60.4	60.7	60.4	60.1	60.0	61.1	61.8
µg/g	Li	6.677	10.234	14.095	12.942	13.312	13.616	14.181	13.150	8.127	6.457
	Be	0.047	0.052	0.068	0.042	0.038	0.039	0.034	0.039	0.037	0.035
	B	0.135	0.156	0.134	0.123	0.118	0.130	0.117	0.121	0.098	0.111

	Data Point	3	8	13	18	23	29	36	43	48	56	63
	Name	San36Opx1	San36Opx1	San36Opx1	San36Opx1	San36Opx1	San36Opx1	San36Opx1	San36Opx1	San36Opx1	San36Opx1	San36Opx1
	Mineral	Opx	Opx	Opx	Opx	Opx	Opx	Opx	Opx	Opx	Opx	Opx
	Distance	30	80	130	180	230	290	360	430	480	560	630
%	SiO2	52.748	52.744	52.674	52.233	52.269	52.541	52.130	52.237	52.701	53.046	53.104
	TiO2	0.232	0.444	0.310	0.307	0.275	0.224	0.277	0.312	0.175	0.249	0.260
	Al2O3	0.639	0.752	0.726	0.811	0.778	0.869	0.886	0.833	0.514	0.599	0.620
	Cr2O3	0.000	0.000	0.010	0.000	0.000	0.007	0.047	0.000	0.000	0.001	0.023
	Fe2O3	1.023	0.131	1.047	1.325	1.193	0.713	1.156	1.372	0.578	0.129	0.442
	FeO	20.517	21.313	21.067	20.766	21.380	21.777	21.391	20.808	20.289	20.915	21.009
	MnO	0.986	0.908	1.007	1.042	0.988	1.014	1.113	0.952	1.029	0.940	0.984
	MgO	22.324	21.918	21.820	21.785	21.389	21.268	21.185	21.724	22.263	22.221	22.137
	CaO	1.471	1.589	1.619	1.507	1.622	1.703	1.717	1.624	1.577	1.546	1.588
	Na2O	0.019	0.016	0.044	0.032	0.035	0.028	0.022	0.035	0.023	0.027	0.050
	K2O	0.000	0.018	0.001	0.000	0.000	0.000	0.000	0.001	0.010	0.023	0.000
	Total	99.958	99.833	100.325	99.808	99.929	100.144	99.924	99.898	99.160	99.696	100.217
cpfu	Si	1.966	1.970	1.962	1.956	1.960	1.965	1.956	1.955	1.977	1.980	1.974
	Ti	0.007	0.012	0.009	0.009	0.008	0.006	0.008	0.009	0.005	0.007	0.007
	Al	0.028	0.033	0.032	0.036	0.034	0.038	0.039	0.037	0.023	0.026	0.027
	Cr	0.000	0.000	0.000	0.000	0.000	0.000	0.001	0.000	0.000	0.000	0.001
	Fe3	0.029	0.004	0.029	0.037	0.034	0.020	0.033	0.039	0.016	0.004	0.012
	Fe2	0.639	0.666	0.656	0.650	0.670	0.681	0.671	0.651	0.636	0.653	0.653
	Mn	0.031	0.029	0.032	0.033	0.031	0.032	0.035	0.030	0.033	0.030	0.031
	Mg	1.240	1.220	1.212	1.216	1.195	1.186	1.185	1.212	1.245	1.236	1.227
	Ca	0.059	0.064	0.065	0.060	0.065	0.068	0.069	0.065	0.063	0.062	0.063
	Na	0.001	0.001	0.003	0.002	0.003	0.002	0.002	0.003	0.002	0.002	0.004
	K	0.000	0.001	0.000	0.000	0.000	0.000	0.000	0.000	0.000	0.001	0.000
	Total	4	4	4	4	4	4	4	4	4	4	4
	Mg#	66.0	64.7	64.9	65.2	64.1	63.5	63.8	65.0	66.2	65.4	65.3
µg/g	Li	2.156	1.874	1.766	1.675	1.856	1.942	1.952	1.942	2.021	2.040	2.112
	Be	0.033	0.030	0.040	0.039	0.038	0.028	0.038	0.034	0.029	0.029	0.031
	B	0.107	0.121	0.118	0.127	0.115	0.125	0.104	0.113	0.086	0.087	0.094

3.2 THERA ANDESITES

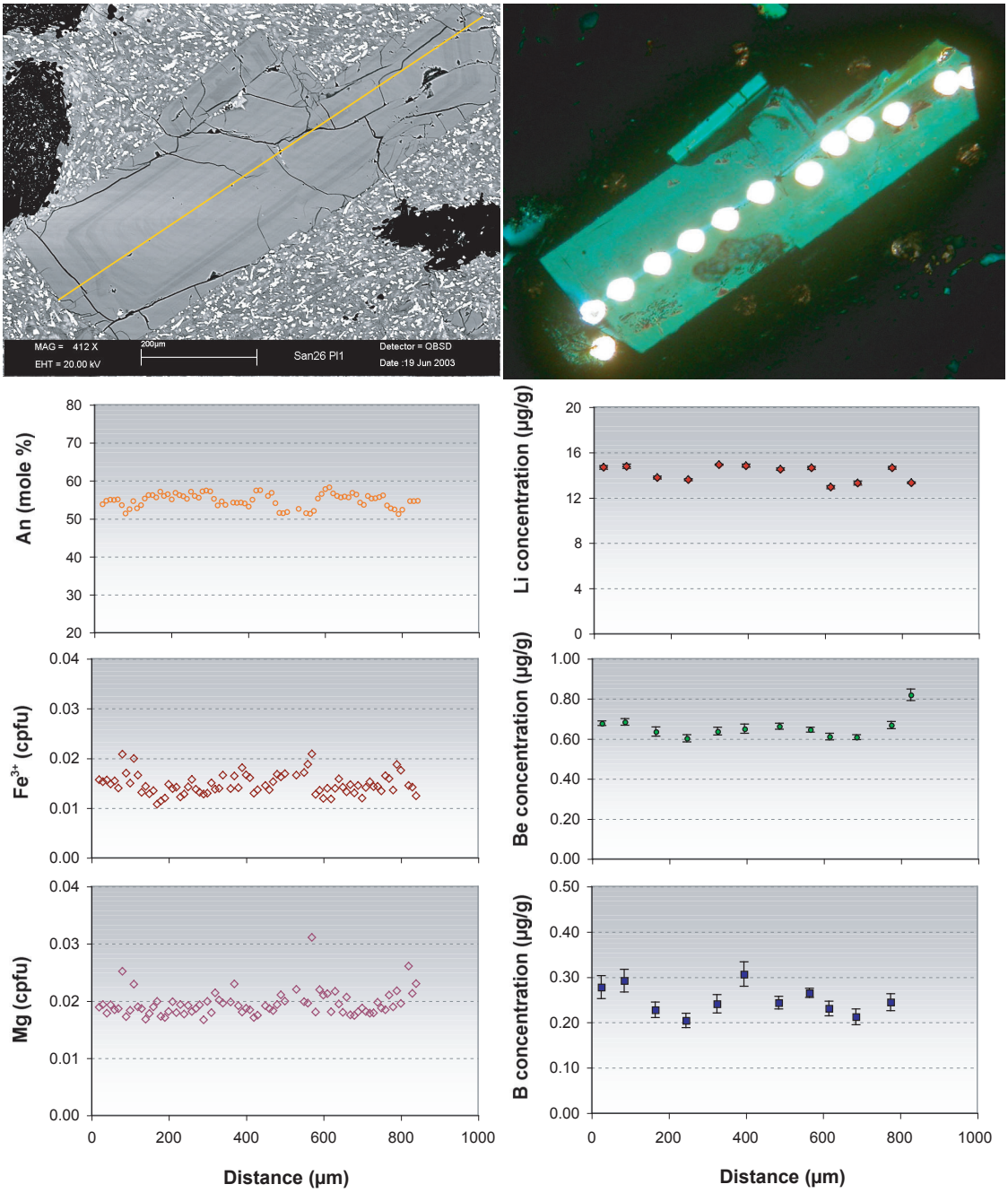

Plagioclase Type-O1: *San26 Pl1*

	Data Point	3	9	17	25	33	40	49	57	62	69	78	83
	Name	s26 pl1	s26 pl1	s26 pl1	s26 pl1	s26 pl1	s26 pl1	s26 pl1	s26 pl1	s26 pl1	s26 pl1	s26 pl1	s26 pl1
	Mineral	Fsp	Fsp	Fsp	Fsp	Fsp	Fsp	Fsp	Fsp	Fsp	Fsp	Fsp	Fsp
	Distance	30	90	170	250	330	400	490	570	620	690	780	830
%	SiO2	54.616	55.271	54.197	53.925	54.402	54.853	55.042	55.324	53.998	54.053	55.044	54.646
	Al2O3	28.821	28.513	29.375	29.369	29.012	28.836	28.561	28.179	29.524	29.018	28.661	28.989
	Fe2O3	0.570	0.509	0.589	0.565	0.593	0.552	0.622	0.919	0.535	0.532	0.560	0.630
	CaO	11.027	10.534	11.704	11.325	10.993	10.845	10.522	10.383	11.554	11.273	10.793	11.184
	Na2O	5.027	5.237	4.835	4.676	5.045	5.260	5.461	5.265	4.858	5.240	5.389	5.107
	K2O	0.265	0.296	0.188	0.247	0.242	0.290	0.283	0.363	0.205	0.252	0.237	0.247
	Summe	100.326	100.360	100.888	100.107	100.287	100.636	100.491	100.433	100.674	100.368	100.684	100.803
		30	90	170	250	330	400	490	570	620	690	780	830
cpfu	Si	2.459	2.483	2.431	2.434	2.451	2.462	2.473	2.487	2.427	2.439	2.469	2.451
	Al	1.529	1.510	1.553	1.562	1.540	1.526	1.513	1.493	1.564	1.543	1.515	1.533
	Fe3	0.019	0.017	0.020	0.019	0.020	0.019	0.021	0.031	0.018	0.018	0.019	0.021
	Ca	0.532	0.507	0.563	0.548	0.531	0.522	0.507	0.500	0.556	0.545	0.519	0.538
	Na	0.439	0.456	0.421	0.409	0.441	0.458	0.476	0.459	0.423	0.458	0.469	0.444
	K	0.015	0.017	0.011	0.014	0.014	0.017	0.016	0.021	0.012	0.015	0.014	0.014
	Summe	4.994	4.990	4.998	4.987	4.996	5.003	5.006	4.991	5.000	5.017	5.005	5.001
mole (%)	An	54.6	53.0	56.3	56.2	54.0	54.2	51.7	53.0	57.1	54.8	52.2	54.8
µg/g	Li	14.666	14.759	13.769	13.575	14.905	14.808	14.508	14.616	12.917	13.283	14.626	13.304
	Be	0.677	0.684	0.636	0.602	0.638	0.650	0.662	0.645	0.611	0.608	0.668	0.820
	B	0.277	0.292	0.228	0.204	0.241	0.306	0.243	0.265	0.230	0.212	0.244	2.756

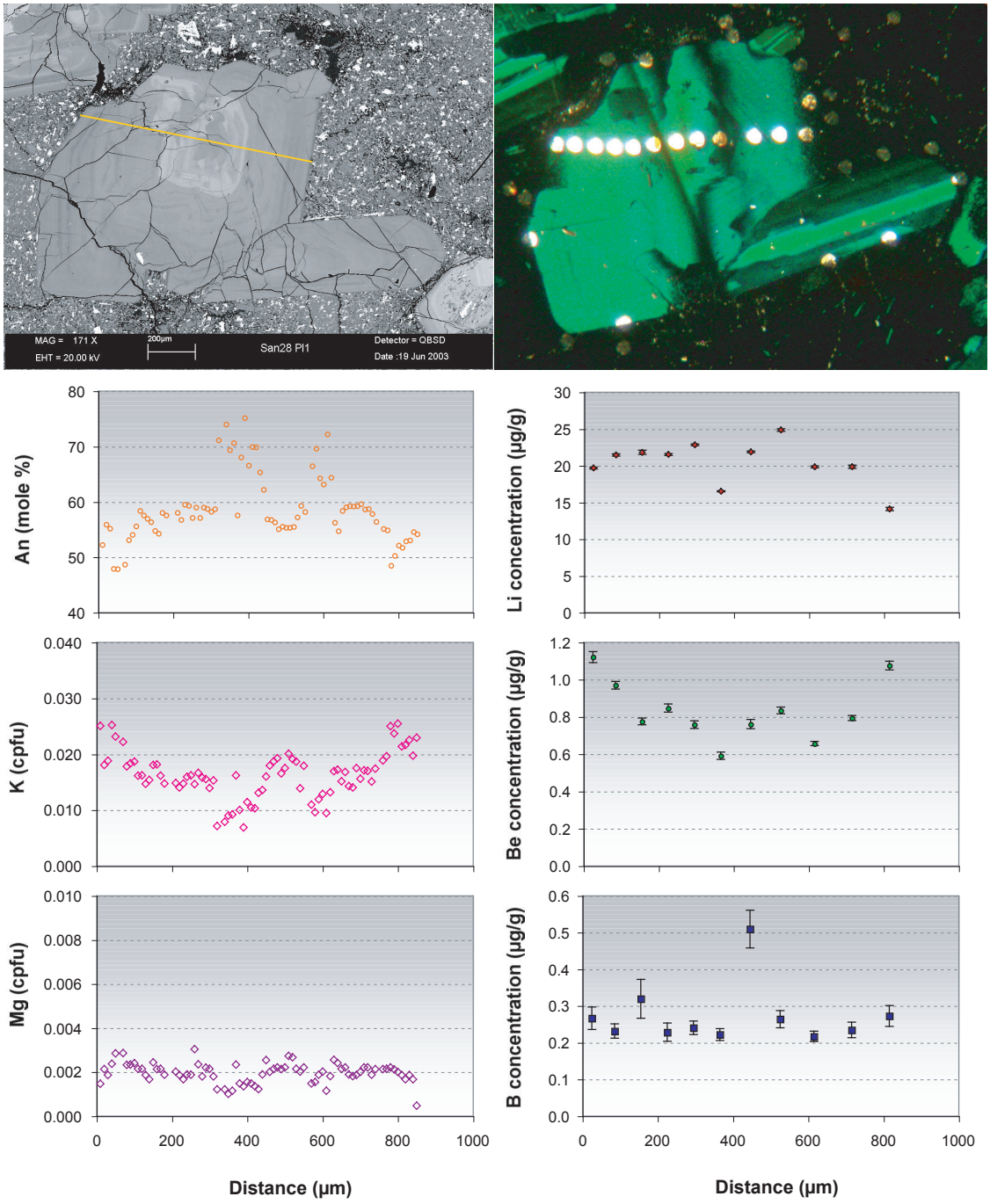

Plagioclase Type-O2: *San28 Pl1*

	Data Point	3	9	16	23	30	37	45	53	62	72	82
	Name	San28Pl1	San28Pl1	San28Pl1	San28Pl1	San28Pl1	San28Pl1	San28Pl1	San28Pl1	San28Pl1	San28Pl1	San28Pl1
	Mineral	Fsp	Fsp	Fsp	Fsp	Fsp	Fsp	Fsp	Fsp	Fsp	Fsp	Fsp
	Distance	30	90	160	230	300	370	450	530	620	720	820
%	SiO2	55.035	55.288	55.198	53.525	53.936	54.312	53.955	54.195	52.365	53.786	55.429
	Al2O3	28.976	28.715	28.867	29.775	29.507	29.553	29.541	29.388	30.471	29.483	28.330
	Fe2O3	0.436	0.475	0.526	0.518	0.513	0.478	0.559	0.393	0.538	0.502	0.502
	MgO	0.028	0.035	0.032	0.025	0.032	0.035	0.038	0.032	0.027	0.033	0.025
	CaO	11.168	11.074	10.939	12.065	11.943	11.689	11.630	11.699	13.100	11.861	10.813
	Na2O	4.994	5.191	5.084	4.530	4.722	4.745	4.862	4.819	3.991	4.595	5.303
	K2O	0.330	0.322	0.318	0.257	0.243	0.284	0.279	0.326	0.229	0.296	0.378
	Summe	100.967	101.100	100.964	100.695	100.896	101.096	100.864	100.852	100.721	100.556	100.780
cpfu	Si	2.462	2.471	2.468	2.408	2.421	2.431	2.423	2.432	2.363	2.422	2.484
	Al	1.528	1.512	1.521	1.579	1.561	1.559	1.563	1.554	1.620	1.565	1.496
	Fe3	0.015	0.016	0.018	0.018	0.017	0.016	0.019	0.013	0.018	0.017	0.017
	Mg	0.002	0.002	0.002	0.002	0.002	0.002	0.003	0.002	0.002	0.002	0.002
	Ca	0.535	0.530	0.524	0.582	0.574	0.560	0.559	0.563	0.633	0.572	0.519
	Na	0.433	0.450	0.441	0.395	0.411	0.412	0.423	0.419	0.349	0.401	0.461
	K	0.019	0.018	0.018	0.015	0.014	0.016	0.016	0.019	0.013	0.017	0.022
	Summe	4.993	4.999	4.992	4.998	5.002	4.996	5.006	5.003	4.999	4.996	5.001
mole (%)	An	53.1	54.3	55.7	58.6	58.6	65.5	58.7	57.4	64.3	58.5	52.6
µg/g	Li	19.680	21.462	21.804	21.516	22.826	16.511	21.885	24.854	19.840	19.850	14.099
	Be	1.121	0.970	0.776	0.847	0.759	0.591	0.761	0.834	0.657	0.794	1.076
	B	0.267	0.232	0.319	0.229	0.241	0.222	0.510	0.264	0.217	0.235	0.273

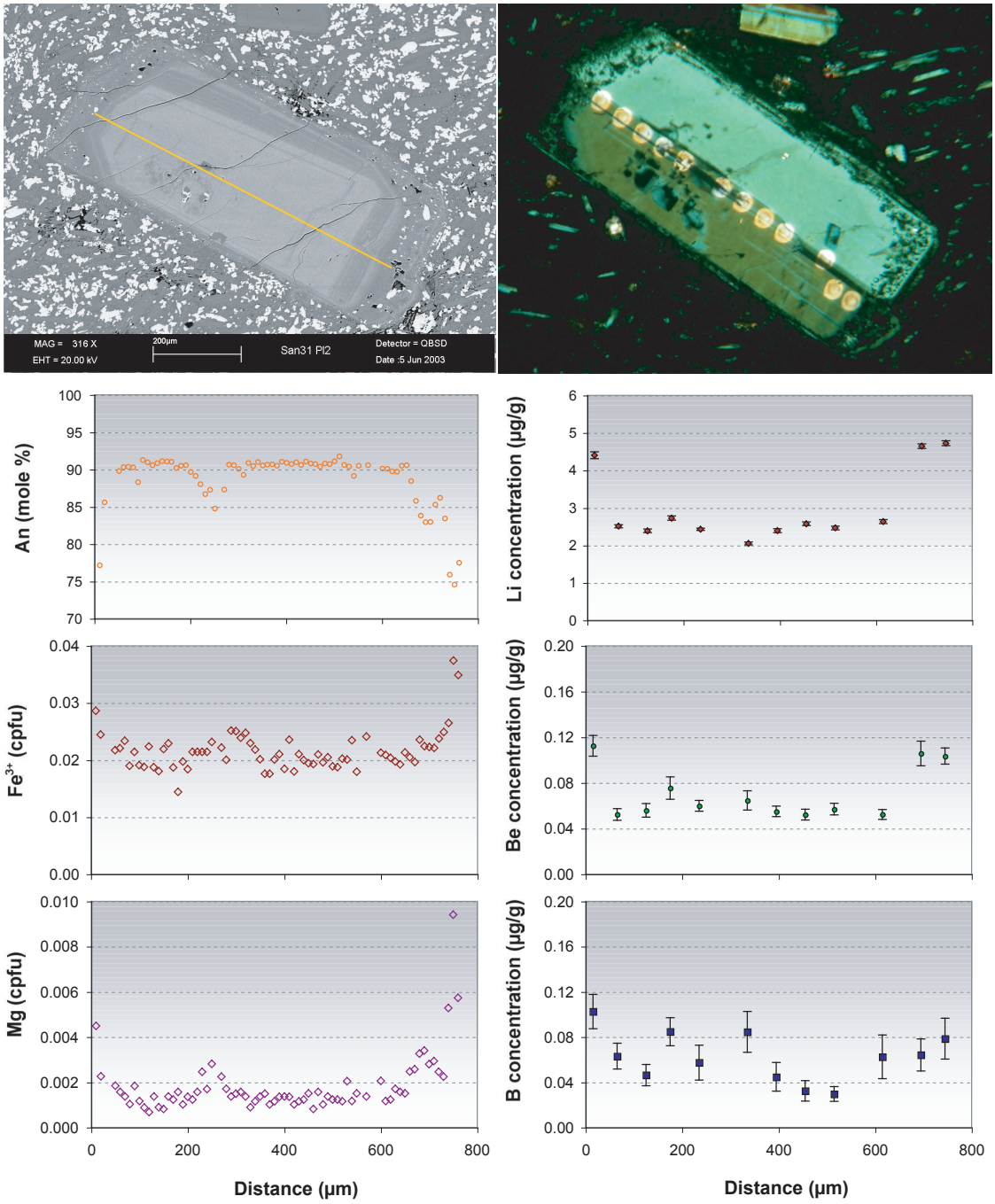

Plagioclase Type-C: *San31 Pl2*

	Data Point	2	7	13	18	24	34	40	46	52	62	70	75
	Name	san31pl2	san31pl2	san31pl2	san31pl2	san31pl2	san31pl2	san31pl2	san31pl2	san31pl2	san31pl2	san31pl2	san31pl2
	Mineral	Fsp	Fsp	Fsp	Fsp	Fsp	Fsp	Fsp	Fsp	Fsp	Fsp	Fsp	Fsp
	Distance	20	70	130	180	240	340	400	460	520	620	700	750
%	SiO2	46.656	45.323	45.522	45.462	46.290	45.443	45.220	45.584	45.533	45.817	47.434	49.721
	Al2O3	34.051	35.517	35.240	35.200	34.922	35.551	35.047	35.359	35.431	35.208	33.624	31.831
	Fe2O3	0.709	0.679	0.543	0.418	0.625	0.635	0.532	0.560	0.589	0.593	0.648	1.095
	MgO	0.033	0.020	0.020	0.023	0.025	0.017	0.020	0.012	0.017	0.018	0.041	0.139
	CaO	17.526	18.378	18.417	18.272	17.919	18.469	18.557	18.328	18.476	18.317	16.889	15.022
	Na2O	1.620	1.074	1.019	1.049	1.436	1.002	1.018	1.026	1.047	1.150	1.906	2.823
	K2O	0.031	0.023	0.027	0.045	0.042	0.034	0.019	0.020	0.020	0.000	0.060	0.141
	Total	100.626	101.014	100.788	100.469	101.259	101.151	100.413	100.889	101.113	101.103	100.602	100.772
cpfu	Si	2.136	2.072	2.084	2.087	2.108	2.074	2.080	2.084	2.079	2.091	2.167	2.259
	Al	1.837	1.914	1.902	1.904	1.874	1.913	1.900	1.905	1.907	1.894	1.811	1.704
	Fe3	0.024	0.023	0.019	0.014	0.021	0.022	0.018	0.019	0.020	0.020	0.022	0.037
	Mg	0.002	0.001	0.001	0.002	0.002	0.001	0.001	0.001	0.001	0.001	0.003	0.009
	Ca	0.860	0.900	0.903	0.899	0.874	0.903	0.915	0.898	0.904	0.896	0.827	0.731
	Na	0.144	0.095	0.090	0.093	0.127	0.089	0.091	0.091	0.093	0.102	0.169	0.249
	K	0.002	0.001	0.002	0.003	0.002	0.002	0.001	0.001	0.001	0.000	0.003	0.008
	Total	5.006	5.008	5.002	5.002	5.009	5.004	5.007	5.000	5.005	5.003	5.002	4.998
mole (%)	An	81.5	90.4	90.9	90.5	86.3	90.7	91.0	90.7	91.0	89.9	83.8	76.1
µg/g	Li	4.403	2.508	2.387	2.726	2.428	2.052	2.392	2.573	2.464	2.636	4.645	4.723
	Be	0.113	0.052	0.056	0.075	0.060	0.065	0.055	0.052	0.057	0.052	0.106	0.103
	B	0.103	0.063	0.046	0.085	0.057	0.085	0.045	0.032	0.030	0.062	0.064	0.079

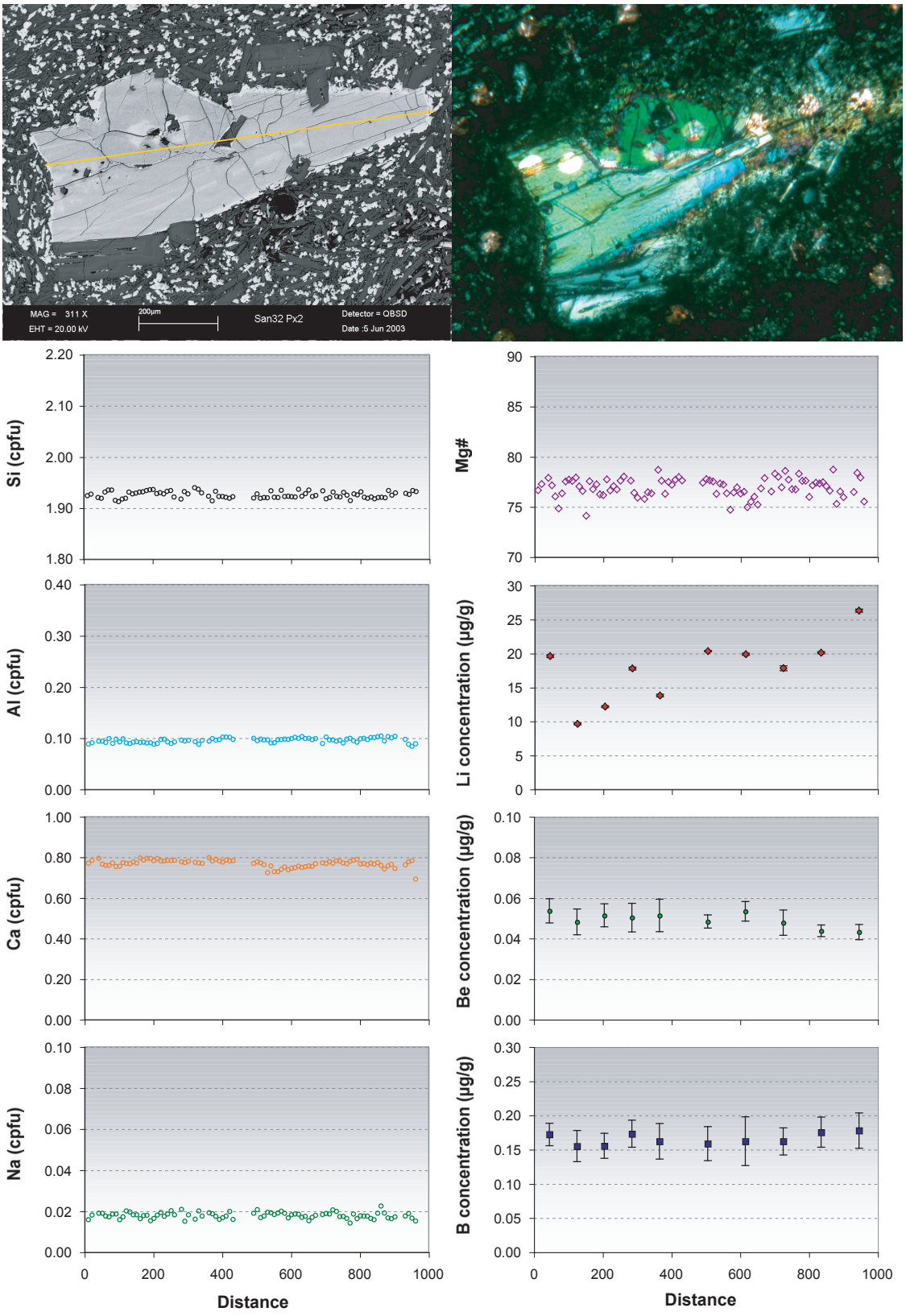

Clinopyroxene Type-U: *San32 Cpx2*

	Data Point	5	13	21	29	37	51	62	73	84	95
	Name	San32Cpx2	San32Cpx2	San32Cpx2	San32Cpx2	San32Cpx2	San32Cpx2	San32Cpx2	San32Cpx2	San32Cpx2	San32Cpx2
	Mineral	Cpx	Cpx	Cpx	Cpx	Cpx	Cpx	Cpx	Cpx	Cpx	Cpx
	Distance	50	130	210	290	370	510	620	730	840	950
%	SiO2	51.891	52.143	51.991	52.049	51.803	51.824	51.824	51.927	51.895	52.365
	TiO2	0.595	0.577	0.490	0.585	0.626	0.594	0.574	0.567	0.534	0.469
	Al2O3	2.186	2.075	2.075	2.180	2.298	2.271	2.281	2.180	2.349	1.956
	Cr2O3	0.035	0.069	0.031	0.000	0.000	0.069	0.041	0.000	0.094	0.015
	Fe2O3	1.765	1.121	1.464	0.762	1.949	1.528	0.322	1.659	1.540	1.247
	FeO	8.255	8.335	7.902	8.623	7.987	8.050	9.199	7.637	8.183	7.981
	MnO	0.389	0.360	0.280	0.248	0.267	0.369	0.280	0.302	0.354	0.373
	MgO	15.631	15.689	15.476	15.649	15.520	15.672	15.453	15.719	15.765	15.791
	CaO	19.380	19.444	20.024	19.519	19.794	19.531	18.932	19.779	19.398	19.838
	Na2O	0.268	0.276	0.255	0.213	0.264	0.237	0.259	0.280	0.224	0.235
	K2O	0.000	0.004	0.000	0.000	0.000	0.007	0.000	0.000	0.000	0.008
	Total	100.395	100.093	99.988	99.827	100.508	100.152	99.165	100.050	100.335	100.278
cpfu	Si	1.920	1.932	1.929	1.933	1.915	1.920	1.938	1.924	1.919	1.935
	Ti	0.017	0.016	0.014	0.016	0.017	0.017	0.016	0.016	0.015	0.013
	Al	0.095	0.091	0.091	0.095	0.100	0.099	0.101	0.095	0.102	0.085
	Cr	0.001	0.002	0.001	0.000	0.000	0.002	0.001	0.000	0.003	0.000
	Fe3	0.049	0.031	0.041	0.021	0.054	0.043	0.009	0.046	0.043	0.035
	Fe2	0.255	0.258	0.245	0.268	0.247	0.249	0.288	0.237	0.253	0.247
	Mn	0.012	0.011	0.009	0.008	0.008	0.012	0.009	0.009	0.011	0.012
	Mg	0.862	0.867	0.856	0.866	0.855	0.866	0.861	0.868	0.869	0.870
	Ca	0.768	0.772	0.796	0.777	0.784	0.775	0.758	0.785	0.769	0.786
	Na	0.019	0.020	0.018	0.015	0.019	0.017	0.019	0.020	0.016	0.017
	K	0.000	0.000	0.000	0.000	0.000	0.000	0.000	0.000	0.000	0.000
	Total	4.000	4.000	4.000	4.000	4.000	4.000	4.000	4.000	4.000	4.000
	Mg#	77.1	77.0	77.7	76.4	77.6	77.6	75.0	78.6	77.4	77.9
µg/g	Li	19.601	9.626	12.166	17.770	13.816	20.321	19.859	17.818	20.091	26.290
	Be	0.054	0.048	0.051	0.050	0.051	0.048	0.053	0.048	0.044	0.043
	B	0.172	0.155	0.155	0.173	0.162	0.159	0.162	0.162	0.175	0.178

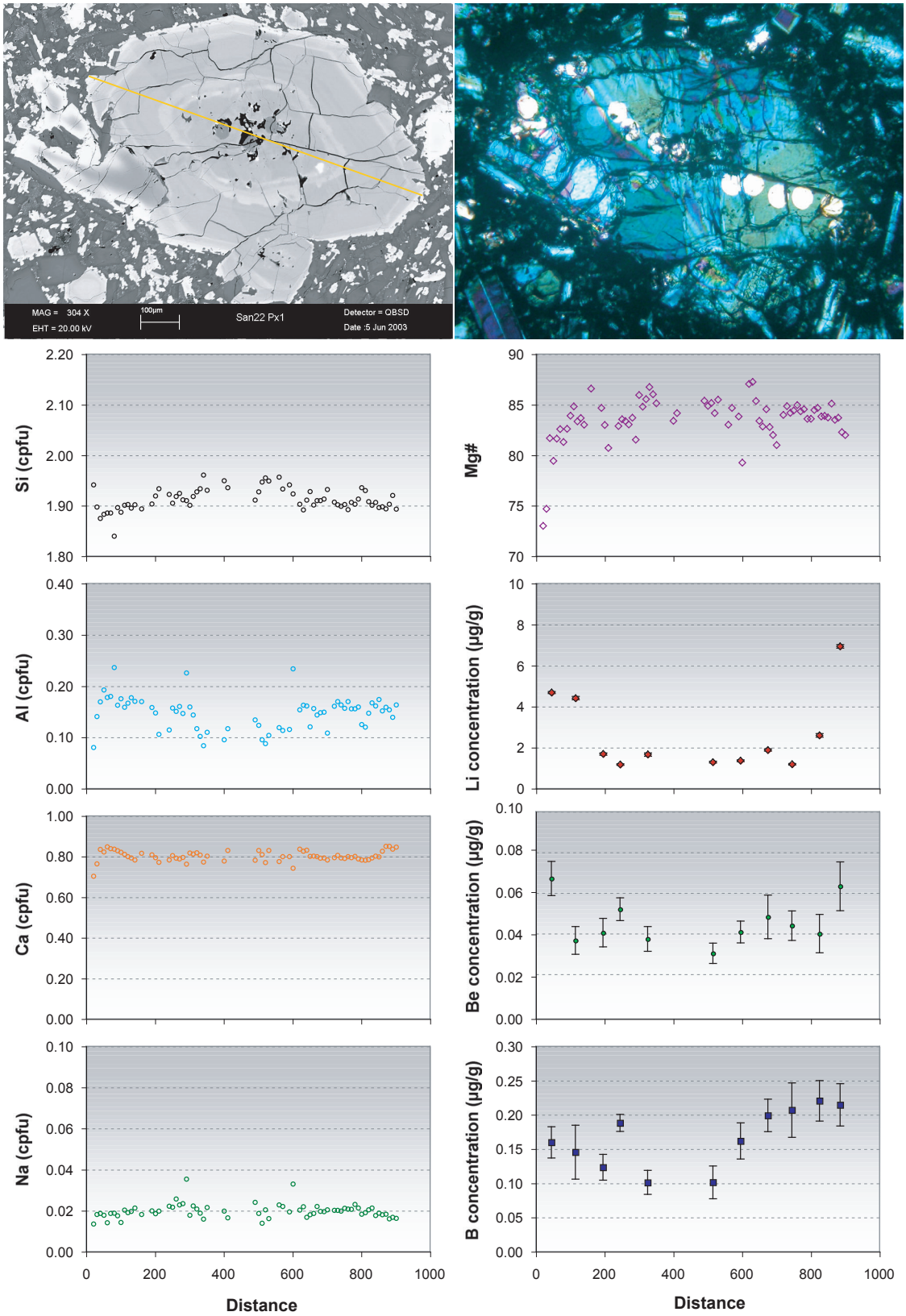

Clinopyroxene Type-Z: *San22 Cpx1*

	Data Point	5	12	20	25	33	52	60	68	75	83	89
	Name	San22Cpx1	San22Cpx1	San22Cpx1	San22Cpx1	San22Cpx1	San22Cpx1	San22Cpx1	San22Cpx1	San22Cpx1	San22Cpx1	San22Cpx1
	Mineral	Cpx	Cpx	Cpx	Cpx	Cpx	Cpx	Cpx	Cpx	Cpx	Cpx	Cpx
	Distance	50	120	200	250	330	520	600	680	750	830	890
%	SiO2	51.189	51.837	52.297	51.657	52.943	53.409	52.256	52.162	52.081	51.957	52.455
	TiO2	0.961	0.437	0.402	0.404	0.270	0.540	0.470	0.345	0.434	0.477	0.532
	Al2O3	4.450	3.868	3.435	3.633	2.379	2.052	5.404	3.454	3.660	3.902	3.242
	Cr2O3	0.305	0.440	0.495	0.690	0.266	0.215	0.409	0.687	0.371	0.463	0.314
	Fe2O3	0.000	0.307	0.000	0.342	0.928	0.000	0.000	0.356	0.838	0.408	0.000
	FeO	6.948	5.813	5.992	5.666	4.734	5.837	6.647	6.084	5.478	5.664	6.100
	MnO	0.139	0.176	0.176	0.134	0.172	0.156	0.169	0.178	0.210	0.150	0.185
	MgO	15.042	16.291	16.377	16.135	17.340	17.390	14.235	16.388	16.619	16.450	15.858
	CaO	20.905	20.368	20.264	20.410	20.670	19.692	18.864	20.226	20.246	20.273	21.365
	Na2O	0.252	0.270	0.263	0.305	0.267	0.291	0.464	0.279	0.302	0.303	0.239
	K2O	0.022	0.000	0.006	0.002	0.004	0.017	0.188	0.000	0.004	0.013	0.020
	Total	100.213	99.807	99.707	99.378	99.973	99.599	99.106	100.159	100.243	100.060	100.310
cpfu	Si	1.884	1.903	1.920	1.906	1.934	1.956	1.924	1.911	1.903	1.901	1.921
	Ti	0.027	0.012	0.011	0.011	0.007	0.015	0.013	0.010	0.012	0.013	0.015
	Al	0.193	0.167	0.149	0.158	0.102	0.089	0.234	0.149	0.158	0.168	0.140
	Cr	0.009	0.013	0.014	0.020	0.008	0.006	0.012	0.020	0.011	0.013	0.009
	Fe3	0.000	0.008	0.000	0.010	0.026	0.000	0.000	0.010	0.023	0.011	0.000
	Fe2	0.214	0.178	0.184	0.175	0.145	0.179	0.205	0.186	0.167	0.173	0.187
	Mn	0.004	0.005	0.005	0.004	0.005	0.005	0.005	0.006	0.006	0.005	0.006
	Mg	0.825	0.892	0.896	0.887	0.944	0.949	0.781	0.895	0.905	0.897	0.866
	Ca	0.824	0.801	0.797	0.807	0.809	0.773	0.744	0.794	0.793	0.795	0.838
	Na	0.018	0.019	0.019	0.022	0.019	0.021	0.033	0.020	0.021	0.021	0.017
	K	0.001	0.000	0.000	0.000	0.000	0.001	0.009	0.000	0.000	0.001	0.001
	Total	3.998	4.000	3.997	4.000	4.000	3.993	3.961	4.000	4.000	4.000	3.999
	Mg#	79.4	83.3	83.0	83.5	86.7	84.2	79.2	82.8	84.4	83.8	82.3
µg/g	Li	4.677	4.406	1.681	1.174	1.655	1.286	1.352	1.880	1.181	2.585	6.931
	Be	0.067	0.037	0.040	0.052	0.037	0.030	0.041	0.048	0.044	0.040	0.063
	B	0.160	0.145	0.123	0.188	0.101	0.101	0.162	0.199	0.207	0.220	0.214

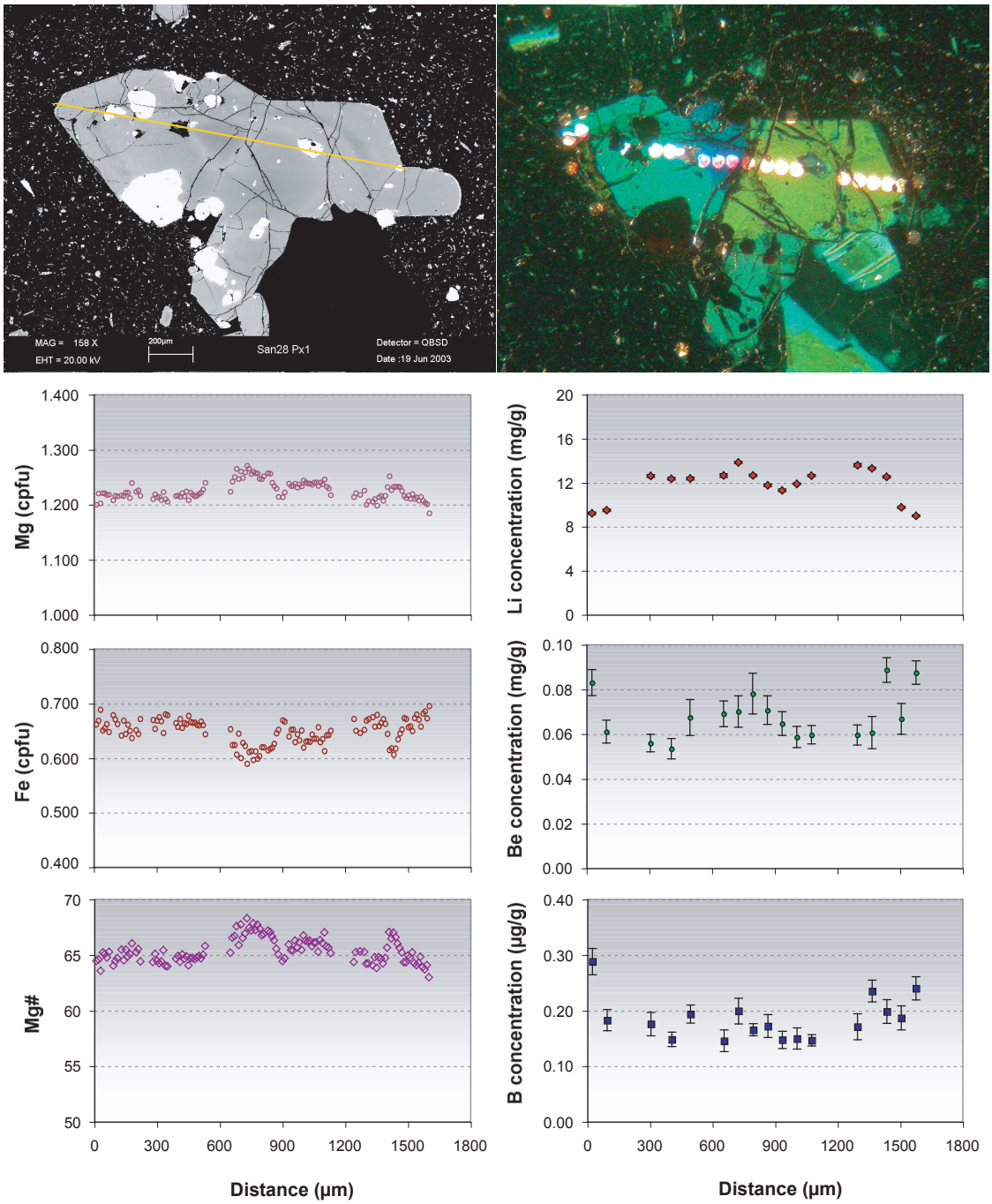

Orthopyroxene: *San28 Opx1*

	Data Point	3	10	31	41	50	66	73	80	87	94	101	108	130	137	144	151	158
	Name	San28Opx1	San28Opx1	San28Opx1	San28Opx1	San28Opx1	San28Opx1	San28Opx1	San28Opx1	San28Opx1	San28Opx1	San28Opx1	San28Opx1	San28Opx1	San28Opx1	San28Opx1	San28Opx1	San28Opx1
	Mineral	Opx	Opx	Opx	Opx	Opx	Opx	Opx	Opx	Opx	Opx	Opx	Opx	Opx	Opx	Opx	Opx	Opx
	Distance	30	100	310	410	500	660	730	800	870	940	1010	1080	1300	1370	1440	1510	1580
%	SiO2	52.404	52.303	52.592	52.939	52.629	52.629	52.340	52.552	52.455	52.742	52.755	52.423	52.233	52.413	52.316	52.460	52.945
	TiO2	0.255	0.255	0.254	0.240	0.277	0.282	0.412	0.370	0.290	0.282	0.269	0.275	0.315	0.265	0.305	0.264	0.355
	Al2O3	0.792	0.852	0.735	0.563	0.833	1.058	1.323	1.358	1.132	0.765	0.933	0.939	0.967	0.880	1.487	0.884	0.767
	Fe2O3	0.000	0.670	0.000	0.480	0.968	1.534	1.509	0.604	0.896	0.366	1.297	1.352	1.084	0.832	1.772	1.149	0.118
	FeO	21.860	21.389	21.489	21.550	21.196	20.166	19.048	19.984	20.738	20.890	20.365	20.216	21.379	21.254	19.991	21.127	22.034
	MnO	0.704	0.640	0.695	0.797	0.686	0.657	0.706	0.615	0.648	0.683	0.722	0.603	0.767	0.755	0.737	0.834	0.749
	MgO	21.399	21.727	21.663	21.847	21.979	22.513	23.022	22.525	22.139	22.167	22.477	22.342	21.515	21.807	22.362	21.784	21.681
	CaO	1.578	1.492	1.644	1.617	1.560	1.624	1.602	1.753	1.615	1.638	1.602	1.652	1.616	1.497	1.615	1.589	1.563
	Na2O	0.015	0.016	0.005	0.028	0.024	0.026	0.022	0.036	0.012	0.027	0.020	0.035	0.035	0.022	0.035	0.011	0.040
	K2O	0.010	0.006	0.006	0.005	0.000	0.007	0.000	0.000	0.000	0.000	0.005	0.000	0.000	0.000	0.000	0.025	0.000
	Total	99.017	99.349	99.083	100.066	100.152	100.497	99.984	99.830	99.926	99.578	100.461	99.859	99.924	99.725	100.621	100.168	100.252
cpfu	Si	1.976	1.965	1.979	1.975	1.961	1.949	1.939	1.952	1.955	1.971	1.955	1.954	1.956	1.962	1.936	1.957	1.973
	Ti	0.007	0.007	0.007	0.007	0.008	0.008	0.011	0.010	0.008	0.008	0.007	0.008	0.009	0.007	0.008	0.007	0.010
	Al	0.035	0.038	0.033	0.025	0.037	0.046	0.058	0.059	0.050	0.034	0.041	0.041	0.043	0.039	0.065	0.039	0.034
	Cr	0.000	0.000	0.000	0.000	0.000	0.000	0.000	0.001	0.000	0.001	0.000	0.001	0.000	0.000	0.000	0.001	0.000
	Fe3	0.000	0.019	0.000	0.013	0.027	0.043	0.042	0.017	0.025	0.010	0.036	0.038	0.031	0.023	0.049	0.032	0.003
	Fe2	0.690	0.672	0.676	0.672	0.661	0.624	0.590	0.621	0.646	0.653	0.631	0.630	0.669	0.665	0.619	0.659	0.687
	Mn	0.022	0.020	0.022	0.025	0.022	0.021	0.022	0.019	0.020	0.022	0.023	0.019	0.024	0.024	0.023	0.026	0.024
	Ni	0.000	0.000	0.000	0.000	0.000	0.000	0.000	0.000	0.000	0.000	0.000	0.000	0.000	0.000	0.000	0.000	0.000
	Mg	1.203	1.217	1.215	1.215	1.221	1.243	1.272	1.247	1.230	1.235	1.242	1.241	1.201	1.217	1.233	1.212	1.204
	Ca	0.064	0.060	0.066	0.065	0.062	0.064	0.064	0.070	0.064	0.066	0.064	0.066	0.065	0.060	0.064	0.064	0.062
	Na	0.001	0.001	0.000	0.002	0.002	0.002	0.002	0.003	0.001	0.002	0.001	0.003	0.003	0.002	0.003	0.001	0.003
	K	0.000	0.000	0.000	0.000	0.000	0.000	0.000	0.000	0.000	0.000	0.000	0.000	0.000	0.000	0.000	0.001	0.000
	Total	3.999	4.000	3.998	4.000	4.000	4.000	4.000	4.000	4.000	4.000	4.000	4.000	4.000	4.000	4.000	4.000	4.000
	Mg#	63.6	64.4	64.2	64.4	64.9	66.6	68.3	66.8	65.6	65.4	66.3	66.3	64.2	64.7	66.6	64.8	63.7
µg/g	Li	9.214	9.488	12.611	12.362	12.371	12.651	13.833	12.656	11.767	11.309	11.889	12.643	13.586	13.305	12.519	9.760	8.985
	Be	0.083	0.061	0.056	0.053	0.067	0.069	0.070	0.078	0.071	0.065	0.059	0.060	0.060	0.061	0.089	0.067	0.088
	B	0.288	0.183	0.176	0.148	0.193	0.146	0.199	0.165	0.172	0.147	0.150	0.146	0.171	0.235	0.198	0.187	0.240

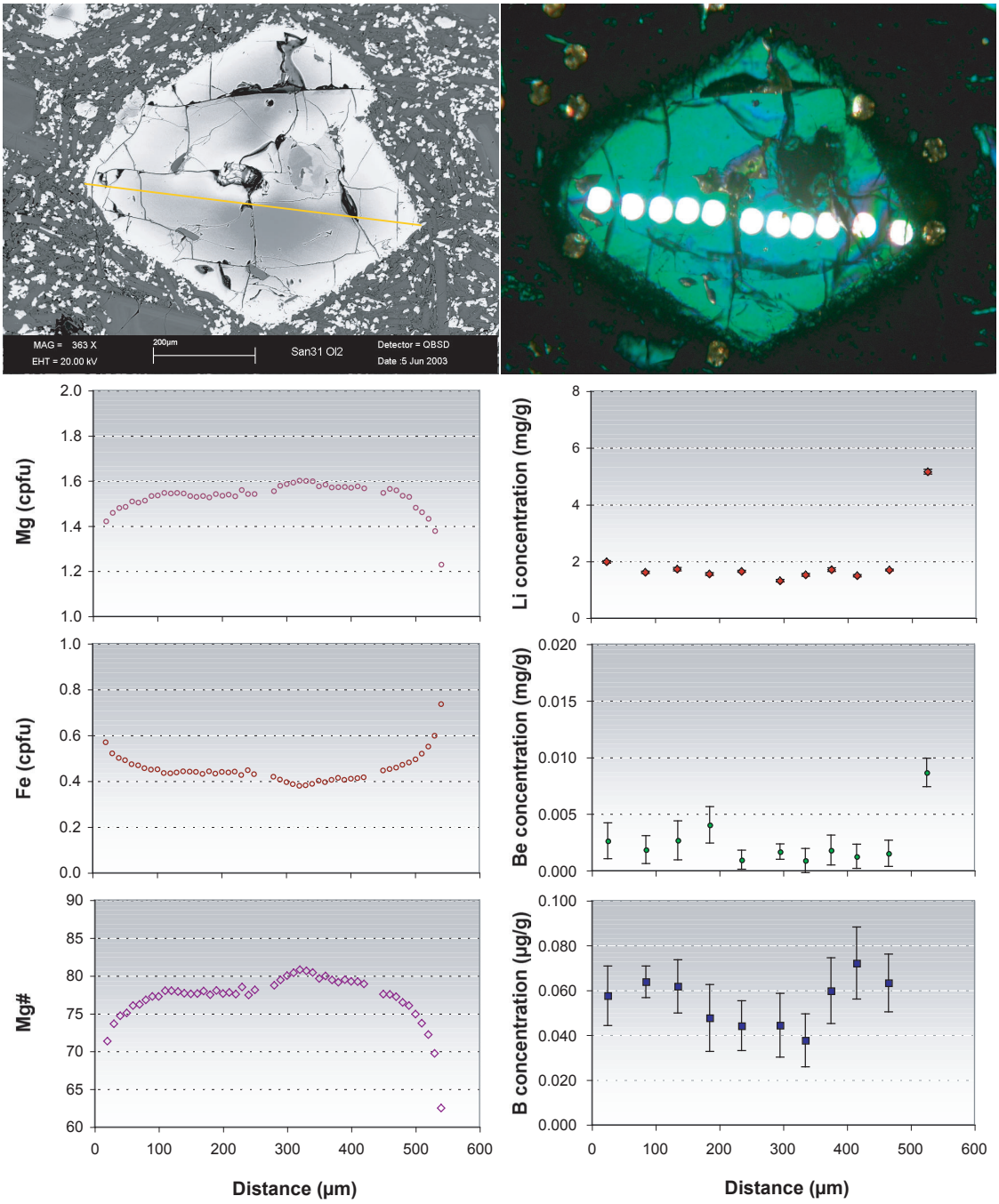

Olivine: *San31 Ol2*

	Data Point	3	9	14	19	24	30	34	38	42	47	53
	Name	s31 ol2	s31 ol2	s31 ol2	s31 ol2	s31 ol2	s31 ol2	s31 ol2	s31 ol2	s31 ol2	s31 ol2	s31 ol2
	Mineral	Oliv	Oliv	Oliv	Oliv	Oliv	Oliv	Oliv	Oliv	Oliv	Oliv	Oliv
	Distance	30	90	140	190	240	300	340	380	420	470	530
%	SiO2	37.846	38.653	38.653	38.672	38.719	39.063	38.905	38.929	38.882	37.557	37.108
	TiO2	0	0	0.02	0.005	0.007	0.028	0.032	0	0	0.005	0.002
	Al2O3	0.049	0.021	0.03	0.017	0.026	0.028	0.008	0.017	0.011	0.019	0.034
	Cr2O3	0.004	0.016	0.004	0.038	0.018	0.02	0.016	0	0.009	0	0.019
	FeO	23.679	20.958	20.662	20.028	20.916	18.56	18.192	19.373	19.499	21.079	26.595
	MnO	0.354	0.377	0.396	0.334	0.297	0.298	0.298	0.276	0.266	0.369	0.411
	NiO	0.019	0.051	0.047	0.129	0.084	0.115	0.141	0.079	0.073	0.05	0.062
	MgO	37.053	39.87	40.241	39.92	40.261	41.628	41.896	41.162	40.936	40.044	34.325
	Ba	0	0	0.003	0.007	0	0.019	0	0.004	0.011	0.016	0
	CaO	0.193	0.157	0.155	0.154	0.139	0.157	0.164	0.168	0.168	0.18	0.204
	Na2O	0.016	0	0	0.003	0	0.015	0	0	0.018	0	0.009
	K2O	0.017	0.016	0	0	0	0.018	0	0.01	0.007	0	0
	Total	99.23	100.119	100.211	99.307	100.467	99.949	99.652	100.018	99.88	99.319	98.769
cpfu	Si	1.000	0.998	0.996	1.003	0.996	0.999	0.997	0.999	0.999	0.982	1.001
	Ti	0.000	0.000	0.000	0.000	0.000	0.001	0.001	0.000	0.000	0.000	0.000
	Al	0.002	0.001	0.001	0.001	0.001	0.001	0.000	0.001	0.000	0.001	0.001
	Cr	0.000	0.000	0.000	0.001	0.000	0.000	0.000	0.000	0.000	0.000	0.000
	Fe2	0.523	0.453	0.445	0.434	0.450	0.397	0.390	0.416	0.419	0.461	0.600
	Mn	0.008	0.008	0.009	0.007	0.006	0.006	0.006	0.006	0.006	0.008	0.009
	Ni	0.000	0.001	0.001	0.003	0.002	0.002	0.003	0.002	0.002	0.001	0.001
	Mg	1.460	1.535	1.546	1.543	1.544	1.587	1.600	1.574	1.569	1.560	1.380
	Ca	0.005	0.004	0.004	0.004	0.004	0.004	0.005	0.005	0.005	0.005	0.006
	Na	0.001	0.000	0.000	0.000	0.000	0.001	0.000	0.000	0.001	0.000	0.000
	K	0.001	0.001	0.000	0.000	0.000	0.001	0.000	0.000	0.000	0.000	0.000
	Total	3.000	3.001	3.003	2.996	3.003	3.000	3.002	3.001	3.001	3.018	2.999
	Mg#	73.6	77.2	77.6	78.0	77.4	80.0	80.4	79.1	78.9	77.2	69.7
μg/g	Li	1.974	1.604	1.716	1.546	1.638	1.309	1.516	1.700	1.486	1.689	5.154
	Be	0.003	0.002	0.003	0.004	0.001	0.002	0.001	0.002	0.001	0.002	0.009
	B	0.057	0.064	0.062	0.048	0.044	0.044	0.038	0.060	0.072	0.063	0.129

	Data Point	3	9	13	28	36	44
	Name	San22Pl2	San22pl2	San22pl2	San22pl2	San22pl2	San22pl2
	Mineral	Fsp	Fsp	Fsp	Fsp	Fsp	Fsp
	Distance	30	90	130	280	360	440
%	SiO2	49.514	49.373	50.483	47.680	49.084	50.391
	Al2O3	31.476	32.474	31.884	33.934	32.532	31.782
	Fe2O3	0.702	0.582	0.445	0.570	0.509	0.700
	MgO	0.209	0.121	0.134	0.098	0.138	0.126
	CaO	14.771	15.514	14.669	16.583	15.411	14.722
	Na2O	3.022	2.708	3.228	1.941	2.695	3.165
	K2O	0.086	0.111	0.129	0.052	0.096	0.128
	Total	99.780	100.883	100.972	100.858	100.465	101.014
cpfu	Si	2.269	2.240	2.282	2.169	2.236	2.279
	Al	1.700	1.737	1.699	1.820	1.746	1.694
	Fe3	0.024	0.020	0.015	0.020	0.017	0.024
	Mg	0.014	0.008	0.009	0.007	0.009	0.008
	Ca	0.725	0.754	0.711	0.808	0.752	0.713
	Na	0.268	0.238	0.283	0.171	0.238	0.278
	K	0.005	0.006	0.007	0.003	0.006	0.007
	Total	5.006	5.004	5.006	4.998	5.004	5.004
mole (%)	An	74.338	76.069	75.405	82.698	75.562	70.346
µg/g	Li	6.313	11.777	11.171	6.609	9.076	7.754
	Be	0.272	0.214	0.200	0.159	0.232	0.265
	B	0.113	0.120	0.314	0.090	0.097	0.123

	Data Point	3	11	21	27	42	50
	Name	San22Pl3	San22Pl3	San22Pl3	San22Pl3	San22Pl3	San22Pl3
	Mineral	Fsp	Fsp	Fsp	Fsp	Fsp	Fsp
	Distance	30	110	210	270	420	500
%	SiO2	52.917	49.758	47.297	47.332	49.244	54.152
	Al2O3	29.570	32.031	33.554	33.464	32.404	28.202
	Fe2O3	0.809	0.588	0.425	0.505	0.549	1.232
	CaO	12.692	15.370	16.653	16.824	15.418	12.101
	Na2O	4.113	2.790	1.913	1.809	2.496	4.091
	K2O	0.214	0.106	0.059	0.069	0.113	0.675
	Total	100.315	100.643	99.901	100.003	100.224	100.453
cpfu	Si	2.395	2.261	2.173	2.173	2.246	2.449
	Al	1.577	1.715	1.817	1.811	1.742	1.503
	Fe3	0.028	0.020	0.015	0.017	0.019	0.042
	Ca	0.616	0.748	0.820	0.828	0.753	0.586
	Na	0.361	0.246	0.170	0.161	0.221	0.359
	K	0.012	0.006	0.003	0.004	0.007	0.039
	Total	4.989	4.997	4.998	4.995	4.987	4.978
mole (%)	An	63.0	75.3	81.2	83.5	77.2	61.6
µg/g	Li	8.836	8.203	9.286	8.388	8.866	11.449
	Be	0.366	0.248	0.221	0.225	0.236	0.379
	B	0.246	0.106	0.119	0.345	0.105	0.239

	Data Point	4	12	20	30	38	46	56	66	75	83	91	99	107	115	123	132	143
	Name	San27Pl1	San27Pl1	San27Pl1	San27Pl1	San27Pl1	San27Pl1	San27Pl1	San27Pl1	San27Pl1	San27Pl1	San27Pl1	San27Pl1	San27Pl1	San27Pl1	San27Pl1	San27Pl1	San27Pl1
	Mineral	Fsp	Fsp	Fsp	Fsp	Fsp	Fsp	Fsp	Fsp	Fsp	Fsp	Fsp	Fsp	Fsp	Fsp	Fsp	Fsp	Fsp
	Distance	40	120	200	300	380	460	560	660	750	830	910	990	1070	1150	1230	1320	1430
%	SiO2	50.900	53.993	54.092	54.278	53.506	53.634	53.852	53.553	53.732	53.504	54.147	53.673	53.867	53.726	54.661	54.160	54.246
	Al2O3	30.490	29.348	29.246	28.959	29.575	29.634	29.558	29.534	29.585	29.655	29.180	29.709	29.554	29.570	28.995	29.139	29.252
	Fe2O3	0.793	0.609	0.535	0.518	0.555	0.569	0.572	0.580	0.600	0.598	0.542	0.550	0.566	0.616	0.605	0.638	0.559
	CaO	13.371	11.461	11.294	11.289	11.605	11.799	11.836	11.949	11.773	11.886	11.533	11.824	11.917	12.008	11.115	11.447	11.561
	Na2O	3.600	4.870	4.818	4.928	4.807	4.695	4.641	4.633	4.650	4.681	4.816	4.622	4.846	4.760	5.025	4.807	4.804
	K2O	0.128	0.247	0.246	0.240	0.224	0.255	0.210	0.242	0.236	0.222	0.208	0.219	0.213	0.229	0.247	0.223	0.231
	Total	99.282	100.528	100.231	100.212	100.272	100.586	100.669	100.491	100.576	100.546	100.426	100.597	100.963	100.909	100.648	100.414	100.653
cpfu	Si	2.334	2.431	2.439	2.448	2.416	2.415	2.421	2.415	2.419	2.411	2.438	2.415	2.418	2.414	2.454	2.439	2.438
	Al	1.647	1.557	1.554	1.539	1.574	1.573	1.566	1.570	1.570	1.575	1.549	1.576	1.564	1.566	1.534	1.547	1.549
	Fe3	0.027	0.021	0.018	0.018	0.019	0.019	0.019	0.020	0.020	0.020	0.018	0.019	0.019	0.021	0.020	0.022	0.019
	Ca	0.657	0.553	0.546	0.546	0.561	0.569	0.570	0.577	0.568	0.574	0.556	0.570	0.573	0.578	0.535	0.552	0.557
	Na	0.320	0.425	0.421	0.431	0.421	0.410	0.405	0.405	0.406	0.409	0.420	0.403	0.422	0.415	0.437	0.420	0.419
	K	0.007	0.014	0.014	0.014	0.013	0.015	0.012	0.014	0.014	0.013	0.012	0.013	0.012	0.013	0.014	0.013	0.013
	Total	4.993	5.000	4.992	4.996	5.004	5.001	4.994	5.000	4.996	5.002	4.994	4.995	5.008	5.007	4.995	4.993	4.994
mole (%)	An	65.0	56.4	56.6	55.2	57.7	58.2	58.4	58.6	58.6	58.4	57.7	58.1	57.8	57.0	55.3	55.9	57.4
µg/g	Li	17.175	26.170	23.636	21.872	19.719	22.832	22.367	21.568	19.271	18.120	18.849	18.385	18.538	19.818	20.002	22.232	25.822
	Be	0.361	0.613	0.659	0.693	0.642	0.626	0.653	0.634	0.641	0.597	0.635	0.626	0.608	0.668	0.629	0.627	0.658
	B	0.158	0.247	0.242	0.262	0.237	0.223	0.261	0.231	0.231	0.245	0.233	0.224	0.241	0.258	0.250	0.224	0.253

	Data Point	4	12	20	28	36	44
	Name	San30Pl2	San30Pl2	San30Pl2	San30Pl2	San30Pl2	San30Pl2
	Mineral	Fsp	Fsp	Fsp	Fsp	Fsp	Fsp
	Distance	40	120	200	280	360	440
%	SiO2	46.718	46.585	46.746	46.707	46.692	46.061
	Al2O3	34.352	34.235	34.242	34.080	34.227	34.342
	Cr2O3	0.000	0.000	0.000	0.000	0.000	0.000
	Fe2O3	1.129	1.180	1.209	1.176	1.060	1.165
	CaO	17.229	17.421	17.515	17.139	17.306	17.744
	Na2O	1.612	1.774	1.724	1.712	1.721	1.596
	K2O	0.049	0.043	0.048	0.019	0.046	0.048
	Total	101.089	101.238	101.484	100.833	101.052	100.956
cpfu	Si	2.130	2.124	2.127	2.135	2.130	2.109
	Al	1.846	1.840	1.836	1.836	1.841	1.853
	Fe3	0.039	0.040	0.041	0.040	0.036	0.040
	Ca	0.841	0.851	0.854	0.839	0.846	0.870
	Na	0.142	0.157	0.152	0.152	0.152	0.142
	K	0.003	0.003	0.003	0.001	0.003	0.003
	Total	5.001	5.015	5.012	5.003	5.008	5.017
mole (%)	AN	86.6	84.3	85.0	84.9	84.7	86.0
µg/g	Li	2.725	4.281	4.051	4.083	3.969	3.531
	Be	0.071	0.092	0.085	0.083	0.083	0.097
	B	0.048	0.054	0.056	0.067	0.055	0.049

	Data Point	3	20	53	60	78	85	92	99
	Name	San32Pl2	San32Pl2	San32Pl2	San32Pl2	San32Pl2	San32Pl2	San32Pl2	San32Pl2
	Mineral	Fsp	Fsp	Fsp	Fsp	Fsp	Fsp	Fsp	Fsp
	Distance	30	200	530	600	780	850	920	990
%	SiO2	48.795	48.519	47.419	47.775	47.854	47.83	48.887	50.162
	Al2O3	31.780	32.356	33.399	32.783	33.326	32.564	32.366	31.875
	Fe2O3	0.927	0.748	0.848	0.807	0.793	0.838	0.799	1.088
	MgO	0.093	0.078	0.073	0.091	0.083	0.081	0.093	0.095
	CaO	14.672	15.124	16.334	15.756	16.043	15.636	15.142	14.605
	Na2O	3.073	2.793	2.157	2.530	2.488	2.531	2.744	3.214
	K2O	0.113	0.086	0.053	0.055	0.060	0.060	0.072	0.105
	Total	99.453	99.704	100.283	99.797	100.647	99.540	100.103	101.144
cpfu	Si	2.247	2.229	2.173	2.198	2.184	2.205	2.235	2.269
	Al	1.725	1.752	1.804	1.777	1.793	1.769	1.744	1.699
	Fe3	0.032	0.026	0.029	0.028	0.027	0.029	0.027	0.037
	Mg	0.006	0.005	0.005	0.006	0.006	0.006	0.006	0.006
	Ca	0.724	0.744	0.802	0.777	0.785	0.772	0.742	0.708
	Na	0.274	0.249	0.192	0.226	0.220	0.226	0.243	0.282
	K	0.007	0.005	0.003	0.003	0.003	0.004	0.004	0.006
	Total	5.015	5.010	5.008	5.014	5.018	5.011	5.003	5.007
mole (%)	An	70.8	76.0	81.0	75.6	79.5	78.3	75.5	69.5
µg/g	Li	5.802	6.843	7.938	8.142	6.297	5.870	6.072	5.542
	Be	0.225	0.180	0.222	0.222	0.202	0.205	0.220	0.253
	B	0.130	0.187	0.115	0.148	0.126	0.127	0.134	0.144

	Data Point	3	8	15	21	25	32	36
	Name	San31Cpx1a	San31Cpx1a	San31Cpx1a	San31Cpx1a	San31Cpx1a	San31Cpx1a	San31Cpx1a
	Mineral	Cpx	Cpx	Cpx	Cpx	Cpx	Cpx	Cpx
	Distance	30	80	150	210	250	320	360
%	SiO2	52.787	52.701	52.834	52.952	53.482	51.358	51.535
	TiO2	0.329	0.330	0.375	0.369	0.322	0.400	0.407
	Al2O3	2.640	2.443	2.460	2.213	2.405	3.830	3.533
	Cr2O3	0.582	0.465	0.453	0.417	0.457	0.704	0.669
	Fe2O3	0.951	0.484	0.466	0.898	0.623	0.855	0.732
	FeO	3.831	4.603	4.477	4.500	4.644	4.715	4.475
	MnO	0.074	0.106	0.177	0.128	0.173	0.179	0.170
	MgO	16.894	16.732	16.871	17.105	17.270	15.646	15.778
	CaO	22.324	21.764	21.740	21.623	21.661	21.961	22.045
	Na2O	0.170	0.193	0.189	0.173	0.191	0.178	0.210
	K2O	0.002	0.000	0.018	0.008	0.000	0.008	0.000
	Total	100.584	99.820	100.060	100.386	101.227	99.834	99.553
cpfu	Si	1.9191	1.9316	1.9309	1.9303	1.9318	1.8903	1.8996
	Ti	0.0090	0.0091	0.0103	0.0101	0.0087	0.0111	0.0113
	Al	0.1131	0.1055	0.1060	0.0951	0.1024	0.1661	0.1535
	Cr	0.0167	0.0135	0.0131	0.0120	0.0131	0.0205	0.0195
	Fe3	0.0260	0.0133	0.0128	0.0246	0.0169	0.0237	0.0203
	Fe2	0.1165	0.1411	0.1368	0.1372	0.1403	0.1451	0.1379
	Mn	0.0023	0.0033	0.0055	0.0040	0.0053	0.0056	0.0053
	Mg	0.9156	0.9142	0.9192	0.9296	0.9299	0.8585	0.8670
	Ca	0.8696	0.8547	0.8513	0.8445	0.8383	0.8660	0.8706
	Na	0.0120	0.0137	0.0134	0.0122	0.0134	0.0127	0.0150
	K	0.0001	0.0000	0.0008	0.0004	0.0000	0.0004	0.0000
	Total	4	4	4	4	4	4	4
	Mg#	88.7	86.6	87.0	87.1	86.9	85.5	86.3
µg/g	Li	5.398	4.084	1.938	0.694	0.857	2.244	6.663
	Be	0.015	0.011	0.010	0.015	0.029	0.012	0.018
	B	0.075	0.048	0.053	0.049	0.151	0.076	0.064

	Data Point	3	8	13	19	26	33	40	47	56	65	72
	Name	San30Opx1a	San30Opx1a	San30Opx1a	San30Opx1a	San30Opx1a	San30Opx1a	San30Opx1a	San30Opx1a	San30Opx1a	San30Opx1a	San30Opx1a
	Mineral	Opx	Opx	Opx	Opx	Opx	Opx	Opx	Opx	Opx	Opx	Opx
	Distance	30	80	130	190	260	330	400	470	560	650	720
%	SiO2	52.656	52.644	53.033	52.671	53.125	53.208	52.892	52.879	52.819	52.425	52.746
	TiO2	0.370	0.380	0.339	0.352	0.312	0.290	0.270	0.265	0.335	0.360	0.415
	Al2O3	1.194	1.294	1.204	1.245	1.086	1.030	1.045	1.081	1.064	1.062	0.805
	Cr2O3	0.072	0.028	0.000	0.006	0.000	0.000	0.000	0.012	0.061	0.018	0.000
	Fe2O3	1.239	1.414	0.767	0.503	1.250	0.651	0.258	1.129	0.809	0.027	0.779
	FeO	18.789	17.080	18.656	18.813	18.561	18.916	19.597	19.560	20.359	21.262	21.370
	MnO	0.550	0.484	0.545	0.611	0.569	0.542	0.435	0.491	0.524	0.528	0.542
	MgO	23.042	21.797	23.170	22.994	23.609	23.314	22.701	22.692	22.366	21.532	21.737
	CaO	2.053	5.023	2.374	2.188	1.907	2.095	2.155	2.127	2.043	2.026	1.920
	Na2O	0.053	0.089	0.036	0.016	0.030	0.038	0.047	0.047	0.018	0.051	0.050
	K2O	0.000	0.006	0.000	0.000	0.000	0.000	0.002	0.006	0.000	0.000	0.028
	Total	100.018	100.239	100.125	99.399	100.449	100.084	99.402	100.289	100.398	99.291	100.392
cpfu	Si	1.947	1.945	1.955	1.956	1.952	1.962	1.968	1.955	1.956	1.968	1.962
	Ti	0.010	0.011	0.009	0.010	0.009	0.008	0.008	0.007	0.009	0.010	0.012
	Al	0.052	0.056	0.052	0.055	0.047	0.045	0.046	0.047	0.046	0.047	0.035
	Cr	0.002	0.001	0.000	0.000	0.000	0.000	0.000	0.000	0.002	0.001	0.000
	Fe3	0.034	0.039	0.021	0.014	0.035	0.018	0.007	0.031	0.023	0.001	0.022
	Fe2	0.581	0.528	0.575	0.584	0.570	0.583	0.610	0.605	0.630	0.667	0.665
	Mn	0.017	0.015	0.017	0.019	0.018	0.017	0.014	0.015	0.016	0.017	0.017
	Mg	1.270	1.200	1.273	1.273	1.293	1.282	1.259	1.251	1.235	1.205	1.206
	Ca	0.081	0.199	0.094	0.087	0.075	0.083	0.086	0.084	0.081	0.081	0.077
	Na	0.004	0.006	0.003	0.001	0.002	0.003	0.003	0.003	0.001	0.004	0.004
	Total	4	4	4	4	4	4	4	4	4	4	4
	Mg#	68.6	69.5	68.9	68.5	69.4	68.7	67.4	67.4	66.2	64.4	64.5
µg/g	Li	4.485	4.655	4.265	3.826	2.347	3.897	4.743	4.651	4.825	4.421	4.249
	Be	0.037	0.041	0.038	0.043	0.034	0.038	0.035	0.038	0.040	0.041	0.036
	B	0.129	0.134	0.113	0.099	0.122	0.086	0.069	0.112	0.090	0.105	0.199

	Data Point	2	6	11	17	21	25	29	33
	Name	San31Cpx2	San31Cpx2	San31Cpx2	San31Cpx2	San31Cpx2	San31Cpx2	San31Cpx2	San31Cpx2
	Mineral	Cpx	Cpx	Cpx	Cpx	Cpx	Cpx	Cpx	Cpx
	Distance	20	60	110	170	210	250	290	330
%	SiO2	52.522	52.530	51.906	50.123	49.409	50.690	49.927	51.803
	TiO2	0.525	0.344	0.432	0.682	0.757	0.619	0.651	0.475
	Al2O3	1.770	2.109	2.190	3.834	4.041	4.457	4.676	2.592
	Cr2O3	0.104	0.134	0.053	0.032	0.044	0.362	0.262	0.164
	Fe2O3	1.106	0.809	1.707	2.840	3.370	2.015	2.622	1.519
	FeO	7.704	5.236	5.776	5.232	5.064	4.502	4.331	6.111
	MnO	0.289	0.139	0.170	0.208	0.217	0.155	0.129	0.291
	MgO	16.490	16.463	15.896	14.342	14.097	14.886	14.664	16.213
	CaO	19.563	21.732	21.279	21.890	21.700	22.489	22.388	20.343
	Na2O	0.177	0.120	0.187	0.314	0.299	0.247	0.216	0.216
	K2O	0.000	0.000	0.014	0.013	0.053	0.006	0.000	0.000
	Total	100.250	99.616	99.610	99.510	99.051	100.428	99.867	99.727
cpfu	Si	1.936	1.936	1.923	1.868	1.853	1.862	1.847	1.915
	Ti	0.015	0.010	0.012	0.019	0.021	0.017	0.018	0.013
	Al	0.077	0.092	0.096	0.168	0.179	0.193	0.204	0.113
	Cr	0.003	0.004	0.002	0.001	0.001	0.011	0.008	0.005
	Fe3	0.031	0.022	0.048	0.080	0.095	0.056	0.073	0.042
	Fe2	0.238	0.161	0.179	0.163	0.159	0.138	0.134	0.189
	Mn	0.009	0.004	0.005	0.007	0.007	0.005	0.004	0.009
	Mg	0.906	0.904	0.878	0.797	0.788	0.815	0.809	0.893
	Ca	0.773	0.858	0.844	0.874	0.872	0.885	0.888	0.806
	Na	0.013	0.009	0.013	0.023	0.022	0.018	0.015	0.015
	K	0.000	0.000	0.001	0.001	0.003	0.000	0.000	0.000
	Total	4	4	4	4	4	4	4	4
	Mg#	79.2	84.9	83.1	83.0	83.2	85.5	85.8	82.5
µg/g	Li	11.990	1.981	0.991	1.029	1.162	1.440	3.072	8.487
	Be	0.121	0.012	0.023	0.050	0.055	0.035	0.029	0.024
	B	0.539	0.054	0.068	0.094	0.106	0.134	0.071	0.071

	Data Point	3	7	11	16	21	26	37	43	47	55
	Name	San22Ol1	San22Ol1	San22Ol1	San22Ol1	San22Ol1	San22Ol1	San22Ol1	San22Ol1	San22Ol1	San22Ol1
	Mineral	Ol	Ol	Ol	Ol	Ol	Ol	Ol	Ol	Ol	Ol
	Distance	30	70	110	160	210	260	370	430	470	550
%	SiO2	38.216	39.324	39.324	39.224	39.598	39.014	38.46	39.275	39.346	39.53
	TiO2	0.023	0.037	0.005	0.033	0	0.007	0.023	0.002	0	0
	Al2O3	0.011	0.015	0.021	0.034	0.028	0.023	0.002	0.055	0.019	0.025
	Cr2O3	0.006	0.019	0	0.001	0.035	0.019	0.035	0	0.012	0.004
	FeO	23.48	16.48	16.612	18.668	16.691	19.443	20.095	17.164	16.867	16.818
	MnO	0.424	0.288	0.314	0.343	0.279	0.331	0.34	0.191	0.298	0.217
	NiO	0.084	0.165	0.158	0.109	0.185	0.093	0.099	0.151	0.188	0.174
	MgO	37.719	43.116	42.727	41.112	42.689	41.19	40.638	43.019	43.468	42.851
	Ba	0	0.032	0.007	0	0	0.01	0	0	0	0.008
	CaO	0.194	0.171	0.176	0.16	0.171	0.168	0.162	0.215	0.176	0.158
	Na2O	0	0.012	0.013	0.001	0.001	0	0.004	0.018	0.016	0.023
	K2O	0	0	0.01	0.001	0	0	0	0	0.004	0.002
	Total	100.157	99.659	99.367	99.686	99.677	100.298	99.858	100.09	100.394	99.81
cpfu	Si	0.999	0.999	1.003	1.006	1.006	0.998	0.993	0.996	0.994	1.003
	Ti	0.000	0.001	0.000	0.001	0.000	0.000	0.000	0.000	0.000	0.000
	Al	0.000	0.000	0.001	0.001	0.001	0.001	0.000	0.002	0.001	0.001
	Cr	0.000	0.000	0.000	0.000	0.001	0.000	0.001	0.000	0.000	0.000
	Fe2	0.513	0.350	0.354	0.400	0.355	0.416	0.434	0.364	0.357	0.357
	Mn	0.009	0.006	0.007	0.007	0.006	0.007	0.007	0.004	0.006	0.005
	Ni	0.002	0.003	0.003	0.002	0.004	0.002	0.002	0.003	0.004	0.004
	Mg	1.470	1.633	1.624	1.571	1.617	1.571	1.564	1.627	1.638	1.622
	Ca	0.005	0.005	0.005	0.004	0.005	0.005	0.004	0.006	0.005	0.004
	Na	0.000	0.001	0.001	0.000	0.000	0.000	0.000	0.001	0.001	0.001
	Total	3.000	3.000	2.997	2.993	2.993	3.001	3.006	3.003	3.006	2.997
	Mg#	74.1	82.3	82.1	79.7	82.0	79.1	78.3	81.7	82.1	82.0
µg/g	Li	3.857	2.285	2.342	2.664	2.446	2.604	3.047	2.427	2.486	2.468
	Be	0.005	0.003	0.003	0.004	0.003	0.003	0.003	0.000	0.002	0.004
	B	0.312	0.201	0.224	0.145	0.099	0.086	0.078	0.080	0.090	0.121